BERGISCHE
UNIVERSITÄT
WUPPERTAL

Bergische Universität Wuppertal
Fakultät 4
Mathematik und Naturwissenschaften
Fachgruppe Physik

Search for Inclined Photon Air Showers with the AugerPrime Radio Detector

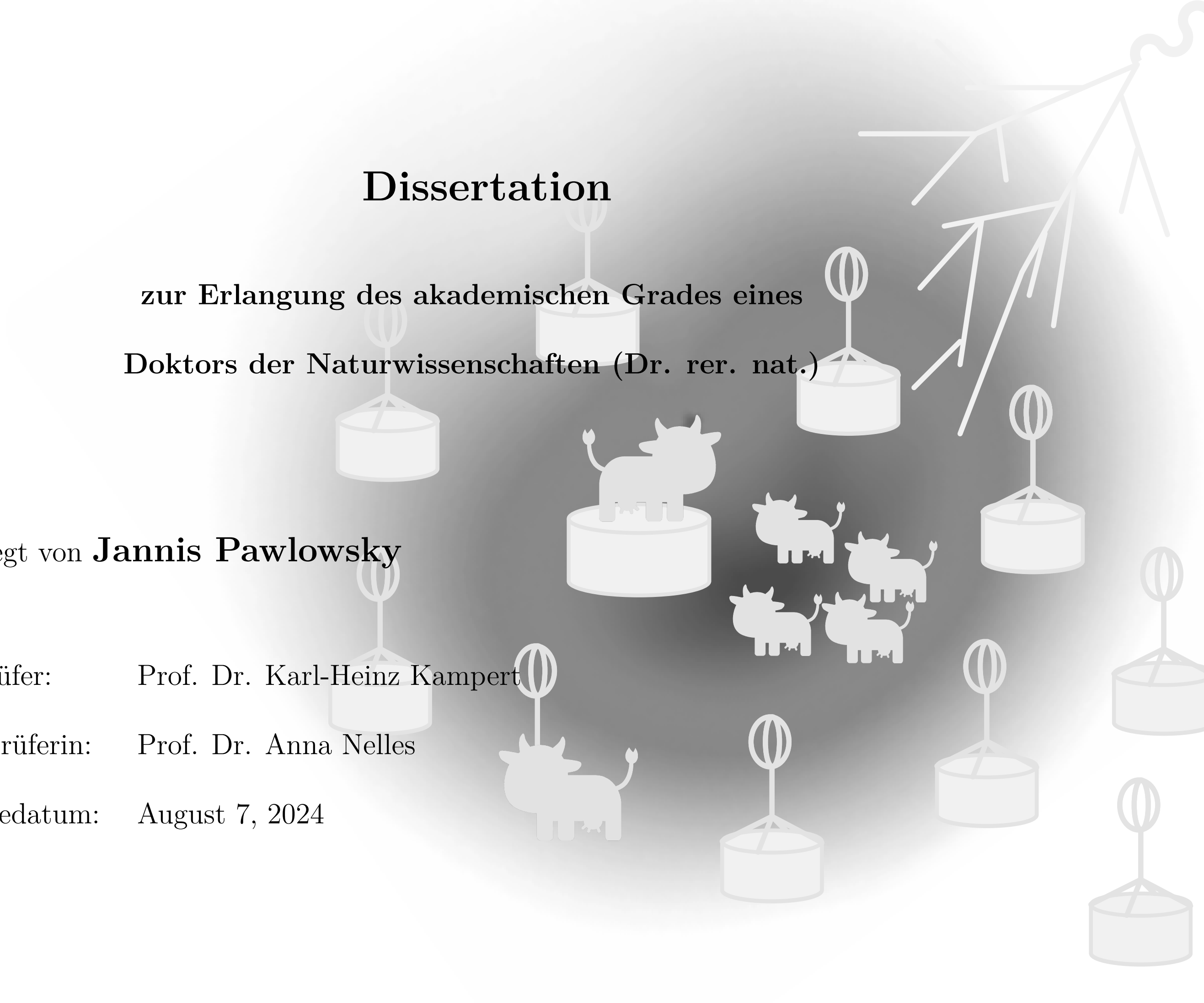

Dissertation

zur Erlangung des akademischen Grades eines

Doktors der Naturwissenschaften (Dr. rer. nat.)

vorgelegt von **Jannis Pawlowsky**

Erstprüfer:	Prof. Dr. Karl-Heinz Kampert
Zweitprüferin:	Prof. Dr. Anna Nelles
Abgabedatum:	August 7, 2024

ABSTRACT

The origin of ultra-high-energy cosmic rays is one of the most important open questions in high-energy astrophysics. The generation of photons by cosmic rays within the source or during their propagation may provide hints to the cosmic ray's origins. As photons are non-charged particles, they traverse on straight lines from their origin, which allows source pinpointing independent of magnetic fields. The detection of such ultra-high-energy photons is one of the main objectives of the AugerPrime upgrade. The incorporated Radio Detector is ideally suited for measuring and identifying the resulting pure electromagnetic air showers. However, for inclined photon air showers, the current setup of the Pierre Auger Observatory shows inefficiencies in the photon detection as the Radio Detector can only unfold its potential when a designated trigger is implemented. This thesis examines the possibility of having a radio trigger at the Pierre Auger Observatory for the photon detection. By utilising CORSIKA air shower simulations, it is demonstrated that the aperture for photons is enhanced by a factor of 3-4 for an aimed trigger in comparison to the current setup. For having an actual implementation of this trigger, this work presents the steps for developing such a trigger: the noise environment in which the trigger has to function, trigger features to counteract limited bandwidth, and the fit into the general trigger scheme of the Observatory. Moreover, a field test is carried out to evaluate the trigger performance under real conditions. The results indicate that a simplistic radio trigger cannot be easily integrated into the regular trigger scheme of the Pierre Auger Observatory due to severe bandwidth limitations. Various options are proposed and studied in order to achieve a significant increase in the aperture while being secure from noise events. In particular, this encompasses requesting particle triggers contributing to the event, or rejecting radio events coming from the Earth's horizon. The thesis concludes by demonstrating the significance of including the Radio Detector in photon searches. Simulation reconstructions suggest a precise and accurate estimation of the photon arrival direction with a resolution of better than 0.5°. Furthermore, one gains direct access to the primary energy with a resolution better than 10%. An outlook on future discrimination studies incorporating the Radio Detector shows promising results for an efficient and solid identification of photons.

ZUSAMMENFASSUNG

Der Ursprung der ultrahochenergetischen kosmischen Strahlung gehört zu den wichtigsten offenen Fragen in der hochenergetischen Astrophysik. Die Erzeugung von Photonen durch kosmische Strahlen während ihrer Ausbreitung kann Hinweise auf ihren Ursprung geben. Da es sich bei Photonen um ungeladene Teilchen handelt, bewegen sie sich in geraden Linien von ihrem Ursprung, was eine Quellenbestimmung unabhängig von Magnetfeldern ermöglicht. Die Detektion solcher ultrahochenergetischer Photonen ist eines der Hauptziele des AugerPrime-Upgrades. Der beinhaltete Radiodetektor ist ideal geeignet, um die resultierenden reinen elektromagnetischen Luftschauer zu messen und zu identifizieren. Im Falle geneigter Photon induzierter Luftschauer zeigt das aktuelle Setup des Pierre-Auger-Observatoriums jedoch Ineffizienzen in der Detektion. Der Radiodetektor kann sein volles Potenzial nur mit einem speziellen Trigger entfalten. Diese Arbeit untersucht die Möglichkeit, am Pierre-Auger-Observatorium einen Radiotrigger für die Photonendetektion zu implementieren. Durch die Nutzung von CORSIKA-Luftschauersimulationen wird gezeigt, dass die Apertur für Photonen bei einem angestrebten Trigger im Vergleich zum aktuellen Setup um das 3- bis 4-fache verbessert wird. Für die tatsächliche Implementierung dieses Triggers präsentiert diese Arbeit die Schritte zur Entwicklung eines solchen Triggers: die Rauschumgebung, in welcher der Trigger funktionieren muss, Triggermerkmale zur Bewältigung begrenzter Bandbreite und die Integration in das allgemeine Triggerschema des Observatoriums. Ferner wird ein Feldtest durchgeführt, um das Triggerverhalten unter realen Bedingungen zu bewerten. Die Ergebnisse zeigen, dass ein simplizistischer Radiotrigger aufgrund erheblicher Bandbreitenbeschränkungen nicht leicht in das reguläre Triggerschema des Pierre-Auger-Observatoriums integriert werden kann. Verschiedene Optionen werden vorgeschlagen und untersucht, um eine signifikante Erhöhung der Apertur zu erreichen und gleichzeitig vor Rauschereignissen sicher zu sein. Dies umfasst insbesondere das Anfordern von Teilchentriggern, oder das Verwerfen von Radioereignissen, die vom Horizont der Erde kommen. Die Arbeit schließt mit einer Demonstration der Bedeutung des Radiodetektors bei der Photonen-Suche. Simulationsrekonstruktionen deuten auf eine präzise und genaue Schätzung der Ankunftsrichtung der Photonen mit einer Auflösung von besser *als 0,5° hin. Ebenso erhält man direkten Zugang zur Primärenergie mit einer Auflösung besser als 10 %. Ein Ausblick auf zukünftige Diskriminierungsstudien unter Einbeziehung des Radiodetektors zeigt vielversprechende Ergebnisse für eine effiziente und solide Identifizierung von Photonen.*

CONTENTS

CHAPTER 1

STRUCTURE AND GOALS OF THIS THESIS

Over the course of the past century, the comprehension of the Universe has undergone a significant transformation. Einstein's general relativity changed physicist's views on how time and space are related, Lemaître revolutionised ideas about the start of the Universe; and Friedmann introduced a theory about an expanding cosmos. However, questions that appear easy to answer at first glance remain unanswered. Which objects are the most energetic and extreme in the Universe? How do they accelerate particles to the highest energies ever observed? Do all particles originate from the same entity? Limited knowledge of galactic and extra-galactic magnetic fields complicates the task of solving these riddles and introduces uncertainties for backtracking of charged particles from Earth to their source. Detecting an ultra-high-energy photon would resolve this conflict; as non-charged particles, photons are not deflected by magnetic fields and would directly pinpoint their creation location.

The Pierre Auger Observatory in Argentina has made the determination of the sources of ultra-high-energy particles for its mission. Its measurements (and of other observatories) of charged particles resulted in a list of source candidates, nonetheless, a single photon detection would result in a major jump towards uncovering the sources of ultra-high-energy particles. This discovery could be provided by the AugerPrime upgrade, which holds the potential to accomplish this break-through. The incorporation of the Radio Detector complements the existing setup and results in an apparatus with optimal sensitivity to purely electromagnetic air showers in the atmosphere, caused by ultra-high-energy photons.

In order to unleash the full potential of the Radio Detector, a designated data read-out is required, which presents itself in the form of an event triggering by the Radio Detector. This work examines the possibility of integrating such a triggering into the general trigger scheme of the Pierre Auger Observatory. It presents the potential of the trigger, the difficulties of implementation, and provides an outlook on analyses in case of actual photon detection. In the end, this work should be the next small piece in the puzzle for demasking the most extreme objects in our universe.

The thesis will commence with a comprehensive overview of cosmic rays in Chapter 2. It will be presented how cosmic rays can generate photons of extremely high energy and their potential propagation to Earth. The incoming particles then produce particle air showers in the atmosphere. It will be discussed how photon-induced air showers differentiate from hadron-induced air showers. Finally, the mechanisms behind the resulting radio emission in these air showers are examined.

Both, air showers and the radio emission can be detected by the Pierre Auger Observatory, which will be outlined in Chapter 3. While the general description is kept brief, it will rather focus on the parts important for this work: the Radio Detector as part of AugerPrime, the triggering and network system of Auger, and previous photon searches. The Chapter will conclude with the description of the general challenge of detecting inclined photon showers with the current setup of the Pierre Auger Observatory, motivating the necessity of a radio trigger.

In order to further elaborate on the challenge of designing a radio trigger, the sources of noise interfering with the detection of radio signals from air showers at Auger are discussed in Chapter 4. With measured test data, it is possible to quantify the occurrence of noise, the properties of noise traces, and perform a categorisation of noise. It will be discussed which noise traces are challenging for a radio trigger and what their origin is. Finally, a methodology has been devised to locate the noise source.

The understanding of the noise interference helps to develop a radio trigger, as described in Chapter 5. The Chapter begins with a description of the designed trigger, combined with additional features for rejecting noise. The trigger concept is subjected to field tests, and the outcomes are analysed. Finally, a discussion of the trigger's integration into the Auger reconstruction framework is conducted.

Using CoREAS simulations, one can quantify the photon trigger efficiency that can be achieved ideally. Moreover, it is discussed what efficiency is feasible for a realistic implementation. This is presented in Chapter 6. Based on the results, various options for an implementation are discussed with their respective benefits and downsides.

In the case of triggering a photon, its properties as arrival direction and primary energy need to be reconstructed, independently of the particles reaching the ground. Chapter 7 focuses on the reconstruction process employing an iterative, particle-independent approach. By utilising this technique, a significant proportion of triggered events can be reconstructed, with a level of precision that is sufficient for identifying the primary particles' source. Furthermore, it is shown that the energy reconstruction performs well and provides direct access to the photon energy. An outlook is presented, which indicates a promising discrimination of photons and hadrons when incorporating the Radio Detector.

Chapter 8 combines the outcome of the aforementioned chapters, demonstrating the anticipated aperture for photons and the resulting sky coverage.

The thesis will conclude in Chapter 9 with a summary of the results and an outlook for future developments of the trigger.

CHAPTER 2

COSMIC RAY AND AIR SHOWER PHYSICS

2.1 Cosmic Rays

Cosmic Rays (CRs) have been under discussion for a long time [1]. There are different definitions of CRs regarding the particle type, but all have in common that CRs are generally high-energy particles originating from outer space and travelling through the Universe. In this work, the term CRs encompasses all charged particles, whereas photons and neutrinos are treated separately. CRs were first discovered by Victor Hess with his famous balloon flights [2], in which he argued that enhanced radiation for increasing altitude in the atmosphere can only be explained with non-terrestrial sources. He was correct in his assumption, but after more than 100 years and numerous experiments, the exact sources of Ultra-High-Energy (UHE) CRs remain uncertain. One approach for unravelling this mystery involves analysing the energy spectrum of CRs, as observed on Earth.

2.1.1 Energy spectrum

The flux of CRs ranges over multiple orders of magnitude and can generally be described by the formula

$$\frac{dN}{dE} \propto E^{-\gamma}, \tag{2.1}$$

where γ is the spectral index and E the energy of the CR. At the low-energy end of the spectrum, the heliosphere of the solar system shields the Earth from low energy CRs [3]. At the edge of the heliosphere, the solar wind slows down due to interactions with the interstellar medium. The speed of the solar wind falls below the speed of sound (relative to the sun), which results in a shock front. The compressed magnetic field then deflects CRs. Thus, it is believed that the Sun is the only source of CRs with energies below a few GeVs reaching the Earth. This energy is concurrently the upper limit of particles energy coming from the Sun [4].

For higher energies, galactic sources begin to dominate and are the main source of CRs up to a feature in the spectrum called the *Knee* at $E \approx 3\,\mathrm{PeV}$ [5, 6]. In this region of energy, the spectrum exhibits a steep decline, with a spectral index of $\gamma \approx 2.7$, which is depicted in Figure 2.1 (left). The *Knee* is assumed to be a feature caused by the maximum energy to which regular galactic sources can accelerate protons, which changes the spectral index to $\gamma \approx 3.1$. Theories of the feature origin are in agreement with measurements indicating a predominant light mass of CRs below the *Knee* and increasing mass until a feature called the *second Knee* at $E \approx 100\,\mathrm{PeV}$ [5, 6]. The *second Knee* is accordingly believed to be the maximum energy to which regular galactic sources can accelerate the heavier elements such as iron. Due to the increased charge of heavier elements, it is expected that they can be accelerated more easily to higher energies, for example by processes like one-shot acceleration [7], or the first and second order Fermi acceleration [8, 9].

While many models explain accelerations of CRs by supernova remnants up to energies of $E \approx 1\,\mathrm{PeV}$ [10], many unanswered questions remain concerning more energetic Galactic CRs. Popular theories suggest that the acceleration to higher energies is caused by exceptional and more energetic young supernova remnants [11], Galactic Wind Halos [12] or Superbubbles [13].

At $E \approx 5\,\mathrm{EeV}$, a new feature appears, the so-called *Ankle* [14]. It is assumed that extra-galactic CRs begin to dominate the spectrum. This also indicates that there is a transition region between the *second Knee* and the *Ankle* with $\gamma \approx 3.3$, where both galactic and extra-galactic CRs can be found. It remains uncertain which sources contribute here and how they accelerate CRs to these energies. Nonetheless, the transition explanation is consistent with the observed mass composition with a light mean mass in the *Ankle* region.

For $E \geq 5\,\mathrm{EeV}$, the spectrum becomes even more mysterious and has only been described more accurately with large collected statistics in recent years. As seen in Fig. 2.1 (right), the spectrum first softens to $\gamma \approx 2.5$ and then hardens to $\gamma \approx 3.1$ at $E \approx 10\,\mathrm{EeV}$. This spectral change is nowadays often referred to as the *Instep*, lasting until $E \approx 50\,\mathrm{EeV}$ [15]. For even higher energies, the spectrum changes to $\gamma \approx 5.1$, which is described as a cut-off setting in. This cut-off is of great interest to current astrophysical research, and there are multiple possible explanations for this:

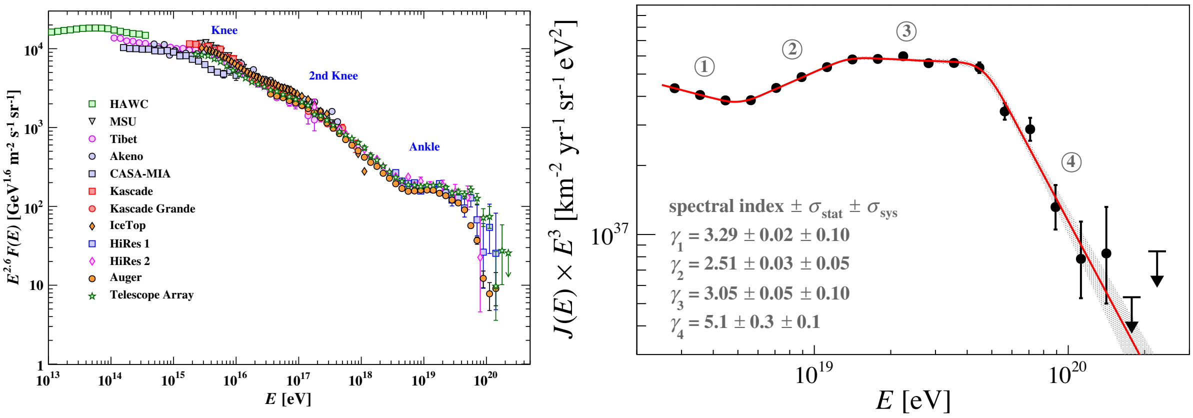

Figure 2.1: (Left) CR spectrum for different energies. The distinct markers and colours represent measured data and upper limits by different observatories. Spectrum features are marked in blue. Note the scaling factor of $E^{2.6}$ for the flux. Plot from [16]. (Right) Zoom of the CR spectrum for energies beyond the *Ankle*. Black markers represent data and upper limits of Auger, the red line depicts the step-wise spectrum fit. Note the scaling factor of E^3 for the flux. Plot from [14].

- **GZK-effect:** The Greisen–Zatsepin–Kuzmin (GZK) limit describes the minimum energy needed for the production of a Δ resonance of protons and blue-shifted cosmic microwave background (CMB) photons [17, 18]:

$$p + \gamma_{\text{CMB}} \rightarrow \Delta^+ \rightarrow p + \pi^0 \tag{2.2}$$

$$p + \gamma_{\text{CMB}} \rightarrow \Delta^+ \rightarrow n + \pi^+. \tag{2.3}$$

  The limit is calculated to be at ≈ 50 EeV and on average, the proton then loses 20 % of its energy to the pions. This energy loss, when coupled with the mean free path lengths of protons, results in the so-called GZK-horizon. No protons with $E \geq 50$ EeV are probable to be observed from sources more distant than 50 Mpc. Nonetheless, events were observed at energies that cannot be explained by the accelerations of sources within the GZK-horizon. This shows that the GZK-limit does not serve as the (sole) explanation for the spectrums cut-off.

- **Photo-disintegration:** When other heavier nuclei collide with highly blue-shifted CMB photons, the nuclei can break apart, reducing the energy of the CR in a process called photo-disintegration [19]. This is also referred to as the GZK-effect for heavier nuclei. It is a process that has a large impact on the spectrum, as the threshold for its occurrence is dependent on the primary particle [20] and could result in multiple breaks in the spectrum. This is connected to the puzzle of mass composition at the highest energies. Only if the mass composition is known, one could evaluate which spectral break is connected to the photo-disintegration.

- **Maximum energy:** Similar to the spectral breaks between the knees, a maximum energy of sources (in this case extra-galactic) could be connected to the features beyond the *Ankle* [21]. It would again be related to the mass of the CR: lighter nuclei would dominate at energies at the *Ankle*, while higher masses would be more frequent at the upper end. The different spectral breaks could be connected to the maximum energies for predominant nuclei.

The highest energy statistics do not allow for any of the three above described scenarios to be refuted. Specifically, the two largest CR observatories, namely the Pierre Auger Observatory and the Telescope Array Experiment (TA), exhibit discrepancies in the energy scale at the highest energies [22]. Therefore, the different data sets allow different interpretations. Auger, as the longer-running observatory with a size approximately four times that of TA, tends to favour the latter two scenarios, although the GZK-limit of protons can also have an impact.

Influences of photo-disintegration and maximum energy of sources predict different mass compositions for increasing energy. Figure 2.2 shows a model for a multi-component fit of the energy spectrum. It establishes that the Auger data can be well described with distinct mass groups for different energies. Protons and helium dominate the spectrum up to $E \approx 10\,\mathrm{EeV}$ and exhibit a sharp decline before $E \approx 25\,\mathrm{EeV}$. Masses up to oxygen gain influence and guide the spectrum up to $E \approx 50\,\mathrm{EeV}$. Here, nuclei with masses up to iron dominate the spectrum until a sharp cut-off is observed at $E \approx 200\,\mathrm{EeV}$. Even higher masses of CRs could exist as well [23]; however, they are not considered in this model. The mentioned models can explain the spectrum of CRs, but it becomes evident that more information on the mass composition is needed to differentiate the influence of the processes and to evaluate if a superposition of all cut-off scenarios is observed.

2.1.2 Mass composition

An indication of the mass of a CR entering the Earth's atmosphere is given by the depth of the air shower maximum, X_max $[\mathrm{g\,cm^{-2}}]$, which is produced by the primary CR (more information on air showers will be presented in Sec. 2.3). It is depicted in Fig. 2.3, which shows the distributions of X_max for proton and iron CRs. The shower maximum of heavy CRs is higher in the atmosphere (lower X_max) and the event-to-event fluctuations are small. For light CRs, this is vice versa [24]. Hence, the mean X_max differs by $\approx 100\,\mathrm{g\,cm^{-2}}$ for protons and iron. Nonetheless, an event-to-event mass

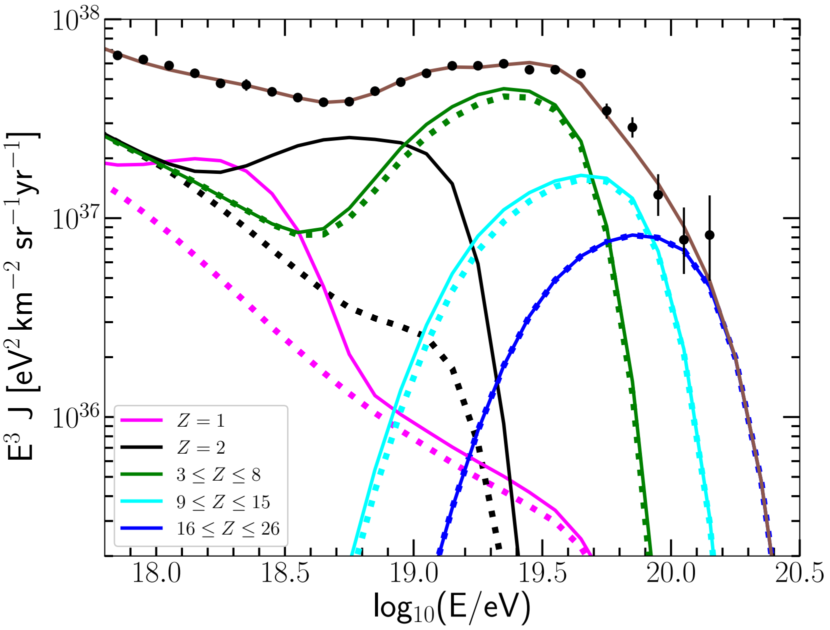

Figure 2.2: Multi-component fit of the CR energy spectrum. Black markers show the data of Auger, different coloured lines indicate CR components (solid: CRs from the source, dashed: secondary particles after CR interaction on the way to Earth). Note the scaling factor of E^3 for the flux. Plot and more model details in [20].

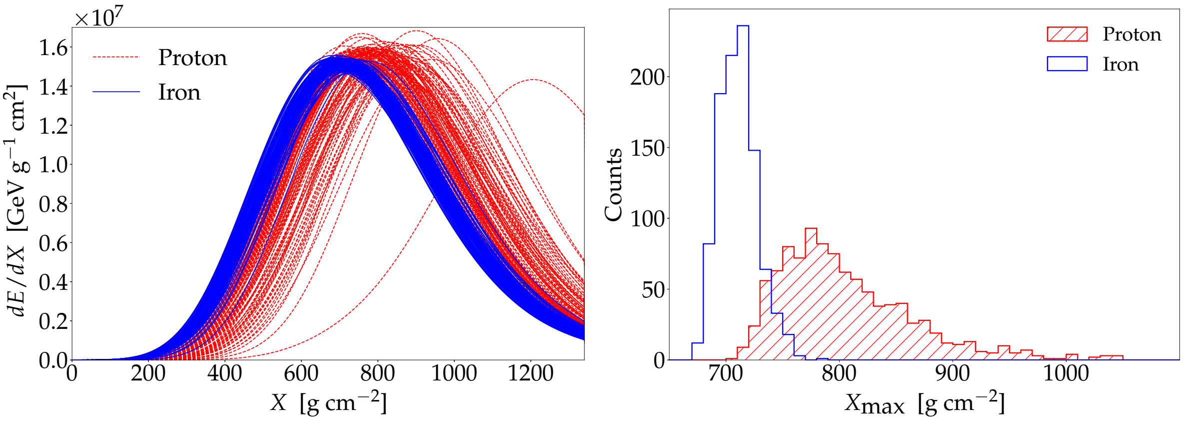

Figure 2.3: Shower development for protons (red) and iron (blue) primaries. (Left) Energy deposit for different shower depths. Each line indicates one simulated air shower. (Right) X_{max} distribution of the before mentioned simulations. Plots from [25].

determination is not possible with X_{max} alone, as the proton fluctuations are higher than the difference in X_{max}. X_{max} only gives an indication of the mass on an event-basis.

The sum of all measurements can still provide an indication of the mass composition, as depicted in Fig. 2.4. Measurements of the mean X_{max} and its standard deviation (a measure of the event-to-event fluctuations) conducted by Auger at different energies are shown. They are compared with theoretical expectations for proton and iron events [26].

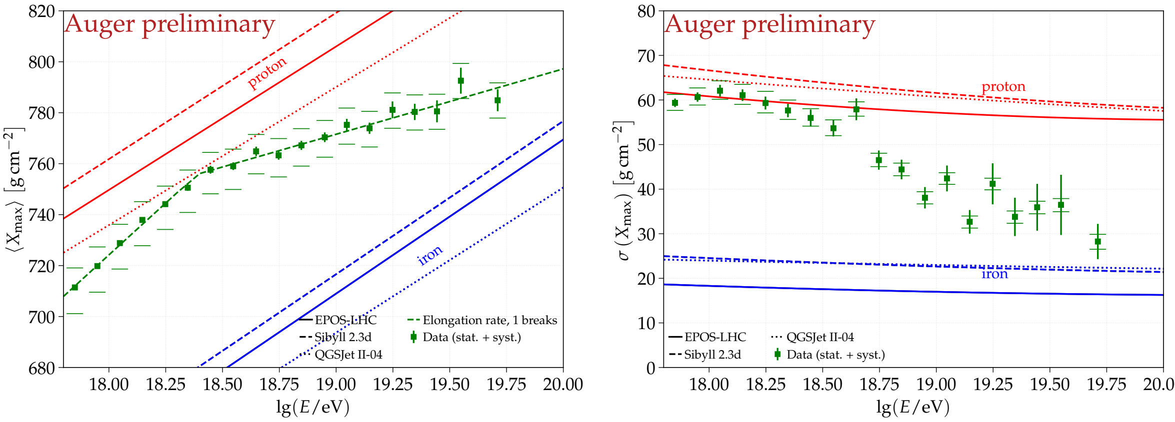

Figure 2.4: (Left) Mean $X_{\max}$ for different energies. Green markers indicate measurements from Auger with their modulation as green line. Red lines show predictions for proton primaries for different hadronic interaction models (solid: EPOS-LHC, dashed: Sybill 2.3d, dotted: QGSJet II-04), while blue lines show the same for iron primaries. (Right) The same as (left) for the standard deviation of $X_{\max}$. Plots from [26].

For the mean of $X_{\max}$, two behaviours are observed. First, the mean of $X_{\max}$ approaches the predictions for protons for increasing energies below the *Ankle*. At the *Ankle*, a break of the general slope is observed and the mean $X_{\max}$ drifts towards the prediction of iron for higher energies. Nevertheless, it is incompatible with the iron predictions within its uncertainties. The behaviour for energies above the *Ankle* is confirmed by the standard deviation of $X_{\max}$. These results are interpreted as a hint for a mixed composition, with light masses at the *Ankle* and heavier masses for energies above the *Ankle*.

With the upgrades of the Pierre Auger Observatory (see Sec. 3) and more information, such as the muon content of the air shower, a mass determination on an event-basis could be possible [27]. This would help to explain features in the energy spectrum, as well as it would improve the understanding of arrival directions and would impact source determination.

2.1.3 Arrival direction

Deflection of CRs is mainly dependent on the rigidity [28], R, of the particle:

$$R = \frac{B}{\rho_{\mathrm{g}}}, \tag{2.4}$$

where B is the magnetic field and ρ_{g} is the gyroradius of the CR. The gyroradius is determined by the CR momentum and charge. Hence, for backtracking a CR to its source, four quantities need to be known: the arrival direction of the CR on Earth, the energy

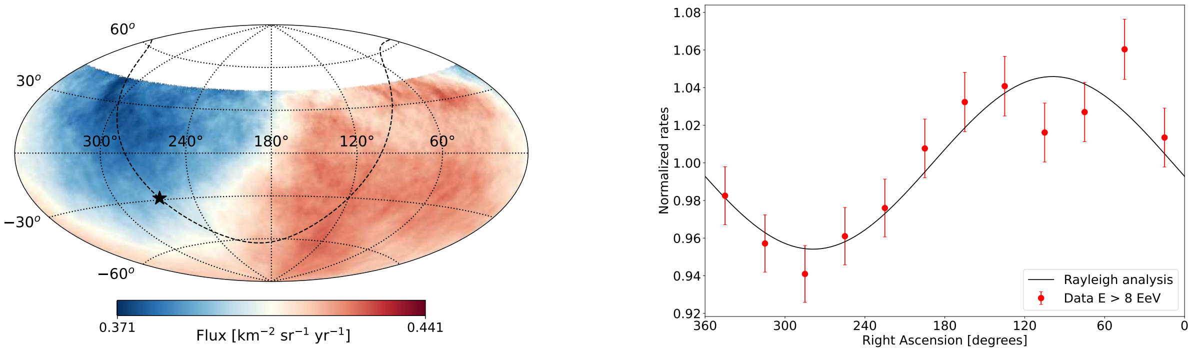

Figure 2.5: (Left) Flux map in equotorial coordinates for CRs with $E \geq 8\,\mathrm{EeV}$. Blue areas indicate lower flux than the average, red areas mean a higher flux. The black line shows the galactic plane with its galactic centre (black star). (Right) Dipole modulation (black line) of the arrival direction in right ascension. Red markers show data from Auger. Plots from [38].

and mass of the CR, and the magnetic fields on the trajectory of the CR. It has been demonstrated that the arrival direction can be accurately determined, whereas only indications for the mass are available. The energy reconstruction of the CR is subsequently linked to its mass and, hence, mass and energy possess substantial uncertainties, yet they can generally be computed. The greatest uncertainty is given due to the galactic and extra-galactic magnetic fields [29, 30]. Both can not be measured directly but only indirectly, for example by Faraday rotation [31]. It generates numerous uncertainties, resulting in a multitude of magnetic field models [32, 33, 34, 35]. With these presumptive models and programs such as CRPropa [36] or CRISP [37], it is feasible to conduct backtracking studies. However, with the limited knowledge of CRs and large uncertainties, no conclusive results concerning the potential sources have been found with backtracking studies.

It is also possible to conduct arrival direction studies, which would eliminate uncertainties in rigidity. CRs at the highest energies have less deflection and straighter trajectories. Hence, they can point back to their sources when accounting for smearing due to small deflections [38]. This type of analysis led to the results of Figs. 2.5 and 2.6. The arrival direction for Auger events with $E \geq 8\,\mathrm{EeV}$ is shown in Fig. 2.5. A large-scale anisotropy is visible in the form of a dipole with an amplitude of $5.8^{+0.9}_{-0.8}\,\%$ with the largest excess at $97° \pm 8°$ in right ascension and -$37° \pm 9°$ in declination. The significance of the dipole is $6.9\,\sigma$. The dipoles maximum excess is $\approx 125°$ away from the Milky Way's galactic centre, which underlines the hypothesis of extra-galactic origin of CRs at the highest energies.

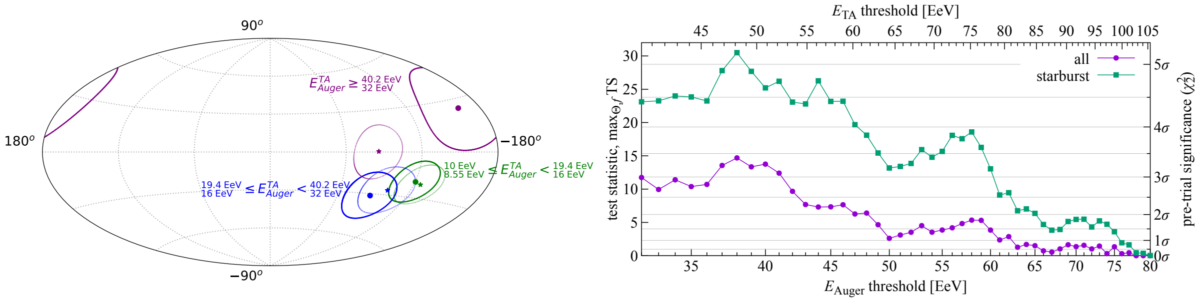

Figure 2.6: (Left) Estimated maxima in CR flux in different energy bins for data measured by Auger and TA. Stars with faint circles indicate analysis with Auger energy scale, points with thick circles result from the TA energy scale. (Right) Test statistic and pre-trial significance at different energies (bottom axis: Auger energy scale, top axis: TA energy scale) for the correlation of CRs with a general galaxy catalogue (purple) and a starburst catalogue (green). Plots from [39].

Since the discovery of the dipole, numerous similar analyses have been conducted for different energy binning [39]. The results are shown in Fig. 2.6. It illustrates the implications of the combined data set from Auger and TA. As the two observatories exhibit discrepancies in their energy scale [22], the outcomes are presented both in terms of Auger and TA energy. The map shows the hotspots for the different energy bins. For lower energies, the different energy scales have marginal effects, whereas for higher energies, the hotspot shifts significantly. The analysis was also conducted for various energy thresholds, and a search for correlation between the arrival direction and a general galaxy catalogue (2MRS) [40] and a starburst galaxy catalogue [41] was conducted. The best result is achieved for a threshold energy of 38 EeV on the Auger energy scale. The search reveals a correlation with a post-trial significance of $2.8\,\sigma$ with the 2MRS catalogue but a $4.6\,\sigma$ correlation with the starburst catalogue. It is estimated that a $5\,\sigma$ significance could be reached in 2025±2 years.

The above-mentioned analyses suggest that starburst galaxies are one source of CRs at the highest energies. However, many questions remain unanswered. It is unclear if all starburst galaxies would contribute, or just a single one. Furthermore, there could be additional sources, such as active galactic nuclei (AGN). This is inferred by other Auger analyses that indicate a contribution from the Centaurus A region [38]. AGNs could have influence at different or the same energies. Many of these puzzles could be solved with the pinpointing of their sources, which is difficult with charged particles. On the contrary, the detection of high-energy photons has the potential to aid in unravelling the aforementioned mysteries.

2.2 UHE photons

UHE photons as messengers for CRs have been discussed for a long time. Even the detection of a single event could provide important information about the sources of CRs and their propagation. Nonetheless, it remains uncertain whether UHE photons will reach the Earth, owing to the opaqueness of the universe.

2.2.1 Production

Photons, as non-charged particles with no mass, cannot be accelerated in the same manner as CRs. They gain their energy from their creation, which can occur in multiple ways.

GZK-photons: In the previous section, the GZK-effect was discussed. Equation 2.2 shows that one case includes the production of a π^0. With an average lifetime of $\approx 8.5 \cdot 10^{-17}\,\mathrm{s}$ [42], it can be inferred that the π^0 immediately decays:

$$\pi^0 \rightarrow 2\gamma \qquad (99.82\,\%) \tag{2.5}$$

$$\pi^0 \rightarrow \gamma + e^+ + e^- \qquad (1.17\,\%) \tag{2.6}$$

In the case of the GZK-effect of protons, the π^0 takes an average of 20 % of the energy [17]. Split between 2-3 particles, one expects UHE photons with energies of one magnitude lower than the interacting proton. Hence, UHE photons could have 10 % of the maximum acceleration energy for extra-galactic protons, which is well in the EeV region. UHE photons can have even higher energies due to heavier nuclei interaction, such as photo-disintegration, pair-production, and occasionally inverse Compton scattering. For the UHE photon spectrum, these processes could be significant contributions [43]. This is depicted in Fig. 2.7 (left), where the integral photon flux is depicted for different CR mass compositions (*c.f.* [43] for the compositions), which were made with Auger predictions. Depending on the mass contributions, the photon flux can fluctuate by an order of magnitude. They agree with a steep decrease in photon flux for energies above 10 EeV. A comparison is made with an (unrealistic) pure proton CR flux, which generally produces a greater photon flux than all Auger mixes. Furthermore, the flux has a later cut-off at about 100 EeV.

CR interactions in the Milky Way: Gamma-rays have already been observed at energies in the TeV region, which are the result of CRs interacting with interstellar matter. This includes Bremsstrahlung, nucleon-nucleon interactions and inverse Comp-

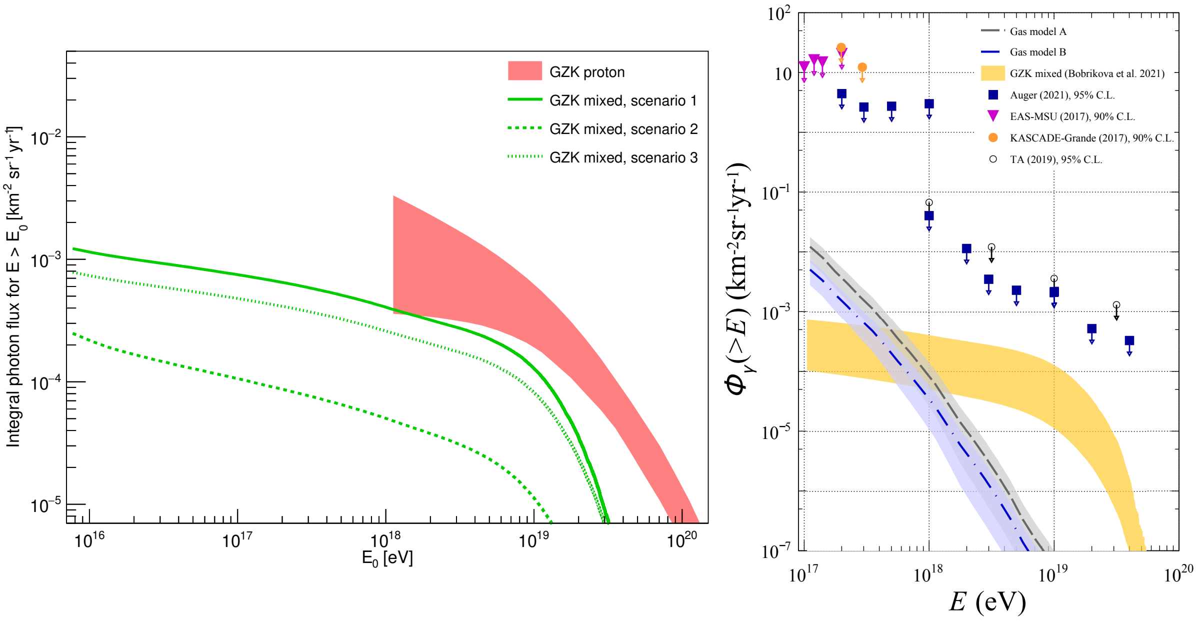

Figure 2.7: Predictions of the UHE flux for different energies. (Left) Simulations for the GZK effect. The green lines indicate different CR composition scenarios, the red-shaded area represents an unrealistic pure proton composition. Plot from [43]. (Right) Simulations for CR interactions with galactic molecular clouds. Blue and grey lines show different cloud models. The yellow shaded area shows the predictions from (left), markers show upper limits. Plot from [44].

ton scattering [44]. It is assumed that these processes also occur at much higher energies when UHE CRs interact with galactic matter, such as molecular clouds [44]. Consequently, the photons could also be produced at much higher energies. The resulting photon yield depends on the composition of both the CRs and of the molecular clouds. Figure 2.7 (right) shows the expected photon flux for two different models of molecular clouds. It is compared to limits set by different observatories and the above discussed GZK photon flux. The photon flux from galactic molecular cloud interactions dominates at energies below 1 EeV, being a factor of 10 higher at photon energies of 0.1 EeV. At 10 EeV photon energy, the flux is insignificant compared to the GZK photon flux.

Photons from super heavy dark matter: UHE photons could also arise from super heavy dark matter (SHDM) [45, 46]. SHDM could decay into photons or interact with visible matter and produce UHE photons, directly or indirectly. Numerous scenarios exist, in which SHDM could interact with the visible sector, resulting in equally numerous possibilities for the observation of UHE photons. Some theories predict maximum photon energies of a few EeV while others extend to 100 EeV. Similar to this, the magnitude of the flux compared to the GZK photon flux varies strongly.

2.2.2 Propagation

UHE photons can be produced in multiple scenarios, which could contribute fully or only partially to the photon flux. The origin of an UHE photon could still be determined from the arrival direction and energy, combined with the mean free path length of photons. The mean free path lengths of photons and CRs at high energies is depicted in Fig. 2.8. The mean free path length of photons is equal to the cosmological horizon for energies below 10 TeV [47]. It rapidly drops to 10 kpc with its minimum at 1 PeV due to the Breit-Wheeler-effect [48]. Here, the high-energy photon collides with a CMB photon

$$\gamma + \gamma_{\mathrm{CMB}} \rightarrow e^{+} + e^{-} \tag{2.7}$$

and subsequently produces an electromagnetic (EM) cascade. For higher energies, the effect diminishes and the mean free path length increases up to 122 Mpc at 1 ZeV. This distance limit is due to the double pair production [49] of UHE photons.

It is important to note that the mean free path length and energy loss length are not equivalent. At high energies, pair production processes are highly asymmetric, with either the positron or the electron receiving the main fraction of energy [50]. The UHE electron subsequently upscatters a CMB photon via Compton scattering, resulting in a new UHE photon. The energy loss length at 1 EeV is significantly higher by a factor of 10 with tens of Mpc in comparison to the mean free path length. Hence, it can be inferred that UHE photons from nearby potential sources (such as Centaurus A, which is located at a distance of approximately 3.4 Mpc) have the potential to reach Earth.

The limited mean free path length and origins of photons at different energies provide new implications for the interpretation of detected UHE photons. The ideal case would be an UHE photon ($E \geq$ few EeV) produced by GZK interactions in the vicinity of the CR source. Due to its high energy, the UHE photon can travel Mpc scales and reach Earth. This would subsequently enable direct identification of the source of CRs, as the UHE photon would not be deflected by magnetic fields on its trajectory. If no source is observed in the direction of the UHE photon, it would indicate that the GZK process happened late on the CRs trajectory. This would not allow for backtracking, but would yield new insights into GZK processes, CR propagation, and composition. Additionally, it could have implications for the mean free path lengths of photons, which are only theoretical.

If photons from the Milky Way centre are detected, the primary concern should be directed towards the distinction between photons originating from CR interactions with interstellar matter and photons originating from SHDM [51]. The energy of the photon could yield information on its origin. Energies of tens of EeV would point to SHDM (*c.f.* Fig. 2.7 as photons due to CR interactions extend only significantly to 10 EeV), while differentiation would become more difficult at lower energies.

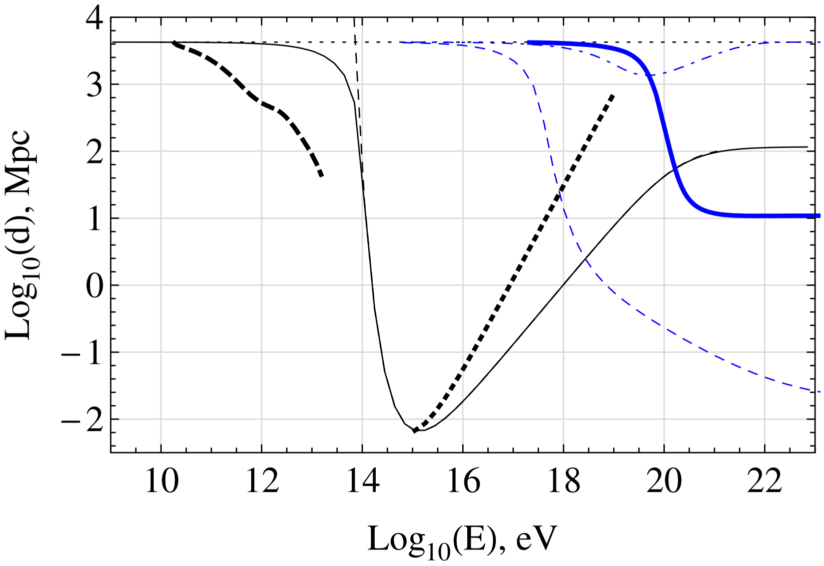

Figure 2.8: Mean free path lengths at different energies for distinct particles. Important lines for this work are the UHE photon prediction (thin black curve) and the prediction of the energy loss length of the photon interaction with the CMB (thick dotted curve). Plot and more details in [47].

2.3 Air showers

The energy spectrum of CRs implies a very low flux at the highest energies. Only one CR is expected per km^2 and year for energies above 10 EeV. As it is probable that UHE photons originate from CRs, they are even more uncommon. Therefore, direct measurements of CRs and photons, such as through satellite experiments, become unfeasible at these energies. On the other hand, indirect measurements on the ground are possible, as the primary particles interact in the atmosphere and produce extensive air showers [52].

A hadronic primary entering the atmosphere collides with an air nucleus such as N_2 or O_2. This results in secondary particles being produced. Depending on the primary type and the primary energy, the collision can have a multiplicity of $\geq 1,000$. The primary energy is split onto the secondary particles, which themselves undergo interactions. This process continues until a critical energy is reached, at which point no interactions are possible anymore. The development of the air showers can be categorised into three components, which are depicted in Fig. 2.9 (left). The first one is the hadronic component, in which baryonic and mesonic secondaries generate a wide range of particles, including other hadrons, as a result of fragmentation and hadronic interactions. Protons, neutrons, charged pions and kaons are predominant here. The hadronic component also feeds the two other components, namely the muonic and the EM component. The muonic component arises from charged kaons and pions decaying. The produced muons are strongly Lorentz boosted, and therefore they can reach the ground before they decay. Otherwise, they decay into electrons (positrons), which feed into the EM component.

The EM shower component can be modelled using the *Heitler*-model [53, 54]. The EM component is primarily fed by neutral pions, which decay into two photons. The photons undergo pair production, and typically result in the creation of one electron and one positron. The charged electrons (positrons) experience energy losses via Bremsstrahlung, resulting in the production of photons once more. This continues in an EM cascade. It is observed that, per interaction, the number of particles doubles while the energy per particle is halved. The cascade continues until ionisation losses begin to dominate over Bremsstrahlung losses. This happens when electrons have less than the critical energy of $E_{\mathrm{crit}} \approx 87\,\mathrm{MeV}$[1], after which more EM particles are absorbed in the atmosphere than are produced. This marks the depth of the shower maximum (X_{max})[2], where more than 10^{10} particles can exist for an extensive air shower.

UHE photons entering the atmosphere can be described fairly easily by the EM component. Most of the energy goes into the EM component, while produced muons contribute only 2 % of the energy. To provide a comparison, hadron air showers exhibit a muonic energy contribution of approximately 10 %. These features can only be reversed in exceptional circumstances. On the one hand, UHE photons can have interactions like photo-disintegration in the atmosphere. If this occurs within the first interactions, a significant portion of the energy goes into the hadronic component [55]. Hence, the photon air shower has an atypically large fraction of energy feeding the muonic component in the end. The likelihood of this happening increases with the increase in photon energy, in which the photon showers resemble proton showers. On the other hand, protons (and rarely heavier nuclei) can also resemble photon events [55]. If one or multiple π^0s receive a major fraction ($\gtrapprox 80\,\%$) of the primary photon energy in the first interaction, the muonic component is atypically small for a proton shower. This happens in $\approx 0.1\,‰$ of proton events. Lorentz boosting, π^0 energy, and the zenith angle define if the proton

---

[1] E_{crit} is generally dependent on the atomic number of the traversed matter and therefore varies. The given value is an often used estimate for air.

[2] The original definition of X_{max} is given by the point of the maximum energy deposit in the atmosphere, which is almost equivalent to the point of maximum number of particles.

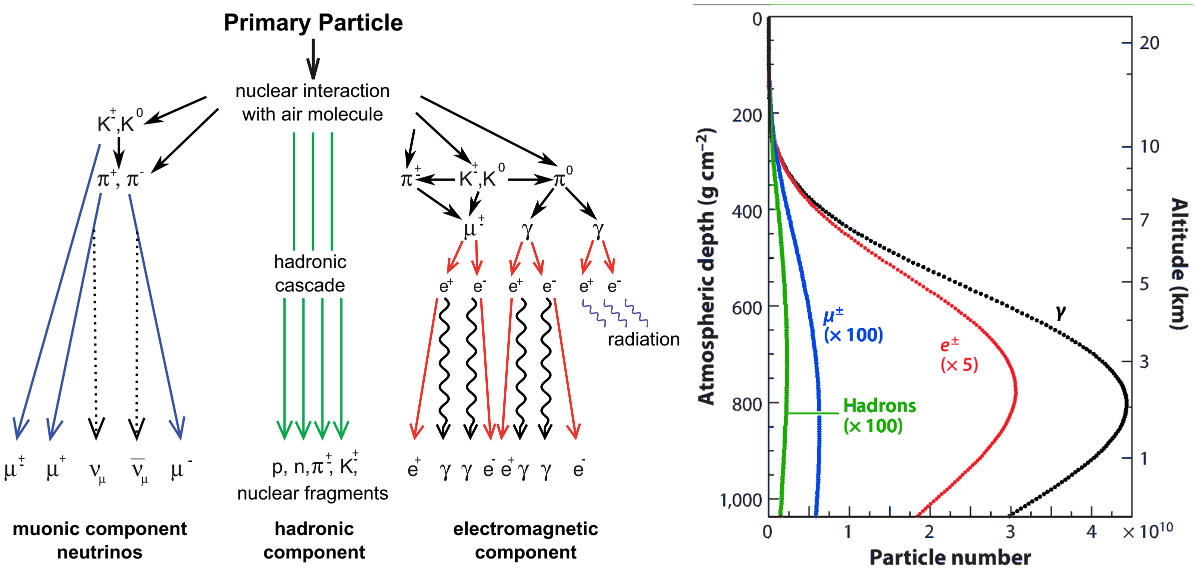

Figure 2.9: (Left) Different components in an air shower. The primary particle produces a muonic component (left, blue), a hadronic component (middle, green) and EM component (right, red). Illustration from [56]. (Right) Particle numbers for a simulated 10 EeV proton air shower at different atmospheric depths and altitudes (for the location of the Pierre Auger Observatory). Shown are the curves for components same as (left). Colour modified version from [52].

primary can be differentiated from a regular photon air shower or if it is considered an irreducible proton background.

Particles produced in an air shower can be detected on the ground. The quantity and types of particles that reach ground detectors are mainly determined by the primary particle type, zenith angle, θ, and the altitude of the experiment. An example composition is depicted in Fig. 2.9 (right). For vertical showers, the geometrical distance between the shower maximum and the detector is in the order of a few kilometres, but also after the shower maximum EM particles are produced. Hence, vertical ($\theta < 60°$) air showers are dominated by EM particles, even at the ground. For inclined events ($\theta > 60°$), fewer EM particles will reach the detector, and the muonic component starts to dominate [57]. Hadrons do not have a significant contribution at the detector level.

2.4 Radio emission in air showers

Vertical air showers at high energies have their shower maximum close to the ground. For exceptionally deep showers, X_{max} can even be below the ground. Inclined showers have their maximum well above ground, and the geometrical distance between detector and shower maximum is large. Therefore, the air showers are fully developed, but few EM

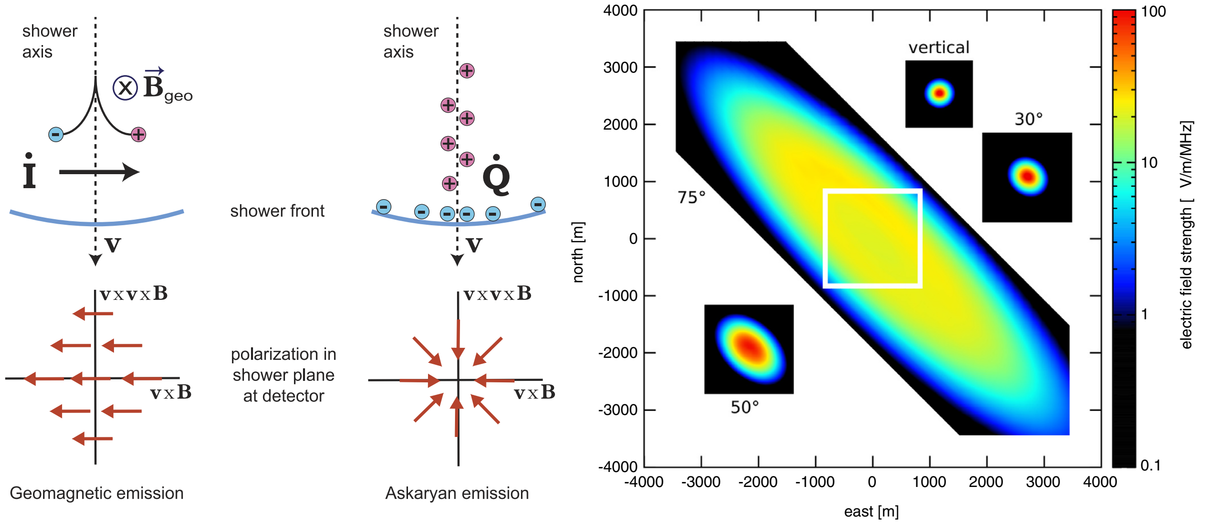

Figure 2.10: (Left) Origin and polarisation pattern for the geomagnetic emission (left) and charge excess emission (right). Illustration from [59]. Footprint sizes for a simulated air shower at different zenith angles with $E = 5 \cdot 10^{18}$ eV. The colour scale represents the electric field strength, where the black colour indicates the galactic noise level. The white square shows the size of the 50° case. Plot from [58].

particles reach the detector due to the larger distance. Information regarding the EM component is lost upon particle absorption. However, this information can be retrieved by measuring the radio emission of air showers, which originates from the movement of charged particles in Earth's magnetic field. There are two effects mainly contributing to the emission [58] in the MHz band that are both illustrated in Fig. 2.10 (left).

2.4.1 Geomagnetic emission

From a macroscopic perspective, charged particles are deflected in the magnetic field based on their charge to mass ratio following the Lorentz force. This would result in EM radiation. However, this description is too simplistic, since charged particles constantly interact with air molecules. Therefore, the length of their unimpeded and free path is relatively small. The radio emission can be explained better with a time varying current. As discussed above, air showers have a maximum number of particles at X_{max}. Earlier and later in the shower development, the particle number is smaller, and equivalently the overall charge is in- and decreasing, respectively. The deflected, coherently moving charges can be viewed as a current perpendicular to the magnetic field. Time varying currents emit EM waves, resulting directly from Maxwells equations. The waves are observed as a radio pulse. This radio pulse is linear polarised perpendicular to the shower axis and magnetic field.

As the geomagnetic emission depends on the increase and decrease in particle numbers, it is important to have a fully developed air shower for a well-defined radio emission. Air showers that reach their maximum close to or even below the ground are not fully developed. Hence, the radio emission is better observable for inclined air showers with maximums distant to ground. Moreover, the azimuth angle, φ, of the air shower is another important ingredient for the strength of radio emission [60]. The geomagnetic emission vanishes for arrival directions parallel to the Earth's magnetic field.

2.4.2 Charge excess emission

The charge excess emission (or Askaryan effect [61]), is the less significant emission in air with a contribution of $\approx 14\,\%$ [62]. It arises from a growing charge difference during shower development [58]. Close to the shower axis, electrons are knocked off from molecules via ionisations. The light, negatively charged electrons move along the extensive shower front, while the heavy, positively charged ions are left behind close to the shower axis. This yields a charge difference, which is growing along with the shower development. According to Maxwells equations, a time-varying charge excess results in radio emission. It is then polarised radially towards the shower axis. Therefore, the superposition of the geomagnetic and charge-excess emission, yields a radially asymmetric radio footprint.

2.4.3 Extensiveness of the radio emission

Radio emission propagates for hundreds of kilometres without being significantly absorbed in the atmosphere. Furthermore, the radio footprint can have a large spread on the ground, while still being detectable. This is depicted in Fig. 2.10 (right), which shows the extensiveness of radio footprints for different zenith angles. For vertical showers, detectable radio signals (above the ubiquitous galactic radio noise) are usually found within a few hundred meters or sometimes up to a kilometre (*c.f* the $\leq 50°$ footprints). In contrast, inclined showers with shower maxima far away can extend over tens of kilometres while having significant signals (*c.f* the $75°$ footprint). It is therefore possible to detect inclined air showers using sparse radio arrays.

2.4.4 Frequency spectrum and coherence

The emission of the dominant geomagnetic effect has a broad-band frequency spectrum, with contributions in the MHz to a few GHz range. However, the detection at ground requires coherence of the radio emission. If the phase differences of signals are too large, they interfere destructively. Therefore, the thickness of the shower front (in which the time-varying current is found) defines the frequency range for coherent radio emission. Shower fronts are typically a few meters thick, which means that coherency is conserved for frequencies below 100 MHz.

The coherence of radio signals is influenced by the refractive index as well. The emission that is radiated under a Cherenkov-like angle of the corresponding refractive index is compressed in time. It results in short but large radio signals at detector stations on a Cherenkov-like ring with the radius r_{Ch}. Moving away from the Cherenkov-like ring leads to less coherent signals, where the pulses are longer and lower in amplitude.

CHAPTER 3

THE PIERRE AUGER OBSERVATORY

This chapter explains the concept and design of the Pierre Auger Observatory. First, the general layout, including the Surface Detector (SD) and Fluorescence Detector (FD), is described. This section is kept brief, there are numerous well-written descriptions of the detector published for more detailed information. More extensive descriptions can be found in [63, 64] for general descriptions of the Observatory, in [65, 66] for details on the FD, in [67] for a description of the Surface Scintillator Detector (SSD). The most important detector for this work, the Radio Detector (RD), including its predecessor, will be presented in greater detail. The chapter concludes with two additional topics of significance for this research, namely the trigger system of the Observatory and the previously conducted photon searches.

3.1 The baseline design

The Pierre Auger Observatory is the world's largest CR Observatory, covering an area of $\approx 3{,}000\,\mathrm{km}^2$ [63]. Based in the Argentinian pampas, the components of the so-called phase-1 comprise 1,600 SD stations arranged on a regular hexagonal grid with a spacing of 1,500 m. Moreover, approximately 60 SD stations are situated in close proximity to another station for cross-checks, or on a reduced grid of 750 m [68] or 433 m [69] for an extension to lower energies down to $\approx 10\,\mathrm{PeV}$, the so-called infill. Additionally, there are four sites with 27 fluorescence telescopes. The layout is shown in Fig. 3.1 (left).

One of the main components of an SD station is the water-Cherenkov Detector (WCD), visible in Fig. 3.1 (right), consisting of a 1.2 m tall round plastic tank with a diameter of 3.6 m. It contains 12,000 litres of purified water and three photomultiplier tubes (PMTs). Muons with an energy exceeding approximately 0.3 GeV [70] entering the tank produce Cherenkov light inside the water. The PMTs detect emitted light

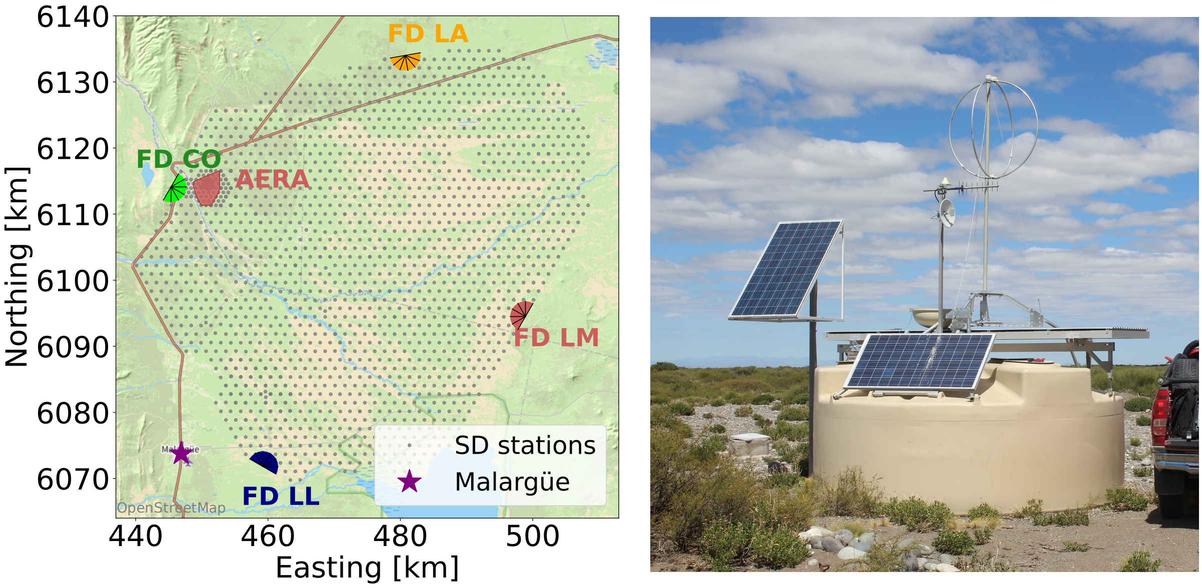

Figure 3.1: (Left) Layout of the Pierre Auger Observatory. Shown are SD stations (grey points), the FD sites (coloured segmented half circles) and the area of AERA (red shape). It is close to the city of Malargüe (purple star). (Right) An upgraded SD station is shown with the yellow WCD, the SSD as side view mounted on top, as well as the RD antenna.

and forward the signals to the Upgraded Unified Board (UUB, or in past days and still in some stations, the Unified Board (UB)) [71]. The signal is then recalculated using calibration variables. In order to account for inefficiencies in PMTs, such as ageing effects, it is necessary to calculate the charge that a vertically entering muon would produce in the PMTs. This is accomplished by recording random background muons and their generated charge [72]. The sum of all muons within a time frame of 60 s yields a pulse height histogram. From this distribution, it is possible to unfold the gains of the PMTs and recalibrate the traces. The new unit of the trace entries is a so-called Vertical-Equivalent-Muon (VEM) and its current I_{VEM}, so the equivalent signal that a vertical entering muon would produce in the tank. Based on this calibrated current, it is determined whether to send a trigger request to the Central Data Acquisition System (CDAS) [73].

During the AugerPrime upgrade, additional components were added to the SD stations and electronics were upgraded [74]. An SSD, which consists of a $\approx 3.8\,\mathrm{m}^2$ scintillator paddle and one PMT to detect the signal, is mounted on top of the WCD and is designated to improve the separation of secondary electrons and muons. The antenna of the RD, which will be described further down, is situated on the top as well for all

Figure 3.2: Antenna types used for AERA. (Left) A logarithmic periodic dipole antenna used in AERA phase I. Picture from [80]. (Right) A butterfly antenna used in AERA phase II and III.

stations in the array. The infill region is partly complemented by the Underground Muon Detector (UMD) [75], which is buried below the surface.

Apart from the aforementioned components, there are numerous devices for measuring environmental aspects, such as rain, wind speed, lightning [76], electric fields [77] and soil parameters [78]. They are used later for calibration of the detectors, correction, and rejection of measurements, or for phenomenological studies. Mentioning all the sensors would exceed the scope of this thesis. Those devices that are utilised in this work will be described at a later stage.

3.2 The Auger Engineering Radio Array

The Auger Engineering Radio Array (AERA) was initially developed as a self-standing project and was only later officially included in the Observatory. The detector was constructed in three phases, with the first antennas deployed in 2011. All three phases combined cover $\approx 17\,\mathrm{km}^2$ with 153 antennas. The first phase comprises 24 logarithmic periodic dipole antennas, while the later phases use butterfly antennas [79]. Both types are depicted in Fig. 3.2. They both have two polarisation directions, one parallel and one perpendicular to Earth's magnetic field. Furthermore, both designs are sensitive to the vertical component of the electric field.

AERA has two types of triggers. One is external, meaning that the read-out of stations is activated in case a WCD with a distance to AERA of less than 5 km is read-out. The triggered events are nearly pure, since random coincidences of particle triggers are rare. There is also a second option, where designated AERA stations (a subgroup of stations) trigger on their signal [81]. These triggers must be filtered, as radio noise is much more frequent and can result in enormous trigger rates. Even though over 99.8 % of self-triggers are rejected by algorithms based on geometry considerations, one still observes a read-out rate of ≈ 1 Hz, which is 50 times higher than the external trigger rate. This high trigger rate is only feasible due to AERA's distinct and more advanced communication system, in contrast to the conventional Auger network.

Typically, for physics analysis, externally triggered data is utilised due to its greater certainty of air shower origin. With this data, significant outcomes in the field of CR detection with radio could be achieved, of which two will be mentioned here. First, a self-standing energy reconstruction of extensive air showers was developed [82]. This makes it possible to have validation of single event energy reconstructions of the other detectors. Furthermore, radio detectors are sensitive to the EM component of air showers, which provides direct access to the EM energy content. This information is useful for primary distinction. It is currently under investigation whether AERA possesses a comparable or even superior energy estimation as the FD. Here, one can compare the Hybrid-events, which are seen by FD and AERA. Due to the limited up-time of ≈ 13 % of the FD [65], the overlap of events is comparatively small. Nevertheless, these events are used to develop a reliable and independent energy scale of AERA [83], which is then utilised for cross-calibration of the other detector components.

The second major accomplishment is the detection of inclined, extensive air showers with large radio footprints. Moreover, it was shown that the radio footprint can exceed the particle footprint for these showers. An isolated, triggered WCD led to a read-out of AERA, which showed the extensiveness of the air shower as the particle footprint and its core was ≈ 15 km distant [84]. Following, the potential of inclined air showers was further investigated. Especially for almost horizontal air showers, radio detection has a considerable prospect. Here, the shower maximum can be more than 100 km distant. Thus, EM-particles are completely absorbed in the atmosphere. [57]. This reduces the sensitivity of the WCD within this parameter range. On the contrary, the radio emission is largely unaffected by absorption and remains significantly detectable on the ground.

3.3 The AugerPrime Radio Detector

Because it is possible to detect inclined air showers with radio, the Radio Detector was added to the AugerPrime upgrade.

3.3.1 Radio Detector hardware

The RD is designed to detect inclined, extensive air showers. It consists of a radio antenna mounted on top of each WCD, thus, RD has a much larger spacing than AERA. The utilised radio antennas were originally developed for LOPES [85] and also utilised by AERA and Tunka-Rex [86]. It comprises two loop antennas with polarisations that are parallel (North-South (NS) channel, sensitive to the East-West (EW) direction) and perpendicular (EW channel, sensitive to the NS direction) to the magnetic field of Earth. It is called the Small Aperiodic Loaded Loop Antenna (SALLA). The RD is sensitive to the EM field in all directions due to its perpendicular arms and loops. In particular, the vertical component is of importance for detecting inclined air showers. The measured signal is then passed through a low-noise amplifier and a digitizer. Finally, the converted signal reaches the FPGA of the RD. Here, basic calculations can be performed, such as an FFT of the signal.

The original design has the RD operating in slave mode with the WCD. The WCD is capable of initiating a station trigger, and the RD is solely read-out if CDAS [73] requests a read-out due to a correlation of multiple triggers. A significant portion of this thesis pertains to the modification of this scheme to incorporate an autonomous trigger on the radio signal, which can initiate a station trigger. This will be discussed in Sec. 5. Regardless of the initiating trigger, in the event that CDAS requests a read-out, the PMT traces and radio traces are transmitted to the UUB and subsequently forwarded to CDAS. Each radio trace compromises 2048 bins at a sampling frequency of 250 MHz (bin width of 4 ns). An example of the radio traces of a measured air shower event is shown in Fig. 3.3.

At the time of writing (08/07/2024), 1308 stations were equipped with a radio antenna, of which 851 also had installed electronics. The installed stations already show the capability of the new detector. One detected event is shown in Fig. 3.4, one of the most energetic events seen so far with a reconstructed EM energy of (28.9 ± 3.3) EeV. It comprises 61 WCD-triggered stations, out of which 29 stations possess a radio trace. Gaps in the event footprint can be explained by stations without RD installed.

With the anticipated completion of the RD in 2024, the Observatory will have a radio detector for CR detection with a yet unseen aperture. With a working range of 65° to 85° in zenith angle, one has an ideal aperture of 1,611 km^2 sr [87]. This increases the mass sensitive range of the Observatory by $\approx 23\,\%$, assuming an ideal efficiency of the WCD between 0° and 60° in zenith angle. Simulation studies suggest that one expects more than 3,000 events above 10 EeV within 10 years [87].

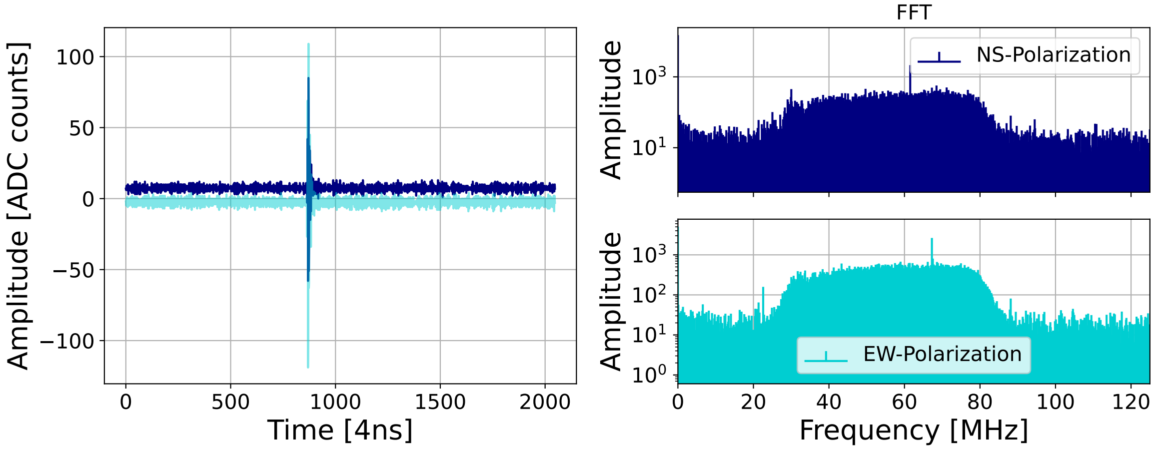

Figure 3.3: (Left) Time traces of an example RD station. The different colours indicate the NS (dark blue) and EW (cyan) polarisations. (Right) The FFT of the time traces.

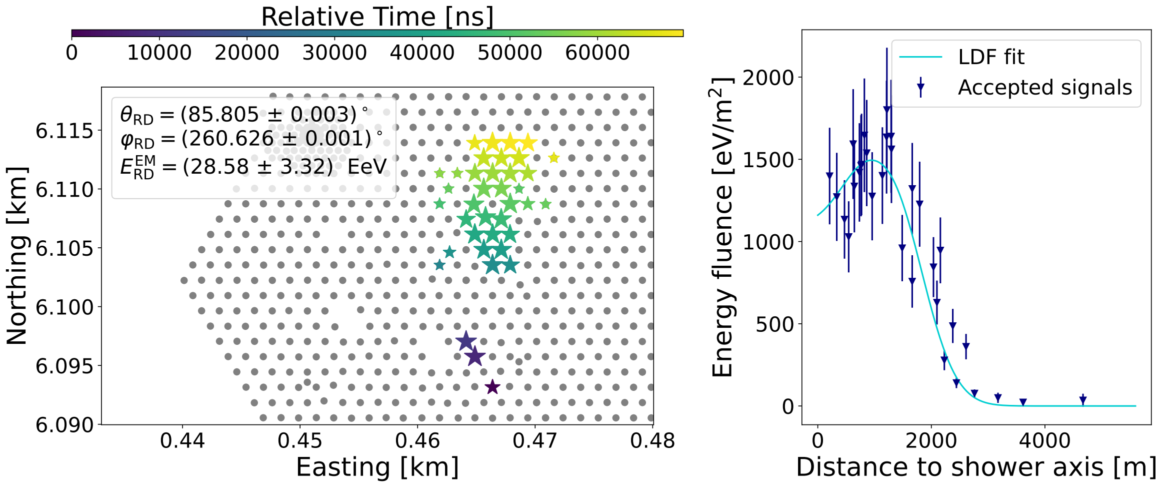

Figure 3.4: Shown is an ultra-high-energy event, which was reconstructed with RD. (Left) Grey points mark stations without RD information, coloured stars indicate stations with RD traces. The colour scale represents the station signal time, while the signal strength is shown by the size of the stars. (Right) The accepted signals of the same event (blue triangles) and its fitted LDF (cyan line).

3.3.2 Radio reconstructions

The measured events can be reconstructed using standard modules in the Auger analysis framework $\overline{\rm Off}\underline{\rm line}$ [88, 89]. The first steps are performed on the raw radio traces. It includes conversions from the ADC counts level to voltages. This voltage is calibrated and equivalent for all detector stations. Furthermore, simple modifications are made, such as removing the channel baselines and interpolating between consecutive bins, in order to achieve an artificially higher trace resolution. The subsequent sequence reconstructs the signals. To achieve this, the arrival direction calculated by the WCD is taken. The antenna response for this particular direction is then selected.

Radio detectors are not equally sensitive in all directions and polarisations, which makes this step important. The detector response is estimated from different components. On the one hand, one can conduct simulations with the NEC (Numerical Electromagnetics Code) software [90], which mimics the detector response for a given design of an antenna. Different arrival directions, polarisations, and reflections are considered in order to reflect the real detector response. It provides a very accurate description of the antenna response, but it may overlook possible inefficiencies and irregularities. Therefore, extensive measurements of the antenna pattern were performed, too. The antenna response to different zenith angles, azimuth angles, and polarisations was measured using a drone [91]. This should provide the best description of the antenna response, even though station-to-station differences are ignored. The fluctuations between stations are considered to be minor.

The simulated or measured antenna pattern is then taken, and the detector response is unfolded in the given arrival direction, resulting in an efficiency corrected signal. One should note here that the RD is dependent on an accurate arrival direction estimate of the WCD. Imprecise WCD outcomes automatically result in imprecise reconstructions of the RD. There are methods to correct for this possible bias, which will be discussed in Sec. 7.1.

The corrected signal can then be split into its different components, e.g. the NS, EW, and vertical components, or the same can be transformed into coordinates of the shower axis. This is important for later reconstructions of the shower. After a successful reconstruction of the signals at the station level, it is possible to determine the characteristics of the air shower. First, an RD arrival direction estimate can be performed. One assumes that inclined air showers have a spherical wavefront, and one can fit it to the timing of the signals [92]. This results in a new estimate of the zenith and azimuth angles of the air shower. The estimated arrival directions of RD and WCD usually differ only slightly within a tenth of a degree. An accurate arrival direction is then essential for a good estimation of shower energy.

An extensive description for the estimation of the shower energy (to be more specific, of the EM part of the shower), can be found in [93]. It should only be briefly outlined here. The energy reconstruction method relies on the lateral distribution function (LDF) of an air shower. One observes a signal in dependence on the shower axis distance. Signal strengths are determined by the geomagnetic energy fluences of the antennas. This energy fluence can be parametrised by the charge excess energy fluence or calculated by

$$f_{\text{geo}} = \left(\sqrt{f_{\vec{v}\times\vec{B}}} - \frac{\cos\phi}{|\sin\phi|} \cdot \sqrt{f_{\vec{v}\times(\vec{v}\times\vec{B})}} \right)^2 , \tag{3.1}$$

where $f_{\vec{v}\times\vec{B}}$ and $f_{\vec{v}\times(\vec{v}\times\vec{B})}$ are the signals strengths in coordinates of the shower axis. The ratio of the ϕ angle defines the core position. One can describe these signals with an LDF consisting of a Gauss and sigmoid function:

$$f_{\text{geo}}(r) = f_0 \left[\exp\left(- \left(\frac{r - r_0^{\text{fit}}}{\sigma} \right)^{p(r)} \right) + \frac{a_{\text{rel}}}{1 + \exp(s \cdot [r/r_0^{\text{fit}} - r_{02}])} \right] . \tag{3.2}$$

Here, r describes the distance to the shower axis and $f_0, r_0^{\text{fit}}, p(r), a_{\text{rel}}, s, \sigma$ and r_{02} are shape parameters with no direct physical significance. This function describes the Cherenkov ring of the emission (dominated by the Gauss function) and the emission towards the shower axis (dominated by the sigmoid function) well. Despite its compatibility with radio emission, this function possesses a drawback of having 7 free parameters in addition to the two core parameters. It is unsuitable for an experimental setup with a relatively low number of detector stations per event, which is often the case for RD. It was demonstrated in extensive simulation studies, that all shape parameters can be parametrised by one single variable, the geometrical distance to the shower maximum (*c.f.* [93] for the parametrisations). At least for hadrons, this yields a satisfactory description, while simultaneously reducing the free parameter for the LDF fit to 3. It is therefore possible to reconstruct the shower energy and its core using only four detector stations. It will be shown in Sec. 7.3 that this does not hold true for photon primaries with the current parametrisation.

Finally, the LDF is integrated to obtain the geomagnetic emission energy, E_{geo}. One scales this energy by the angle of the shower axis to the magnetic field and applying a density correction to get the corrected geomagnetic emission energy S_{rad}. By using a power law for the parametrisation, S_{rad} yields the EM energy of the air shower with high resolution and minimal bias:

$$S_{\text{rad}} = \frac{E_{\text{geo}}}{\sin^2(\alpha)} \frac{1}{(1 - p_0 + p_0 \cdot \exp(p_1 \cdot [\rho_{\text{max}} - \langle\rho\rangle]))^2}, \tag{3.3}$$

$$E^{\text{EM}} = 10\,\text{EeV} \left(\frac{S_{\text{rad}}}{S_{19}} \right)^{1/\gamma} , \tag{3.4}$$

where ρ is the air density at shower maximum and ρ_{max} is a scaling value. For simulated hadrons, it yields a standard deviation of the ratio between reconstructed and simulated

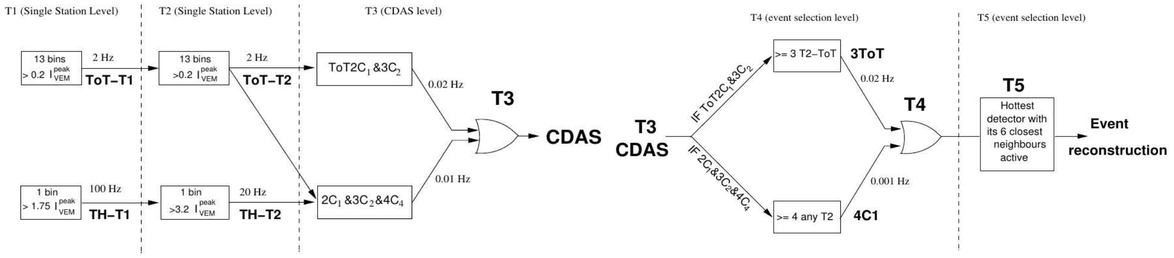

Figure 3.5: Schematic of the triggering system of the Observatory. Shown are the different trigger levels from left to right and their corresponding requirements. Illustration from [94].

EM energy of less than 5 %. The accuracy can only be achieved when one has enough signal stations for the reconstruction. Hence, the triggering of these stations is an important aspect.

3.4 Trigger and communication system at Auger

The triggering system of Auger [94] is designed to output a maximum number of events that can be reconstructed. The only limitation is the available bandwidth, which is 1,200 bits/s per station. It relies on a network that was not significantly upgraded since the primary design of Auger. The AugerPrime upgrade does not include new hardware for the network. Therefore, any changes or additions to the system must always satisfy strict requirements regarding the resulting network load. As the bandwidth is near its maximum, only slight increases to the network load are allowed. In particular, the system is incapable of handling sudden bursts of triggers, which could potentially result in a failure. As will be later demonstrated, a radio trigger is in particular challenged by bursts of triggers.

The triggering system comprises different levels as depicted in Fig. 3.5. The first trigger (T1) is on station level. There are currently four triggers activated, the Threshold trigger (TH) and the Time-over-Threshold trigger (ToT), which existed since the beginning of the Observatory, and the Multiplicity-of-Positive-Steps trigger (MoPS) [95] and Time-over-Threshold-deconvoluted trigger (ToTd) [96], which were introduced in 2013.

The T1-TH requires that all three PMTs inside the station record a signal with at least one bin above $1.75\,\mathrm{I_{VEM}}$ [94]. It is designed for the detection of muon-rich and inclined events. Due to background muons and low-energy air showers, one has a relatively high trigger rate of about 100 Hz. This is 50 times greater than the T1-ToT rate. The ToT is designed for more vertical showers and serves as a trigger for stations located far from the core of large air showers events. A coincidence of (at least) two PMT signals is necessary. The signals themselves have a lower threshold of $0.2\,\mathrm{I_{VEM}}$, yet must persist for at least 13 bins above this threshold.

The two new triggers are especially designed for the detection of small signals and for neutrino events. The T1-ToTd unfolds the exponential decay of the signal, which is caused by diffusive Cherenkov-light scattering inside the water. Afterwards, the T1-ToT condition is applied. The T1-MoPS counts the number of positive increases (steps) in the signal. The step sizes should be within a specified lower and upper limit, as determined by the magnitude of noise and muon signal. If four of the steps are found to be within a 3 µs time window, then a T1-MoPS is created.

All ToT-like T1s (ToT, ToTd and MoPS) are automatically promoted to a T2, the second trigger level, which is also on station level. The T1-TH, however, must ensure that all three PMTs have coincidence, with all signals being greater than $3.2\,\mathrm{I_{VEM}}$. This reduces the TH-T2 rate to $\approx 20\,\mathrm{Hz}$ compared to a rate of $\approx 2\,\mathrm{Hz}$ for ToT-like triggers [97]. All T2s are then sent to CDAS with their respective timestamp, and CDAS then decides whether or not the third trigger level T3 is fulfilled. There are two different T3 configurations, both based on geometric considerations. They are illustrated in Fig. 3.6. The first one is the ToT$2C_1\&3C_2$ configuration. In this case, solely T2-ToTs are involved. A second T2-ToT must be located within the first cone C_1 around the central (first) trigger, and a third T2-ToT must be located within the second cone C_2. The alternative configuration may comprise a variety of T2s, either mixed or pure. It is called $2C_1\&3C_2\&4C_4$, following the same scheme: a second trigger has to be inside the first cone, a third trigger within the second and a fourth one inside the fourth cone. For both configurations, it is requested that the time coincidence for all contributing triggers is within $\pm(3+5C_n)$µs of the central trigger. If a T3 is created with the T2s, then the station data is requested by CDAS for the time of the trigger. Additionally, all stations with a T1-TH inside the time window are also read-out. A key aspect of this work will be the size of the T3. For very inclined air showers, the footprint exceeds more than 4 cones (station rings around a station). Hence, the air shower produces more than one T3 cluster. If the clusters have common triggers or all triggers are within 100 µs, which is usually the case for air showers, they will be merged later. The bandwidth is a limiting factor when it comes to the read-out of events. The transfer of data from one T3 event usually takes between 5 and 20 minutes, depending on the number of stations. Therefore, the number of T3s is quite low, with ≤ 10 T3s per station and day. The T3 data is subsequently saved by CDAS and can be reconstructed.

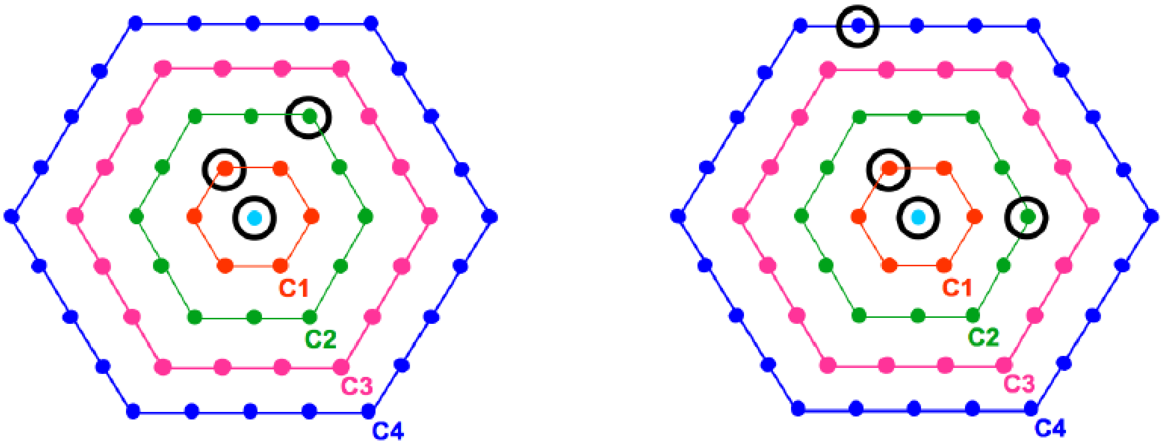

Figure 3.6: Shown are the two configurations for building a successful T3. The points mark station positions. The different colours indicate the different cones around the central station. Black circles show an example trigger in the station. Illustration from [94]. (Left) The ToT$2C_1\&3C_2$ configuration. (Right) The $2C_1\&3C_2\&4C_4$ configuration.

In order to ensure a high data quality, there are two additional physics trigger levels, T4 and T5. They are applied offline and filter events with unphysical timing (unphysical in this context means that the event is not of air shower origin but from background noise). Depending on the trigger types, the T4 performs a plane wave fit, which should succeed. The T5 then ensures that events close to the edge of the array are also reconstructable.

3.5 Photon searches at Auger

The trigger system is a sophisticated system, but it was specifically designed for the detection of hadron induced showers. Hence, photon searches at the Pierre Auger Observatory suffer from the strict but needed limitations of what to trigger on. Nonetheless, photon searches were previously conducted by utilising the diverse detector components of phase-1. In the following, the standard variables for the discrimination of photons and hadrons are presented, afterwards the results from the photon searches are discussed.

3.5.1 Variables for the discrimination of photons and hadrons

The main differences between photon and hadron induced air showers are due to their different shower developments and their muonic contents.

$X_{\mathbf{max}}$: The shower depth is a strong discrimination parameter due to the different heights of the maximum for primary photons and hadrons. As presented in Sec. 2.3, an air shower consists of different components. The hadronic and muonic components are important for the hadron induced showers. The interaction and decay of these particles determine the maximum depth of the shower. For a photon-induced shower, the number of produced muonic and hadronic particles is often negligible, but the EM component matters. The radiation length of $\lambda_{e^\pm} \approx \frac{9}{7}\lambda_{\mathrm{brems}} = 25.4\,\mathrm{g\,cm^{-2}}$ [42] is significantly smaller than the mean interaction length of lighter nuclei ($\lambda_p \approx 90\,\mathrm{g\,cm^{-2}}$) and mesons ($\lambda_\pi \approx \lambda_K \approx 120\,\mathrm{g\,cm^{-2}}$). However, photon-induced showers have a deeper maximum depth in the atmosphere, as they normally have a multiplicity of two per interaction or decay, whereas hadronic interactions can have multiplicities of 1,000 or more. Hence, the energy of hadrons is distributed on more particles. X_{max} might be one of the strongest variables, but it is also a sophisticated variable. Not for all showers an accurate X_{max} can be determined.

Station risetime: Connected to the maximum shower depth is a lower level variable, the so-called risetime. The risetime of WCDs at Auger is defined as the time difference between the integrated signal's levels of exceeding 10 % and 50 %. The time span is dependent on the maximum depth of the shower, as different heights lead to different time smearing of the signal. This is illustrated in Fig. 3.7. Higher shower maximums result in smaller smearing of the signal.

Furthermore, the muon content can play a significant role in this scenario. Muons usually travel faster than EM particles through the atmosphere, reaching the WCDs first. In photon-induced showers, the integrated signal can now exceed the 10 % threshold of the integrated signal, but the muonic component is not strong enough to also exceed the 50 % threshold. As a result, the threshold is only reached when the slower EM particles reach the detector. This prolongs the risetime significantly. The combination of all station risetimes yields a strong discrimination parameter in the end.

The muon density in the shower: The muon content in the air shower is another excellent discriminator. However, it has the same issue as X_{max} being a high-end variable. It is difficult to measure the muon density of air showers on a single event base with only the WCD. Therefore, additional detector components are necessary, such as the UMD or SSD. Hence, the muon density was not used in many analyses in the past.

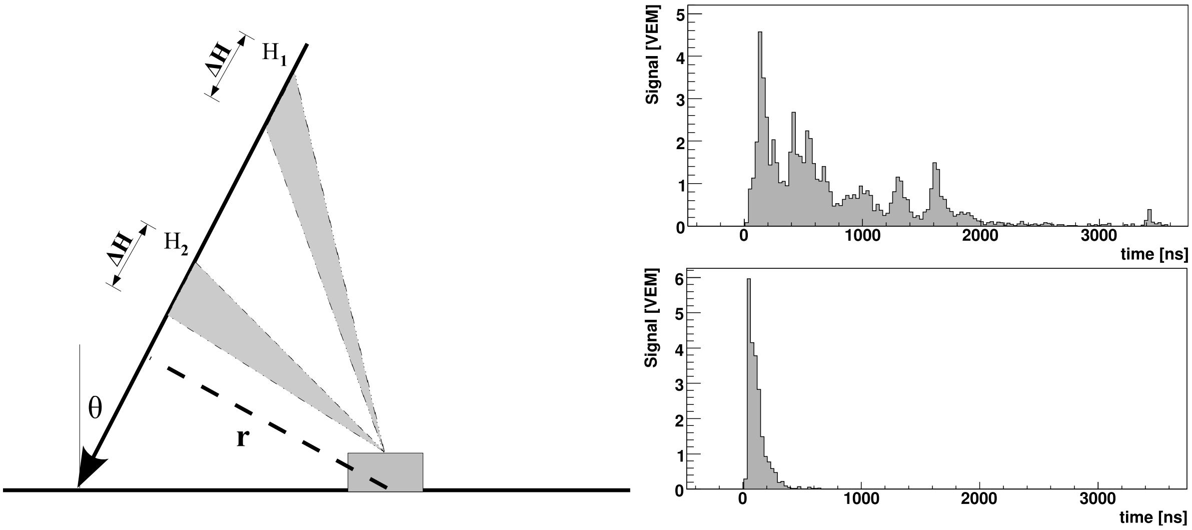

Figure 3.7: (Left) Depicted is the influence of the maximum shower height on the arrival time smearing. Large heights result in a smaller smearing of the signals. Illustration from [98]. (Right) Shown is the signal for an EM particle dominated shower (top, wide signal distribution) compared to a muon dominated shower (bottom, sharp signal distribution). Plots from [57].

Steepness of the LDF: The muon content is also linked to the particle LDF of the air shower. The LDF describes the radial dependence of the particle density with respect to the shower axis. The EM component dominates the LDF in close proximity to the shower axis, as the EM particles tend to exhibit less deviation from the shower axis. For larger distances, the muonic component begins to dominate and contributes more to the LDF. Since the muon content is low for photon-induced showers, the LDF is steep and strong signals can only be found near the shower axis. Hadron-induced showers have a significant signal contribution farther away from the shower axis. The LDF is not as steep. There are primarily two functions that describe this behaviour and yield discrimination variables. First, the LDF can be fitted by the following:

$$S(r) = S(1000) \cdot \left(\frac{r}{1000\mathrm{m}}\right)^{\beta} \cdot \left(\frac{r + 700\,\mathrm{m}}{1700\,\mathrm{m}}\right)^{\beta+\gamma} . \tag{3.5}$$

r denotes the distance from the core, S(1000) is a fitting variable describing the signal strength at a distance of 1000 m, and β and γ are fitting parameters for the steepness of the LDF. Second, a similar variable for the steepness of the LDF can be calculated by:

$$S_b = \sum_{i=1}^{N} S_i \left(\frac{r_i}{1000\mathrm{m}}\right)^{b} . \tag{3.6}$$

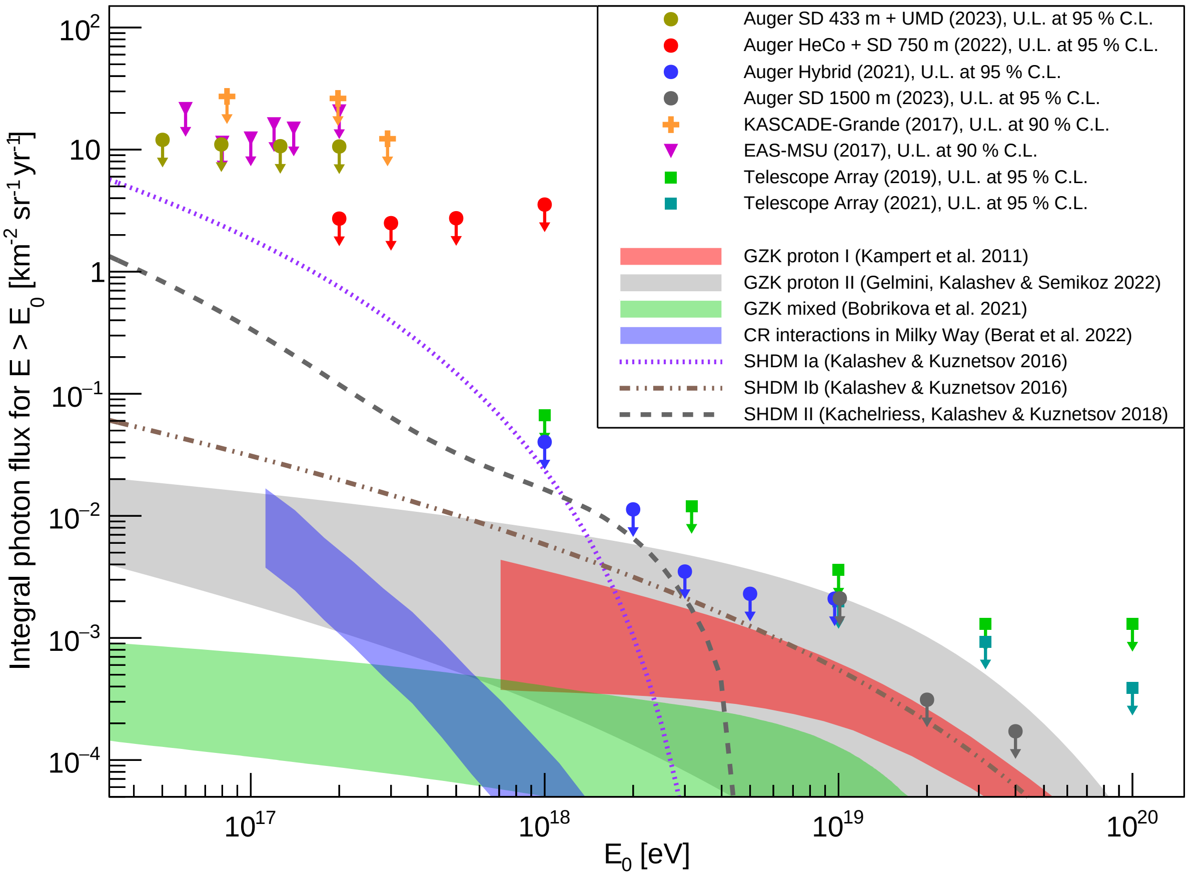

Figure 3.8: Shown are the integral photon flux limits at different energies. The markers show the limits from [99] (olive circles), [100] (magenta triangles), [101] (orange crosses), [102] (red circles), [103] (blue circles), [104] (grey circles), [105] (turquoise squares),[106] (green squares). The coloured bands and lines indicate predictions from different CR and dark matter scenarios.

Here, S_i is the signal of station i and b is a constant number. This constant number is usually between 2-4, depending on which energy range and primaries one looks at.

3.5.2 Previous photon searches

The discrimination parameters are combined and result in the searches shown in Fig. 3.8. At lower energies, the photon flux limits are achieved by using the low-energy extension of the Observatory, the infill. For energies below 1 EeV, two analyses were performed. One analysis for photon energies between 50 PeV and 200 PeV includes the 433 m array in the infill and the UMD [99]. The infill WCDs trigger potential photon showers and measure their energy content, consisting mostly of EM particles. The UMD then measures the quantity of high-energy muons reaching ground, resulting in a distinction between photon- and hadron-induced signals. The data utilised for the analysis comprises a time frame of approximately 15.5 months, as the UMD was only installed within the past few years. Nevertheless, the data set includes 15,919 events, all of which have zenith angles below 52°. With this data set, the most stringent photon flux limits were established in this energy region, but no photon candidates were observed.

At energies above 200 PeV, one can use the co-located FD sites HEAT and Coihueco in combination with the 750 m SD array [102]. The intersection of them yields a hybrid reconstructed data set of 2,204 events with zenith angles below 60°. The data set is affected by the low uptime of the FD and the steepness of the energy spectrum. The FD contributes with a reconstruction of X_{max}, while the WCDs provide information about the LDF. Again, the most stringent photon limits in this energy region were achieved by combining the variables. No photon candidates were observed.

At even higher energies, one can use the regular SD grid, which results in an overlap with all five FDs [103]. In the energy region from 1 EeV to 10 EeV one has a data set consisting of $\approx$ 32,000 events with zenith angles below 60°. The FD provides the reconstruction of X_{max}, whereas the WCD information is used in a universality approach [107] to anticipate the signal contribution of the muonic component. Combining these variables resulted again in the most stringent flux limits in this energy region. It is noteworthy that 22 photon candidates were identified, which aligns with the anticipated background of falsely identified hadron showers.

At the highest energies above 10 EeV, one is limited by the exposure. An FD detection cannot be required as it would limit the number of events due to its low up-time. Hence, only the SD is used [104]. 48,947 events were detected in a zenith angle range from 30° to 60°. The combined risetime and LDF variables yield the most stringent flux limits in this energy region. 16 photon candidates were identified with energies above 10 EeV, which is consistent with the expected background.

3.5.3 Motivation for an RD trigger for new photon searches

The photon searches conducted at the Pierre Auger Observatory share a common feature: they yield the strongest photon flux limits at the highest energies. Furthermore, many photon candidates were detected. Nevertheless, up to date, no event has been identified to have been photon-induced with complete certainty. WCDs alone may yield a large exposure, but the identification of photon events suffers from limited knowledge of the air shower with only the WCDs. The incorporation of the FD or UMD can enhance discrimination; however, it may limit the statistic due to its low exposure. Including the RD in the future could help to resolve this challenge. Being mounted on each WCD and having nearly 100 % up-time, the RD yields a large exposure. Furthermore, as the RD is sensitive to the EM component, it can improve the discrimination between EM and muon-dominated events.

Another issue could be resolved by the RD, which is connected to the scope of this thesis. All photon searches at Auger are restricted in their zenith angle range to below 60°. If one examines the development of photon-induced showers at higher zenith angles, it becomes apparent that there exists a limitation to the present setup. Large zenith angles result in substantial geometric distances between the detector and the shower maximum. These distances result in the absorption of most of the EM particles in the atmosphere before reaching ground [57]. EM particles reaching the detector concentrate close to the shower axis and leading to significant signals only at few stations, often not enough for a read-out. The muonic component, on the other hand, is weak for photon-induced showers, as depicted in Fig. 3.9. It shows the number of detected muons in all stations for Monte Carlo (MC) photon simulations, created with CORSIKA [108] and reconstructed using $\overline{\text{Off}}\underline{\text{line}}$ (*c.f.* Sec. 6.1 for information on the simulation set). The plot confirms the result presented in [57]: the zenith angle of the air shower has a minor impact on the number of detected muons (at least up to a zenith angle of 80 °). The geometrical distance between detector and shower maximum increases, which indeed favours the absorption of muons. However, the projection of the WCDs in the shower plane gains in size, which actually increases the probability of a muon to hit a WCD. The energy is far more important, for $E^{\gamma}_{\mathrm{MC}} \leq 10\,\mathrm{EeV}$ almost all showers have only 10 or less muons being detected. Muons are more spread than EM particles and also reach stations more distant to the shower axis. With ≈ 3-4 muons needed for a particle trigger, it becomes obvious that the muon number is insufficient for triggering enough stations for a read-out. Only for higher energies, more muons reach the detector, which translates to an increased trigger efficiency.

The trigger efficiency is depicted in Fig. 3.10. One achieves an energy weighted trigger efficiency, $\mathcal{E}^{\mathrm{T3}}_{\gamma}(\mathrm{WCD})$, for the zenith angle range between 65° and 85° of less than 20 %. It looks even worse for the highest zenith angles, where a reasonable trigger efficiency is achieved only for the highest energies.

The RD could help to resolve this issue. EM particles may already be absorbed in the atmosphere, but radio emission from air showers can traverse hundreds of kilometres and still be detectable. A possible discrimination is created by not having much particle information. Events with few or even no particles reaching the detector but a strong radio emission hint to a photon origin. Hence, if one introduces a trigger of the RD based on the radio signals, one could trigger these events, which were not detected before and

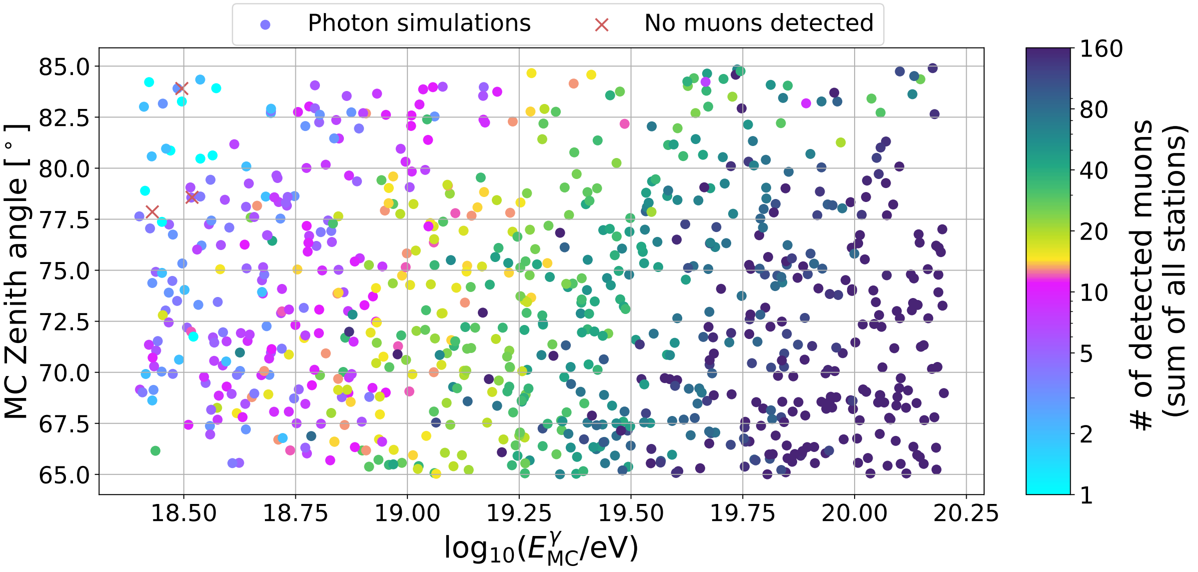

Figure 3.9: Number of detected muons (coloured points) as a function of primary energy and zenith angle. Red crosses indicate a simulation without detected muon. Background muons were not included in the simulation.

have simultaneously a strong discrimination power. In the following, the development of this RD trigger is discussed.

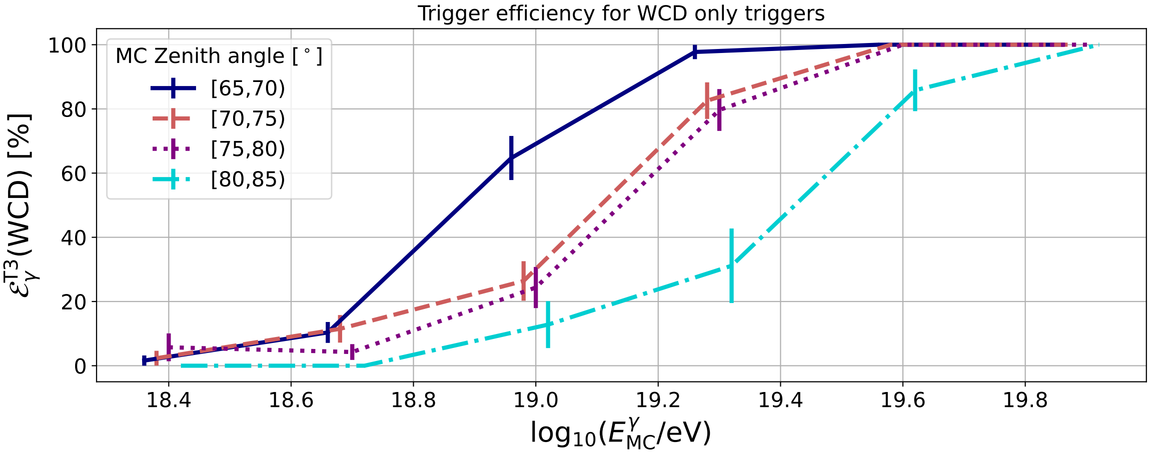

Figure 3.10: Photon trigger efficiency of the WCD at different energies. The different colour and line styles represent distinct zenith angle ranges.

CHAPTER 4

Radio noise at Auger

Parts of this chapter have already been published in:

J.Pawlowsky, J. Rautenberg
"Radio noise at the Pierre Auger Observatory - (almost) everything one needs to know",
Internal note of the Pierre Auger Collaboration (2023), GAP 2023-041

This Chapter is based on the data, which were available at the time of analysis. With more data available, the method developed in Sec. 4.4 was adapted by others, extended and in the end reversed for calibration purposes, which is nowadays a standard method in Auger (*c.f.* [109], Sec. 2.3 for more information).

In order to develop a radio trigger, it is essential to understand the type of noise present at the Pierre Auger Observatory. In the following, a classification of the noise is conducted, and then an analysis of potential sources is employed.

4.1 Overview of the data used

To evaluate radio noise, it is necessary to have a suitable data set. It is particularly important to obtain data, which is not solely triggered by the particle detectors, as almost all radio signals of interest for this study are not related to particle air showers but are anthropogenic Radio Frequency Interference (RFI). For this purpose, noise measurement campaigns are designed that rely on temporarily removing stations from the data acquisition and saving periodically noise traces to a USB stick, since a remote read-out via the standard Auger communication system is not possible. It is evident that in this configuration, only a limited number of stations and traces can be read-out.

The first campaign was conducted in March 2022 with four stations in the radio Engineering Array (EA). The second campaign was repeated in the EA for six stations[1] in November 2022. Learning from the first campaign, a timestamp on UTC second-base was added to the traces. However, the employed firmware of the RD FPGA had a bug, and the traces of both radio channels were scrambled. A method was developed to unscramble the data, but due to another bug, an analysis can only be performed for the first 950 bins of the traces. The third campaign was conducted in March 2023. With an increased availability of RD hardware, it was possible to record data for longer measurement periods and a wider range of spatial variations. An overview of the measured stations can be found in Fig. 4.1 with additional information in Tab. 4.1. It should be noted that the data taking is periodic (no physics trigger, but continuous triggering). The traces were initially saved to the buffer of the UUB and subsequently converted into files containing 5,000 measurements each, and then saved to the USB-stick. During the writing of the files, no additional traces could be recorded. The writing process took approximately the same amount of time as the recording. Thus, there is a constant pattern of recordings and voids of data.

In the following, an analysis of the measurements is presented. As the data from the third campaign contains the most information about noise sources and their time development, the data from that campaign will be shown predominantly. Unless otherwise specified, other measurements did not reveal any supplementary or contradictory information. Moreover, the weight of each observed data point is noteworthy to mention. As one measures with a sampling frequency, f_{samp}, between 10 Hz - 100 Hz and each trace is t_{trace} long, ranging between 3.8 µs - 8.192 µs, only a fraction of the time is actually recorded. Hence, each shown trace represents $1/(f_{\mathrm{samp}} \cdot t_{\mathrm{trace}})$ data points. For the standard configuration of $f_{\mathrm{samp}} = 100\,\mathrm{Hz}$ and $t_{\mathrm{trace}} = 8.192\,\mu\mathrm{s}$, it results in a time fraction of $\approx 0.1\,\%$ and a weighting factor of 1,221. If the polarisation channel is not explicitly mentioned and only one variable is presented, the root of the geometric sum of both channels will be used as a measure of the noise.

---

[1] Initially seven stations were included but `Station 1736` had an LNA with a broken channel and will not be discussed further.

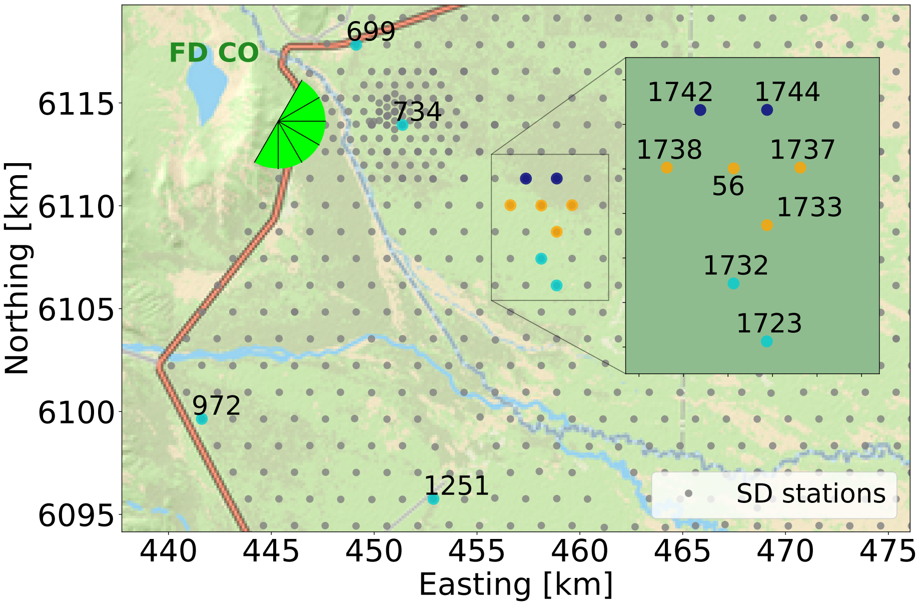

Figure 4.1: Map of the stations with recorded periodic data. The colours of marked stations indicate the campaign (campaign I: orange, campaign II: orange and dark blue, campaign III: light blue).

Table 4.1: Overview of the measurement campaigns

Station	Time	f_{samp} [Hz]	# Traces [10^6]	t_{trace} [4 ns bins]	Location	Comment
Campaign I						
56	21 h	100	4	2048	EA	No timestamp
1737	21 h	100	4	2048	EA	No timestamp
1742	21 h	100	4	2048	EA	No timestamp
1744	21 h	100	4	2048	EA	No timestamp
Campaign II						
56	21 h	100	4	950	EA	Firmware bug
1733	21 h	100	4	950	EA	Firmware bug
1737	21 h	100	4	950	EA	Firmware bug
1738	21 h	100	4	950	EA	Firmware bug
1742	21 h	100	4	950	EA	Firmware bug
1744	21 h	100	4	950	EA	Firmware bug
Campaign III						
699	74 h	10	2.2	2048	El Sosneado	
734	47 h	100	4	2048	UMD loc.	Noisy env.
972	74 h	10	1	2048	Transformer close	
1251	74 h	10	1	2048	La Junta	
1723	40 h	100	4	2048	Extended EA	
1732	40 h	100	4	2048	Extended EA	

4.2 Description of observed features

First, a general overview of observed frequencies and amplitudes is presented. Figure 4.2 depicts the frequency spectrum of the EW channel of `Station 699` over the course of nearly 3 days. The average of 5,000 traces was used to obtain 800 bins for the time axis (800 files with 5,000 traces each), while the FFTs of the traces yield a binning of 125 MHz / 1024 bins = 0.12 MHz/bin. The colour scale indicates the intensity of individual frequencies obtained from the FFT. The same time binning was also applied to the RMS of the traces, as depicted at the bottom.

A notable decrease in intensity is observed below 30 MHz and above 80 MHz, which is consistent with the applied limits of the band-pass filter. Furthermore, one obtains multiple continuous horizontal lines. The bands around 59 MHz and 67 MHz are worth mentioning. At $f_{\mathrm{bc}} = 58.887\,\mathrm{MHz}$, a beacon line [110] is observed, which is used for calibrating AERA and is emitted at the FD site Coihueco. This line is especially visible in the North-West of the Observatory. A much stronger frequency is known at approximately 67 MHz, originating from a TV station. It is assumed that this line derives from Malargüe or its vicinity. It will be demonstrated that it is well visible across most of the array, and that it decreases in intensity with increasing northing of the array. The aforementioned frequencies and other continuously observed frequency bands are well-known and are suppressed in air shower reconstructions. They do not impede measurements or triggering, and they can serve as calibration and validation of analysis.

Furthermore, there are frequencies that are not continuous, but appear at specific periods of the day. A spectrum of frequencies ranging from 27 MHz−30 MHz is observed, exhibiting strong activity during the daytime, while remaining predominantly quiet during the night. The band is known as citizen band radio [111] (CB-radio), used for example for Walkie-Talkies, data transfer or remote controls. Time-wise, a resemblance exists between the frequency of approximately 35 MHz, which is nowadays utilised for CB-radio as well. It is evident that these frequencies are relatively quiet during the nighttime in Argentina.

Another noteworthy frequency is located at 55 MHz, with clearly defined times during which it appears. Moreover, it is better defined as a single frequency than the 27 MHz − 30 MHz band (*c.f.* 00:00 UTC). Occasionally, when the intensity is exceptional strong, it also emits into adjacent frequencies (*c.f.* at approximately 03:00 UTC).

The plot demonstrates not only horizontal lines, but also vertical lines with appearances over multiple hours. They are also identifiable by the significantly increased RMS. During these periods, a noise source is present that emits into all frequency bands. Therefore, existing noisy frequencies, such as the 55 MHz line, will be amplified. It will

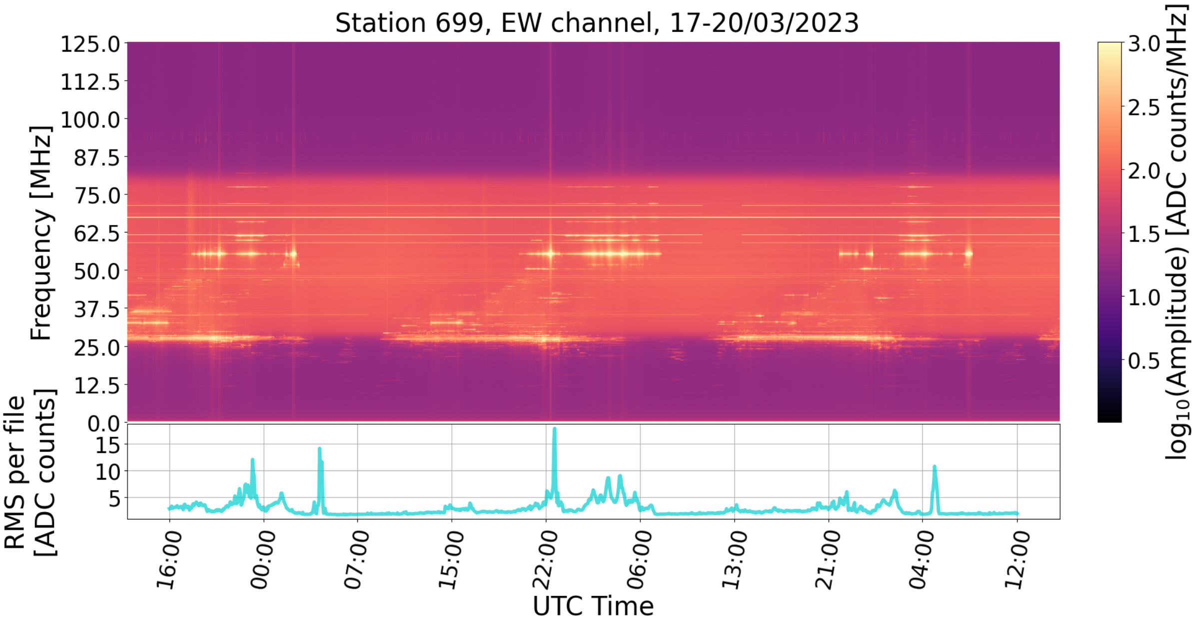

Figure 4.2: Frequency spectrum over time for `Station 699` in the March 2023 campaign for the EW channel. Brighter colours indicate a strong amplitude of the respective frequency. The light blue curve depicts the RMS of the traces at specific times.

be later demonstrated that the majority of these periods can be correlated with lightning occurrences.

While both March measurement campaigns show a similar noise baseline for the different frequencies, the November data appears overall less noisy. This can be seen in Fig. 4.3 for `Station 1737`. The November data seems to have more well-defined periods of noise. The frequencies are more clear-cut, but this could also be the result of the different binning in the FFT due to the reduced trace length. Hence, the strength of single frequencies is challenging to compare. Notwithstanding, the overall picture appears to exhibit a greater degree of noise quietness, with fewer periods of strong noise, as demonstrated by the RMS of the traces. The cause of this behaviour remains uncertain. Two explanations are probable: first, both March campaigns were done with the same firmware version, while the November campaign was done with a newer one. The firmware may have influenced the gain of the channels and thus the recorded noise strength. A more probable explanation would be found in a seasonal dependence. The noise can vary depending on human activity within the Observatory, seasonal temperature changes or the galactic noise [112]. The latter dependence may require consideration during calibration and reconstruction, but it should not pose a challenge to neither data reconstruction nor triggering. Transient events are more of a concern and will be discussed in the following more detailed.

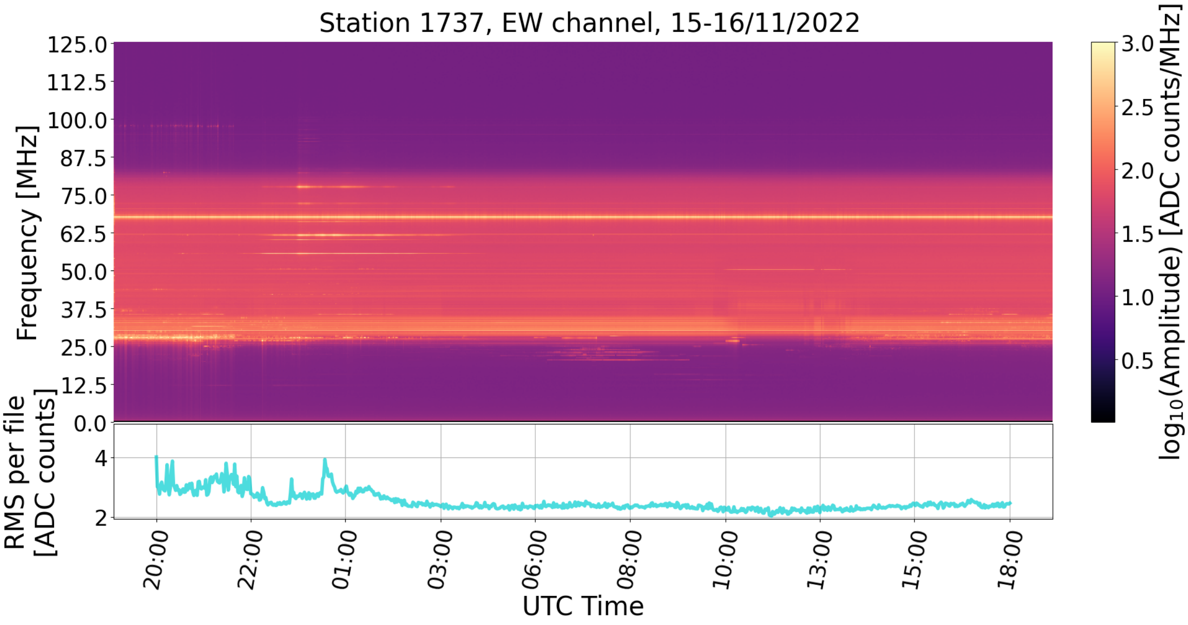

Figure 4.3: Frequency spectrum over time for `Station 1737` in the November 2022 campaign for the EW channel. Brighter colours indicate a strong amplitude of the respective frequency. The light blue curve depicts the RMS of the traces at specific times.

4.3 Noise categorisation

In order to understand the occurrence of challenging noise better, a categorisation of noise is performed.

4.3.1 Regular noise

It is important to note that traces typically exhibit a relatively low noise level, with fluctuations of a few ADC counts. This is depicted Fig. 4.4. The distribution of the maximum trace amplitude is depicted for `Station 1737` for March 2022. The majority of traces for both channels have maximums of below 20 ADC counts with a peak at around 10 ADC counts (marked by **A**). One example trace is depicted in Fig. 4.5. Fluctuations of ≈ 6 ADC counts are seen for both channels. The frequency spectrum shown on the right shows a flat spectrum in the sensitive band between 30 MHz and 80 MHz, with the exception of single peaking frequencies such as the 67 MHz line. These traces are the irreducible radio background, but they are no challenge for triggering or reconstruction. In contrast, amplitudes are observed in Fig. 4.4 that are concerning (marked by **B**). A small fraction of traces with amplitudes exceeding 80 ADC counts are observed. These noise traces vanish when looking at summarised parameters, such as the average of

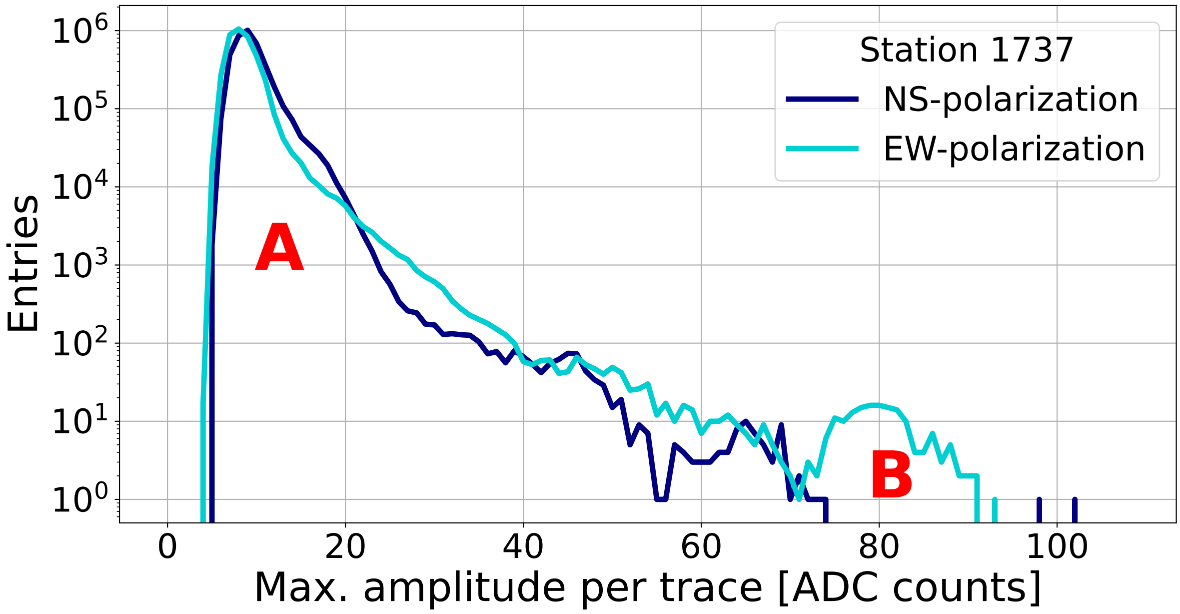

Figure 4.4: Distribution of the maximum trace amplitudes for `Station 1737` for the March 2022 campaign. The colours indicate the distributions for the NS (dark blue) and EW (light blue) channels. Regular **A** and worrisome amplitude **B** distributions are indicated.

amplitudes, but they appear to be correlated within noise bursts. Despite lasting only a few seconds, these periods have the potential to generate significant trigger rates and ultimately lead to a malfunction in the data acquisition process. The source of these traces is presented in the following.

4.3.2 Lightning as a noise source

The radio emission of lightning is well known and is often used for lightning detection. The Pierre Auger Observatory operates five lightning sensors, one at each FD side and one at the campus in Malargüe [76]. Commercial lightning detectors have been installed, which measure the radio emission of lightning within the frequency range of 10 kHz−90 kHz. These devices are capable of detecting lightning from distances of up to hundreds of kilometres. The different positions and the timing capability of the detectors make it possible to triangulate the lightning. All lightning occurrences are then written to a database, along with their estimated position and time of detection. This data serves as a hint for explaining single peaks and noisy traces seen in the recorded periodic data, and investigating the correlation to the periodic noise data helps to understand the influence of lightning on the trigger rate.

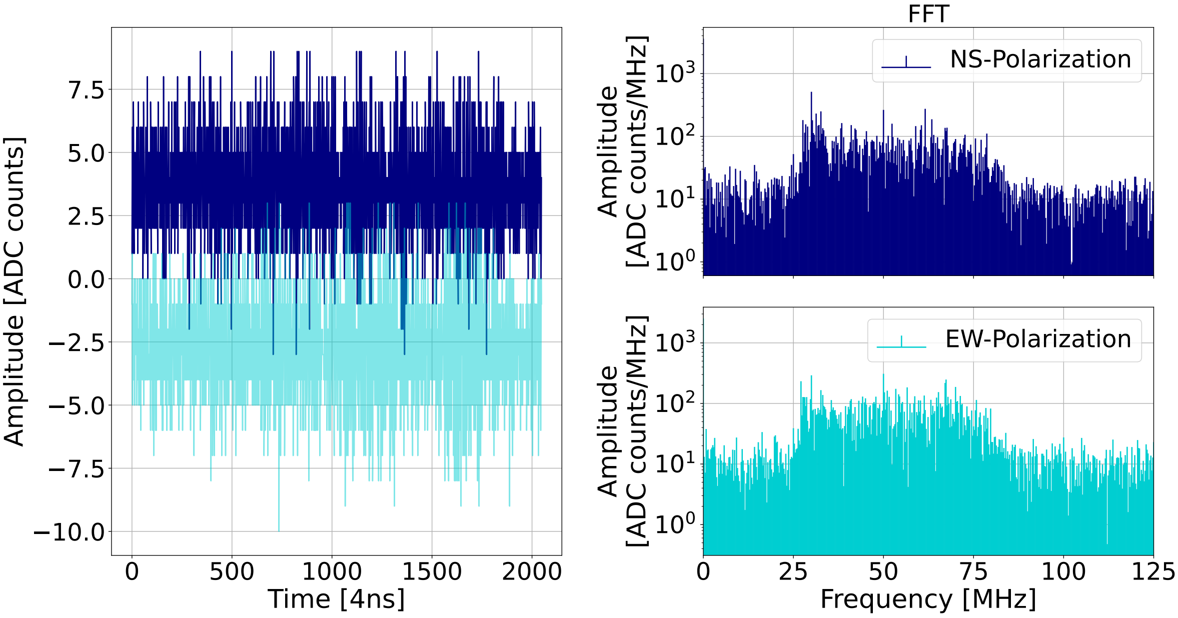

Figure 4.5: (Left) Example regular noise traces for the NS (dark blue) and EW (light blue) channel. (Right) The frequency spectra of the traces.

During the noise measurement campaign conducted in March 2023, a significant number of lightnings was observed. This results in noise traces with a pattern as shown in Fig. 4.6. The observed noise lacks a clear structure, consisting of multiple single peaks of medium and high amplitude, with maximums in the region of the foreseen RD trigger thresholds (≈ 25 ADC counts as a benchmark for an aimed trigger threshold). The noise pattern is similar to the noise identified as lighting in [76]. As a result of inaccuracies in the timing and positions, it is not feasible to establish a direct correlation between individual noise traces and entries in the lightning database. Nonetheless, a quantitative correlation between noise traces with high amplitudes and lightning occurrences can be established.

The link between those events is shown in Fig. 4.7, which depicts the maximum trace amplitude of `Station 1732` for approximately 40 hours. In order to make the figure legible, less than 0.1 % of all traces are plotted. Multiple periods are observed in which the noise bursts, which results in significantly higher trace amplitudes. During noise quiet periods, such as the first full day between 06:00 UTC and 11:00 UTC, the maximum trace amplitude is typically below 10 ADC counts. After 18:00 UTC, a strong increase in trace amplitude is observed, with maximums of hundreds of ADC counts. The values are significantly exceeding the trigger thresholds, which would result in a reasonable increase in aperture for cosmic ray air showers. During the lightning time of 15 hours, approximately 27k traces were recorded with amplitudes larger than 25 ADC counts.

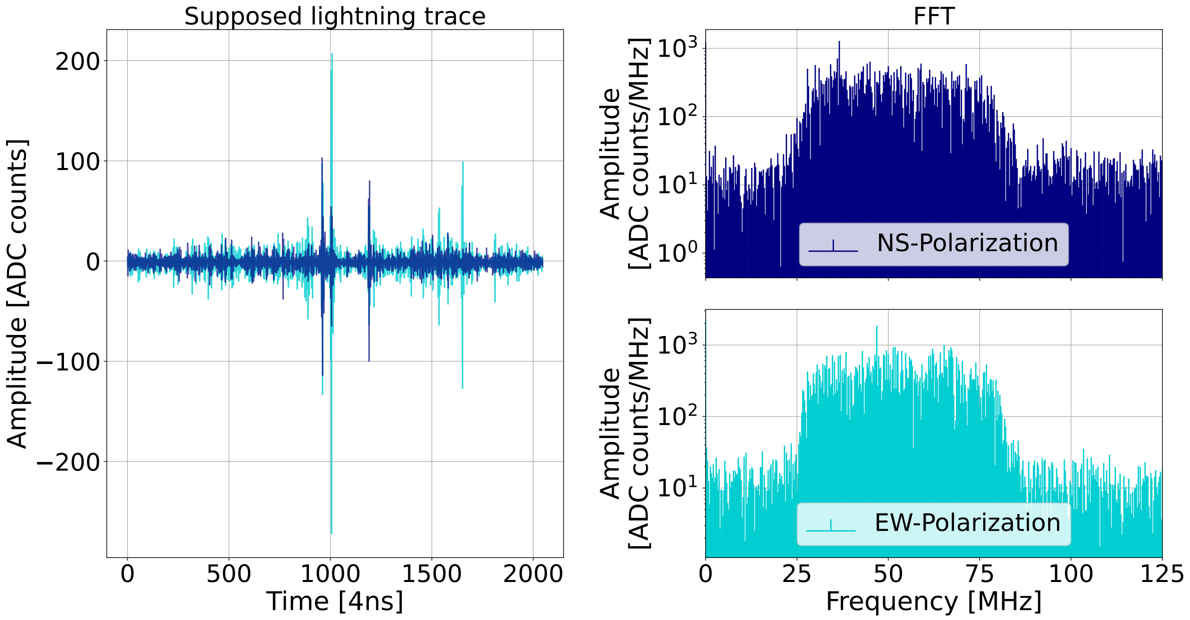

Figure 4.6: (Left) Example noise traces for the NS (dark blue) and EW (light blue) channel, with peaks due to lightning. (Right) The frequency spectra of the traces.

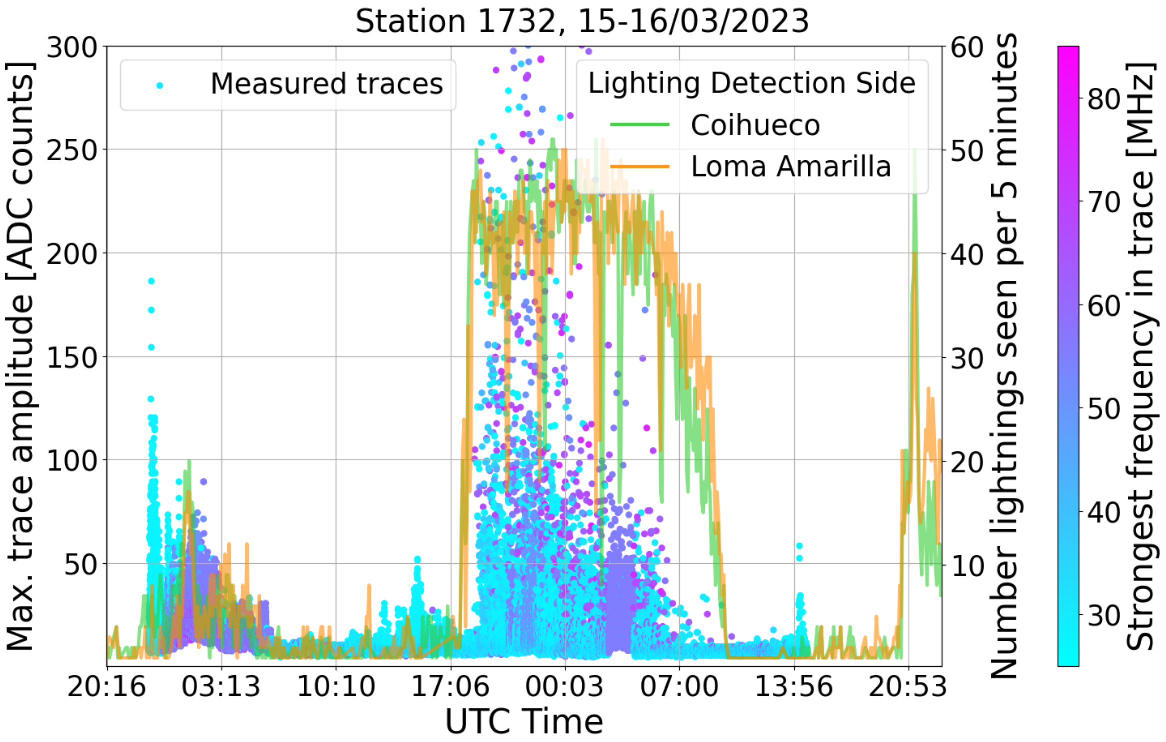

Figure 4.7: Time development of the maximum trace amplitude of `Station 1732` during the third noise campaign. The points represent one recorded trace each. The colour indicates the dominant frequency of the traces. To keep the plot legible, less than 0.1 % of the measured points are plotted. Lightnings recorded per 5 minutes are shown for the FD sides Coihueco (green) and Loma Amarilla (yellow)

Considering the recording time fraction, 33M traces would have exceeded the threshold, resulting in an average trigger rate of 611 Hz. This rate is approximately 25 times higher than the average station trigger rate for all particle triggers combined. It is also exceeding the available bandwidth, and without any safeguarding, it would lead to an immediate failure of the central data acquisition. The strongest frequency of each recorded trace yields another hint that the observed noise traces are caused by lightning events, as its radio emission radiates almost uniformly throughout the whole sensitive frequency range. There exists no singular frequency that dominates the spectrum, with the exception of brief periods, such as between 03:00 UTC and 04:00 UTC, where the lightning noise appears to overlap with another noise source with a distinct frequency of 55 MHz. The occurrences of lightning within 5 minutes (solid lines) of two stations (Coihueco and Loma Amarilla) show many detected lightnings, with peaks of 50 lightnings within 5 minutes. The number of lightnings should not be directly correlated with the maximum amplitude of single traces (but rather the intensity of lightning and the distance). However, one observes a correlation with the average of all trace amplitudes. This is demonstrated in Fig. 4.8, which depicts the average maximum trace amplitude and number of lightnings with the same time binning of 5 minutes (left) and their correlation (right). The correlation is strong, with a value of 0.91. A diminished correlation coefficient likely results from the presence of distinct overlapping noise. Especially at the beginning of the recording, one does not observe many lightnings, but there are still large average maximum trace amplitudes. The dominant single frequencies of 27 MHz and 55 MHz (*c.f.* Fig. 4.7) hint to a mono-frequent human made noise source during these periods coinciding with the lightning.

Lightning is a challenging event for a potential RD trigger due to multiple factors. Lightning events happen more or less randomly. The occurrence of lightning may be favoured by the season of the year and the daytime. However, single lightning events cannot be predicted. Moreover, the structure of lightning noise may be discernible visually from that of air shower events, but the patterns are too similar to reject them with simple methods like peak counting. Advanced machine learning techniques might be capable of distinguishing, but they are difficult to implement at the FPGA trigger level [113]. In conclusion, it is improbable that a radio trigger can be active during lightning conditions. Furthermore, the measured data is most probable flawed and not suitable for air shower reconstruction [114, 115].

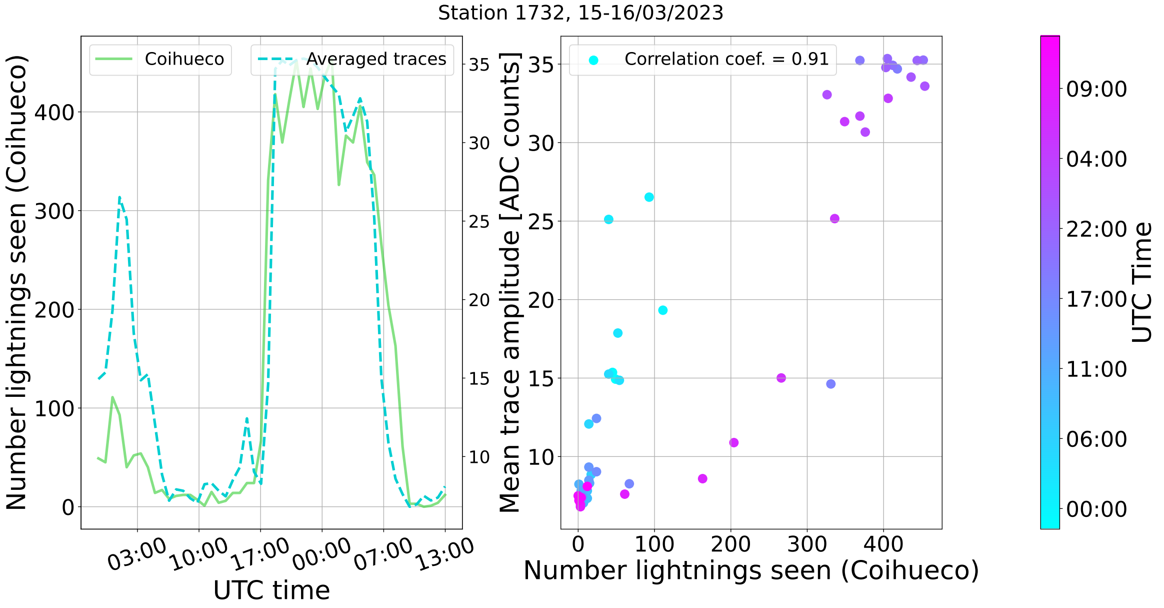

Figure 4.8: (Left) Time development of the number of observed lightning at Coihueco (green solid line) and mean trace amplitude of noise (dashed blue line). Both variables have the same time binning of one hour. (Right) The correlation is depicted for the aforementioned variables (points). The colours indicate the time of recording. A correlation coefficient of 0.9 is obtained.

4.3.3 Daily occuring noise

The data recordings also indicate that some noise sources appear daily. This may be attributable to sources that are commonly utilised by citizens (such as the 27 MHz band), or noise that is generated during daily routines, such as the daily transmission of data. The latter can be examined by searching for similar traces and patterns on different days. The challenge comes when one does not record continuously, but only a fraction of the time. Therefore, it is uncertain whether the traces recorded depict the same time, even if two stations measure within the same timeframe. Therefore, one must search for reoccurring noise patterns on a more macroscopical scale. Instead of analysing individual traces, it is preferable to examine summed parameters of the trace, such as the RMS. Two stations from two noise campaigns are chosen, with the difficulty of missing timestamps in the first campaign. During the analysis of the RMS for one channel against time, striking structures were identified and subsequently searched for in the time development of the other station. Figure 4.9 indicates a match of patterns for different stations with a time difference of 8 months. The trace numbers of the November campaign were shifted to align with the structure of the March data. A striking match between the two measurements reveals that the pattern origin is identical. A daily

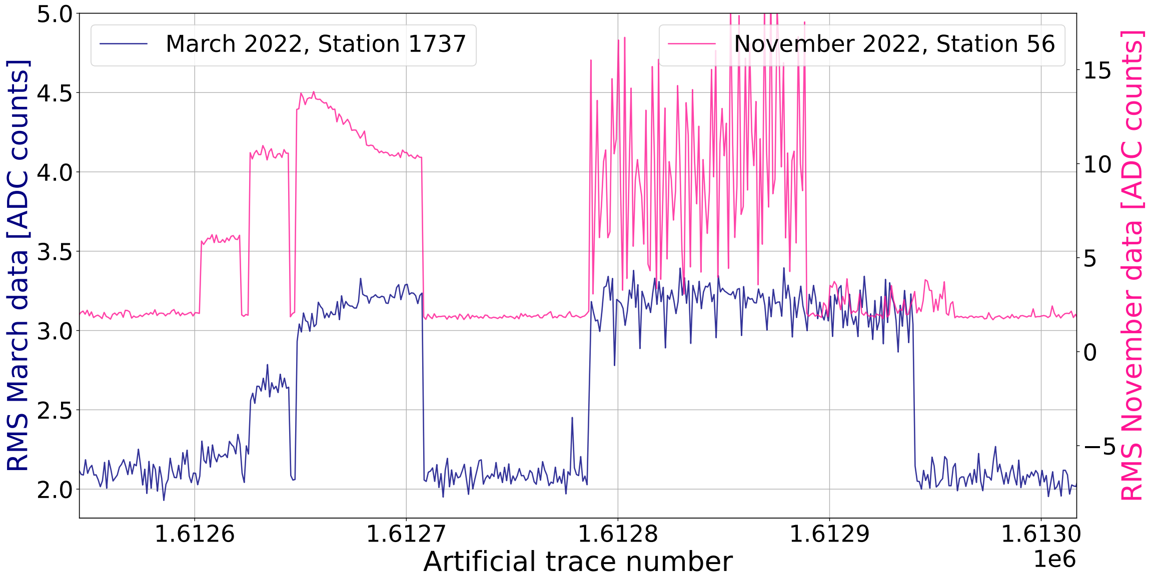

Figure 4.9: Development of the RMS of `Station 1737` for the March 2022 campaign (blue) and of `Station 56` for the November 2022 campaign (magenta). The November 2022 data is shifted in the trace number to have a matching pattern.

computer routine or data transmission serves as an explanation. This is supported by the small deviations between the patterns. Differences in computation time might lead to a shift in time.

This hypothesis is compatible with the observed frequencies. The patterns exhibit a correlation with the enhancement of the 27 MHz and 55 MHz bands, indicating the presence of transmission protocols, as depicted in Fig. 4.10. The traces can have amplitudes exceeding thresholds, which could be used for a radio trigger. Since these traces are also consecutive and the burst of noise can last for hours, a method for suppressing these traces is needed (*c.f.* Sec. 5.1.2). Otherwise, it would result in trigger rate bursts, disrupting normal data acquisition. It appears impracticable to raise the trigger threshold during these times, as the elevated threshold value would render the air shower detection ineffective. A frequency-based rejection is difficult due to hardware limitations of the FPGA. It is possible to dismiss these tracks based on their distinct morphology. While air showers have a clear signal peak lasting for just a few hundred nanoseconds, these traces exceed thresholds ubiquitously over the whole trace.

An important information about the origin of noise is its source. Particularly, it is important to distinguish between internal noise, such as that generated by the detector station, and external noise. Internal noise is spatially limited and can be eliminated through the modification of hardware. To verify whether the noise is external, one

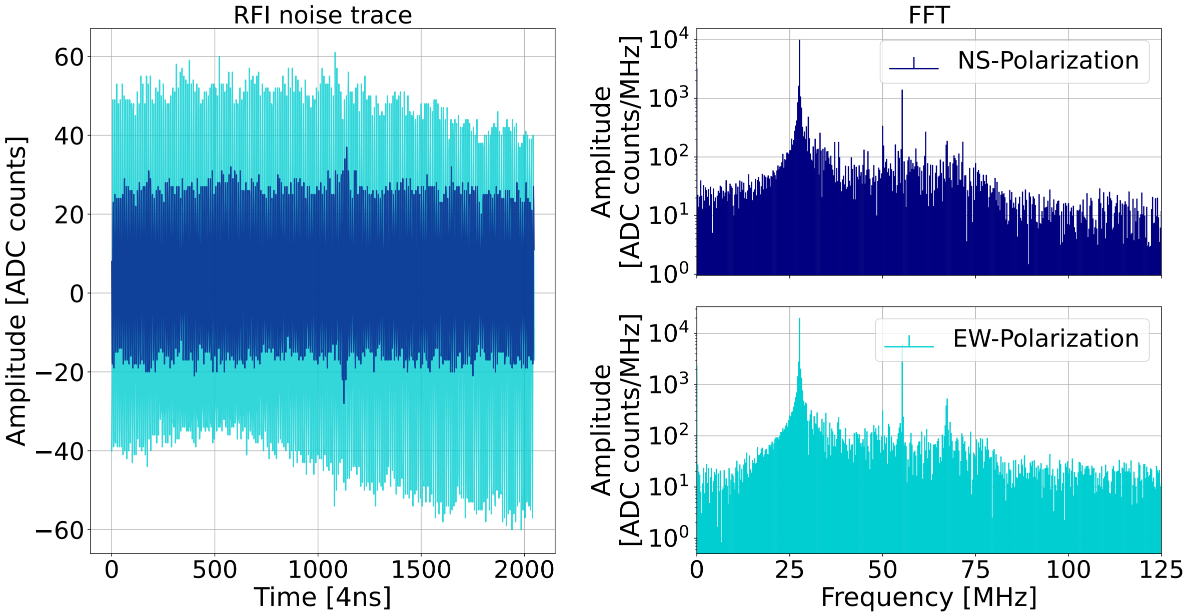

Figure 4.10: (Left) Example noise traces for the NS (dark blue) and EW (light blue) channel for a period with strong 27 MHz line. (Right) The frequency spectra of the traces.

can use the antenna stations by AERA. These antennas can be very distant from SDs. Therefore, it is not expected that the noise produced by the SDs will be observed by the AERA antennas. The AERA antennas measure noise periodically every 100 s. This data can be used for the cross-check. One station (Station 53) was selected due to its flawless operation and the absence of any SDs directly adjacent to the antenna. The data of one day during the March 2023 campaign is depicted in Fig. 4.11. The AERA antenna observes the same frequencies as discussed above. It also demonstrates patterns of frequency occurring at specific times. It suggests that there is an external noise source, which can be seen on a large scale of the array.

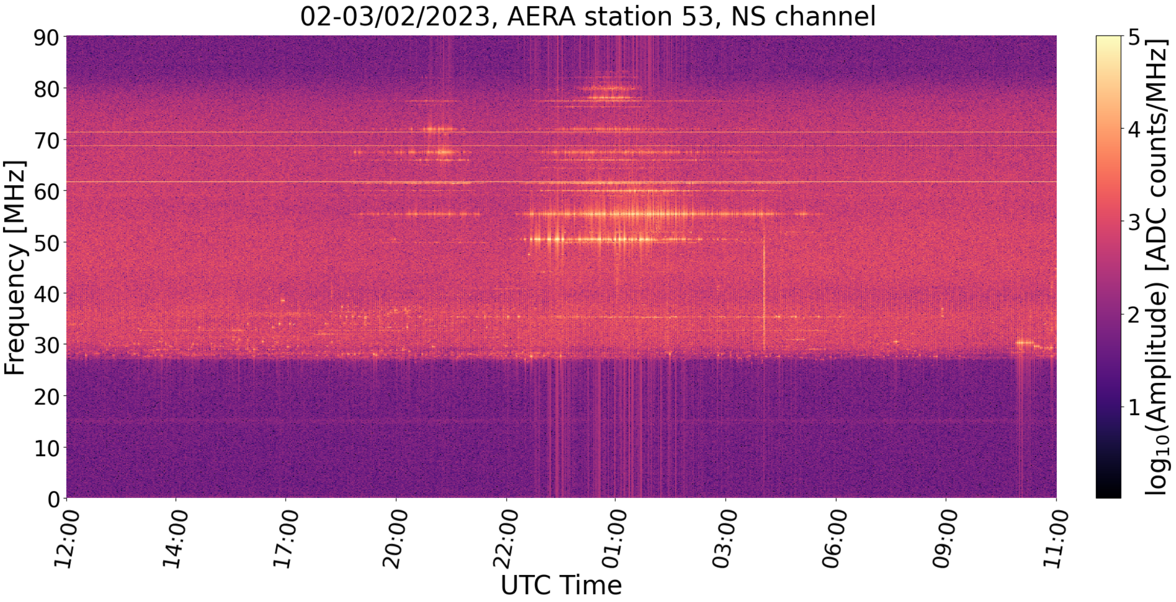

Figure 4.11: (Frequency spectrum over time for AERA station 53. Brighter colours indicate a strong amplitude of the respective frequency.

4.4 Source localisation

External noise could be further reduced. Sources could be modified in agreement with the owner, or the detection efficiency could be reduced by increasing the trigger threshold in specific directions. Other experiments, such as the radio experiment RNO-G, exhibit a temporal increase in their efficiency for specific directions in the case of intriguing astrophysical experiments in the respective direction [116]. Vice versa, one could reduce the efficiency for directions of noise flares.

4.4.1 Noise localisation with AERA

Multiple noise studies were conducted for AERA [117]. One study involves the continuous measurement of an antenna using self-triggered data for an extended period. Another study uses the AERA phase 1 configuration and triangulates sources utilising event data. The main findings of both studies are summarised in Fig. 4.12. The frequency spectrum for different azimuth angles (left) shows features seen before for the RD data. A band at 27 MHz is faintly visible, coming from all directions. The 55 MHz feature can be observed in the North direction. Although the characteristics are discernible, they are less evident than those depicted for RD (*c.f.* Fig. 4.2). This is likely caused by the frequency scale, including frequencies below 15 MHz. These frequencies are typically significantly reduced, utilising band-pass filters. Moreover, the averaging

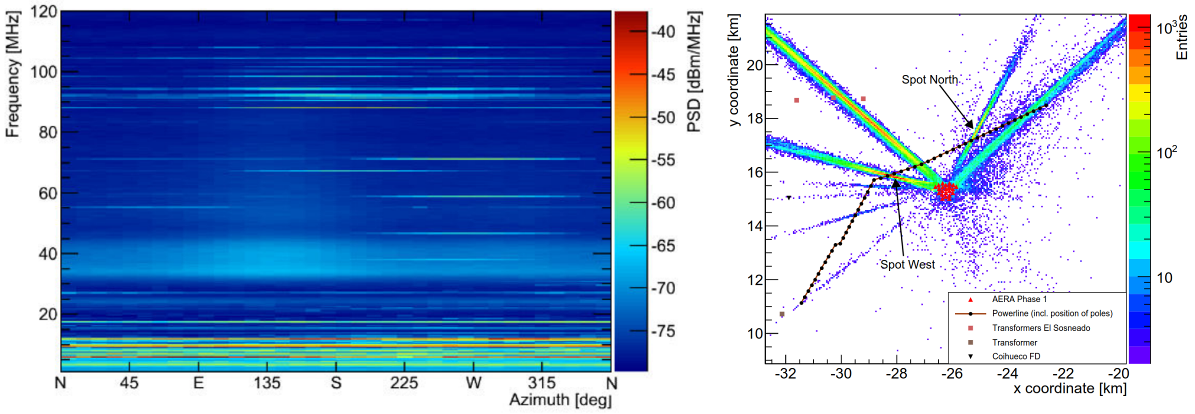

Figure 4.12: Noise study results from [117] for AERA. (Left) Frequency spectrum for different azimuth directions, the colour indicates the strength of the frequencies. (Right) Determination of possible sources in the region of AERA.

over time yields a less evident pattern as the aforementioned characteristics are only present for brief durations. Hence, developments in time for specific directions are not shown. In the overall noise localisation map of Fig. 4.12 (right), two noise sources were identified, called the North and West spots, which are within a few kilometres of AERA. With modern satellite pictures, it is possible to identify the likely sources[2]. Since they are quite local, they might be interesting for AERA due to their short distance, but not relevant for RD, which covers the whole array. These local sources will be seen by only a few stations.

4.4.2 Noise source localisation - polarisation method

AERA has the advantage of having many antennas at different positions, which measure simultaneously due to their common self-trigger. Therefore, it is feasible to conduct a precise and straightforward reconstruction of noise events by utilising a triangulation of sources. The periodic data of RD does not have these factors, so polarisation information from single stations must be used.

The RD antennas consist of the NS and EW channels, both being also sensitive to the vertical direction. Therefore, both channels can be analysed separately and subsequently combined to examine the source directions. The steps to localise sources are detailed below. First, the frequency spectrum is calculated individually for each channel. The spectra yield the amplitude of the frequencies of interest. For locally stable sources, one should observe a constant relation, depending solely on the general strength of the

---

[2] for the West spot: `https://goo.gl/maps/Rs6825iEbvAKY1ZdA`, and for the North spot: `https://goo.gl/maps/2hxHfpnWX2WszHXYA`

source at this time. Since the frequencies of interest may be vanishing for periods, it is important to study their behaviour on short time scales. One example of the constant behaviour is depicted in Fig. 4.13, which shows the amplitudes of the 67 MHz line for `Station 1732` for one saved data file, consisting of 50 seconds of data. As the location of 67 MHz is roughly known (in close proximity to Malargüe), the line is utilised for calibration and validation of the employed method.

A stable relation of the two channels is obtained. The slope of the linear fit describes the relation between the channels. The allowed axis offset accounts for a generally higher noise level in one direction. The slope yields the azimuth angle φ to the EW-axis via

$$\varphi = \arctan(m). \tag{4.1}$$

Although only one angle has been calculated, there exist four possible directions of noise: the calculated direction, its continuation in negative direction, and the mirrored directions. This is illustrated in Fig. 4.14 (left). If only one angle is mentioned in the following, the most likely source direction will be chosen. The calculation of the azimuth angle is repeated for all the available data for the designated station. To ensure that no other factors, such as lightning, interfere, it is requested that a correlation of 0.8 is obtained for both channels. Therefore, unstable noise times are ignored.

Figure 4.14 (right) shows the calculated φ for `Station 1732`, each entry representing one analysed data file. An evident accumulation of data points is observed at an angle of approximately 77°, in close proximity to the direction of Malargüe, as depicted by the red line. Small deviations may result from a variety of factors, including but not limited to varying gains in the channels, resulting in a modified slope, and the absence of the antenna pattern during the analysis (as it was not available at the time of analysis). Further, misalignments of the antenna directions could result in biases. Misalignments were observed mostly in the order of a few degrees, in particular after strong winds. Thus, the difference between the direction of Malargüe and the calculated angles is satisfactory for the time being.

Combining all stations, the source can be localised, shown in Fig. 4.15 (left). All calculated noise directions (four directions, *c.f.* Fig. 4.14) are virtually drawn on the map and each time two lines cross on the map, a count is registered for the crossing point. Not all combinations of stations are allowed. For instance, given their proximity, `Station 1723` and `Station 1732` would naturally possess numerous crossing points within their respective regions. Moreover, in the event that a station lies between the presumed source and another station, this combination is prohibited. The map is binned on a $4{\times}4\,\text{km}^2$ grid and a 2D histogram is applied. For the 67 MHz line, two hotspots

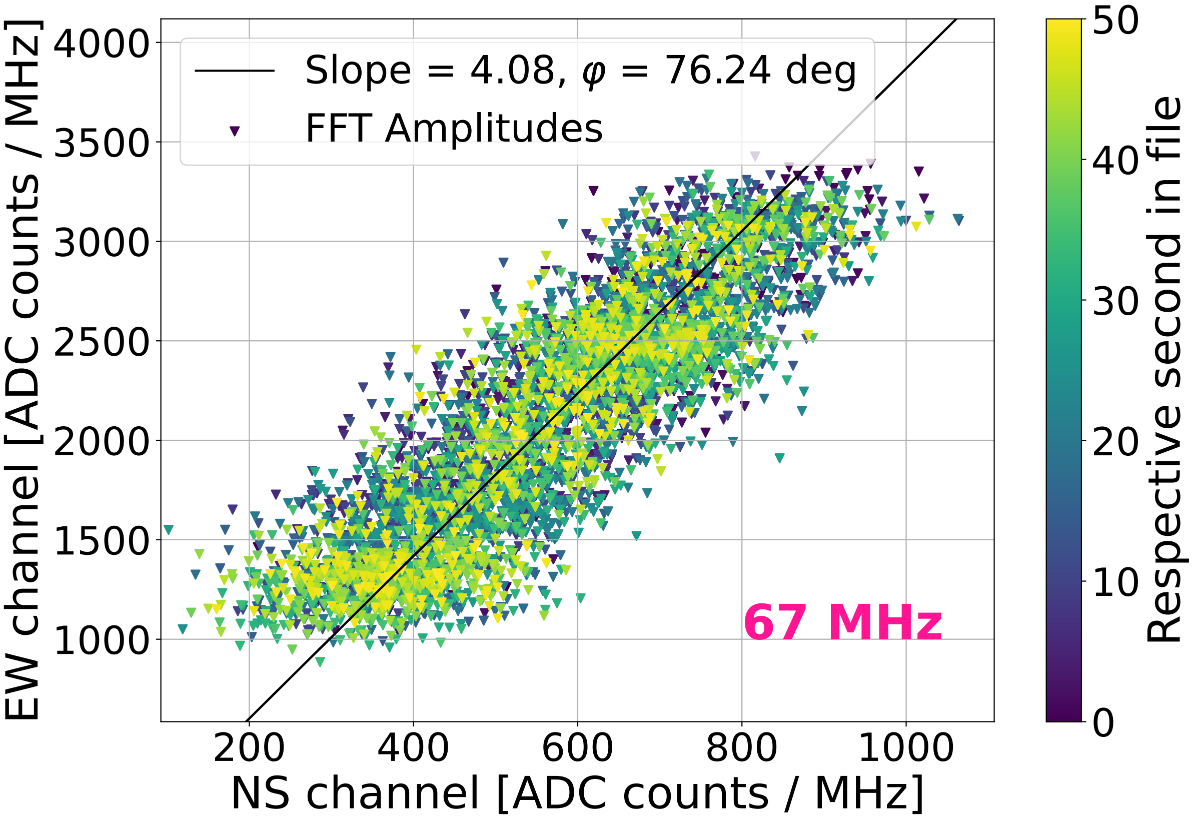

Figure 4.13: Strength of the amplitudes of the 67 MHz line for one example recorded file for the different channels. The colour scale indicates the time within the file. The black line shows the performed fit.

appear, one near Malargüe (South) and one above El Sosneado (North) with each more than 500,000 crossings. Due to the mirroring of the calculated angles, multiple hotspots are expected. Figure 4.15 (right) additionally illustrates the distribution of amplitudes of the 67 MHz line for `Station 972` and `Station 699`. For `Station 972`, significantly larger amplitudes are seen than for `Station 699`, which suggests that the source is expected to be in the South. Likely sources are a large radio tower[3] or a communication tower in the East of Malargüe[4]. Other sources in Malargüe are possible, but the results serve already as validation that the method yields a strong spatial delimitation of the possible source.

---

[3] `https://www.google.com/maps/@-35.4354065,-69.5740941,296m/data=!3m1!1e3?entry=ttu`

[4] `https://www.google.de/maps/place/Base+Comunicaciones+-+Malarg%C3%BCe+-+TI+CUYO/@-35.4791617,-69.5516702,937m/data=!3m1!1e3!4m6!3m5!1s0x967a79573292b837:0x206067ed40c53fef!8m2!3d-35.4793213!4d-69.5524786!16s%2Fg%2F11t0rcsb2p?entry=ttu`

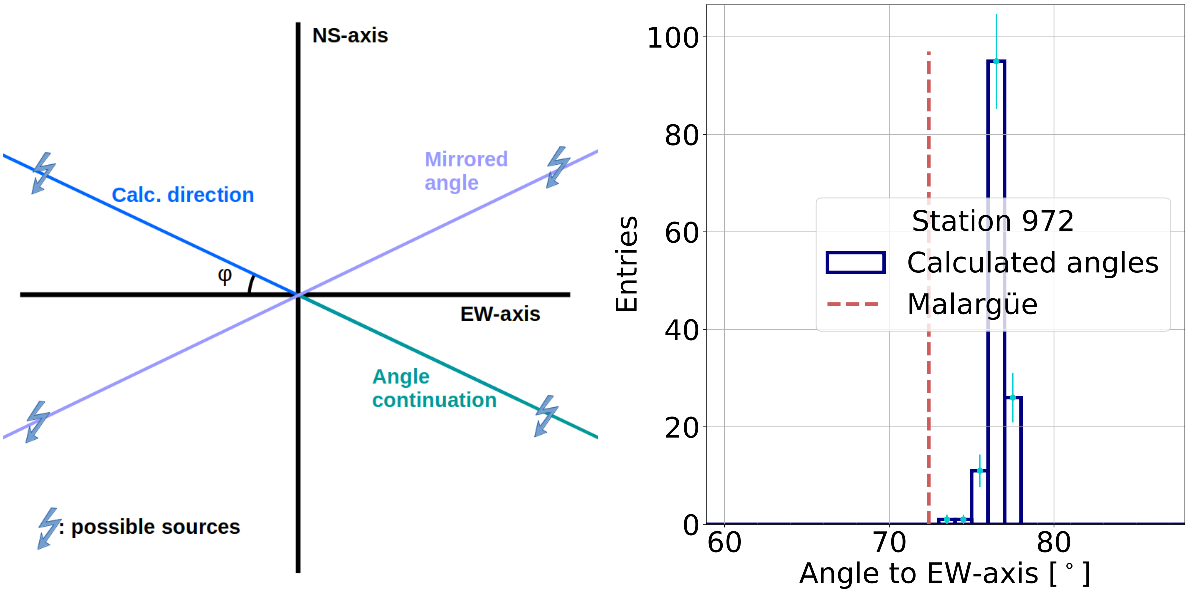

Figure 4.14: (Left) Possible source directions from the calculated source angle. The blue line shows the calculated line, the green one its continuation. With the used method, the mirroring (purple) at the EW axis is allowed. (Right) Distribution of the calculated angles for `Station 1732` for the 67 MHz line. The red vertical line indicates the direction of Malargüe.

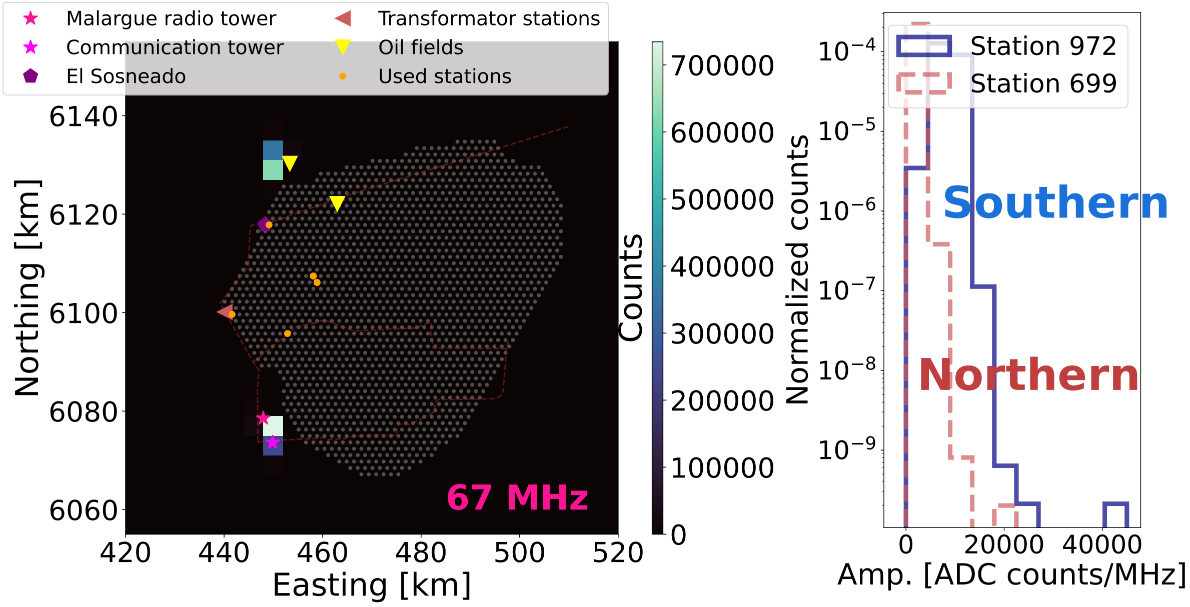

Figure 4.15: (Left) Map of the calculated source location for the 67 MHz line. The colour scale indicates the number of crossings of calculated angles for the different stations. The grey dots mark the positions of SD stations, the orange ones indicate the used stations in the source localisation. Other markers represent locations of interest. (Right) Distributions for selected stations (`Station 699`: red, `Station 972`: blue) of amplitudes of the 67 MHz line.

4.4.3 55 MHz source

The exercise is repeated for the 55 MHz line. Since the source seems to be changing over time, it is even more important to carefully select the used data. There seems to be specific times of day when the source is active, for example caused by computer routines which send data daily at certain times. During the active source phase, one experiences robust correlations and favourable matches, whereas the inactive phase yields meaningless outcomes. This is depicted in Fig. 4.16. The data of a file during both the active (left) and inactive (right) phases is shown. For the active period, a good fit is performed on the amplitudes, which show an ordered behaviour over time, with the strongest amplitudes early in time. For the inactive phase, no strong correlation is visible, and no fit has been performed.

The selection of active times for the 55 MHz line that did not coincide with lightning conditions is small. Therefore, the quantity of fits and crossings executed in the map, as depicted in Fig. 4.16, has been significantly reduced in comparison to before. Notwithstanding, a significant hotspot is observed, located in the North, above El Sosneado. Two weaker spots have been observed to be more prevalent in the South, but it is anticipated that they are mirrored. This is in agreement with the observed amplitudes, which are more strongly distributed towards large values for the station most North, `Station 699`, as opposed to the southern station, `Station 972`. Therefore, there are strong indications that there exists a singular source in the North that produces the 55 MHz line. A source could not be determined using online maps, even when using finer binning. As the terrain becomes hilly in this region, it is possible that the source localisation may exhibit a slight bias due to a stronger vertical component of the signal. Therefore, one may observe a mixing in the channels.

4.4.4 27 MHz source

The noise of the 27 MHz line may have a similar structure in the traces and may also occur at similar times as the 55 MHz line, but the source localisation yields an entirely different picture. This is shown in Fig. 4.18 (left). The amplitudes are strongly varying in strength. Nevertheless, it still appears that the signals have specific directions for certain times. For example, at early times one observes data points (marked by **A**), which have strong amplitudes in the NS-channel. For later times (marked by **B**), one observes a strong signal in just the EW-channel, indicating that the source is close to the NS-axis. This fluctuation in different directions on a very short timescale is incompatible with only one spatial steady or even moving source. It is rather interpreted as multiple

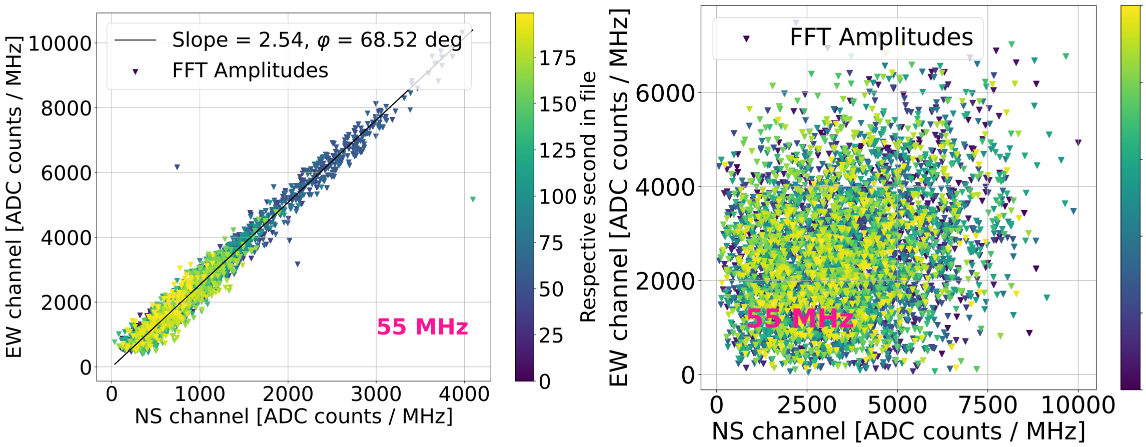

Figure 4.16: (Left) Strength of the amplitudes of the 55 MHz line for one example recorded file for the different channels. The colour scale indicates the time within the file. The black line shows the performed fit. (Right) The same but no fit was performed due to a weak correlation of the channels.

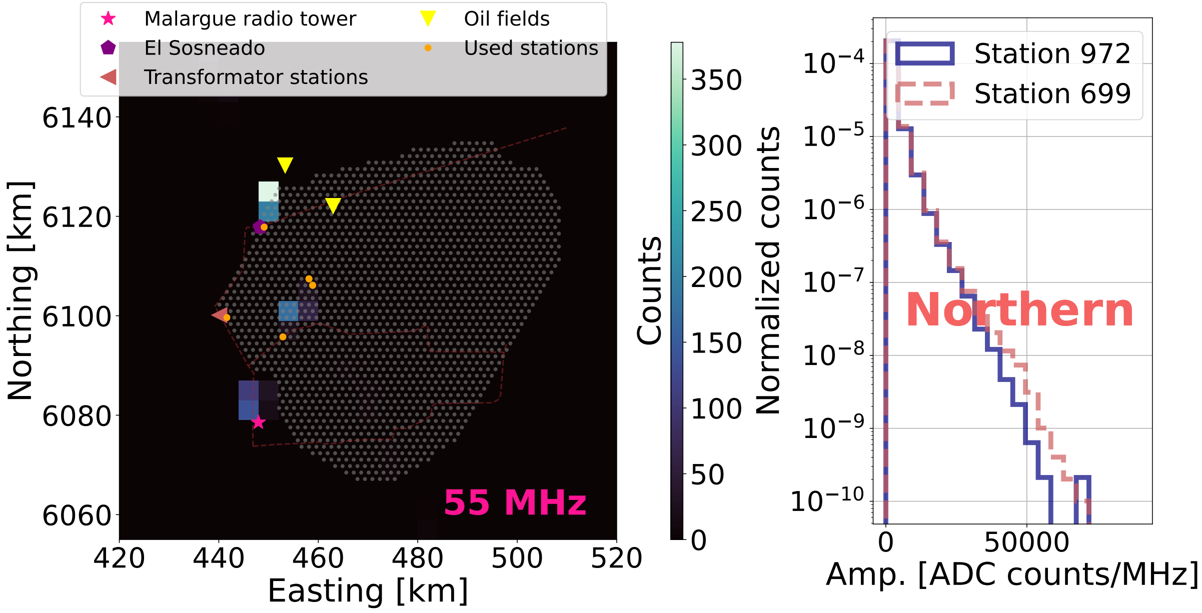

Figure 4.17: (Left) Map of the calculated source location for the 55 MHz line. The colour scale indicates the number of crossings of calculated angles for the different stations. The grey dots mark the positions of SD stations, the orange ones indicate the used stations in the source localisation. Other markers represent locations of interest. (Right) Distributions for selected stations (`Station 699`: red, `Station 972`: blue) of amplitudes of the 55 MHz line.

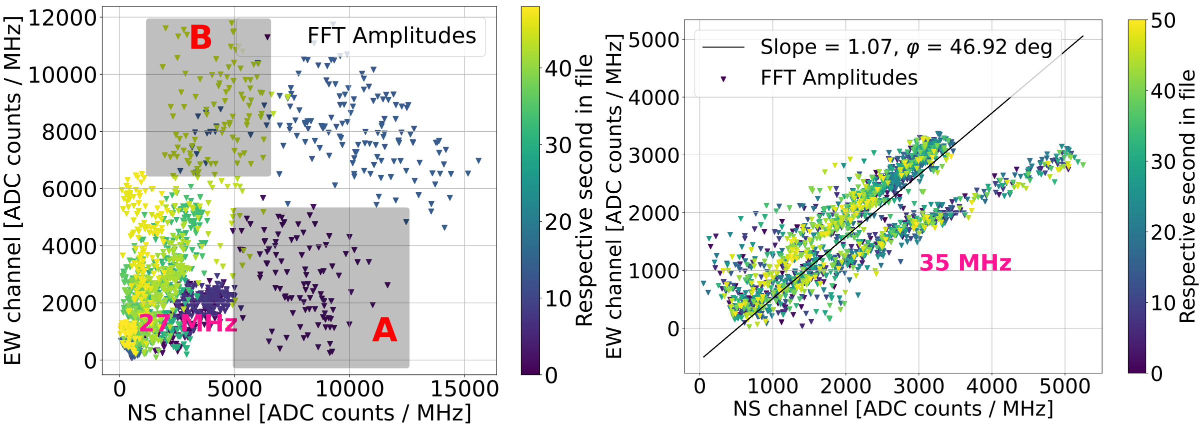

Figure 4.18: (Left) Strength of the amplitudes of the 27 MHz line for one example recorded file for the different channels. The colour scale indicates the time within the file. The black line shows the performed fit. The red boxes indicate interesting features. (Right) The same for the 35 MHz line without any markings.

sources being in all directions, which are active on short time scales. This is in agreement with the specification of the 27 MHz line. As previously described, this frequency band is commonly used by citizens, and therefore, every person using its remote control could be a source. A reduction of the noise at the source is therefore not possible.

4.4.5 35 MHz source

The frequency of 35 MHz is not the most concerning. However, it does reveal an intriguing source determination. This is shown in Fig. 4.18 (right). The performed fit does not accurately depict the data for the plot of amplitudes. This is because there are two distributions, and therefore two source directions, which are clearly visible. The conventional approach proves ineffective, and it is only upon requesting a significant correlation of 0.95 that meaningful outcomes can be obtained. At present, the selection comprises solely instances in which a singular noise source is present and a singular noise distribution is discernible. The resulting noise source map, shown in Fig. 4.19, is therefore inconclusive with multiple possible source locations. The distribution of amplitudes shown on the right does not provide a significant other interpretation.

4.4.6 Discussion of other possible noise sources

Despite the identification and classification of numerous noise sources, it is evident that additional noise characteristics will emerge in the future. A spatial spread was achieved with the third measurement campaign; nonetheless, all campaigns predominantly pop-

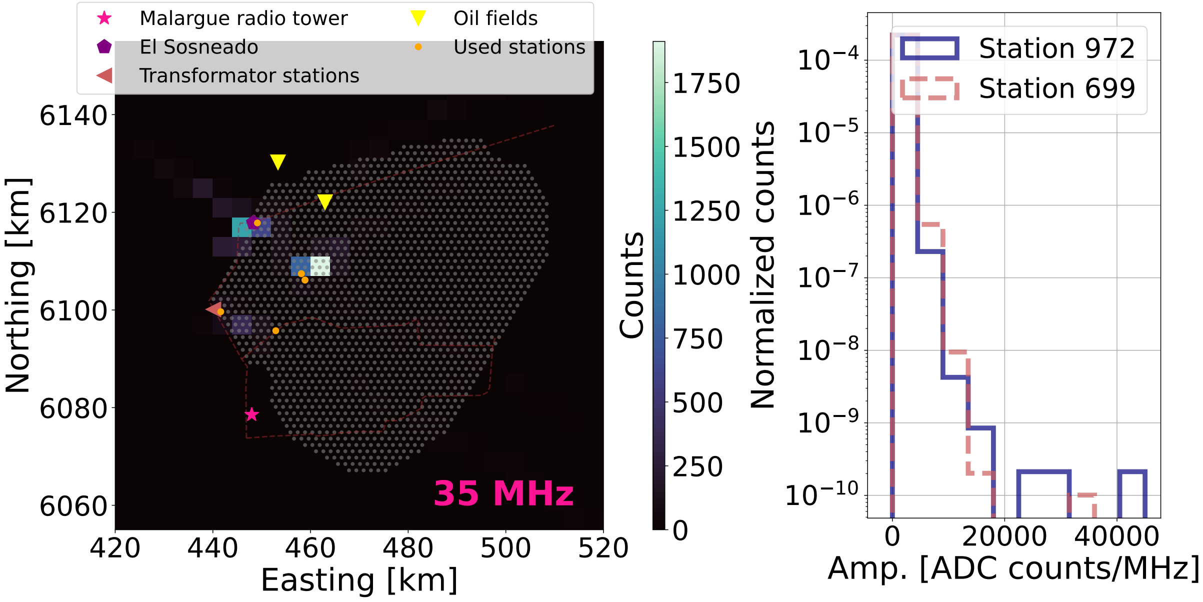

Figure 4.19: (Left) Map of the calculated source location for the 35 MHz line. The colour scale indicates the number of crossings of calculated angles for the different stations. The grey dots mark the positions of SD stations, the orange ones indicate the used stations in the source localisation. Other markers represent locations of interest. (Right) Distributions for selected stations (`Station 699`: red, `Station 972`: blue) of amplitudes of the 35 MHz line.

ulate the North-West region of the array. Measurements in the South near Malargüe or in the East might reveal challenges that are not observed by now. Moreover, challenges may occur very local, such as stations situated next to power lines. Additionally, noise emitted by nature may not be fully understood. On-ice and in-ice experiments (such as RNO-G) observe the triboleclectic effect [118], arising most probable due to sliding ice during strong winds and yielding high trigger rates. The same effect should be discussed for sand grains sliding over the soil in the North at Auger.

CHAPTER 5

DEVELOPMENT OF A RADIO TRIGGER

This chapter describes the different steps for implementing an RD trigger. It begins with a description of the trigger design, with individual components to yield a feasible and efficient implementation. It will be briefly described, how the trigger is simulated in Offline. Following, results from field tests of the trigger are presented.

5.1 Concept of the trigger mechanism

Air shower signals have a clear and characteristic shape. This shape makes it possible to have different designs for the trigger. For example, shape matching triggers are popular [119], in which the shape of the signal is compared to expectations from air showers. If the shape coincides, a trigger is fired. Another option is to use the Hilbert envelope to determine the signal strength. If the signal strength exceeds a predetermined value, one may trigger a signal read-out. At the same time of triggering, one has to deal with noise, as shown in Chapter 4. One type consists of mono-frequent signals (e.g. the 27 MHz line), which are ubiquitous over the entire trace. The second type consists of signals coming from electrical discharges, which have a very similar shape as air shower signals. Both above-mentioned triggering methods are effective at rejecting the first category of noise, but still trigger on the second category of noise. Furthermore, both methods necessitate computational power, as integrations and multiplications must be executed, which is not available on the RD FPGA.

Another possibility is using the Signal-To-Noise Ratio (SNR), which could yield the best trigger efficiency. The possibility of using an SNR for the case of a photon search will be discussed in Sec. 6.3. Nevertheless, it was decided that a constant trigger threshold would suffice for a first implementation. An SNR would make the exposure calculation difficult, as it requires an extensive noise library from different periods and locations across the entire array, which is currently not given. In the future, with a functional initial trigger version, one could try to implement more sophisticated solutions.

5.1.1 Threshold trigger design

A classic threshold trigger does not require many resources and is additionally effective at triggering air showers. This design is susceptible to ubiquitous noise; however, it can be extended as discussed in Sec. 5.1.2 to veto the noise. The algorithm of a threshold trigger is depicted in Fig. 5.1. A threshold, called the high threshold T_H, is applied to the raw ADC traces of each channel. Three things are to mention here. By design, T_H can be fixed or be variable, determined by the noise level. Second, the two RD channels possess their individual voltage supply, and both channels can have different baselines, which is also different from 0 ADC counts. Hence, T_H is shifted by the corresponding baselines upward or downward. If T_H is used, it accounts for the baseline correction and represents the absolute value. Thus, the threshold can also be exceeded for negative values of the signal. Thirdly, T_H is applied for both channels individually. This introduces a directional bias. Air showers coming aligned with one of the channels have an increased probability of being detected. For azimuth arrival directions at a 45° angle to the RD polarisation, one expects a lower trigger efficiency (disregarding other effects) as the signal is split into both channels. This could be corrected by taking the root of the geometric sum of both channels. However, this is currently not possible due to missing bits on the RD FPGA, as most of the bits of the RD FPGA are already taken up by an FFT, which is essential for monitoring. Therefore, inter-channel calculations are currently not feasible, and the trigger must operate on a single channel basis. With a more efficient FFT, it would be feasible to liberate bits and perform calculations across multiple channels. However, this would require extensive research.

When the threshold is exceeded, an RD T1 trigger is created on the RD FPGA. The T1 is then subsequently transmitted to the UUB and automatically elevated to an RD T2. It is equivalent to the other T2 triggers, being foreseen to contribute in the T3-building. Only if a T3 is formed, a read-out of the contributing stations is requested. For the T3 building, a trigger time has to be defined. For instance, in Fig. 5.1, multiple bins exceed the indicated trigger threshold. The trigger time is now defined as the first bin exceeding the threshold. This definition has advantages and disadvantages. On the one hand, a trigger can be initiated as soon as an exceeding of the threshold is detected. Other definitions of the trigger time, such as the time of the signal maximum, could lead to a delay of the sending of the trigger. Particularly, the presence of ubiquitous noise signals could potentially result in undesirable behaviour. On the other hand,

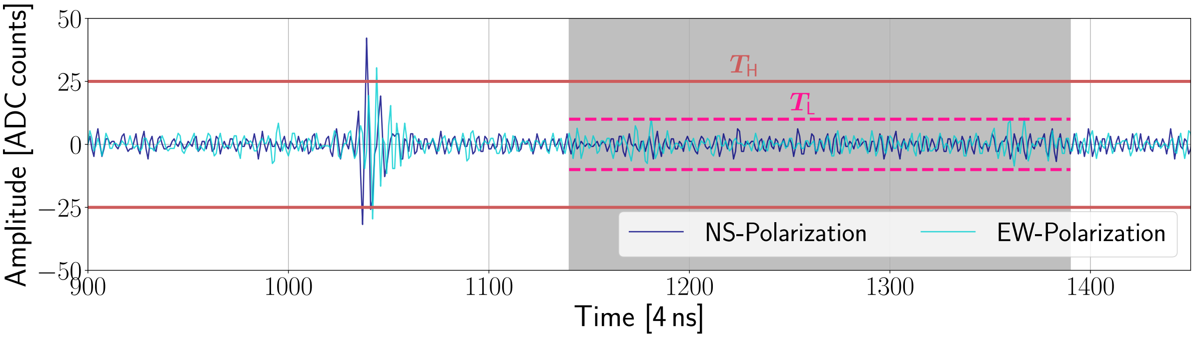

Figure 5.1: Illustration of the trigger design: the blue lines show the RD traces of the two channels of a triggered signal. The solid red lines indicate the trigger threshold, T_{H}. The dashed magenta lines show the vetoing threshold, T_{L}, which is checked for in the grey area.

the definition of the trigger time can also lead to artefacts in edge cases. Stations with smaller signals may exhibit inconsistent trigger times in comparison to stations with larger signals. The time of the maximum amplitude should only depend on the geometry of the station and shower maximum and is the same independent of the signal amplitude. This does not hold true for the time of first exceeding the trigger threshold. The greater the signal amplitude at maximum, the earlier the trigger threshold will be exceeded. Hence, the time definition is inconsistent for small and large signals. The inconsistency is only marginally in terms of the triggering scheme, where time buffers in the order of µs are included, while the inconsistency is in the order of hundreds of nanoseconds. Hence, the proposed time definition seems like the natural option.

One feature of the RD automatically prevents sending multiple triggers for the same signal, if T_{H} is exceeded multiple times. When a trigger is created, the RD FPGA immediately buffers the data. The writing of the data results in a dead-time of the data stream, which is not only observed for the RD trigger but for all triggers at a station, as they all trigger the read-out of the RD. An estimation of this dead-time can be derived from trigger test data to be $\approx 0.45\,\mathrm{ms}$.

The particle triggers of the WCD and the RD trigger should be able to form T3s together. Therefore, the timing of the WCD and RD signals should be discussed. Radio waves travel through the atmosphere at a velocity that is influenced by the refractive index of the air. Muons produced by air showers have slower or faster velocities, depending on their energy. As a result, the time difference between RD and WCD can be both positive and negative. A conservative estimation of the time difference can be conducted to demonstrate the magnitude of the differences. An inclined air shower with a zenith angle of 75° has a typical geometrical distance between the shower maximum and the

Table 5.1: Arrival times of radio and particle signals for a shower of 75° zenith angle, assuming a shower maximum at 50 km to the ground.

	Energy [GeV]	Time for 50 km [µs]	Time difference to radio emission [µs]
Radio emission		166.83	
Muon	1	167.54	0.71
Muon	4.21	166.83	0
Muon	50	166.78	-0.05
Muon	500	166.78	-0.05

detector of 50 km. A constant refractive index of 1.0003 [120] is assumed, irrespective of the height, resulting in a propagation of the radio signal of 166.83 µs. It is assumed that all muons and emissions are produced at shower maximum and scattering processes are neglected. The muon energy of an inclined air shower is typically in the GeV-region [42]. The relativistic velocity is calculated via:

$$v = c \cdot \sqrt{1 - \left(\frac{E_0}{E}\right)^2}. \tag{5.1}$$

Repeating this exercise for varying muon energies yields Tab. 5.1. It can be seen that for muon energies of a few GeV, the radio emission reaches the detector less than 1 µs earlier. An energy of 4.21 GeV leads to a simultaneous arrival time, higher energies result in muons reaching the detector 0.05 µs earlier. All time differences for muons $\geq$ 1 GeV are significant less than 3 µs, which serves as a buffer in the T3 building. Considering the lower refractive indices at higher altitudes, the time difference becomes even more modest. Hence, particle and radio triggers are consistent in time and require no further shifting.

5.1.2 Noise filter to reduce RFI noise

The morphology of noise and its characteristic occurrences were presented in Chapter 4. With this knowledge, a veto mechanism is introduced to avoid triggering on mono-frequent noise, which have no similarity to air shower signals. Air shower signals possess a clearly defined pulse. Shortly after the maximum of the signal, no further signal contribution should be observed. In contrast, mono-frequent noise is ubiquitous over the whole trace. Therefore, it is probable that a significant signal will also be detected in the time after the observation of a first signal. This feature can be used to veto mono-frequent noise. Applied to the trigger mechanism, a second low threshold, T_L (baseline corrected), is introduced. This threshold was also depicted in Fig. 5.1. It is searched for peaks above T_L in a time window $[\mathcal{O}(500\,\mathrm{ns})]$, shifted by a delay $[\mathcal{O}(100\,\mathrm{ns})]$ behind the sample exceeding T_H. This shift moves the search window behind the main contribution of the air shower signal. If there are more than N_bin occurrences of samples exceeding the threshold, the trigger will be vetoed and not sent by the station. The algorithm is applied to each potential trigger, which means that for one signal, it is applied to every bin exceeding T_H. Since air shower signals have a decreasing peak amplitude after the maximum, no air shower signal will be vetoed, as at least one of the later bins will not be vetoed.

In the ideal case, mono-frequent noise is vetoed, which is tested using the periodically triggered noise data sets. The ratio of vetoed traces for different configurations of the vetoing is shown in Fig. 5.2. Four data periods of four stations with distinct characteristics were used, which were described in Sec. 4.1. The parameters of the veto mechanism have a different impact. Shifts of the noise window by delays of 100 ns and 400 ns were tested, as well as window lengths of 400 ns and 600 ns. These parameters appear to have minimal impact, as they yield similar rejection rates. The difference is minimal and could be explained by the typical frequencies of noise. The shifts and window lengths could be related to the periodicities of the noise. T_L and N_bin have a larger impact. The most loose combination of $T_\mathrm{L} = 15$ ADC counts and $N_\mathrm{bin} = 20$ results in a rejection ratio of $\approx 93.5\,\%$ for `Station 1732` and below 99 % for `Station 1742`. Decreasing N_bin to 10 but increasing T_L to 17 ADC counts yields an overall improved rejection rate, with almost 95 % for `Station 1732` and almost 100 % for `Station 1742`. The strictest configuration (T_L =13 ADC counts, $N_\mathrm{bin} = 10$) yields the largest rejection ratio, with almost 98 % for `Station 1732` and full rejection for `Station 1742`. All other combinations are found between the most strict and loose configurations. The lowest rejection ratio is generally found for `Station 1732` and the highest one for `Station 1742`. `Station 1732` possesses numerous traces associated with lightning events. Here, the vetoing quota is lower compared to the other stations, as pulses instead of mono-frequent noise are dominant. The vetoing mechanism is deliberately not rejecting, as many traces are air shower signal-like. The data from `Station 972` from November 2022 and `Station 1737` from March 2023 are driven by mono-frequent noise with only short periods with pulses occurring. The data for `Station 1742` from March 2022 is quiet, with mostly mono-frequent noise. Therefore, the results meet the expectations.

Overall, all settings improve the rejection of noise traces and would help to decrease the trigger rate caused by noise. However, the most stringent setting may pose challenges if an overall increase in noise level is observed for certain stations, with fluctuations close to T_L. If that was the case, air shower signals would be rejected. The final and best

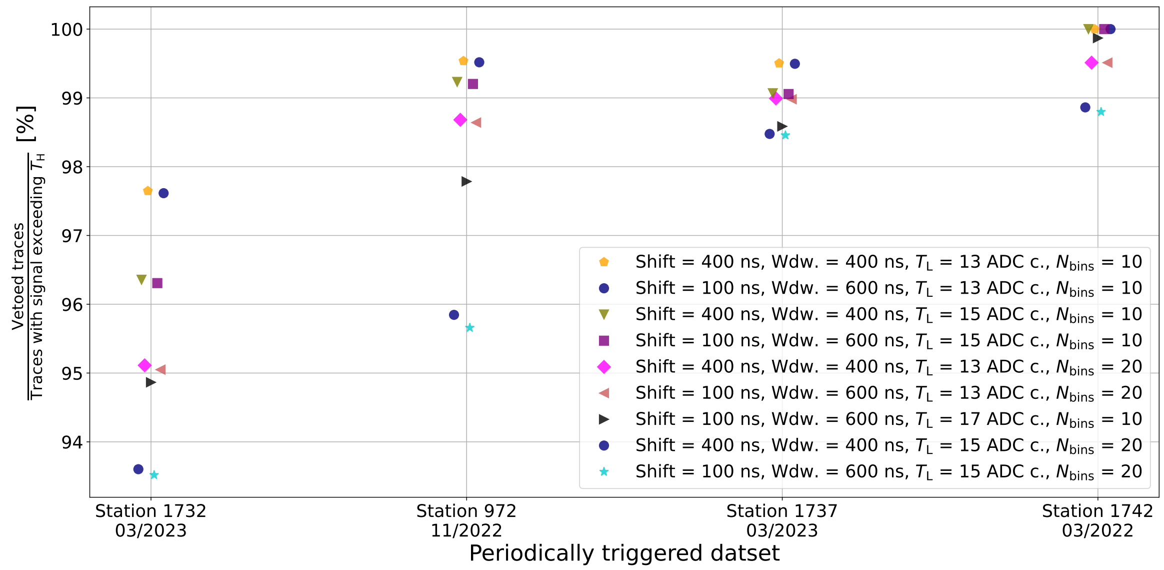

Figure 5.2: The rate of vetoed traces to all triggered traces is shown for different data sets of periodically triggered traces. The different colours and markers indicate different settings of the vetoing mechanism.

values for the setting have to be further investigated with RD triggered data. To be most sensitive to air showers, the next analyses and tests use a loose setting of $T_L = 15$ ADC counts and $N_{\text{bin}} = 20$. Even with more stringent settings, the acceptance of triggers, such as only 1 %, can result in excessively high trigger rates if the noise occurs in a sudden burst. In order to enhance noise reduction, a mechanism is required to prevent the constant triggering during noise bursts, as outlined in the subsequent section.

5.1.3 Inhibit of triggers during noise bursts

The vetoing mechanism of triggers is suitable for rejecting short mono-frequent noise. However, it fails to reject pulse-shaped noise signals. As air shower events also exhibit pulse-shaped signals, it is a desired feature. However, it is important to reject pulse-shaped noise, as they occur far too frequently. This accumulation of events is simultaneously the most significant distinction between pulse-shaped noise and air shower signals. Air showers are rarely occurring and are not correlated to the previous one. Noise signals come in bursts and hence, if one observes a noise signal, there is a high probability that another noise signal will be observed within a short period.

In the context of the triggering scheme, this characteristic helps to reject noise traces. If one observes within a second more than a certain number,$N_{\text{inh}} = 2$, of RD T2s at a single station, it is probable that additional triggers of noise origin will occur, and it is not advisable to transmit these T2 triggers to CDAS due to the small probability of air shower origin and bandwidth limitations. The triggers would all probably lead to read-outs of stations, as these noise triggers are highly correlated, as it will be shown in Sec. 5.3. Instead, the sending of RD T2s is inhibited for the time T_{inh}, but triggers are still counted. Only if within the period T_{inh}, the number N_{inh} in one second is not observed again, the inhibit stops after T_{inh}. Otherwise, the inhibit continues for another T_{inh} while counting triggers. This will reduce the up-time of the RD trigger and also decreases the trigger efficiency for air showers. But it is expected that many more noise signals will be rejected. Hence, the ratio of triggered air shower signals to triggered noise signals will significantly increase.

For a coherent noise burst, such as during lightning, only the first two RD T2s are sent, and triggers are inhibited until the noise burst is over. As a first estimate, the behaviour of the inhibit can be simulated for the recorded periodically triggered traces (*c.f.* Sec. 4.1). Since the periodic data sets represent only a small fraction of the recording period, one must account for the time between traces that is not recorded. Hence, the subsequent approach is used: the data is divided into periods of each one second and the number of pseudo-triggers (traces with amplitudes exceeding the threshold of 25 ADC counts) is counted. $N_{\mathrm{inh}} = 2$ is tested, hence, if multiple triggers are within one second, the algorithm would initiate an inhibit with $T_{\mathrm{inh}} = 10\,\mathrm{s}$. If a single trigger is observed in one second, a window of $\pm\frac{10{,}000}{2\cdot f_{\mathrm{samp}}}$ [s] is applied for a coincidence search to another trigger. The coincidence search window length is determined by the expected number of triggers per second during a noise burst ($\mathcal{O}(10)$) and the fraction of recorded time in a second. If no other trigger is observed in this window, the trigger is assumed to be a singular event (air shower event). It is assumed that if other triggers are observed, they originate from the same noise burst. All triggers that were not recorded in the periodic data are represented by them now. With the recorded triggers, a kernel density estimation with a kernel width of 60 s is performed to get the PDF of the triggers. The expected number of triggers (determined by the weighting factor due to f_{samp}) is distributed in time via the PDF. The inhibit can be replicated using the generated points. Since the periodic data is not ideal for this simulation, large uncertainties remain. Regardless, this exercise should be a proof of concept to reduce the number of noise triggers.

Figure 5.3 depicts the result of the simulated inhibit. For `Station 972` and a read-out rate of $f_{\mathrm{samp}} = 10\,\mathrm{Hz}$, it was demonstrated that primarily a daily pattern of mono-frequent noise is observed. Furthermore, `Station 1732` is depicted, for which lightning events with spiky traces were observed. `Station 972` has an inhibited time

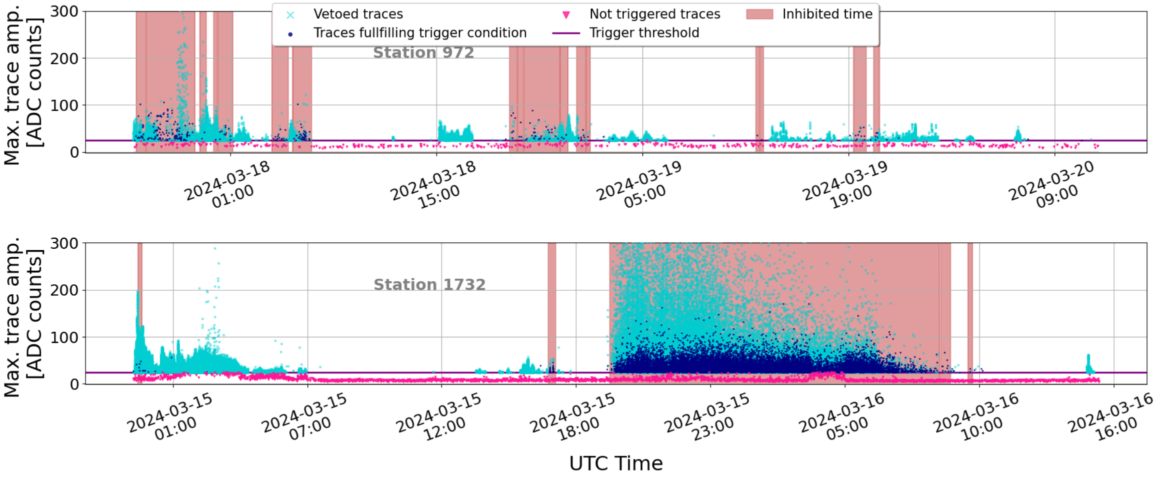

Figure 5.3: For `Station 972` (top) and `Station 1732` (bottom), the inhibit is simulated for the time of the respective data set. The dark blue points show the trace amplitude of pseudo-T2s, bright blue colour indicates a rejection of the vetoing mechanism. Magenta points show 0.1 % randomly picked traces where the maximum amplitudes are below the anticipated trigger threshold of 25 ADC counts. The red areas show where the inhibit is active in the simulation.

fraction of 22.2 %. For the measurement time, each day around 19:00 UTC an inhibit begins. The inhibit is almost entirely coherent and lasts for a couple of hours. Between the daily inhibits at 19:00 UTC, one observes almost no inhibits and there is 100 % uptime for tens of hours. It should be noted that `Station 972` is in proximity to a street, houses, and transformation station. Therefore, the daily inhibit time is expected. `Station 1732` exhibits a distinct behaviour as it is situated at a greater distance from potential anthropogenic noise sources. There is one long inhibit due to the lightning events, but there is almost no inhibit observed outside these events. The measured period has an inhibited time fraction of 36.5 %. It is anticipated that the fraction of inhibited time will be lower on days when no lightning is observed. The station behaviour should also be more representative for the majority of the array, as most stations are more distant to anthropogenic noise sources. The order of the simulated inhibited time fraction will be shown to be in agreement with the observed fraction from tests in Sec. 5.3.

5.2 Trigger simulations in Offline

With a trigger design as developed in Sec. 5.1, an implementation in Offline was done to study the effect on fully simulated cosmic ray events in dependence of the shower parameters (*c.f.* Chapter 6). The challenge comes as the implementation should be minimal invasive to the other parts of the simulation framework. This is difficult, as the framework was developed without the possibility foreseen of having triggers apart from particle triggers. Hence, the applications strongly depend on having particle information. For instance, if there are no particles simulated in the WCD included in the simulation, the station will be rejected automatically as no trigger is anticipated. Subsequently, the whole simulation procedure is not performed for this station. Following, PMT traces of stations lacking particle information are not generated and replicated. If the station remains in the simulation due to an RD trigger, it will run into errors when the not created objects are accessed in the reconstruction. Therefore, it is not sufficient to just implement the RD trigger alone, but one must also care for the creation and simulation of WCD objects at the same time. This requires a major change in the existing modules and the module-sequence itself. The following are the most important steps of the implementation. Parts of the code can be found in Appendix A, all changes can be found in the merge requests 297 and 524 in the internal Auger GitLab repository. In total, the merges include modifications to 21 files and the creation of 14 files.

The created module `RdSimulationRadioTrigger` is the core of the implementation. The module consists mainly of a loop over all stations and over both raw ADC traces for each station. For each trace, the trigger is simulated, including setting T_H to the baseline corrected value, checking for bins exceeding the threshold, and vetoing in case of an RFI-like trace. The settings for the module can be changed in the configurable `xml`-file. This includes settings for the noise rejection, the trigger threshold but also the trigger method. For testing purposes, one can choose the actual implementation of a channel-wise constant trigger threshold in ADC counts, or the geometrical sum of both channels, or a threshold based on the SNR. If a trigger is observed for one station, the station object will receive a newly created RD trigger and its associated properties, such as the trigger time. It is important at this point to simulate the WCD traces depending on the trigger time. Otherwise, the application will experience errors when trying to reconstruct the traces at a later point. Therefore, the simulation of traces was transferred from a WCD module to a general detector file.

In order to generate the traces, one must ensure the existence of the connected objects, such as simulated PMTs and stations. The creation of WCD stations is done by modifying the module `RdStationAssociator`, whereby the creation of all simulated radio stations can be activated now via a flag. Hence, it cannot happen that stations and WCD traces are requested in the reconstruction, which are not existent objects. The last significant modification is the reordering of the module sequence. It is not sufficient that the WCD stations are created, but also the belonging PMTs and traces must exist. Hence, the complete simulation of the radio detector response is positioned prior to the WCD detector response. All WCD stations with simulated RD trace are created, before the WCD trace simulation, which would normally only occur in the case of existent particles in the tanks.

5.3 Testing of the trigger in field conditions

Parts of this section have already been published in:

J.Pawlowsky, J. Rautenberg
"Outline and results of the second RD trigger field test", Internal note of the Pierre Auger Collaboration (2024), GAP 2024-015

The trigger test began on the 26^{th} of December 2023. The aspects and objectives of the test are discussed in the following. The results are shown until the 15^{th} of March when the internal note was completed. Cross-checks for the time after did not show any significant differences.

5.3.1 Test outline

The RD trigger test is composed of two stations, `Station 635` and `Station 663`. They are located at the south-eastern edge of the infill, but they have a spacing of 1,500 m. They are shown in Fig. 5.4. There were mainly two arguments for selecting these two stations:

> **Accessibility:** The infill stations possess enhanced communications hardware in comparison to the rest of the array. Thus, the implementation of software and changing of settings is less complicated and can be adapted on short notice.
>
> **Noise situation:** The noise situation in the vicinity of the infill and AERA is known to be a noisy area. Hence, it could potentially represent an extreme (worst-case) background situation when extending the RD trigger to the entire array. First, it is possible to have self-induced noise due to the increased density of stations and due to the UMD locations. Both stations have UMD communication systems, but have no UMD hardware installed, yet. Secondly, one has already

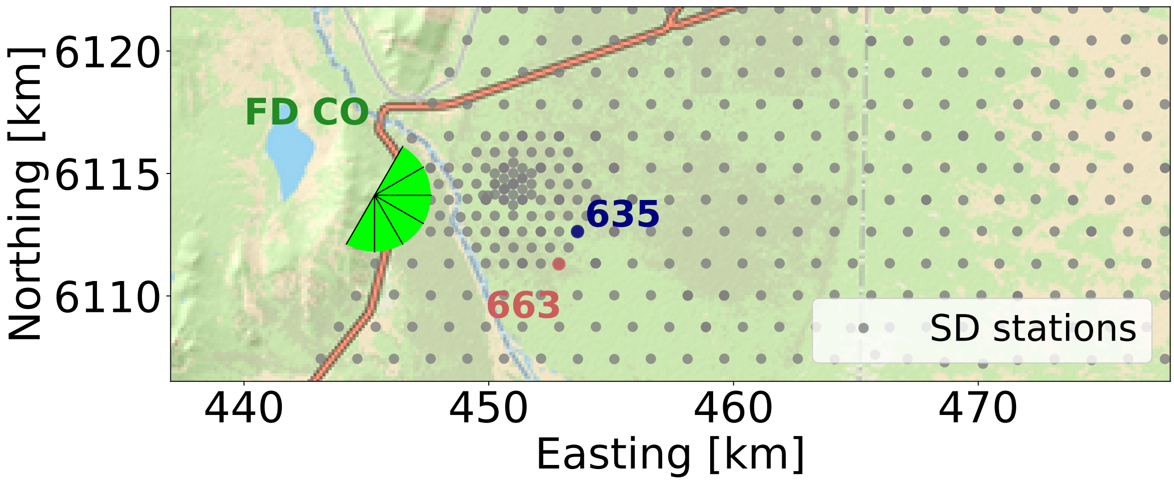

Figure 5.4: Locations of the two stations used. They mark the South-Eastern border of the infill.

seen in the past that there are not-Auger related noise sources in this area [117]. It would be a good sign to have an acceptable trigger rate in this area for the implementation on a larger scale.

Another aspect to be considered is the quantity of stations involved in the field test. The primary objective is to prevent any potential stress or danger for CDAS. Especially, the T3 rate (the event read-out rate) has to be restricted to comply with the limited communication bandwidth. As a benchmark, one typically experiences a T3 rate of less than 10 per station and day (10^{-5} Hz). A straightforward way to limit the T3 rate is to implement the RD trigger in only two stations. The minimum requirement for having a T3 is a correlation between at least three stations. Even in the event that the RD constantly sends triggers, they only produce T3s in the event of a random coincidence with a particle trigger from a third nearby station.

With this test outline, the following questions a priori defined will be answered:

1. Do all implemented trigger features (triggering, vetoing, inhibit) work as intended?
2. With a working inhibit, does one have an acceptable RD T2 rate?
3. What are the best values for N_{inh} and T_{inh} and what is the resulting dead-time of the stations?
4. Are the sent RD T2s correlated between the stations, and what rate of T3s is expected by adding more stations?

The test was conducted with different values for the trigger threshold and inhibit. An overview can be found in Tab. 5.2. The test was started on 26th of December 2023. The time period until the 19th of January 2024 was used to debug unwanted features that were found to be connected to the inhibit. This will be discussed in Sec. 5.3.2. On 19th of January, the irregularities were resolved and a new version with new inhibit settings was implemented. During the next five days, no triggers were observed for `Station 635`, as it was constantly inhibiting. Therefore, the trigger threshold was increased to 30 ADC counts, thereby resolving the matter. The trigger rates analyses will focus on the time after the 24th of January. Moreover, the rate of just one station is discussed. The other station did not show any significant different behaviour at that time.

Table 5.2: Overview of the tested values for the trigger settings

Period	UTC Time (mail timestamp)	Action	T_H [ADC] `635 (663)`	T_inh [s]	N_max
A	2023-12-26	Start	25 (25)	2	12
B	until 2024-01-19	Debugging	25 (25)	2	12
C	2024-01-19 14:41	Reasonable setting	25 (25)	10	2
I	2024-01-24 19:50	Threshold for `635`	30 (25)	10	2
II	2024-01-30 22:20	inhibit time	30 (25)	60	2
III	2024-02-05 20:43	Trigger threshold	75 (75)	10	2
IV	2024-02-13 00:24	Renewed settings	50 (50)	10	1
V	2024-02-28 19:13	Renewed settings	30 (20)	10	1
VI	2024-03-04 20:19	Renewed settings	30 (30)	10	1

5.3.2 Inhibit of RD T2 triggers

The RD T2 inhibit is a key component of the test. When it was first implemented, unexpected features were observed. This is illustrated by the measured distributions of trigger rates for two periods, shown in Fig. 5.5. For period **A**, one observes first a decline of the trigger rate. At 9 triggers per second it increases again with a peak at 12 triggers per second. Furthermore, one observes triggers rates that exceed 12 RD T2s per second. The distribution arises from two factors. First, N_max was set to 12, which explains the peak at 12 triggers per second. Entries that would have had a greater number of triggers per second are frequently capped in this bin. The second effect, however, results in seconds with more than 12 triggers. During this period, not all RD triggers were

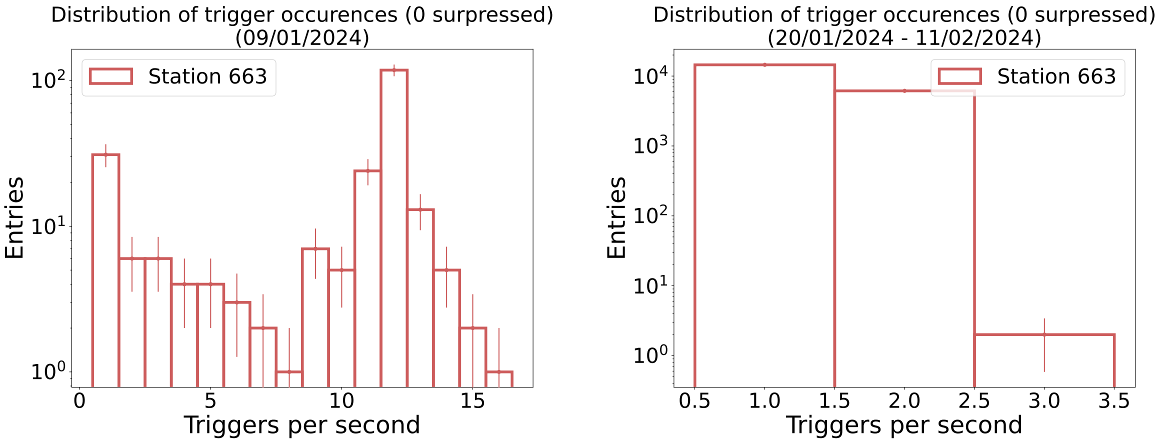

Figure 5.5: Distribution of triggers per second with unexpected high trigger rates above the inhibit threshold of 12/s (left) and the expected rates for the period with the improved implementation of the inhibit and a threshold of 2/s (right).

inhibited, but only the so-called primary triggers were inhibited. A primary trigger is the first T2 trigger of a station within a T3 building window. Subsequently, if there is another trigger from the same station within the T3 building window, it is called a delayed trigger. This creates an artifact in the distribution that could potentially be dangerous, as it could upgrade a particle T1-threshold trigger to a T2. Furthermore, it could affect the correct counting of triggers per second. After discovering this issue, these delayed triggers were also inhibited. This results in the right plot, where N_{max} was set to 2. A nearly perfect inhibit can be observed. The frequency of one trigger per second and more than one trigger per second is almost equal. This indicates the bursting of noise. If an RD trigger is observed, there is a nearly 50 % likelihood that additional RD triggers will occur. In $\approx 0.3\,\%$ of the cases, one observes a feature in the inhibit, namely that a third trigger per second is sent. This happens if the trigger is too close to the other two. The inhibit begins only in the clock cycle subsequent to the second trigger. Therefore, a third trigger is sent if it was initiated in the same clock cycle. Since this is only an edge case and should not endanger CDAS or the method in general, it will not be further investigated. It is important that one inhibits the RD T2 rate effectively, which reduces the RD T2 rate to a desired value. For example, the required value of the RD T2 rate is 1 % of the threshold trigger T2 rate, which results in a rate of 0.2 Hz. Therefore, setting the inhibit to $N_{\mathrm{max}} = 2$ and $T_{\mathrm{inh}} = 10\,\mathrm{s}$ would result in a compatible maximal rate of 0.2 Hz.

5.3.3 RD T2 rate

It is essential to know how often RD T2s occur, even though the inhibit is working and reduces the RD T2 rate to an acceptable level. The number of RD T2s per hour is shown in Fig. 5.6. Starting with period **I** and $T_{\mathrm{inh}} = 10\,\mathrm{s}$, $N_{\mathrm{max}} = 2$ and $T_{\mathrm{H}} = 25\,\mathrm{ADC\,counts}$ one observes that the rate of RD T2s is bursting. There are hours with no triggers at all, and other times there are hours with up to 200 triggers. This expected bursting behaviour is precisely the reason for implementing the inhibit. In period **II**, the inhibit time was increased to 60 s, resulting in a significant decrease of the RD T2 rate to a maxima well below 100 / hour. It most likely reduced the up-time of the trigger, but to quantify the effect, the dead times would need to be recorded, which was only done at a later point (*c.f.* Sec. 5.3.6). In period **III**, the inhibit time was set back to 10 s, but the trigger threshold was raised to 75 ADC counts. This resulted in an enhancement of the trigger rate. It is notable that the rate has now higher peaks during bursts with rates of $\approx$ 300 / hour compared to period I with a lower trigger threshold. There are two interpretations: the period could be significantly noisier, leading to more triggers. There is no evidence or indication that this is the situation. It is more probable that the inhibition could become less effective as not enough signals are above 75 ADC counts during a burst. Thus, the up-time is higher; however, triggers are sent, which would have been inhibited with a threshold of 25 ADC counts. There is no definitive conclusion that can be drawn from the recorded data, however, the second option appears to be more probable. Furthermore, it appears that extending the inhibit time exerts a greater impact on the trigger rate than increasing the trigger threshold. Towards the end of period **III** (in the night from the 11th to 12th February), there were massive power cuts in Malargüe. During the power outages, 12 hours of T2 data is missing. After the power cuts, it appears that the noise situation is significantly more noise quiet, as indicated by the low trigger rate. A few hours after the power cuts (and without knowledge of the power cuts) T_{H} was decreased to 50 ADC counts, and more importantly, N_{max} was set to 1 (period **IV**). This setting is extremely strict, as an inhibit is initiated after each trigger. Although it is not a desired setting for a field implementation, it is intriguing to observe how it affects the different rates and the dead-time. One observes a continuation of the downward trend towards low trigger rates, as only single triggers are observed over the course of days. A script reading periodically the registers of the RD FPGA excluded a constant inhibit, hence, it appears that the noise situation indeed changed due to the power cuts. Another sign that the low trigger rate is not an artifact of the inhibit, is the peak on the 18th of February. This peak is caused by lightning events [121], which shows that one still receives triggers. One plausible explanation for the noise silence is

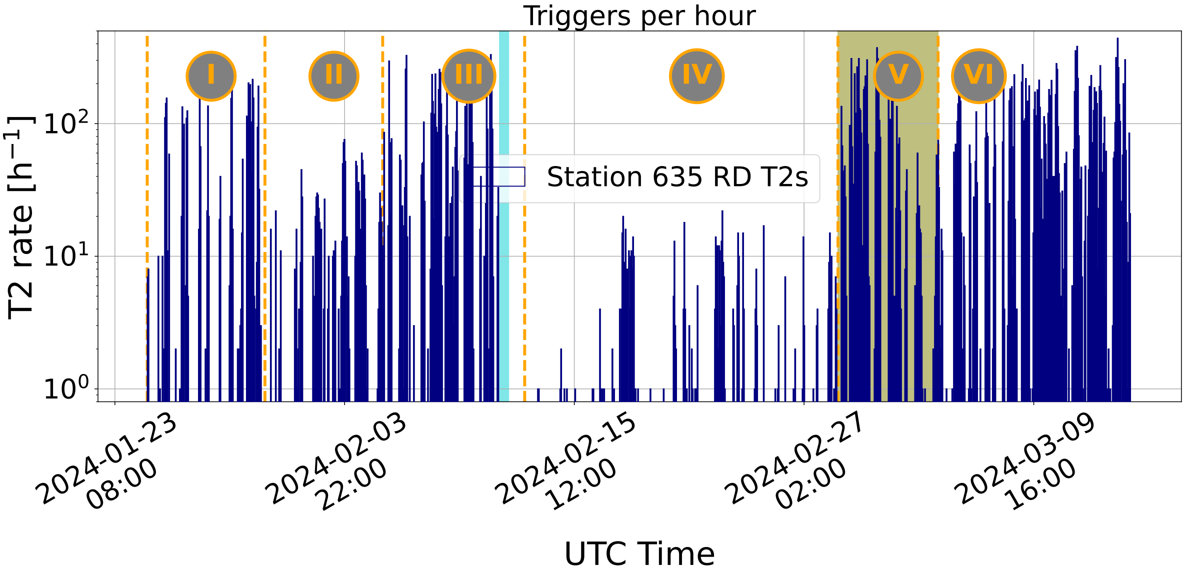

Figure 5.6: RD T2 rate per hour for `Station 635` over the test time. It is separated into different periods, marked by the orange lines. The light blue area points to the massive power cuts in Malargüe. The green area marks period V with constant inhibit for `Station 663`.

that the source may have been deactivated due to the power outage and has not been restarted. This also implies that the noise quiet period might be more representative of the entire array, as the number of noise sources in the infill region is higher than at other locations. The source appears to be active again from the 21st of February on, where daily bursts are seen but are limited by the strict inhibit values (this will be better seen in Sec. 5.3.6 when looking at the up-time).

Even though the noise situation is much better at that time than before the extensive power cut or after the presumed restart of the source, one cannot expect that it stays like that. If the implementation of the full array is discussed, one should take the period before the power cuts into consideration. Only if the RD trigger is compatible in these conditions, one can implement the trigger for the whole array without endangering CDAS.

In period **V** and **VI**, the rates look again similar to periods **I** to **III**. Only for period **V** a trigger threshold of 20 ADC counts was tested for `Station 663`, which led to a constant inhibit. Changing the setting in period **VI** resolved this issue.

5.3.4 Expected T3 rate

To ensure that no T3s are formed by only RD triggers, only two stations were used in the test. Nonetheless, a precise estimation of the T3 rate in the presence of additional

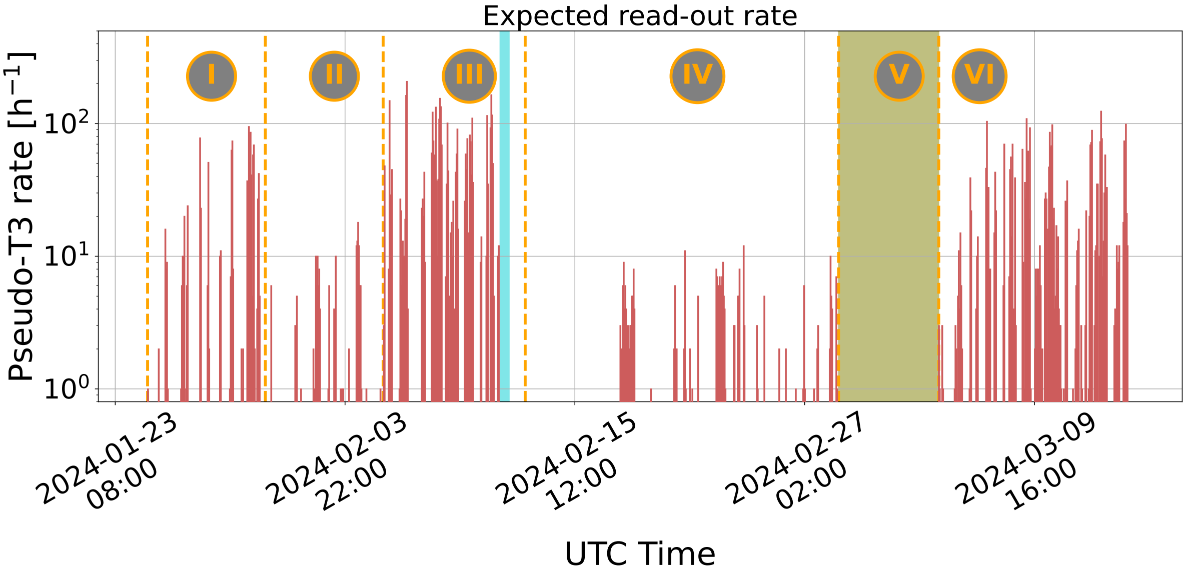

Figure 5.7: Pseudo-T3 rate per hour for the time period of the test. Different periods are marked by the orange lines. The light blue area points to the massive power cuts in Malargüe. The green area marks period **V** with constant inhibit for `Station 663`.

RD trigger stations is feasible utilising simple assumptions. One can compare the RD T2 times of the two stations. The T3 making criteria of trigger coincidences is applied with a time difference Δt between triggers of $(3{+}5C_n)$ µs. Since the stations have a spacing of 1.5 km, the triggers of the two stations can be part of one T3 if they have a $\Delta t \leq 8$ µs. The resulting events are called here pseudo-T3s, and they are created by using the conservative assumption that a signal causing triggers in both stations coincidentally would have also triggered a nearby station. This assumption may not hold true for all signals, but it is reasonable to assume that a majority of signals would reach a third station. In any case, this provides an upper limit for the T3 rate for pure RD-T3s, which can be used for an evaluation. The number of pseudo-T3s per hour is depicted in Fig. 5.7.

The plot indicates that the pseudo-T3 rate behaves similarly to the RD T2 rate. All the features previously mentioned can be found here as well. The noise bursts with peaks of almost 100 pseudo-T3s / hour in period **I**. In period **II**, it is reduced by the increment of T_{inh} to a maximum rate of approximately 20 pseudo-T3s / hour. The overall maximum in the rate is seen in period **III**, with hundreds pseudo-T3s / hour. After the power cut, and with the new settings, the number of pseudo-T3s is reduced. Only for the lightning event on the 18th of February, a distinct burst is observed, where multiple pseudo-T3s can be observed over a period of hours. Even though it is relatively quiet during this time, the pseudo-T3 rate is well above the normal T3 rate. One could argue that the particle triggers also produce significantly more T2s and T3s during the lightning event, but nevertheless it should be focused on making the RD trigger compatible with the CDAS requirement. The possibility that the particle triggers may pose danger to CDAS during these events is not a sufficient justification for the RD trigger to endanger CDAS.

Period **V** does not show any pseudo-T3s, as `Station 663` was in the state of constant inhibit. Period **VI** then again looks similar to the first three periods, with up to 100 pseudo-T3s per hour.

The reason for the substantial rate of pseudo-T3s, even when few RD T2s are observed, is due to the high proportion of RD T2s that would also produce a T3. This is referred to as the conversion rate, shown in Fig. 5.8. One must once again distinguish between the various periods. Period **I** shows a conversion rate at the beginning of 10 %, being enhanced later to 35 %. In period **II**, the daily conversion rate fluctuates between 10 % and 30 %. Period **III** shows a rather stable rate of 50 %. Period **IV** shows the largest fluctuations. As there are less RD T2s and the lightning event is also included, the conversion rate can be observed at 0 % and 100 %, but seems to be more stable at 50 %. During all periods, the conversion rate is extremely high compared to the conversion rate of particle triggers. A particle trigger conversion rate of 10^{-6} is obtained if one assumes a stable particle T2 rate of 22 Hz and a particle T3 rate of less than 10 per day. Therefore, the RD conversion rate is four orders of magnitude higher. This disparity is easily understandable, as particle noise exhibits a Poissonian distribution and lacks correlation between stations. Thus, a random but high energetic background muon hits only one station, which is not enough for the creation of a T3. Instead, a random but strong background radio signal will reach multiple stations, thus resulting in a T3.

It is evident in Fig. 5.9 that a single radio signal reaches multiple stations. It shows the absolute time difference between the triggers in case of a pseudo-T3. First, the distribution is not uniform. A significant decrease is seen for time differences $\geq$ 6 µs. Due to the station spacing of 1.5 km, triggers can only be generated from the same signal if there exists a time difference of approximately 5 µs or less (without accounting for station time uncertainties). Any time differences greater than the horizontal signal case are indicative of random trigger coincidences. It demonstrates that this group constitutes a minority, and nearly all factors point to a common signal. Moreover, one observes a peak at around 5 µs. Therefore, it indicates that the most prevalent noise emanates from a source (or sources) located in the North.

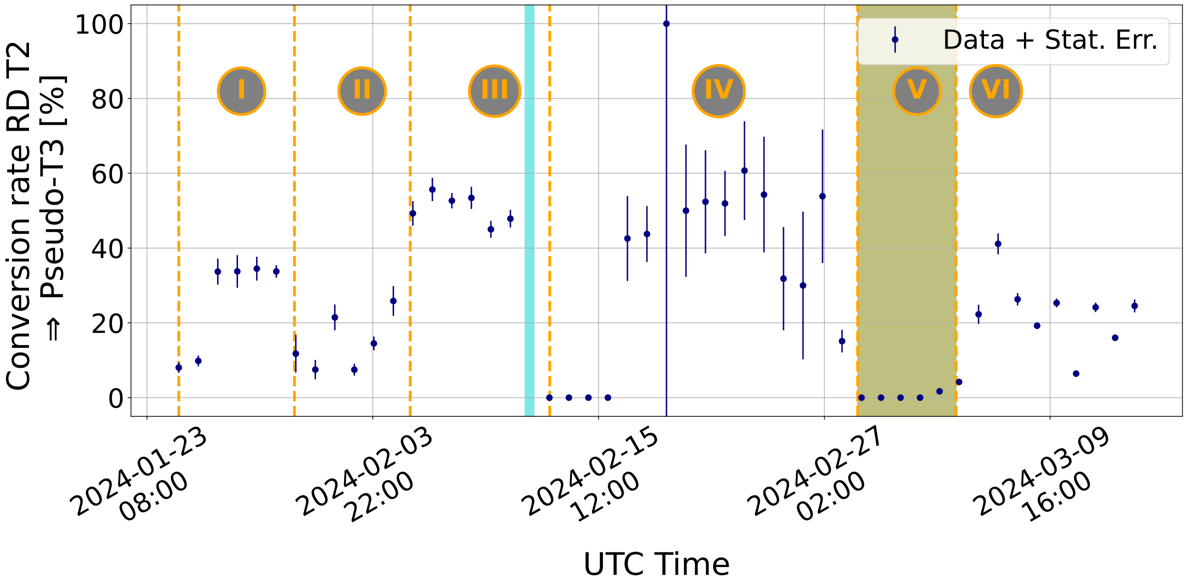

Figure 5.8: Conversion rate of RD T2s to pseudo-T3s per day for `Station 635` over the test time. The orange lines mark different periods. The light blue area points to the massive power cuts in Malargüe. The green area marks period V with constant inhibit for `Station 663`.

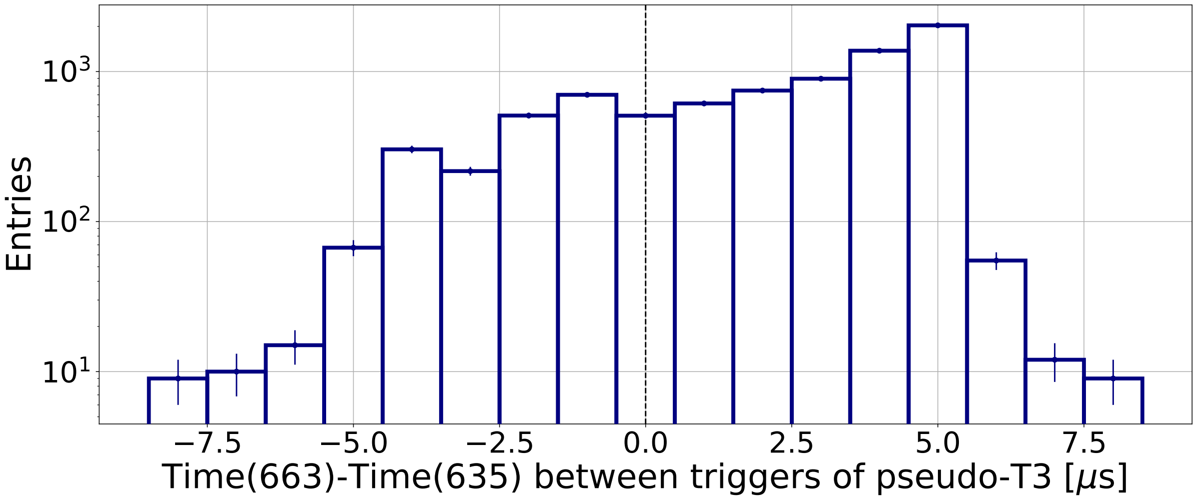

Figure 5.9: Time between RD T2s if a pseudo-T3 is observed. The peak at 5 µs corresponds to a horizontal signal from a source on the line of the two stations.

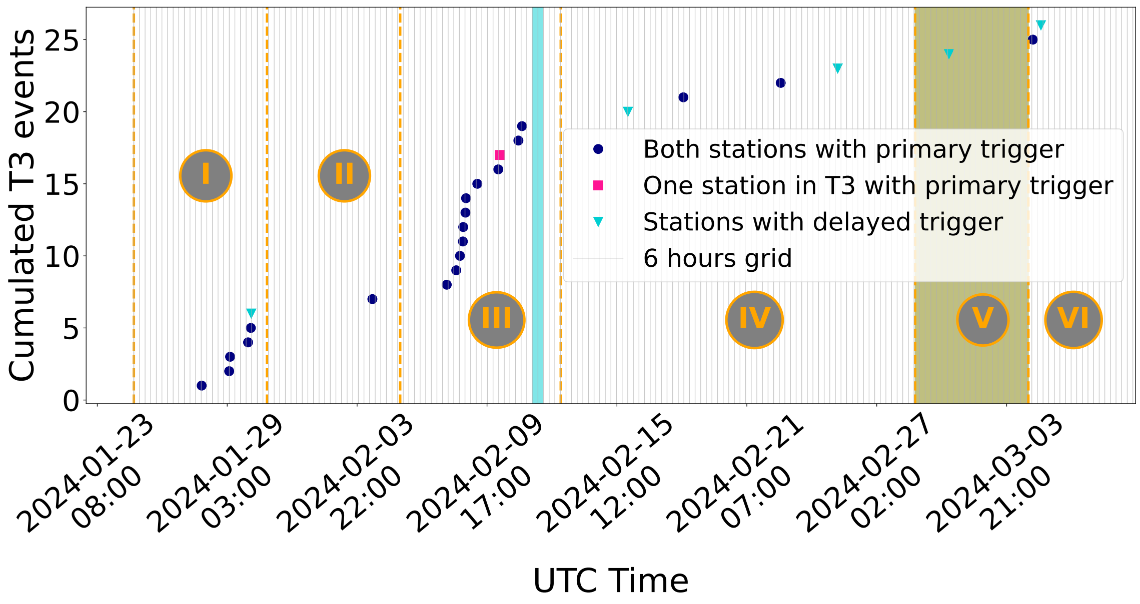

Figure 5.10: Cumulative number of T3s for the time period of the test. The black lines mark different periods. The gray grid shows a spacing of 5 hours. The different markers stand for two primary RD triggers in a T3 (dark blue circles), one primary RD trigger in a T3 (magenta squares) and the RD as delayed triggers in a T3 (light blue triangle).

5.3.5 Observed T3s

By chance, RD T2s can form a T3 with a random particle trigger in one of the nearby stations. Subsequently, the data of the stations is read-out. Figure 5.10 shows the cumulative number of T3s over time, which included at least one RD trigger. Most of the shown T3s include RD triggers of both test stations. One T3 comprises only one RD station, while two T3s possess delayed triggers. Therefore, the T3 would have also most likely happened without the RD trigger. One observes that the majority of T3s occur during period **III** within a short time interval. It is evident once again that the settings for inhibit are ineffective for this period. Excluding this period, one observes 7 T3s within ≈ 25 days which are caused because the RD trigger was activated. This is an acceptable number of events for this time frame, hence, one can be sure that this does not endanger CDAS. Moreover, the aforementioned lightning events occurred on the 18th of February are noteworthy, in which a single T3 was produced. This is important, since RD triggers could correlate with particle triggers caused by lightning.

It is important to take a closer look at the read-out data. The traces of one example T3 is shown in Fig. 5.11. For the two stations, one sees a clear and strong radio signal, which fulfils all criteria for correctly producing RD T2s. They are not distinguishable

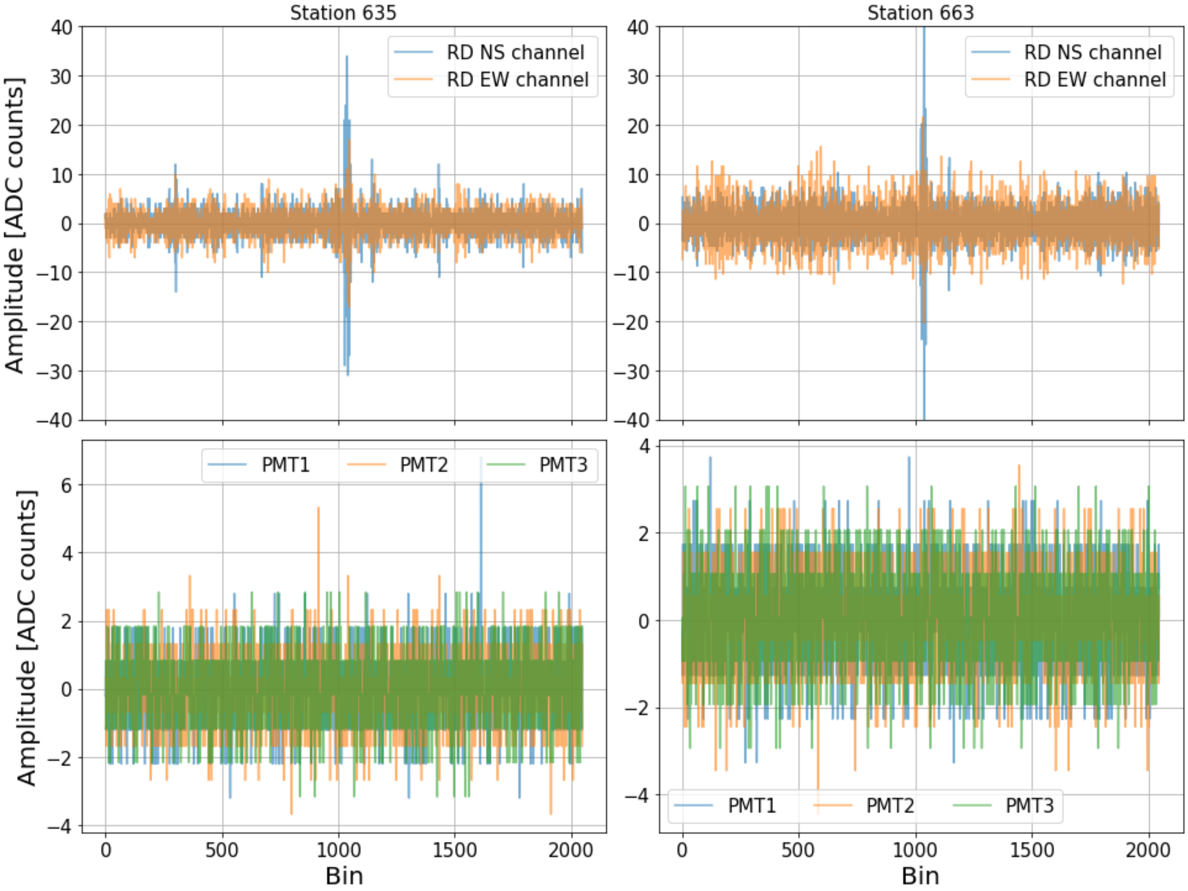

Figure 5.11: Example signals of a T3 with RD triggers involved. On the left, `Station 635` is shown, `Station 663` on the right. The top row shows the RD signals of the different channels, the bottom row shows the PMT signals of the WCD.

by eye from an air shower signal. Only the minor spikes in a consistent pattern for `Station 635` indicate an active noise source. The PMT traces do not show any significant particle signal, which also suggests that noise may be the origin of the triggers. The fact that the radio signals are not distinguishable from air shower signals suggests that it is difficult to further reduce the number of RD T2s with noise origin, without rejecting many air shower signals. It is more efficient to reject events on CDAS level.

5.3.6 Fraction of inhibited time

For the evaluation of the RD T2 inhibit, an important aspect is the self-induced artificial down-time and connected to this the up-time. The up-time is shown in Fig. 5.12. The up-time was only tracked from the 15th of February onward, and was only recorded with an external script running on the UUB and reading registers from the FPGA of the RD. The seconds are counted, which are marked as dead or alive. It is only a temporary solution and there are flaws with this method, which can immediately be seen. There are instances where the up-time exceeds 100 %. For example, on the 15th at 07:00 UTC, 5,000 seconds of up-time were counted within one hour. Additionally, other smaller spikes can be seen exceeding 100 % or simply deviating from the general plateau. It is likely that this is caused by the FPGA being read out from the script and from the general data stream simultaneously, which leads to the corruption of the data. Eventually, the information about the inhibit should be transmitted and registered via the monitoring data, which will then resolve the issue. The upper plateau of the up-time indicates another irregularity. It fluctuates around 90 %, but the missing 10 % cannot be explained by inhibited time. When the up-time values fluctuate around 90 %, the down-time typically falls to 0 %. Hence, there are seconds which are not counted for any of those two. The reason is currently unknown. Since the plateaus are quite sharp at 90 % and no triggers are usually seen at this time, one can assume that the corrected up-time should be around 100 %. Next, it is observed that both stations exhibit similar up-time behaviour, and the lines are nearly identical. This indicates that there is a high correlation between triggers of stations. This is crucial later to have a high number of active hexagons in the array.

In general, the up-times in close proximity to the power outages on the 11th of February tend to be higher. Besides the dips on the 17th of February (probably caused by lightning), the plateau is stable until the 21st. A prolonged drop in the up-time is followed by an oscillating pattern. This is expected, since one has a daily reoccurring pattern of noise bursts. Hence, one has an overall up-time of $\approx 60\,\%$ for both stations and an up-time of $\approx 55\,\%$ for periods after the 22nd of February in period **IV** when the pattern appears stable. Period **VI** subsequently shows a slightly increased up-time of around 61 %.

All numbers are likely $\approx 5\,\%$ below the actual up-time due to the missing seconds issue. It is important to note that this is only a first implementation and can be improved later. Moreover, the test is at a rather noisy location, possibly the noisiest location in the array. It is anticipated that stations located in quiet regions of the array will exhibit significantly higher up-times, which was already demonstrated in Sec. 5.1.3.

5.3.7 Proceeding of the RD test and development

Upon answering the a priori questions with the test, new discussion points arise. It is important to discuss how to proceed with the field test and which trigger version could be scaled to the entire array at the moment. It should be noted that at the time of writing, no test bench or comparable test setup for CDAS changes is available. Furthermore,

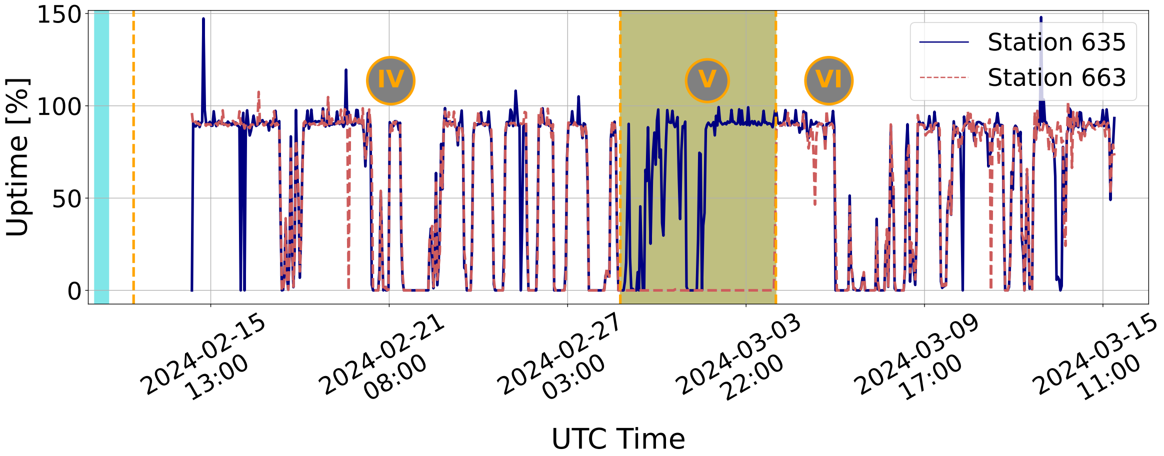

Figure 5.12: Up-time of the stations per hour for the time period of the test. `Station 635` is shown as solid blue line, `Station 663` as red dashed line.

no collection of stations for testing exists. Moreover, currently, the recording of a large amount of reliable data is crucial due to internal processes. Therefore, interventions should be minimal invasive.

An initial step would include the establishment of single RD trigger stations that are distributed throughout the array, with a minimum distance of 4 cones. One could send RD triggers from the stations without producing radio T3s and endangering CDAS. The firmware and trigger settings must be defined before copying them to the UUB and FPGA, as the regular array outside of the infill does not have a fast connection. Thus, quick changes or corrections are not possible. The drawback of this continuation is the lack of trace information (besides coincidental T3s), which would further aid in identifying triggers at various array locations.

Alternately, certain stations may be excluded from the regular data stream. All triggers and their respective traces can instead be written to a USB-stick. It is therefore possible to study the morphology of the traces. Nevertheless, this would necessitate significant person-power for a substantial number of locations and stations, as the data must be manually gathered. Furthermore, it is challenging to establish a strong correlation between stations then.

If the RD trigger functions for now only as a T1 trigger, trigger data could be recorded using the regular data stream. The trigger data would only be read out in the event that there is a particle trigger T3. This would obviously not help with the detection of air shower events, but it could help to understand the morphology of triggers better. However, this would yield a biased data set, as mainly air shower events are read-out then, but no noise events.

An idea, which is more advanced, includes the modification of one so-called Base Station Unit (BSU). The SD array is distributed on different BSUs. Each BSU is responsible for the communication and data stream of their SD stations. Moreover, every BSU runs its own CDAS instance. The BSUs have different sizes, but as benchmark, one can assume that one BSU typically controls 6 % of the array. One BSU would be designated for testing. Therefore, modifications to the CDAS instance or station firmware would be possible without endangering the complete data stream. Thereby, flawed and unreliable data could be filtered easily. For this test BSU, one must also define an intermediate or long-term solution to avoid having too many T3s. This solution ought to be robust even during periods of noise and for all locations. As discussed in Sec. 5.3.5, the conversion of RD T2s to T3s is significantly reduced, if particle triggers are required to contribute to a T3. In this particular instance, it was due to the limited number of stations that had the RD trigger activated. However, it is possible to implement this behaviour at the CDAS level: T3s can only be constructed if at least one particle trigger is involved, whereas pure RD T3s would not be allowed. The actual implementation is relatively simple at the CDAS level and can be reduced to just a few lines of code. This will be discussed in the following Sec. 5.4. However, the implementation will be on the cost of a CDAS convention of just discriminating threshold T2s and ToT-like triggers (ToT, MoPS and ToTd). It should be discussed which of the used conventions are outdated and should be discarded in order to achieve the best possible scientific result.

With the implementation of the proposed solution, one could step-by-step increase the number of test stations and see the effect on the T3 rate. Starting again with two stations, one can add a third test station close to the existing two, in order to prove that the CDAS implementation works and has no worrying edge cases. If the outcome is positive, one could further increase the number of stations. It is important to mention that the proposed solution reduces the photon trigger efficiency, in particular for inclined photon events. This will be discussed in Chapter 6. However, the solution would be an interim step towards an autonomous RD trigger. By implementing a significant number of stations, the learning from the test would be significantly enhanced, which helps to improve the trigger.

5.4 Proposed CDAS modifications

The read-out probability is significantly reduced by requiring particle triggers to participate in the T3 building (*c.f.* Sec. 3.4 for the concept of the T3s and cones, C_n). However, it is still possible for RD triggers to coincide with particle triggers, resulting

Table 5.3: Probabilities for coincident T3s

Requirement	Assumed particle T2 rate [Hz]	Coincident T3 probability
1 ToT-like T2	2	0.0063
1 ToT-like T2 & only ToT2C_1&3C_2	2	0.0008
1 particle T2	24	0.076
2 particle T2s	24	0.0002

in T3s. The probability can be calculated as follows: a station is chosen to have an RD trigger and, for having a conservative estimation, stations within the surrounding cones also have a correlated RD trigger. The probability that a surrounding station i has a random particle trigger, which is time-wise within the T3 building time window, can be calculated via

$$p_i(r_{\mathrm{T2}}, C_n) = (2 \cdot (3 + 5 \cdot C_n)\,\mu\mathrm{s}) \cdot r_{\mathrm{T2}} \cdot \begin{cases} 1, & \text{if T3 condition fullfilled} \\ 0, & \text{otherwise} \end{cases}, \tag{5.2}$$

where r_{T2} is the trigger rate [Hz]. The first term describes the probability of a trigger of being in the T3 time window (in negative or positive direction) in dependence on the cone C_n, in which the station is in. The sum of all stations yields the probability for a correlated, extensive radio signal leading to a T3. The exercise is repeated for different requirements, a summary is shown in Tab. 5.3.

Requiring one particle ToT-like trigger in the T3 and only using the ToT2C_1&3C_2 configuration for T3-building yields a good suppression and still results in a significant increase in trigger efficiency compared to just using WCD triggers. The suppression yields a coincidence T3 probability of 0.0008. This translates into approximately one created random T3 for every 1,250 correlated RD triggers. The T3 rate is then dependent on the settings used for the inhibit, but can range between one random T3 per station per 10 days down to one random T3 per station per month.

This modification would need to be implemented at the CDAS level. The modification itself is comparably straightforward and is outlined below. However, during the time of this work, no test machine of the CDAS system was existing. Therefore, modifications could only have been implemented and evaluated on the live-machine, which is responsible for the entire data collection of the Observatory. Although the changes should not affect the regular, already existing data taking logic, there are concerns regarding running parallel processes, computation times and server connections. Thus, it was agreed to implement changes only when they can be validated by running on a test CDAS-machine, which has to be designed first. Therefore, the performance on an actual system could not be evaluated, but the proposed changes will be discussed in the following. The proposed changes of the code can found in Appendix B.

The trigger information sent from the station to CDAS consists of a 4-bit number, which is illustrated in Tab. 5.4. One bit is used to indicate a TOT-like trigger. In case this bit is 0, it has to be a threshold trigger. The other bits are not of relevance then. Hence, all numbers from 0-7 are used for a threshold trigger, converting the bits to a decimal system. Due to the way CDAS is constructed, it is difficult to change this. In case of a ToT-like trigger, the mentioned bit is 1. Depending on the trigger, one of the other bits is 1 (MoPS, ToTd, ToT). In general, it is the concept to employ combinations of these bits as diagnostic tools to ascertain the functionality of all triggers. Hence, combinations of bits are sent if multiple triggers are seen and all numbers ≥ 8 are occupied with ToT-like triggers. This diagnostic tool is not working at the moment of writing, but could be activated again.

During the previously discussed trigger test, the RD trigger was sent via trigger flag 8. Therefore, it is classified as a ToT-like trigger and can be identified as an RD trigger if no other ToT-like trigger exists. This approach is effective in general, with the exception that number 8 is also employed as a marker for a so-called 'large saturation' signal sent by the remaining Unified Boards (UBs, the predecessor of the UUB). At the moment of writing, 45 UBs still send triggers. Analysing the rate of sent triggers with number 8 from these stations, the rate is not significantly different from the corrupted package rate. Hence, it is possible to continue using this flag, as it currently does not yield any information. Regardless, one should discuss if diagnostics are still needed and if it is desired to send the RD trigger with one of these numbers. Furthermore, the combination of an RD trigger and a particle trigger would be a useful information[1].

A sketch of the currently long-running version of CDAS with the addition of the proposed modifications is shown in Fig. 5.13. The heart of CDAS is the so-called `Xb` process. Here, the sub-process `XbPm` collects all T2 triggers, which were sent by the stations to CDAS. Based on the trigger flag, the trigger can be differentiated. All regular triggers [Th-T2 (trigger flag 1), MoPS (9), ToTd (10), ToT (12)] are forwarded to the `XbAlgo`-sub-process. The Scaler trigger (7), which does not contribute to the T3-building, is specifically excluded from the collection of triggers in the `XbPm`-process. However, the same process can also be specifically requested to only read the Scaler triggers, if the `XbPm`-process gets a corresponding parameter as function input. All triggers contributing

---

[1] Another aspect is to introduce a general trigger test flag instead of one of the diagnostics. But this discussion is beyond the scope of this work.

Table 5.4: Trigger flags in CDAS

Trigger name	**Number**	**Comment**	
Threshold	1		
External	5		
Scaler	7		
Large Sat (UB)	8	TOTVALUE	ToT-like
RD (UUB)			
MoPS	9		
ToTd	10		
ToTd+MoPS	11	Diagnostic	
ToT	12		
ToT+MoPS	13	Diagnostic	
ToT+ToTd	14	Diagnostic	
ToT+ToTd+MoPS	15	Diagnostic	
Free (UUB)	0,2,3,4,6		

to the T3 building are processed in the `XbAlgoFindCluster` function, in which possible T3 clusters are built with the different T3-configurations. Here, the trigger flag determines if the triggers are ToT-like (flag ≥ 8). The T3 clusters are merged if they have common stations, and unique T3 requests are sent back to the stations.

RD triggers of the field test were collected by the `XbPm`-process and were treated as the other ToT-like triggers. The proposed CDAS modification would change this in multiple steps. For purposes concerning CDAS conventions and infrastructure, the RD trigger will be sent with the trigger flag set to 4. To not endanger the regular data taking, a parallel `XbRD`-process is created. It controls the `XbPm`-process and via a newly designed function parameter (similar to the Scaler parameter) a collection of all ToT-like triggers and the RD triggers is requested. The triggers are then sent to `XbAlgoFindClusterRD`, which tries to build T3 clusters using the ToT$2C_1\&3C_2$ configuration. It is slightly modified so that all T3 clusters need to have at least one particle ToT-like trigger contributing. The clusters should then be merged with the clusters of the regular `Xb`-process, and unique T3 requests are being sent to the stations.

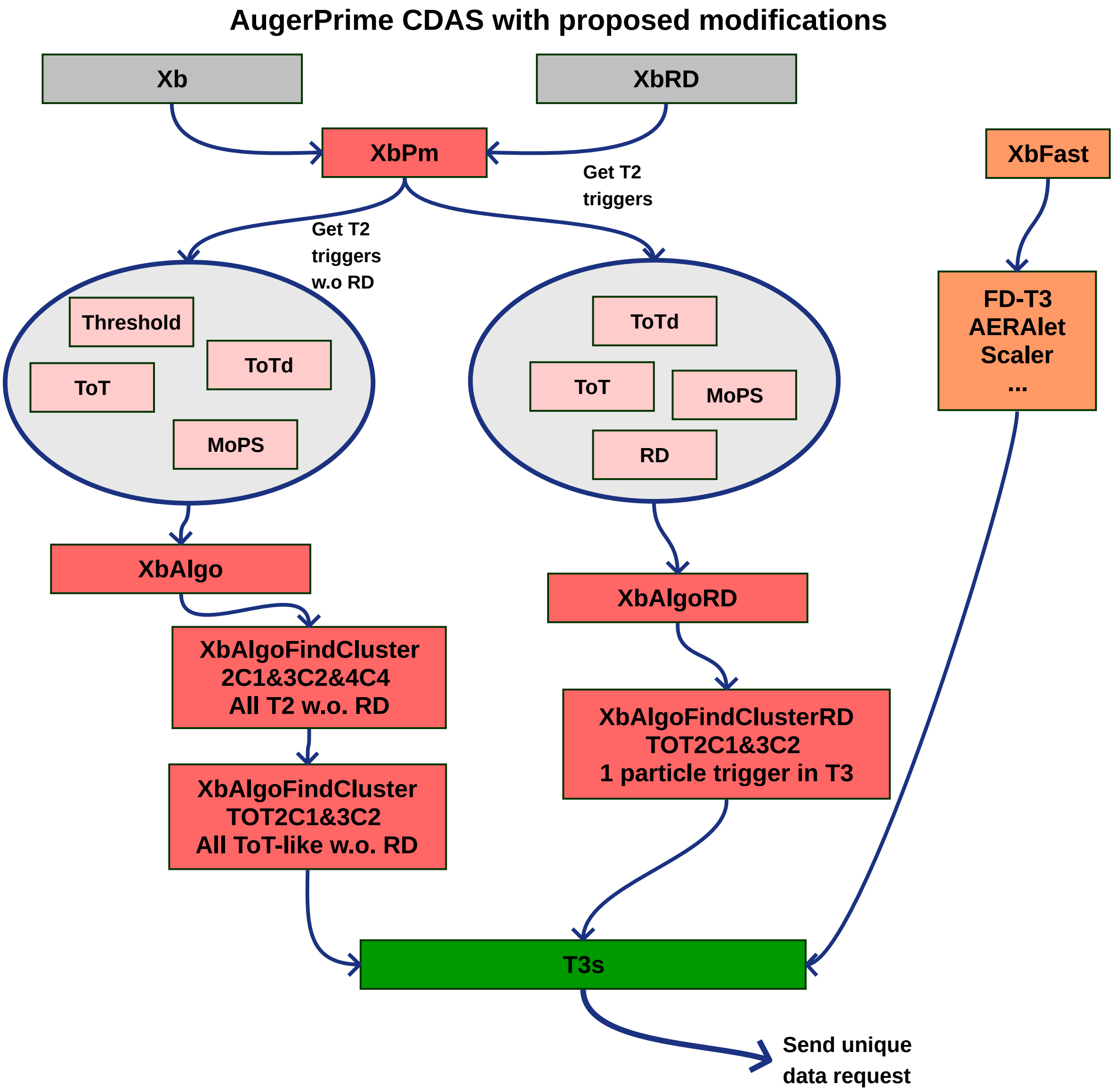

Figure 5.13: Schematic of the CDAS process. The left and right part correspond to the actual version of CDAS. The middle part depicts the proposed additions.

CHAPTER 6

DETECTION OF INCLINED PHOTON AIR SHOWERS

In this chapter, the trigger and reconstruction efficiency for photon induced air showers, $\mathcal{E}_\gamma$, regarding distinct constant trigger thresholds, T_H, will be examined using CoREAS [122] (and thereby also CORSIKA) simulations. Some trigger thresholds may not be applicable (for example 10 ADC counts) in reality due to the noise level, but are anyway investigated. It is valuable information, which efficiency could be achieved with maybe newer hardware. The efficiencies for different T_H are presented, but it will be more detailed for $T_\mathrm{H} = 25$ ADC counts, as this threshold is the value considered for an implementation. It will not only be discussed how well one can trigger photons, but it will also be shown that not all triggered showers can be reconstructed, especially due to the lack of particle signals in the WCD. The chapter will begin with the efficiency for the ideal case of pure radio trigger T3 acceptance, which will provide the ideal and aimed for scenario. Subsequently, the implementation of the anticipated initial trigger version with the proposed CDAS modification is analysed and compared.

6.1 Simulation set

For the analysis of trigger efficiency, reconstruction ability and discrimination, two CoREAS simulation sets were created [123]. Both sets have the same input parameters, including primary energy, zenith angle, azimuth angle, magnetic field (Auger location) and random seed, but differ by their primary particles. One set consists of proton primaries, while the other one consists of photon primaries with activated preshowering [124]. Both sets have each $\approx 1{,}700$ showers with eight distinct azimuth angles ($\varphi_\mathrm{MC} \in [0°, 45°, ..., 315°]$), using the CORSIKA convention of 0° pointing towards North) and zenith angles following a squared cosine distribution. The energy was simulated with an E_MC^{-1} spectrum with the range $\log_{10}(E_\mathrm{MC}/\mathrm{eV}) \in [18.4, 20.2]$. The photon simulations are weighted in the following according to an assumed E^{-2} spectrum, while the proton simulations follow the spectrum of Auger[1] published in [14]. For each event, realistic noise is imported from the periodic data set to simulate the noise influence at Auger, with minimal cleaning to reduce the influence of strong RFI.

6.2 Trigger efficiency for a radio trigger

The photon trigger efficiency defined as

$$\mathcal{E}_{\gamma}^{\mathrm{T3}} = \frac{\#\ \text{triggered events}}{\#\ \text{all events}} \qquad \text{(weighted)} \tag{6.1}$$

should generally increase with lower T_{H}. This behaviour as well as the efficiency of radio reconstruction

$$\mathcal{E}_{\gamma}^{\phi,\theta} = \frac{\#\ \text{radio reconstructions}}{\#\ \text{all events}} \qquad \text{(weighted)} \tag{6.2}$$

is shown in Fig. 6.1. A radio reconstruction is defined by having a successful spherical wavefront fit. All weighted statistical uncertainties are calculated here and in the following via the method in [125]. The figure (left) illustrates the case of having all combinations of T3 accepted, such as pure particle or radio T3s or a mixture of the distinct T2s. The results are in line with the expectations. For $T_{\mathrm{H}} \leq 15\,\mathrm{ADC}$ counts, $\mathcal{E}_{\gamma}^{\mathrm{T3}}$ of $\approx 85\,\%$ is achieved. At $T_{\mathrm{H}} = 25\,\mathrm{ADC}$ counts, still more than $60\,\%$ of the photons are detected. It rapidly decreases and converges for the highest T_{H} towards the $\mathcal{E}_{\gamma}^{\mathrm{T3}}$ of the WCD detector, which is slightly less than $20\,\%$ for this zenith angle range. Furthermore, the reconstruction efficiencies are observable. One observes a similar behaviour with increasing T_{H}. This is best seen in the ratio plot (right). The curve shows peaks at $T_{\mathrm{H}} = 20\,\mathrm{ADC}$ counts with decreasing efficiencies on both sides, but still in the order of $50\,\%$-$75\,\%$. This is anticipated as for higher T_{H}, fewer stations are triggered in the event, which directly affects the reconstruction probability. For low T_{H} the SNR decreases, hence, reducing the ability to discriminate signal from background, which then lowers the probability to reconstruct the event. Applying more sophisticated cuts, could improve the reconstruction efficiency, especially for lower trigger thresholds.

Figure 6.2 shows the simulated events with their respective zenith angle and energy, separated by their reconstruction level. In the case of $T_{\mathrm{H}} = 10\,\mathrm{ADC}$ counts, it can be observed that reconstructed events can be detected for all energies and zenith angles,

---

[1] Even though protons should not contribute at the highest energies, but it is weighted so for simplicity reasons.

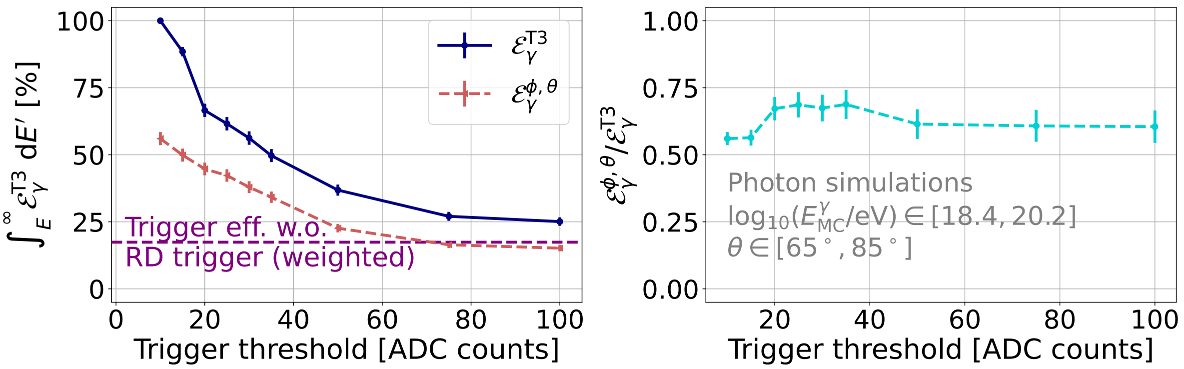

Figure 6.1: (Left) Integrated efficiency for $E_{\mathrm{MC}}^{\gamma} \geq 10^{18.4}$ eV and $\theta \in [65°, 85°]$ tested for constant trigger thresholds. The lines indicate the efficiencies of triggering (blue solid) and reconstruction (red dashed). The constant purple line shows the case based on only WCD triggers. (Right) Ratio of the trigger to reconstruction efficiency for different trigger thresholds.

with the exception of the lowest zenith angles and energies. For $T_{\mathrm{H}} = 25$ ADC counts, the region of lowest energies and zenith angles exhibits a low number of triggered events. The present signals are too small to yield an event reconstruction. For $T_{\mathrm{H}} = 75$ ADC counts a clear energy dependence is visible. It appears that at lower energies, air showers often fail to generate sufficient signals in the stations, irrespective of the zenith angle. Another possible reason for the triggering of those events could be a triggering by the WCD, and not a contribution from the RD. This is only partially true, as it is observed that numerous events, particularly at energies exceeding 10 EeV and with large zenith angles, are not detected in the case of no activated RD trigger. Assuming a falling energy spectrum of E^{-2}, these are the most probable events.

This is also shown in Fig. 6.3, where $\mathcal{E}_\gamma^{\mathrm{T3}}$ for different triggering settings is shown. One observes that the combination of RD and WCD triggers yields the largest $\mathcal{E}_\gamma^{\mathrm{T3}}$. For $T_{\mathrm{H}} = 25$ ADC counts and at the lowest energies, $\mathcal{E}_\gamma^{\mathrm{T3}}$ is dominated by the RD trigger. In the region of $E_{\mathrm{MC}}^{\gamma} \approx 10^{19.5}$ eV the individual trigger efficiencies are equal for RD and WCD, but yield a combined $\mathcal{E}_\gamma^{\mathrm{T3}}$ of close to 100 %. The combined efficiency continues for the even higher energies to approach 100 %, but now it is being dominated by the WCD trigger. The RD trigger efficiency fluctuates around ≈ 80 % and does not increase due to its low sensitivity at low zenith angles (*c.f.* in the following), as the radio footprint is frequently insufficiently developed, without regard to the primary energy. All energies have in common that the combination of the WCD and RD trigger is greater or equal to the individual trigger efficiencies. It is expected that more triggers will result in more read-outs, but possible artefacts such as timing issues could result in inefficiencies.

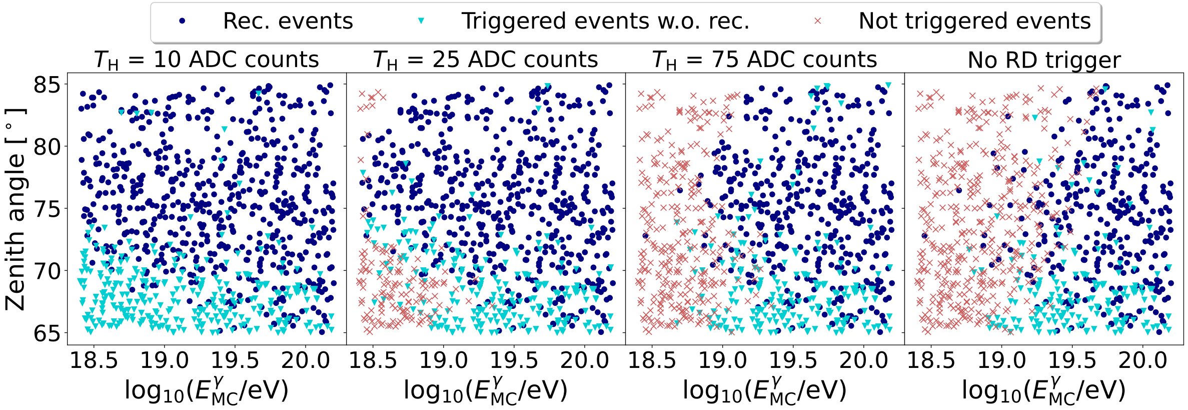

Figure 6.2: Reconstruction level of events at different zenith angles and energies. The different columns show different scenarios (from left to right) of RD trigger thresholds of 10 ADC counts, 25 ADC counts and 75 ADC counts and the current case of no RD trigger. The plot differentiates between not triggered (red crosses), triggered but not reconstructed (cyan triangles) and triggered and reconstructed (dark blue circles) events

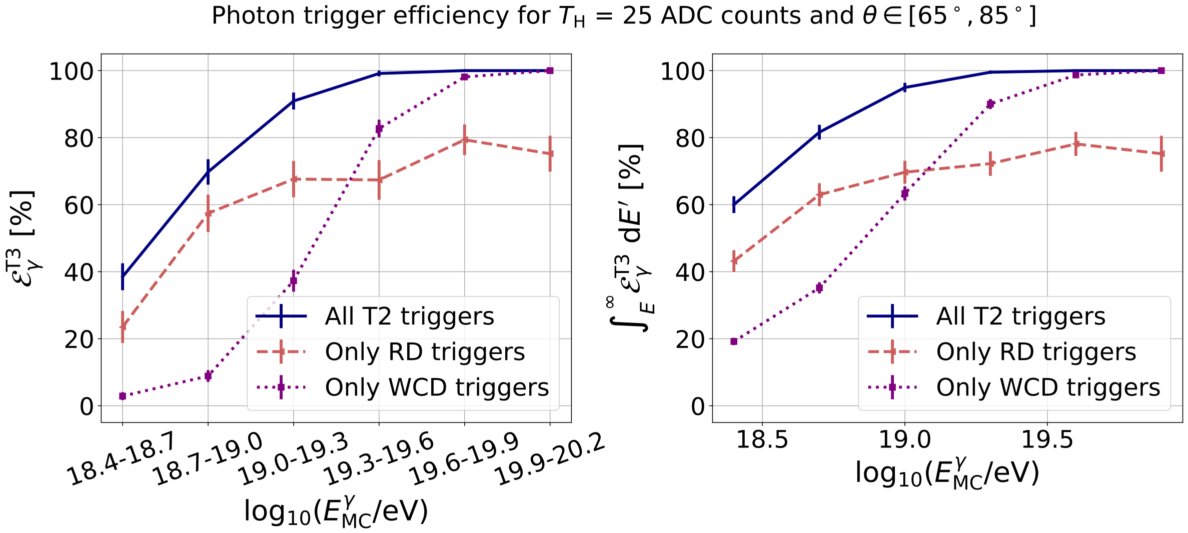

Figure 6.3: (Left) Differential photon trigger efficiency for different energy bins. The cases of only WCD triggers (purple dotted), only RD triggers (red dashed) and the combination of both (blue solid) are shown. (Right) Same as (left), only for the integrated trigger efficiency.

The energy integrated efficiencies exhibit the largest improvements at low energies, with ≈ 60 % integrated efficiency for the combination of RD and WCD triggers, compared to ≈ 20 % for the WCD only trigger case. At energies above 10 EeV the combined triggers yield nearly full efficiency, while the WCD trigger case exceeds only the 60 % benchmark.

It was already shown that the increase in $\mathcal{E}_{\gamma}^{\mathrm{T3}}$ compared to the case of only WCD triggers is dependent on the energy. Observable is also an significant influence of the zenith angle. One can quantify the impact of these two variables, as illustrated in Fig. 6.4 (left) for the case of $T_{\mathrm{H}} = 25\,\mathrm{ADC\,counts}$. The energy dependence is straightforward to describe. With an increase in energy, it is consistently observed that the $\mathcal{E}_{\gamma}^{\mathrm{T3}}$ trigger efficiency increases until it reaches almost full efficiency. The zenith angle dependence exhibits distinct features. At the lowest zenith angles between 65° and 70°, $\mathcal{E}_{\gamma}^{\mathrm{T3}}$ is low at low energies and only for energies higher than 20 EeV one gets fully efficient. The RD with its large station spacing is not suitable for this zenith angle range, as the radio footprint is too small or not fully developed to trigger enough stations. Nevertheless, the ratio plot (right) shows an increase by a factor of ≈ 3 at the lowest energies, when including the RD trigger compared to only WCD triggers. The zenith angle range of 70° to 75° yields for the lowest energy an efficiency of $\mathcal{E}_{\gamma}^{\mathrm{T3}} \approx 50\,\%$ and it is almost fully efficient for energies greater than 10 EeV. Compared to the WCD triggers only case, it improves $\mathcal{E}_{\gamma}^{\mathrm{T3}}$ by more than a factor of 10 for the lowest energies, and a decreasing improvement factor for higher energies. The zenith angle range of 75° to 80° shows the best $\mathcal{E}_{\gamma}^{\mathrm{T3}}$, yielding 80 % efficiency already at the lowest energy bin and being fully efficient for all higher energies. The enhancement can be quantified by a factor of 10 for the lowest energy bin, and a factor of 20 for energies between $10^{18.7}\,\mathrm{eV}$ and $10^{19}\,\mathrm{eV}$. For higher energies, the enhancement is nearly identical to that observed in the previously mentioned zenith angle range. The zenith angle range of 80° to 85° appears contradictory to the overall behaviour, with $\mathcal{E}_{\gamma}^{\mathrm{T3}}$ of only $\approx 40\,\%$ for the lowest energy bin. The undifferentiated interpretation of the previous zenith angle ranges would result in the expectation of the highest $\mathcal{E}_{\gamma}^{\mathrm{T3}}$ even at the low energies. In fact, the highest zenith angles lead to the largest illumination of the array, with many stations having a large SNR, which was already observed for hadron simulations in [87]. Nevertheless, having the highest number of stations with large SNR is not equivalent to the trigger probability. The stations have a high SNR, but still, the signals do not exceed $T_{\mathrm{H}} = 25\,\mathrm{ADC\,counts}$, and therefore the event is not triggered. Due to the large zenith angle, there is a large distance between the shower maximum and the station. The signals are not strong enough for the lowest energy bin to consistently activate a sufficient number of stations for a read-out. Only for large energies, the signals are always strong enough to achieve full efficiency. The factor of efficiency improvement cannot be calculated for the lower energies, as the WCD has no sensitivity here at all, only for higher energies one sees a clear improvement with factors of ≈ 6.5 ($\log_{10}(E_{\mathrm{MC}}/\mathrm{eV}) \in [19, 19.3]$) and 2.7 ($\log_{10}(E_{\mathrm{MC}}/\mathrm{eV}) \in [19.3, 19.6]$).

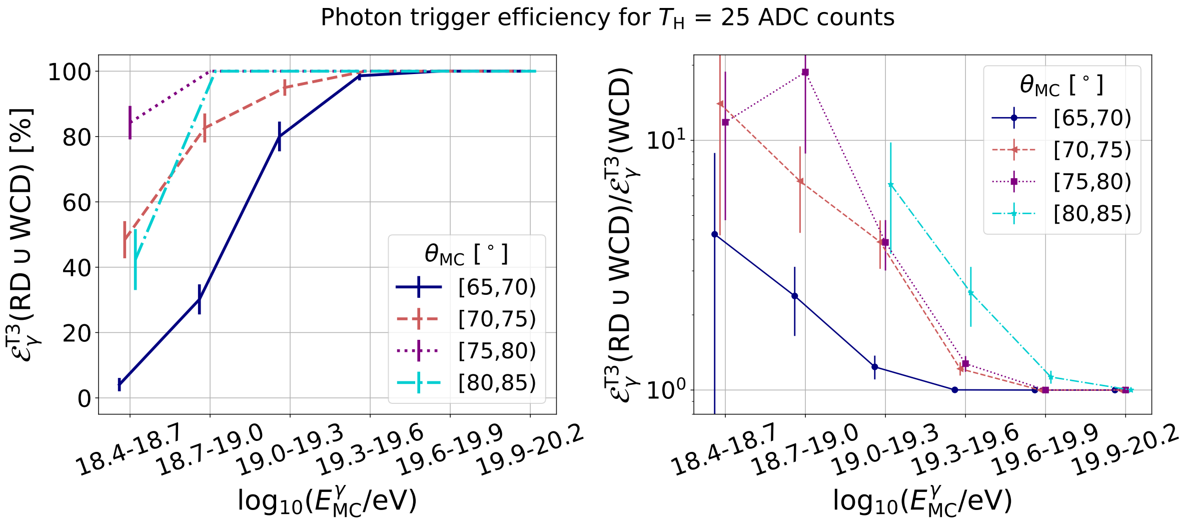

Figure 6.4: (Left) The differential trigger efficiency for different energies is shown. The different colours and line styles indicate different zenith angle ranges. (Right) The improvement factor of the trigger efficiency in case of adding the RD trigger compared to only WCD triggers. The colours and line styles are the same as before. The highest zenith angle range (cyan dashed-dotted) shows only results for energies $E \geq 10\,\mathrm{EeV}$ as the trigger efficiency is close to 0 for only WCD triggers at the lower energies.

$\mathcal{E}_\gamma^\mathrm{T3}$ exhibits a dependence on the azimuth angle as well, as illustrated in Fig. 6.5. Three types of dependence can be distinguished. The two extremes are cases of showers coming from North or from South, and the third case depicts all azimuth angles in between. For the arrival direction from the South, the opening angle to the direction of Earth's magnetic field results in the strongest geomagnetic radio emission. Already for the lowest energy bin, $\mathcal{E}_\gamma^\mathrm{T3} \approx 70\,\%$ is observed, increasing for the energy bin of $\log_{10}(E_\mathrm{MC}/\mathrm{eV}) \in [18.7, 19]$ to more than 80 % and being fully efficient for higher energies. The opposite arrival direction yields the weakest radio emission, which is also apparent for $\mathcal{E}_\gamma^\mathrm{T3}$. For $\log_{10}(E_\mathrm{MC}/\mathrm{eV}) \in [18.4, 18.7]$, the efficiency is only slightly above 10 %, but increasing to almost 60 % for $E \in [10^{18.7}\,\mathrm{eV}, 10^{19}\,\mathrm{eV}]$. For $\log_{10}(E_\mathrm{MC}/\mathrm{eV}) \in [19, 19.3]$ only the combination with low zenith angles (*c.f.* Fig. 6.2) prevents full efficiency, which is only achieved for energies above $10^{19.6}$ eV. The other azimuth angles behave the same way and yield efficiencies between the extreme cases. At the lowest energies, $\mathcal{E}_\gamma^\mathrm{T3}$ is around 30 %-40 %. For $\log_{10}(E_\mathrm{MC}/\mathrm{eV}) \in [18.7, 19]$, $\mathcal{E}_\gamma^\mathrm{T3}$ increases to almost 70 % and being almost fully efficient for all energies above 10 EeV. All azimuth angles have in common, that they yield significant enhancement factors for energies below $10^{19.3}$ eV.

An RD trigger has been shown to have an impact on the trigger efficiency for photons. Moreover, this also impacts the number of stations involved in detected events. Especially for high zenith angles, it increases the number of triggered stations n_T per

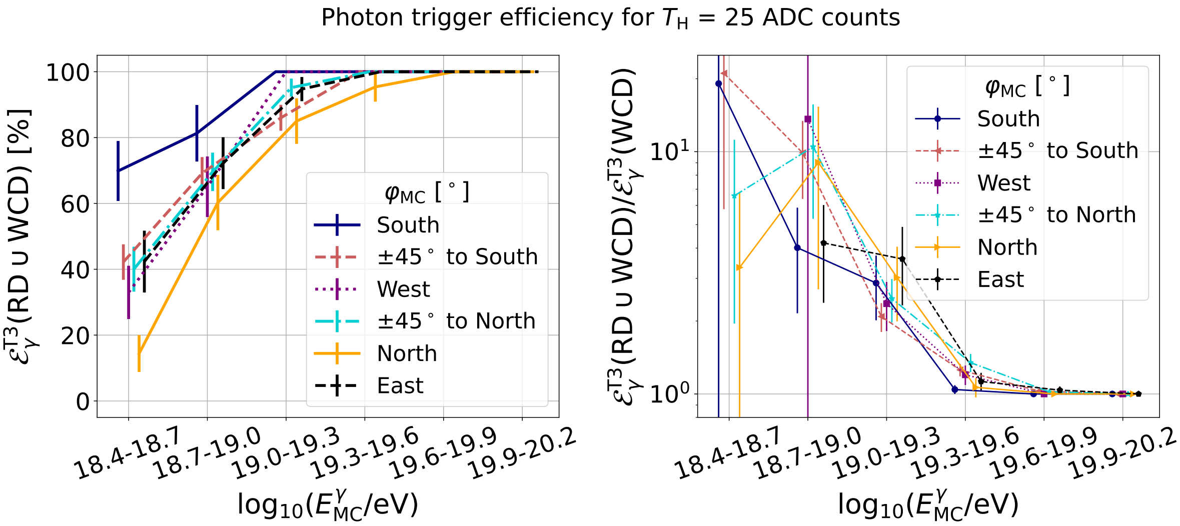

Figure 6.5: (Left) The differential trigger efficiency for different energies is shown. The different colours and line styles indicate different azimuth angle ranges. (Right) The improvement factor of the trigger efficiency in case of adding the RD trigger compared to only WCD triggers. The colours and line styles are the same as (left). Some azimuth angle ranges (purple and black lines) show only results above certain energy, as the trigger efficiency is close to zero for only WCD triggers at the lower energies.

event. This is shown in Fig. 6.6, where n_T for the configuration of only WCD or only RD triggers is shown. All events are displayed, which are individually triggered by both configurations. The zenith angle has a significant impact on which configuration observes more triggered stations. For $\theta < 70°$, both configurations show similar n_T with less than 10 triggered stations. The radio footprint is limited by the relatively small zenith angles and does not extend over extensive areas. For $70° \leq \theta \leq 77.5°$, only few events show a larger n_T for the RD trigger, the majority has still less than 10 read-out stations. At the same time, n_T increases for the WCD configuration to 10-20 stations. This is in agreement with the general behaviour of particle detectors for $\theta \leq 80°$, as already described in [57]. Due to the inclination, the density of stations in the shower plane is higher, favouring a greater number of stations with a trigger. At first glance, the larger n_T for the WCD configuration seems contradictory to the previously discussed trigger efficiency for RD and WCD. Even though RD has a smaller average n_T, it has a larger trigger probability. It is possible to resolve this discrepancy by considering the muon density and average muon signal in WCDs for inclined showers. An inclined muon deposits a signal of $\approx 1.25\,\mathrm{VEM}$ for θ of about 65° and $\approx 2\,\mathrm{VEM}$ at around 77.5°[57]. Thus, 2-3 muons are required to create a T2 trigger, which contributes to the T3-building. For a T1 trigger, only 1-2 muons are needed. However, they do not contribute to the T3-building. Therefore, especially distant from the shower axis, the muon

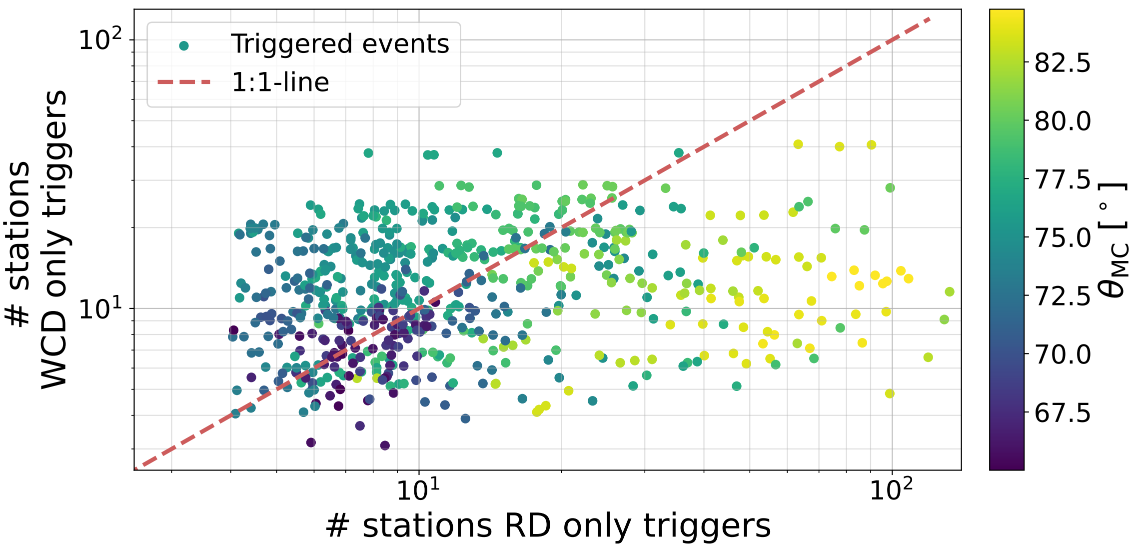

Figure 6.6: Comparison of the number of triggered stations for the case of only RD triggers and only WCD triggers for simulated events which were triggered by both trigger configurations. The colour scale indicates the zenith angle of the air shower.

density for photon air showers is on average not large enough to create T2 triggers but only T1 triggers. Moreover, the low muon density of photon air showers also results in a sparse particle footprint on the ground. Many stations are triggered, but still, the T3 building conditions are not satisfied. As a conclusion, if the event is read-out, there are many involved stations with a large fraction of T1 triggered stations. However, a trigger for the event is not given in all cases. The RD configuration does not encounter the challenge of a sparse footprint due to statistical fluctuations, as the radio wave exhibits only a continious radial dependence.

For $\theta \geq 77.5°$, one obtains a shift and the RD configurations has now a higher n_{T}. With increasing zenith angle, n_{T} also increases rapidly for the RD configuration. Furthermore, events with more than 100 RD triggered stations are observed, whereas the same events yield only ≈ 10 WCD triggers. Here, the sensitivity of the RD at large zenith angles becomes evident.

It is observed that the combination of RD and WCD triggers produces the most beneficial results (assuming that more signal containing read-out stations yield a better reconstruction). It is possible to obtain the number of triggered stations per event, as depicted in Fig. 6.7, for the current configuration of just WCD triggers and the combination with RD triggers. All bins containing at least 5 triggered events are displayed. The expected general behaviour for both cases is observed, with higher energies and zenith angles leading to more triggered stations. Only for the highest energy bin in combina-

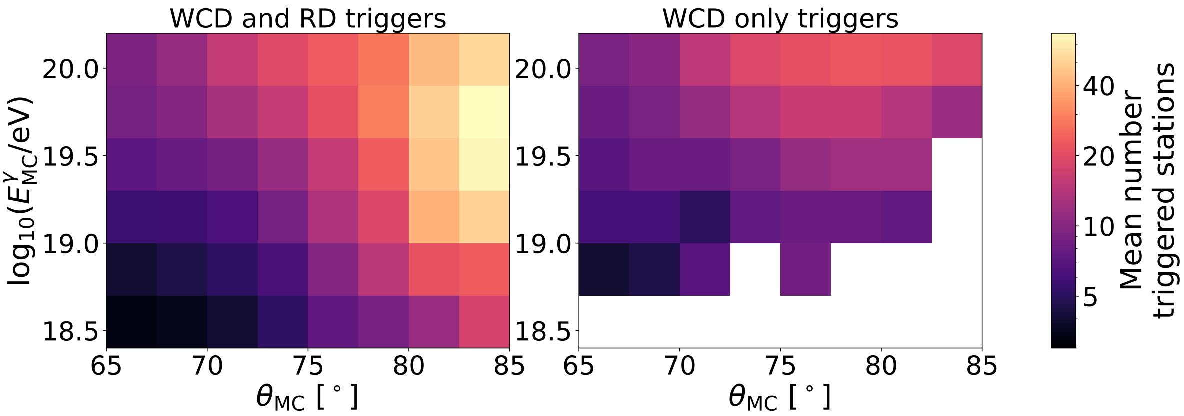

Figure 6.7: The mean number of triggered stations is shown (colour scale) for different energy and zenith angle ranges. (Left) Combination of RD and WCD triggers. (Right) Case of only WCD triggers.

tion with high zenith angles, a small decrease in the number of triggered stations can be seen. No trivial explanation can be found for this behaviour. Incorporating RD triggers generally increases the number of stations per event, which is expected. Two factors have a significant impact here. First, the radio footprint can exceed the particle footprint. Hence, it extends the number of triggered stations at the border of the event. Second, one has a displacement of the radio and particle core. Thus, the RD trigger adds stations despite having the identical footprint size.

6.3 Trigger efficiency for an SNR trigger

Instead of using a constant trigger threshold with a vetoing mechanism, one could alternatively use a trigger threshold based on transformed observables like the SNR. The channel wise SNR is here defined as

$$\mathrm{SNR(bin)} = \frac{\text{Abs. amplitude}}{\text{RMS(Noise window)}}, \tag{6.3}$$

where the noise is taken from the first 200 bins of the trace. If the SNR exceeds a predetermined threshold, an RD T2 will be generated. Generally, the SNR should have an almost linear relation with the constant trigger threshold in ADC counts. Moreover, it is sensitive to noise levels, which is both a benefit and a drawback. The positive aspect is that one would not require a vetoing mechanism. One would not trigger on noise peaks, as the SNR would be low due to the large RMS, but would still be sensitive to large signals during strong RFI periods. For instance, ubiquitous mono-frequent noise with peaks in the order of ±25 ADC counts are not causing triggers as the SNR would be close to one. The trigger would not be completely deactivated, but it could still trigger on significant peaks, such as pulses in the order of hundreds of ADC counts. The drawback (and the reason that this was not selected as the initial implementation for tests) is the difficulties it presents. Without a thorough understanding of the noise level, comprehending the reason behind which pulses were triggered and which pulses were not detected, poses a challenge. The noise level must be transmitted despite the absence of any trigger. This should be accomplished through the monitoring data, which is sent every 400 s. Only with this information, it is possible to perform exposure calculations. Furthermore, given that the general noise level at distinct locations of the array may vary significantly, it can be challenging to comprehend the behaviour of the trigger, which is important particularly in the beginning.

One can calculate an ideal trigger efficiency for low noise levels from the periodic data. The weighted trigger efficiency for different thresholds in units of the SNR is depicted in Fig. 6.8. Full efficiency is seen for the lowest but due to bandwidth limitations unfeasible values of $\mathrm{SNR} = 3$ and $\mathrm{SNR} = 4$. It decreases to $\approx 90\,\%$ ($70\,\%$) for an $\mathrm{SNR} = 5$ (6). The SNR value of 7.22[2] has almost equal trigger efficiency as observed for a constant trigger threshold of 25 ADC counts. For higher SNR, $\mathcal{E}_{\gamma}^{\mathrm{T3}}$ slowly converges towards the trigger efficiency of the WCD.

The reconstruction efficiency ratio (right) indicates a similar behaviour as for a constant trigger threshold. It has a peak of ≈ 0.65 at an SNR of 7.22, and decreases on both sides. For low SNR, the reconstruction efficiency ratio has its minimum due to the same reasons as previously described for the constant trigger threshold.

It appears that using an SNR as a trigger threshold would be an appropriate alternative to a constant trigger threshold. As a constant trigger threshold provides enhanced insight and facilitates comprehension of the trigger behaviour, it will be further continued with a constant threshold. However, the utilisation of the SNR should be revisited in the future.

---

[2] The value of $\mathrm{SNR} = 7.22$ is used as standard cut in RD reconstructions as this was determined to be the value for a 99 % signal probability in case of a regular noise level.

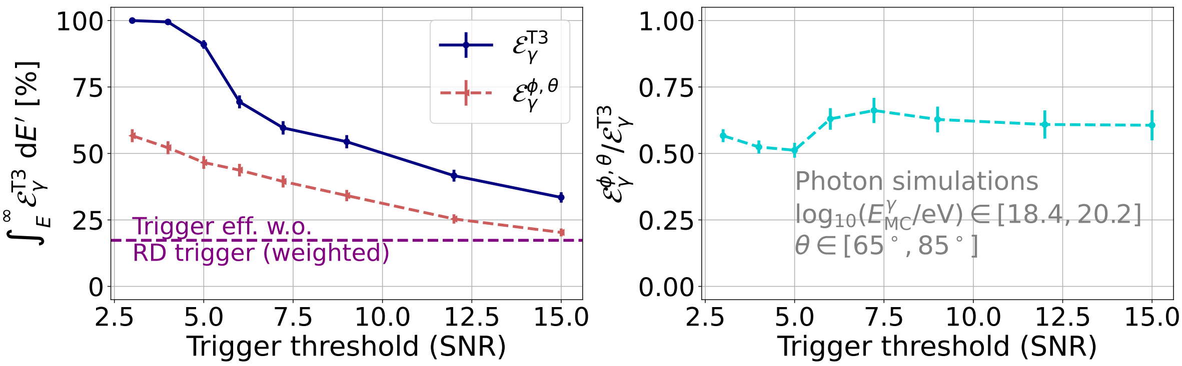

Figure 6.8: (Left) Integrated efficiency for $E_{\mathrm{MC}}^{\gamma} \geq 10^{18.4}$ eV and $\theta \in [65°, 85°]$ tested for SNR trigger thresholds. The lines indicate the efficiencies of triggering (blue solid) and reconstruction (red dashed). The constant purple line shows the case without activated RD trigger. (Right) Ratio of the trigger to reconstruction efficiency for different trigger thresholds.

6.4 Trigger efficiency with implemented CDAS modification

It was discussed, which efficiency could be achieved for an ideal scenario of accepted pure RD T3s for a radio threshold trigger. It was also demonstrated that this configuration does not appear to be compatible with the present hardware limitations of the communication bandwidth. Hence, to limit the number of T3s, particle triggers are requested to participate in the T3 building (*c.f.* Sec. 5.4). This restriction is investigated with $\overline{\text{Off}}\underline{\text{line}}$ simulations. Figure 6.9 shows the differential (left) and integrated (right) trigger efficiency for diverse scenarios. The WCD only trigger case yields a significantly reduced trigger efficiency compared to the case of activated RD trigger with the proposed CDAS modification (the trigger efficiency with the CDAS modification is denoted as $\mathcal{E}_\gamma^{\mathrm{T3}*}$). For $E \in [10^{18.4}\,\mathrm{eV}, 10^{18.7}\,\mathrm{eV}]$, $\mathcal{E}_\gamma^{\mathrm{T3}*}$ increases by nearly a factor of 4 from $\approx 1.3\,\%$ to $5\,\%$. The absolute increase is higher for the higher energies, resulting in improvements of $9.3\,\%$ to $20.2\,\%$ ($E \in [10^{18.7}\,\mathrm{eV}, 10^{19}\,\mathrm{eV}]$), $35.6\,\%$ to $62.1\,\%$ ($E \in [10^{19}\,\mathrm{eV}, 10^{19.3}\,\mathrm{eV}]$) and $81.7\,\%$ to $93.8\,\%$ ($E \in [10^{19.3}\,\mathrm{eV}, 10^{19.6}\,\mathrm{eV}]$). For even higher energies, all cases yield nearly full efficiency. However, a comparison with pure RD T3s indicates that one does not detect events at low energies, which were previously detected for pure RD T3s. The photons at the low energies could be the most frequent occurrence for an E^{-2} energy distribution. However, opaqueness at low photon energies could shift the maximum of the photon distribution to energies above 10 EeV (*c.f.* Sec. 2.2). Thus, it is unclear if the flux of photons at these low energies is significant.

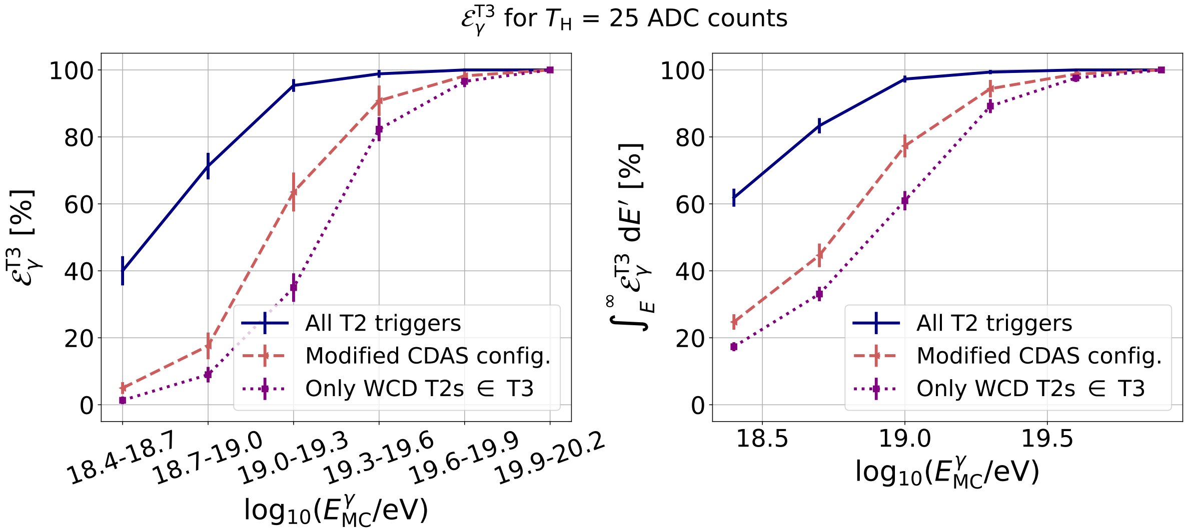

Figure 6.9: (Left) The differential trigger efficiency is shown for different energies. The different lines indicate the cases of only WCD triggers (purple dotted), adding RD triggers but with the proposed CDAS modification (red dashed) and adding RD triggers without any restrictions (blue solid). (Right) Same as (left), only for the integrated trigger efficiency.

The energy integrated trigger efficiency highlights the improvement compared to the WCD only case. For energies below $10^{19.3}$ eV, one observes an absolute improvement in efficiency between $\approx 9\,\%$ to $18\,\%$. It also indicates that requesting WCD triggers is most influential at the lowest energies. Here, the integrated trigger efficiency for the pure RD trigger case is higher by factors of 2 to 3 compared to the other cases. Only at higher energies, the difference between the cases vanishes.

Another factor to consider is the quality of the events, when evaluating the possible gains from the proposed CDAS modification. One example simulated event is shown in Fig. 6.10, which was not triggered with only the WCD, but by including RD triggers with the CDAS modification. In fact, the event was triggered by multiple T3 clusters which were later merged, and each cluster had WCD triggers. The footprint indicates that the event is of high quality, with many stations triggered, and it is anticipated that the radio footprint will be effectively distinguished from noise. Furthermore, the discrimination from hadrons is predicted to be strong, as the combination of such a strong radio footprint and a weak particle footprint (few stations triggered by the WCD) points directly to an air shower induced by a neutral particle. Hence, one does not only increase the photon triggering efficiency, but it is also expected to detect events with higher quality and strong discrimination power. It is important to note that this

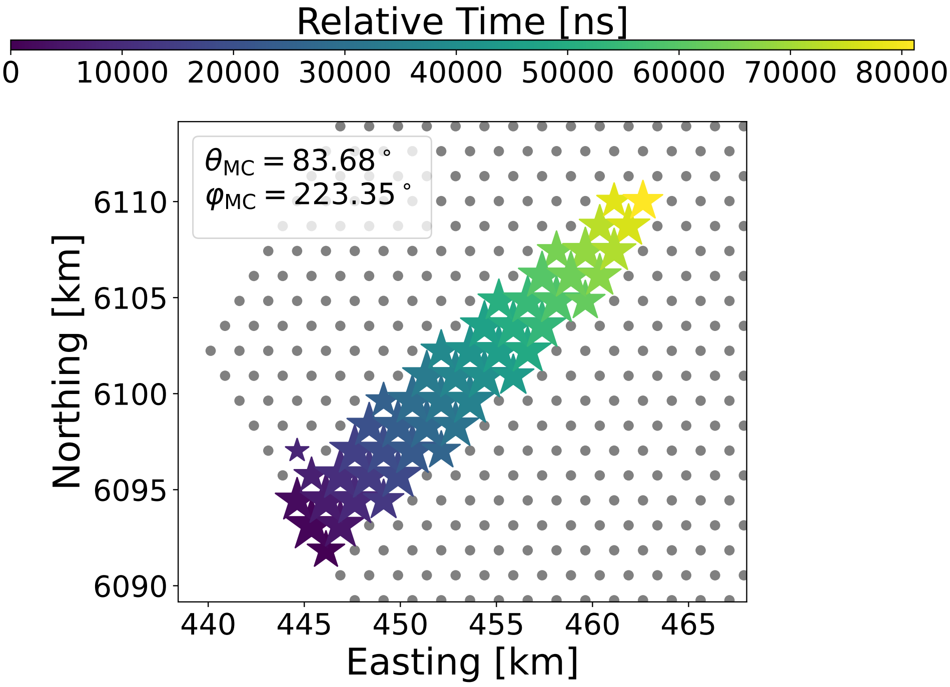

Figure 6.10: Example photon event gained by adding RD triggers with the proposed CDAS modification. The radio footprint of the event is shown. Grey points mark stations not triggered, coloured stars indicate triggered stations. The colour scale represents the station signal time, while the signal strength is shown by the size of the stars.

statement is even stronger for events without particle triggers, which are not triggered by the proposed CDAS modification.

As just shown, requesting WCD triggers influences the trigger probability. The impact is different strong for the distinct zenith angle ranges. Clearly, the bottleneck is the WCD trigger. Hence, it influences $\mathcal{E}_\gamma^{\mathrm{T3*}}$ at high zenith angles the most, where the WCD becomes less sensitive. This is shown in Fig. 6.11. The picture is quite different from the observed zenith angle dependence in Fig. 6.4. All zenith angle ranges yield a similar $\mathcal{E}_\gamma^{\mathrm{T3*}}$. $\mathcal{E}_\gamma^{\mathrm{T3*}}$ for $\theta \in [65^\circ, 70^\circ]$ changes the least, e.g. only by $\approx 10\,\%$ for $E \in [10^{18.7}\,\mathrm{eV},\, 10^{19}\,\mathrm{eV}]$ and by $\approx 5\,\%$ for $E \in [10^{19}\,\mathrm{eV},\, 10^{19.3}\,\mathrm{eV}]$. The effect of the CDAS modification is more evident in the other zenith angle ranges. Here, all zenith angles $\geq 70^\circ$ lose almost all trigger efficiency for the lowest energies. The factors of improves almost linear with energy until $10^{19.6}\,\mathrm{eV}$. For higher energies, almost no reduction is obtained.

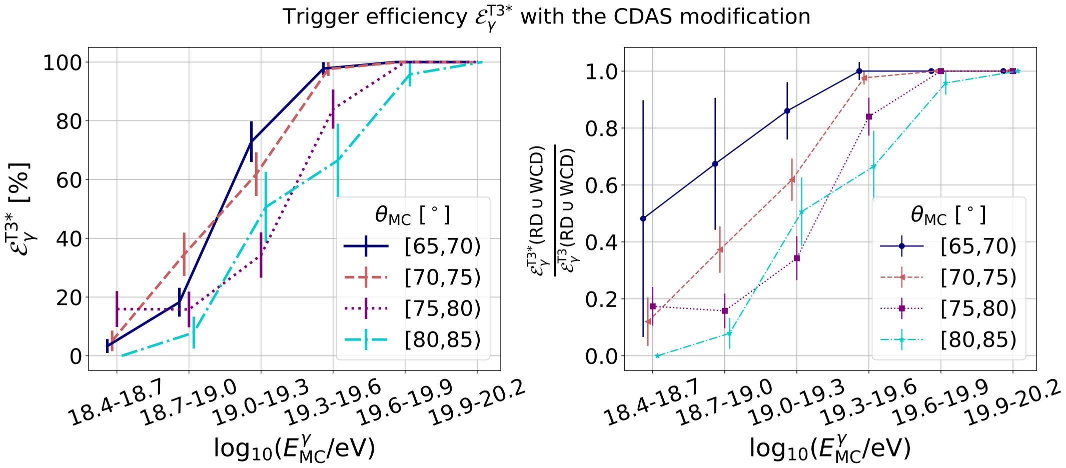

Figure 6.11: (Left) The differential trigger efficiency at different energies is shown. The different colours and line styles indicate different zenith angle ranges. (Right) The ratio of the trigger efficiency in the case of requiring the CDAS modifications compared to the case without restrictions. The colours and line styles are the same as (left).

6.5 Possible improvement of the trigger efficiency

It has been demonstrated that requesting WCD triggers in a T3 event significantly reduces the trigger efficiency compared to the case of allowing pure RD T3s, e.g. $\approx 35\,\%$ in integrated efficiency for energies above $10^{18.4}$ eV. An improvement of this trigger efficiency should prioritise recovering such events lost due to requesting WCD triggers. Events that are not even triggered by pure RD T3s are even harder to trigger without significantly increasing the noise read-out. In the following, different methods are discussed, which could in principle be implemented on CDAS level in order to achieve increased trigger efficiency. Nonetheless, the implementation of these configurations is only feasible following extensive research. This can only be done with realistic conditions and additional information about the trigger rates at different times and locations. This information is provided solely after the implementation of a test setup. In the following, the general methods are discussed and short calculations with limited information are performed to determine feasibility.

6.5.1 Online zenith angle reconstruction

The daily and very frequent noise is expected to be of anthropogenic origin with the sources mostly on the ground. Hence, two features can be found:

1. Nearly all noise comes from the horizon.

2. Nearly all events from the horizon are noise.

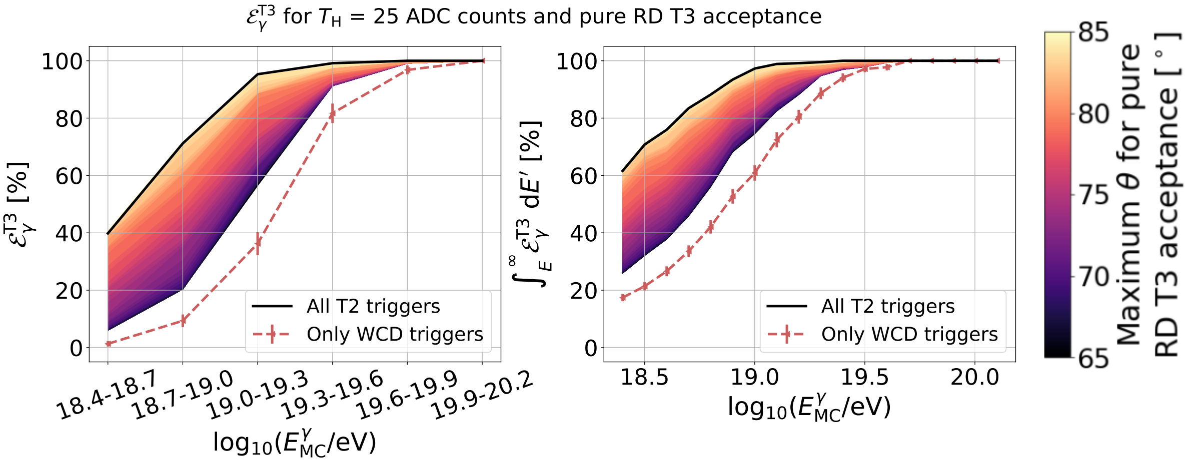

Figure 6.12: (Left) Trigger efficiency at different energies. The cases of only WCD triggers (red dashed) and adding RD triggers without restrictions (black solid) are shown. The coloured lines show the trigger efficiency in case a pure RD T3 acceptance for a maximum zenith angle is introduced. (Right) Same as before, only for the integrated trigger efficiency.

Therefore, one could adapt the CDAS modification to request WCD triggers only for events which come from the horizon. Events not from the horizon could be triggered without restrictions. One would gain almost all air shower events, as they rarely come from the horizon, while still rejecting most of the noise. The improvement of the trigger efficiency is shown in Fig. 6.12, for the differential and integral case. Different maximum zenith angles are tested, for which a pure RD T3 is allowed. Clearly, having the maximum at $\theta_\mathrm{max} = 65°$ yields $\mathcal{E}_\gamma^{\mathrm{T3}*}$ for the preliminary planned CDAS implementation, while $\theta_\mathrm{max} = 85°$ yields the ideal scenario of all simulated events being allowed to have pure RD T3s. Everything in between is the result of a combination of two effects, namely an increase in trigger efficiency for higher zenith angles and a decrease in exposure for higher zenith angles. Setting $\theta_\mathrm{max} = 80°$ yields a reasonable buffer to the horizon, but recovers a major fraction of air shower events. The integrated trigger efficiency increases from $\approx 30\,\%$ to more than $50\,\%$, compared to $60\,\%$ for the ideal scenario. For energies larger than 10 EeV it enhances $\mathcal{E}_\gamma^{\mathrm{T3}*}$ from $\approx 75\,\%$ to more than $90\,\%$.

The challenge is to make a cut on θ_max on CDAS level, where only station position and trigger time (cut at the µs) are known. A method for an online reconstruction was already investigated in [126], which is also discussed here. The components of the arrival direction vector are defined in Cartesian coordinates as follows:

$$x = -\frac{c(t_2 - t_0)(x_1 - x_0) - c(t_1 - t_0)(x_2 - x_0)}{(x_1 - x_0)(y_2 - y_0) - (x_2 - x_0)(y_1 - y_0)}, \tag{6.4}$$

$$y = -\frac{c(t_2 - t_0)(y_1 - y_0) - c(t_1 - t_0)(y_2 - y_0)}{(x_1 - x_0)(y_2 - y_0) - (x_2 - x_0)(y_1 - y_0)}, \tag{6.5}$$

$$z = \left|\sqrt{1 - x^2 - y^2}\right|, \tag{6.6}$$

where c is the speed of light, t_i is the station trigger time and (x_i,y_i) the station coordinates for station i. Since there are three unknown parameters, only three stations are required to solve this equation system. To reduce uncertainties due to imprecise trigger times and other timing issues, one repeats the exercise for all combinations of three stations in the T3. This yields

$$N = \frac{n!}{(n-3)! \cdot 3} \tag{6.7}$$

combinations for n triggered stations. Each combination j then results in its own estimated arrival direction via:

$$\theta_j^{\text{online}} = \arccos\,(z_j), \tag{6.8}$$

$$\phi_j^{\text{online}} = \arctan\,(y_j/x_j). \tag{6.9}$$

All combinations can then be combined to calculate a final arrival direction by taking the median as an estimator.

This exercise was performed for all simulated events, which were triggered for the ideal scenario without CDAS restrictions, but were not triggered if requesting WCD triggers in the T3. Two things are to mention. First, the study from [126] was brought closer to reality. An implementation would likely be applied on each tested T3 cluster, not on the final and merged T3 clusters of one event, like it was done in [126]. Second, minimal quality cuts were applied. Three calculated θ_j^{online} are requested, as well as that the combination of involved stations should have distances larger than the minimal 1.5 km grid distance. The results are shown in Fig. 6.13. One example event with all reconstructed θ_j^{online} shows a good agreement between the median reconstructed and MC zenith angle (left). Repeating this for all events yields a slightly asymmetric distribution (right), with a mean at 3.8° and a spread of 2.6°. Only a few events have deviations $\geq 7.5°$.

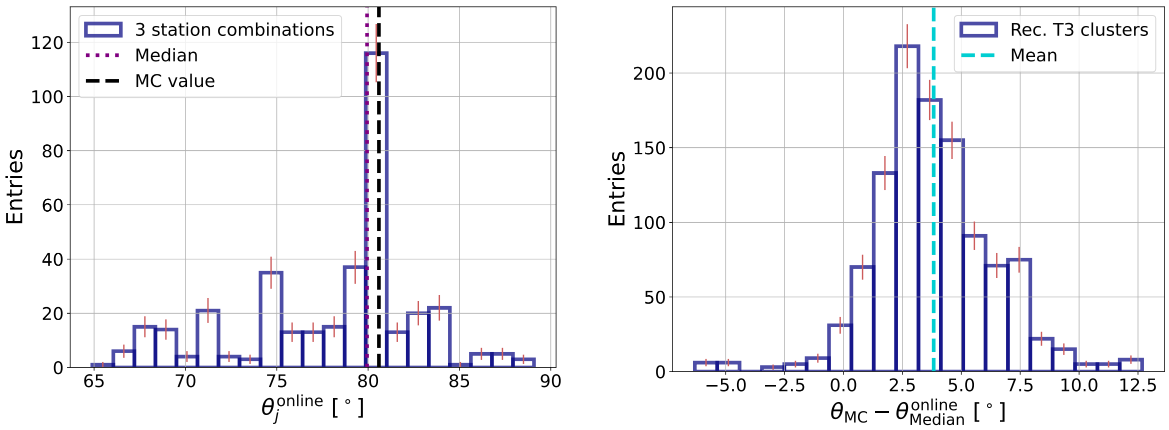

Figure 6.13: (Left) All reconstructed zenith angles based on the trigger times for one example event are shown. The dotted purple line shows the median value, the black dashed line indicates the MC zenith angle. (Right) Deviation of the reconstructed median zenith angle from the true MC values. The cyan dashed line shows the mean of the distribution.

The distribution indicates that it is theoretically feasible to perform this type of online reconstruction with a sufficient level of precision to identify events that are not originating from the horizon. Nonetheless, the more significant information is whether events from the horizon can be identified as such. For incoming events that are almost horizontal, the mean trigger time disparities among the stations increase. Therefore, the imprecision of the trigger timestamp is less important, and the accuracy of the reconstruction should increase. Hence, it is anticipated that the events from the horizon can be identified. Some events will have bad reconstructions, and the rate of these misreconstructions has to estimated to prove the feasibility for a pure RD T3 acceptance, for which data is needed. It is only possible to obtain unbiased data when implementing the RD trigger and saving the T2 data. Hence, a preliminary version with reduced efficiency should be implemented, and only subsequently it would be improved.

6.5.2 Stationary noise source rejection

Strongly connected to the zenith angle acceptance is a rejection of constant source directions. The azimuth angle of events has similar online reconstruction accuracy as the zenith angle. Therefore, if a stationary noise source in the vicinity of the Observatory is known, one can reject a range of azimuth angles based on the location of the triggered stations. For sources located far outside the array, it is possible that the azimuth angle range remains constant for all stations. For noise sources close to the array, it will vary depending on the station location. Noise sources inside the array could be detected more easily, as the trigger times increase radially in all directions. The correlation between a zenith angle in close proximity to the horizon and a radially increasing trigger time points directly to noise origins.

The technique possesses numerous drawbacks. Contrary to the zenith angle acceptance, one has a station location dependence. Implementing this into CDAS is difficult and will need intensive studies. Therefore, the location dependence renders exposure calculations unjustifiably complicated. Lastly, the method is not adequately safeguarded against novel noise sources. It could result in a burst of T3s and the crash of CDAS if a new noise source appears. This is not expected for the zenith angle acceptance, considering all noise sources should be on ground. Therefore, the method seems not beneficial and one could consider it as additional rejection from known noise sources rather than as a pure RD T3 acceptance.

6.5.3 Footprint shape rejection

The shape of the footprint could result in more efficient rejections and allow for pure RD T3 acceptance. The radio footprint of air showers (*c.f.* Fig. 6.10) and noise sources should be discriminable. Non-directional noise sources, such as sparking power lines, would result in a radially symmetric footprint. Combining the horizontal traversing wave with the speed of light, it directly points to its noise source. Directional noise sources, such as transmitters, would not exhibit an elliptical footprint on the ground. Depending on the opening angle of the source, it resembles a beam passing through the Observatory or a small cutout of a circle. By calculating the eccentricity of the ellipse for air showers, it is possible to identify the showers while rejecting noise footprints. This calculation can be done via a Principal Component Analysis (PCA), which is also under investigation by other experiments, such as GRAND [127]. The main axis of the PCA and its orthogonal yield the eccentricity of the ellipse. In order to have data for studies, running the RD trigger without pure RD T3 acceptance for a while is needed.

6.5.4 Sub-threshold trigger combinations

A different ansatz is the combination of RD and WCD information already on station level, instead of calculating the fraction of triggers on CDAS level. Having a WCD signal and RD signal simultaneously in one station is a clear hint of air shower origin. To produce a threshold trigger of the WCD, few muons have to hit the WCD. One could reduce the threshold to e.g. the equivalent signal of one muon. If at the same time an

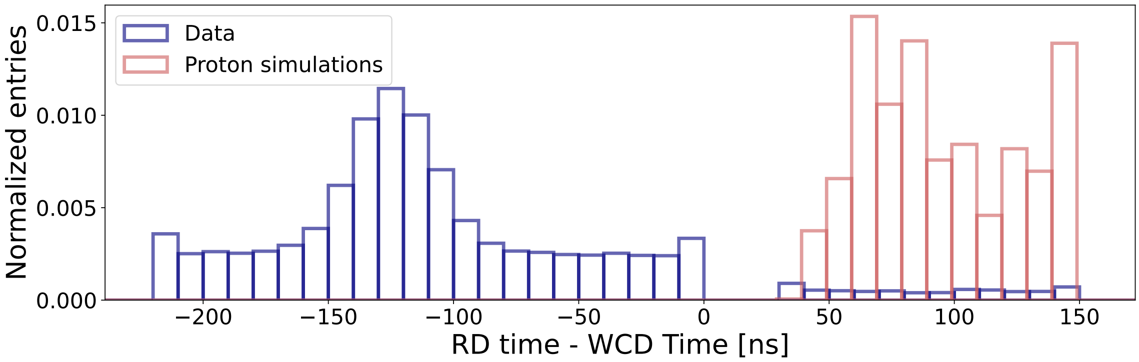

Figure 6.14: Time difference between RD and WCD signals for data (blue) and proton simulations (red). The absolute time difference is shifted for both cases equally to have values around 0. The real time difference can be defined differently but is of no importance here.

RD threshold (which can be lower than the regular T_{H}) is exceeded, a trigger different from the regular RD trigger would be created. In CDAS, this trigger would then be treated as WCD trigger. Hence, it could help to overcome the hurdle of having WCD triggers in the T3.

Studying this possibility first needs verification of the simulations. As discussed in Sec. 5.1, radio and particle signals arrive at different times. The time difference in data is smaller than the buffer of 3 µs in the T3 building. Hence, it does not influence triggering on CDAS level. However, if one searches simultaneously for signals in the WCD and RD in their respective traces, the time difference has an impact. If an RD threshold is exceeded, it is necessary to define a time window in which to look for a WCD signal, and vice versa. Time window lengths could be in the same order as the time difference of radio and particle signals. The time difference is also not constant but influenced by the distance to the shower maximum, which is then linked to primary energy and zenith angle. Therefore, intensive studies should be performed first regarding the time difference and also the synchronisation of the detectors. Electronic processes and timing uncertainties have the potential to influence the calculated time difference. This is, for example, seen in comparisons of data and simulations, which is depicted in Fig. 6.14.

The signal time differences indicate that there is a discrepancy between simulations and data. Both have an artificial offset caused by electronic processes, which is replicated in simulation. The absolute time difference between the two peaks is difficult to determine, since the RD trace is read-out so that the peak is at a specific location in the trace. This reduces the impact of electronic time delays, but it makes an absolute time determination difficult. Currently, the simulations and data do not align and result in discrepancies ranging from physical arrival time differences, thereby limiting the significance of all studies. First, an explanation for the differences between the data and simulations must be found, and only then the possibility of a combined trigger can be explored.

6.6 Trigger efficiency increase for proton induced air showers

The RD trigger has been specifically designed to enhance the trigger efficiency significantly for neutral air showers. However, it can also improve the detection and reconstruction of hadron showers. In particular, at low energies and large zenith angles, it has a potential to trigger events, which were not previously detected. This is depicted in Fig. 6.15, where the trigger efficiency for different energies is shown in the zenith angle range from 65° to 85°. A comparison between the current configuration and the one with RD triggers reveals a significant increase in trigger efficiency of about 10 % for energies between $10^{18.4}$ eV and $10^{18.7}$ eV. Higher energies indicate a nearly full efficiency of the WCD, and no further enhancement is observed. The ratio between the current configuration and the one including RD triggers, separated by the zenith angle, shows an increase by a factor of 1.5 for the zenith angle range between 80° and 85° For zenith angles of 70° to 80°, an increase by a factor of ≈ 1.1 is seen. Below 65° no increase is seen.

One example event, which is not triggered without the RD trigger, is depicted in Fig. 6.16. The footprint has clear structure, yielding a high probability for an accurate angular reconstruction. The shown fitted LDF indicates good agreement with the reconstructed signals. The newly gained events can probably be accurately reconstructed. This reduces the energy threshold for full efficiency.

Similar to photons, an RD trigger adds new stations to the event, which would normally be below the particle trigger threshold. However, sub-threshold signals can also contribute useful information for the event reconstruction. Particularly at large zenith angles with numerous low signal stations, this can be advantageous. The advantages of the RD trigger in terms of the number of triggered stations can be observed in Fig. 6.17. The number of stations for the configuration of just the WCD triggers and the combination with RD triggers is shown. The majority of events occur at or near the identity line. Single events above the line can be explained by artefacts in $\overline{\text{Off}}\underline{\text{line}}$ simulations, e.g. if multiple T3 distinct clusters are found. For zenith angles above 80°, a major fraction of events deviates significantly from the line and adds tens of new stations to the event.

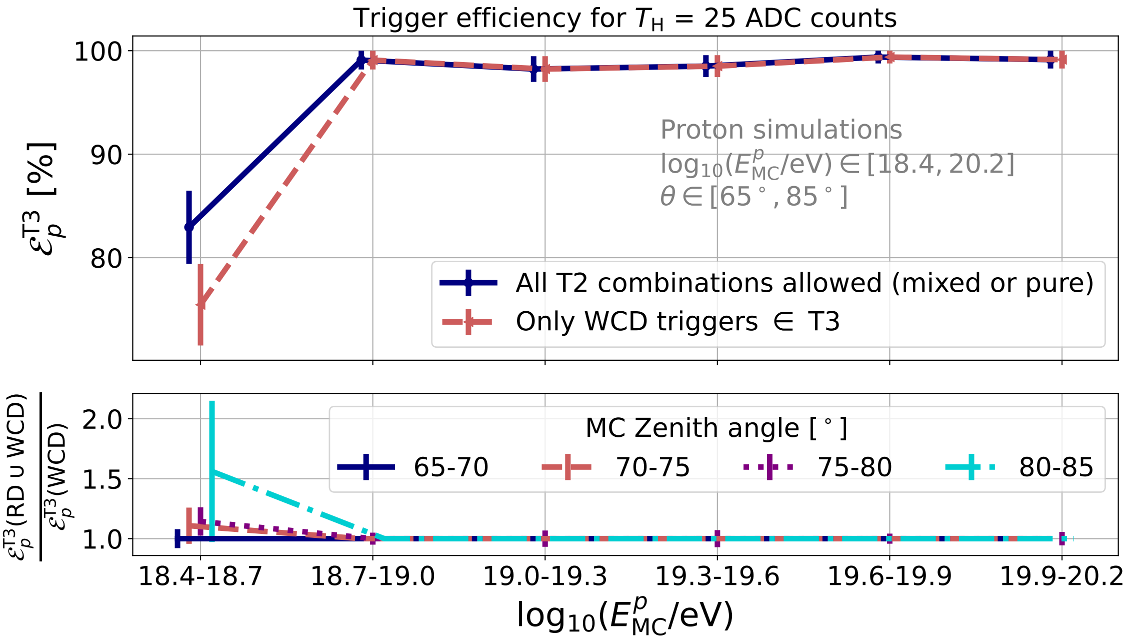

Figure 6.15: (Top) The differential trigger efficiency at different energies is shown for proton simulations. The different lines indicate the cases of only WCD triggers (red dashed) and adding RD triggers (solid blue). (Bottom) The ratio of the two cases, separated by different zenith angle ranges, marked by the different colours and line styles.

It provides a significant amount of information regarding the LDF and significantly enhances the reconstruction accuracy for RD.

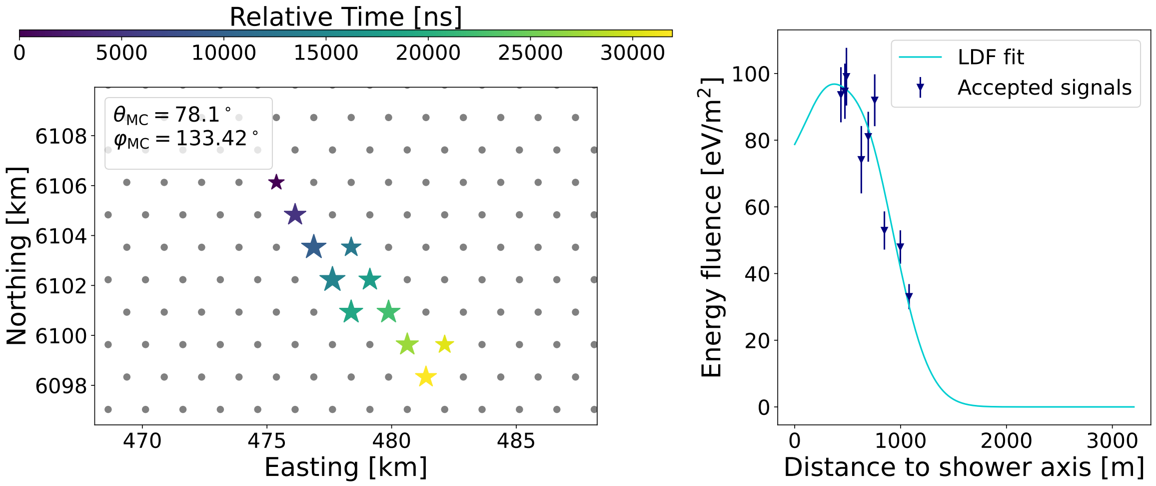

Figure 6.16: Example proton event gained by adding RD triggers without restrictions. (Left) The radio footprint of the event is shown. Grey points mark stations not triggered, coloured stars indicate triggered stations. The colour scale represents the station signal time, while the signal strength is shown by the size of the stars. (Right) The accepted signals of the same event (blue triangles) and its fitted LDF (cyan line).

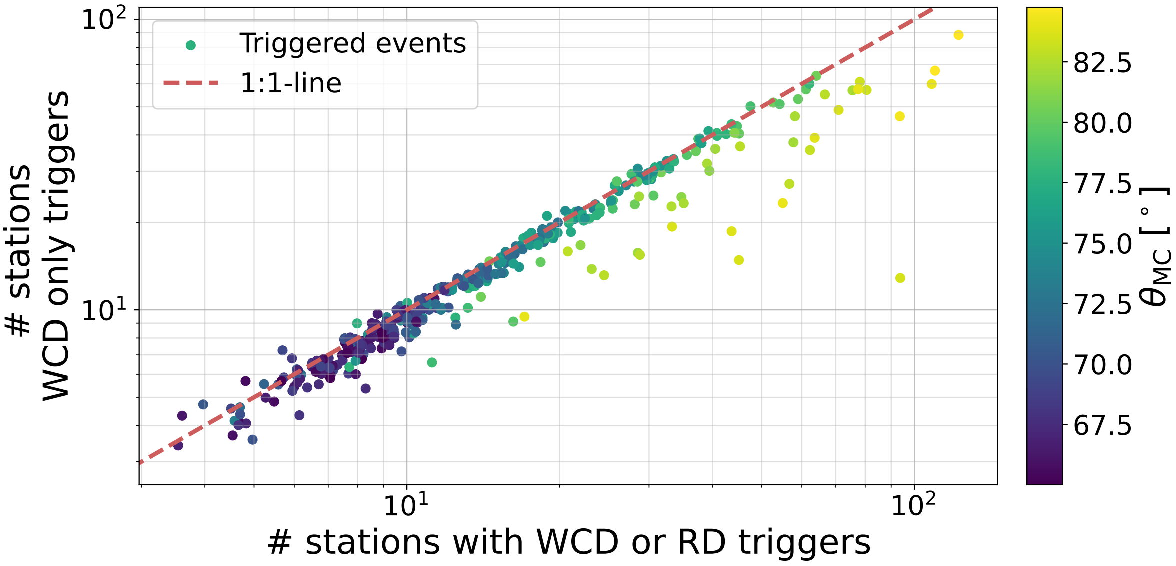

Figure 6.17: Comparison of the number of triggered stations for the case of adding RD triggers to WCD triggers (x-axis) and only WCD triggers (y-axis) for simulated events which were triggered by both trigger configurations. The colour scale indicates the zenith angle of the air shower.

CHAPTER 7

RADIO RECONSTRUCTION OF INCLINED PHOTON AIR SHOWERS

As described in Sec. 2.2, photon primaries can be door-openers for the determination of sources of UHE CRs. In addition to the detection of UHE photons, a reliable event reconstruction is required to retrace the events to interstellar objects. This predominantly includes the reconstruction of the primary composition and energy, as well as the arrival direction consisting of azimuth and zenith angles. This Chapter focuses on the three latter properties. The matter will be examined through CoREAS simulations (*c.f.* Sec. 6.1), with a fixed trigger threshold of 25 ADC counts. Furthermore, unless otherwise stated, the configuration of pure RD triggered events is used, as this is the ideal and aimed-for solution in the end.

7.1 Iterative reconstruction chain

The reconstruction chain, as described in Sec. 3.3 is adapted for photon air showers. Only with a given known arrival direction of the air shower, a precise reconstruction of all event properties is possible. While for hadron showers the arrival detection is usually provided by the analysis of the WCD data, one cannot rely on it for photons. In the preceding chapter, it was observed that there were events triggered by the RD, which were not triggered by the Auger particle detectors. Even if the particle data is read-out after an RD trigger, it is improbable that the events are accurately reconstructed with the particle data. Thus, it is necessary to employ a method that is completely independent of the particle detection.

An iterative determination of the arrival detection can satisfy this requirement. The method is illustrated in Fig. 7.1. Initially, various combinations of uniformly distributed

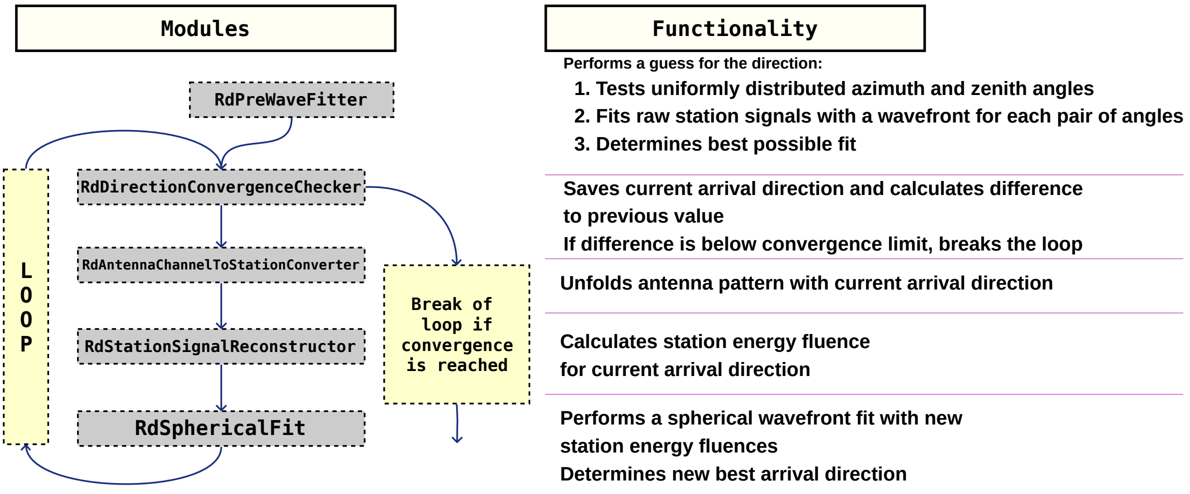

Figure 7.1: Schematic of the iterative reconstruction procedure. The modules used in Offline are shown on the left, their functionality is briefly described on the right.

azimuth and zenith angles are subjected to testing. Each pair undergoes a spherical wavefront fit with the raw station signals (in µV without an unfolded antenna pattern). The best fit is determined by the reduced chi-square and taken as starting value for a subsequent loop: The antenna pattern is unfolded with the given starting values of zenith and azimuth angles. Afterwards, the station signals (in µV/m) are reconstructed. Ultimately, a spherical wavefront fit is performed once more, resulting in novel zenith and azimuth angles. This procedure is now repeated and after each iteration, it is checked whether the estimated angles differ from the previous iteration or whether they converged. If the level of convergence falls below a predetermined threshold, the loop is terminated and the zenith and azimuth angles are taken as the ultimate values. The method was previously implemented in Offline, however, due to a lack of necessity it was no longer maintained and eventually deprecated. With the introduction of the RD trigger and the new capabilities of detecting neutral primaries, the module underwent a revision.

The iterative procedure has the ability to reconstruct photon air showers for which no WCD information is available. However, the standard reconstruction is more reliable, as the iterative reconstruction can fail to converge towards the true value. This should only happen for a minor fraction of events, which would have been reconstructed with the standard method. The benefit of the iterative procedure outweighs this, which is also depicted in Fig. 7.2. Four distinct configurations and the respective reconstruction efficiency, $\mathcal{E}_{\gamma}^{\phi,\theta}$, are considered. The most significant differences result from the activation of the RD trigger. The two cases without a present RD trigger show a $\mathcal{E}_{\gamma}^{\phi,\theta}$ of $\approx 10\,\%$. The two cases with activated RD trigger show at least a factor of 2 more recon-

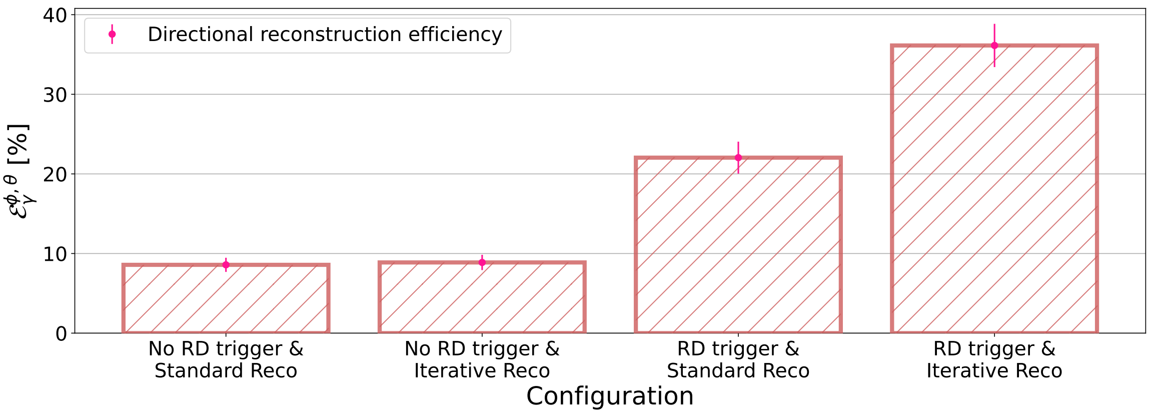

Figure 7.2: The reconstruction efficiency is shown for different configurations of Auger (No RD trigger, RD trigger) and different reconstruction methods (standard reconstruction, iterative reconstruction).

structed events. Smaller variances can be observed in the distinction between standard and iterative reconstruction. $\mathcal{E}_\gamma^{\phi,\theta}$ increases absolutely by 0.3 % (relatively 3.4 %) for the case of no RD triggers and by 14.1 % (64 %) for activated RD triggers.

The previous Chapter already showed a zenith angle dependence for the trigger efficiency (*c.f.* Fig. 6.4). The general dependence persists for the reconstruction efficiency, and the effect is even more pronounced for low zenith angles. This is depicted in Fig. 7.3, which shows $\mathcal{E}_\gamma^{\phi,\theta}$ for different zenith angles ranges and energies on the left. The right panel shows the ratio to the trigger efficiency. For $65° \leq \theta \leq 70°$, no reconstruction efficiency is observed at the low energy ranges, while $\approx 5\,\%$ and $\approx 30\,\%$ trigger efficiency was observed at the respective energies. Only for higher energies, events are reconstructed. However, it represents between $\approx 10\,\%$ and $\approx 50\,\%$ of the triggered events. Higher zenith angles of $70° \leq \theta \leq 75°$ indicate an enhanced reconstruction efficiency of $\approx 20\,\%$ at the lowest energy range. It increases linearly with logarithmic energy until it reaches almost full efficiency for $E \geq 10^{19.3}$ eV. Similar behaviour is observed in the comparison with $\mathcal{E}_\gamma^{\mathrm{T3}}$, nearly 40 % of triggered events are reconstructed. This number continues to increase until it reaches nearly 100 % for $E \geq 10^{19.3}$ eV. For $\theta \geq 75°$, $\mathcal{E}_\gamma^{\phi,\theta}$ is almost identical with $\mathcal{E}_\gamma^{\mathrm{T3}}$ and nearly all triggered events are reconstructed as well. This behaviour is expected as higher zenith angles result in more triggered stations, which generally increases the reconstruction probability. Almost full reconstruction efficiency is achieved for $E \geq 10^{18.7}$ eV.

The reconstruction probability for photons increases significantly when using the iterative method. As the detection and reconstruction of even a single photon event would be a major achievement, the method with the better efficiency should be used. Hadron

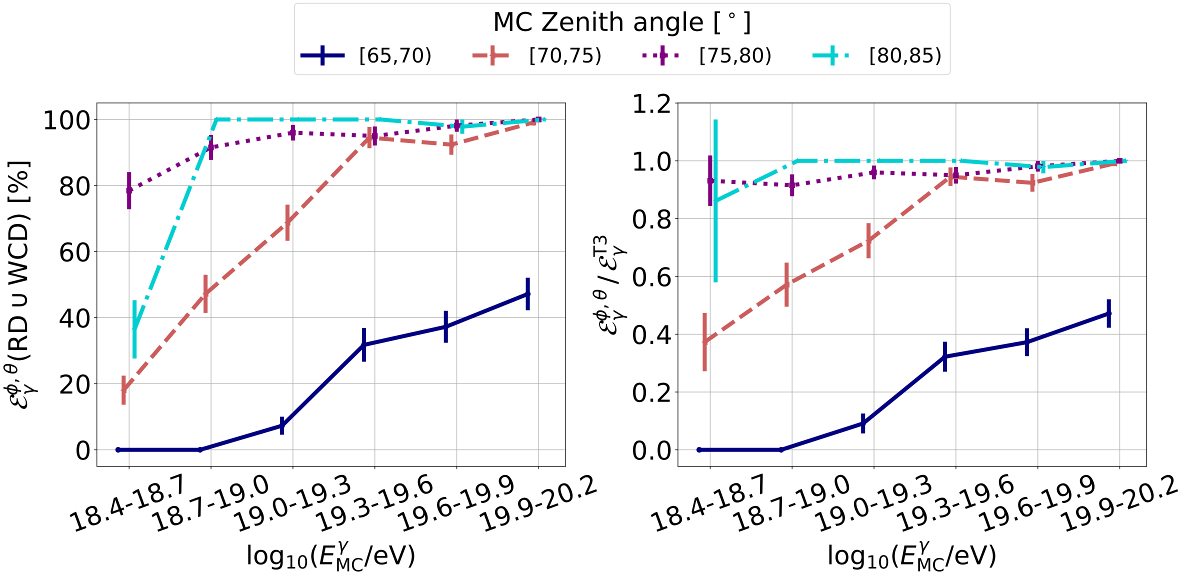

Figure 7.3: (Left) The differential reconstruction efficiency at different energies is shown. The different colours and line styles indicate different zenith angle ranges. (Right) The ratio of the reconstruction and trigger efficiency is shown. The colours and line styles are the same as before.

showers are far more frequent, and it is not necessary to reconstruct each single event to achieve a reasonable statistic. Here, the focus should be on an accurate reconstruction, which is more pronounced for the standard reconstruction, as it will be shown in the following sections.

7.2 Arrival direction reconstruction

The reconstruction accuracy can be validated for zenith and azimuth angle. The zenith angle is shown in Fig. 7.4, in which the left part shows the absolute difference of the MC and reconstructed zenith angle. It is found that the majority of events have a precise reconstruction with an average deviation of 0.04°, with only few events differing from the MC value by more than 1°, resulting in a standard deviation of 0.5°. In order to keep the plot legible, it is limited to ±2°, which suppresses ≈ 1.3 % of events. These extrema have deviations between 5° and 32° (only positive values) and do not show an obvious bias for any investigated variable. However, they have generally an increased reduced χ^2 value of the wavefront fit. The right part of the figure depicts the distributions of the absolute deviation. For neither of the binning variables, a bias is observed. The medians exhibit a deviation from the true value by less than 0.1° for all investigated cases.

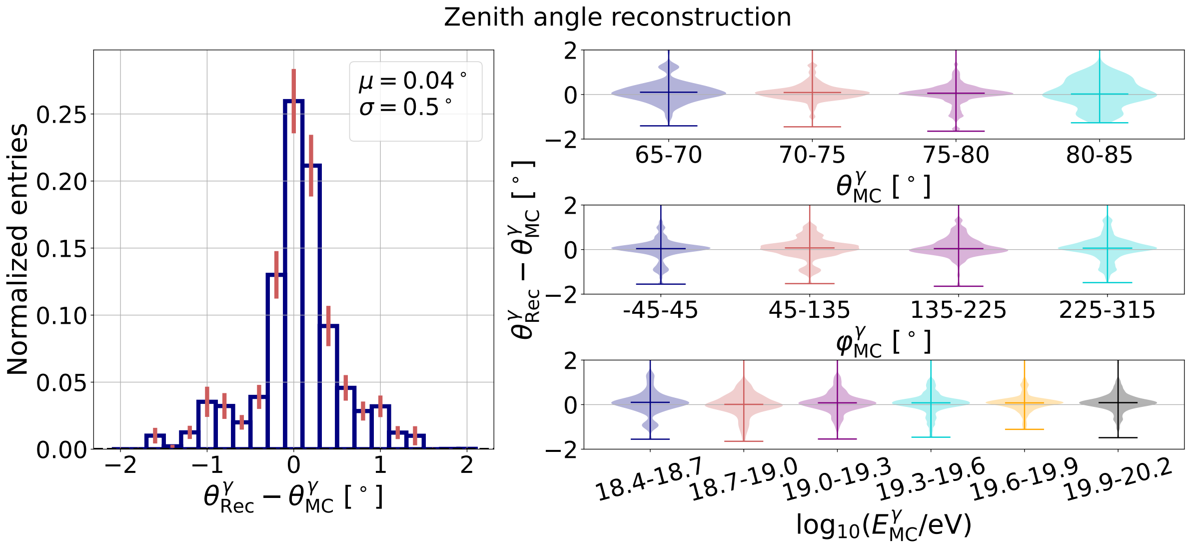

Figure 7.4: (Left) The deviation of the reconstructed from the MC zenith angle is shown as distribution. Note that the limits of the x-axis suppress events (*c.f.* text). (Right) The distribution binned by MC zenith angle (top), MC azimuth angle (middle) and MC energy (bottom). The colours indicate different bins, the horizontal lines indicate the maximum, median and minimum value.

Small artefacts in the distributions are observed, which represent themselves as bumps distant from the main peak. They are likely related to limited statistics. All distributions exhibit a similar behaviour, with the exception of the highest zenith angle bin, where the distribution is significantly wider than the others. This is indicated by the standard deviation of the distribution, which is shown in Fig. 7.5. It presents a comparison of the bias and standard deviation for both the standard and iterative reconstructions. The bias is nearly constant for all zenith angle ranges for the iterative reconstruction, whereas it increases for the standard reconstruction from -0.17° at low zenith angles to 0.06° at the highest zenith angles. The only trivial explanation considered for these two different behaviours is the core displacement of the radio and particle footprint, as the standard reconstruction takes the WCD core, whereas the iterative reconstruction uses the radio barycentre. This could result in different features, as the core displacement is zenith angle dependent [128]. Different behaviours for the two reconstruction methods are also observed for the standard deviation. The standard reconstruction yields a decreasing standard deviation with an increasing zenith angle. It is expected that more triggered stations at higher zenith angles will result in a higher reconstruction precision. Contrary, the iterative reconstruction results in an almost constant standard deviation of $\approx 0.5^\circ$ for $\theta \leq 80^\circ$ and an increased value of more than 0.6° for higher zenith angles. It appears that the iterative reconstruction has poorer

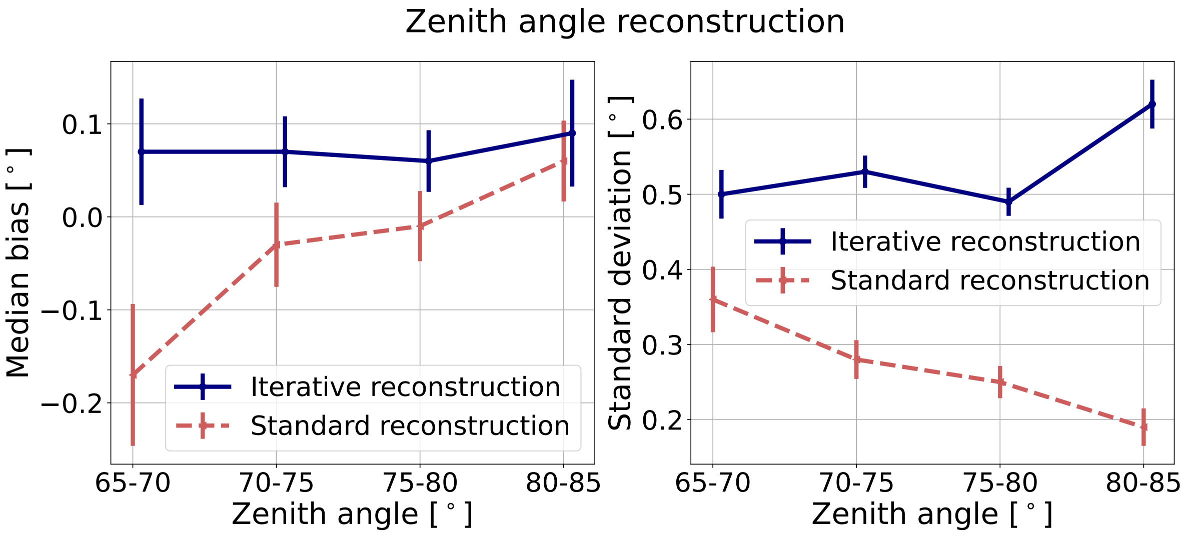

Figure 7.5: (Left) The median as estimator for the bias of the zenith angle reconstruction is shown as a function of the zenith angle. The solid blue line represents the iterative reconstruction, while the dashed red line shows the standard reconstruction. (Right) Same as (left) but for the standard deviation.

precision for high zenith angles. At these angles, it is possible that the method will encounter local minima in the fitting procedure and converge, even though it is not the global minimum. With a predefined value from the WCD, it avoids running into local minima but starts close enough to the global minimum. This would be supported by the number of stations included: more stations involved also result in more local minima.

The exercise is repeated for the azimuth angle reconstruction. Figure 7.6 shows the comparison between the reconstructed and MC azimuth angle and its distributions. The scatter plot is again cut at ±2°, 1.1 % of events are suppressed by the axis limits. They exhibit no discernible bias towards the variables discussed. The distributions of the deviations on the right exhibit no concerning characteristics, with the strongest dependence observed for the zenith angle. Low zenith angles result in a more spread distribution, whereas high zenith angles result in a narrow distribution as one has more signal stations.

The zenith angle dependence of the azimuth angle reconstruction is further investigated with the bias and standard deviation shown in Fig. 7.7. The bias is almost non-existent, with all data points, with the exception of one, being consistent with zero. No significant difference is observed for the two reconstruction methods. The standard deviation indicates an improvement for the iterative method for higher zenith angles, with 0.5° for $65° \leq \theta \leq 70°$ and 0.2° for $\theta \geq 75°$. The iterative method indicates an improvement of the standard deviation with increasing zenith angles and is at the same

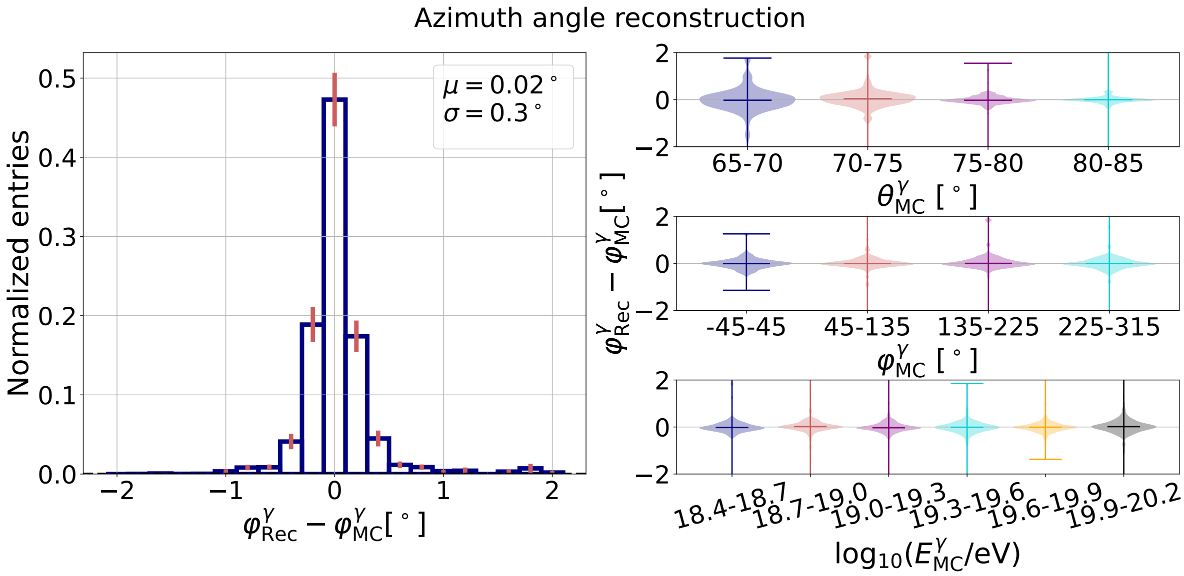

Figure 7.6: (Left) The deviation of the reconstructed from the MC azimuth angle is shown as distribution. Note that the limits of the x-axis suppress events (*c.f.* text). (Right) The distributions of the deviation from (left), binned by MC zenith angle (top), MC azimuth angle (middle) and MC energy (bottom). The colours indicate different bins, the horizontal lines indicate the maximum, median and minimum value.

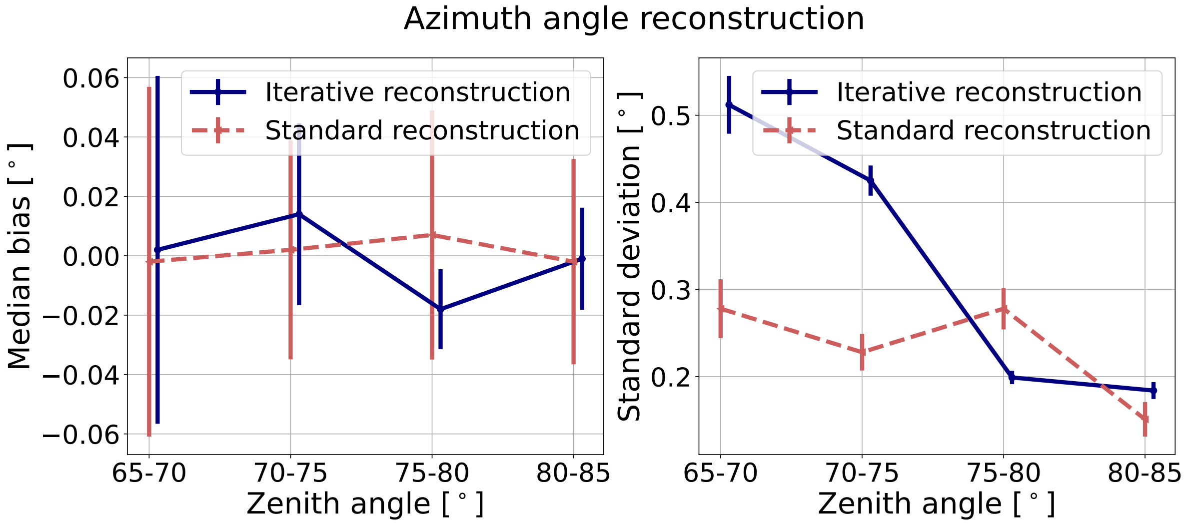

Figure 7.7: (Left) The median as estimator for the bias of the azimuth angle reconstruction is shown as a function of the zenith angle. The solid blue line represents the iterative reconstruction, while the dashed red line shows the standard reconstruction. (Right) Same as (left) but for the standard deviation.

level as the standard reconstruction at the highest zenith angles. It is expected that the reconstruction will improve with higher zenith angles due to larger time differences between stations. It mitigates the influence of timing uncertainties.

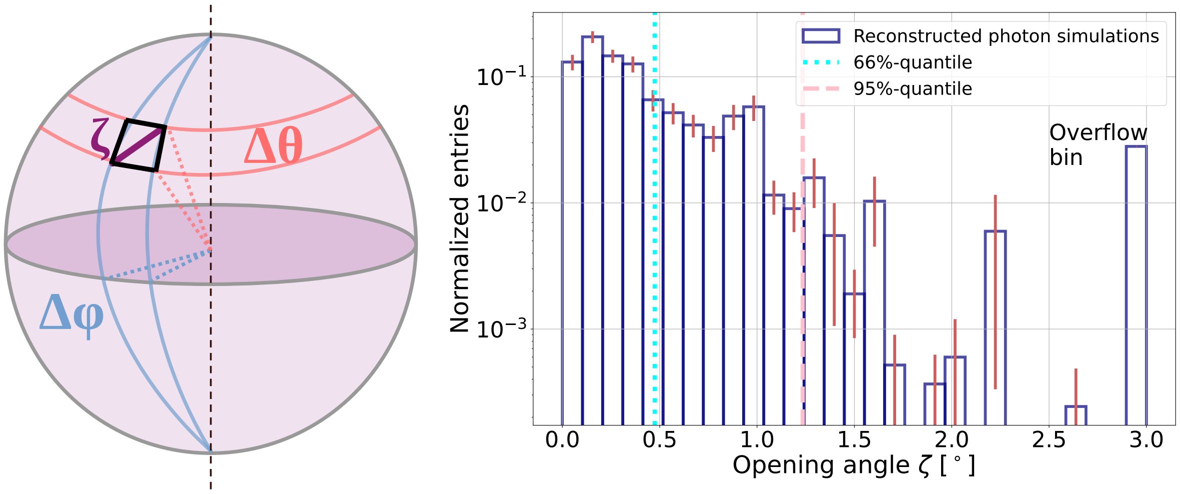

Figure 7.8: (Left) Illustration of the opening angle and its calculation. (Right) Distribution of the calculated opening angles. The bright blue and pink lines mark the 1σ and 2σ quantiles. Opening angles with values larger than 3° are summarised in the most rightish bin.

It is observed that the azimuth angle reconstruction exhibits a smaller spread and bias compared to the zenith angle reconstruction. This is an anticipated result, the reconstruction of the azimuth angle is generally more precise for a flat detector plane and inclined showers. The azimuth angle is in the plane of observers, and the timing of stations is directly correlated to the arrival direction.

Deviations in the reconstruction of zenith and azimuth angle can be combined into the opening angle, ζ, which is illustrated in Fig. 7.8 (left). For small zenith and azimuth angle deviations, a right angle is assumed, and the opening angle can be determined via:

$$\zeta = \sqrt{\Delta\theta^2 + \Delta\varphi^2}. \tag{7.1}$$

ζ is calculated for all reconstructed events and the result is shown in Fig. 7.8 (right). It is observed that 66 % of events are within $\zeta \leq 0.5°$ and 95 % within $\zeta \leq 1.25°$. Only few events have large opening angles, and thus, source determinations would likely be possible in most cases. These values are similar to the accuracy of the WCDs for inclined showers, with an accuracy slightly better than 0.5° [129]. A comparison can also be done with other neutral particle observatories. Imaging Cherenkov telescopes (such as HESS, MAGIC, VERITAS) state a resolution for low-energy gammas of about 0.1° [130]. IceCube shows neutrino correlations to astronomical sources with angular separations comparable to the shown distribution [131, 132].

Table 7.1: Applied cuts and their efficiency

Cut	Eff. after single cut [%]	Eff. after all cuts [%]
Triggered	60.9	60.9
Succ. reconstruction	41.7	41.7
≥ 1 station within 1 r_{ch}	34.4	33.7
Energy fit $\chi^2/ndf \leq 30$	36.9	31.9
Energy fit $\chi^2/ndf \leq 10$ (MC only)	33.4	30.2
$\Delta\theta, \Delta\varphi \leq 0.5°$ (MC only)	32.4	22.6
$E^{\mathrm{EM}}_{\mathrm{MC}} \geq 10\,\mathrm{EeV}$ (MC only)	18.9	8.4

7.3 Energy reconstruction

The radio reconstruction of the EM energy, E^{EM}, is dependent on an accurate shower geometry reconstruction, as discussed in Sec. 3.3.2. It is also shown above that the majority of events have an accurate arrival direction estimation. Nonetheless, features in photon simulations are observed, which show a biased E^{EM} reconstruction. Such events will be discussed in the following, furthermore, a modification of the reconstruction is presented.

7.3.1 Observed bias for the reconstruction of the EM energy of photons

In order to validate and improve the reconstruction, different quality cuts are applied. The cuts are shown in Tab. 7.1 and can be separated in MC cuts and data cuts. The MC cuts are strict in order to achieve a high-quality data set. The MC data set is used to train and validate methods. Data cuts could also be applied to real data, and they determine the accuracy of the final results.

The radio reconstruction for inclined air showers employed by Auger from [93] was developed for hadron air showers. The method yields precise and accurate outcomes for hadrons with small spread and minimal bias. However, this small bias becomes more important for photon induced air showers. The effects of the bias can be seen in Fig. 7.9. On the left, the relative deviation of MC to reconstructed E^{EM} is shown as distribution. The relative deviation is estimated via

$$\text{Relative deviation} = 2 \cdot \frac{E^{\mathrm{EM}}_{\mathrm{Rec}} - E^{\mathrm{EM}}_{\mathrm{MC}}}{E^{\mathrm{EM}}_{\mathrm{Rec}} + E^{\mathrm{EM}}_{\mathrm{MC}}}, \tag{7.2}$$

which regards asymmetries of distributions. A significant asymmetry is observed with a tendency to an underestimation of E^{EM} with a mean of -2.7 % and a skewness (the

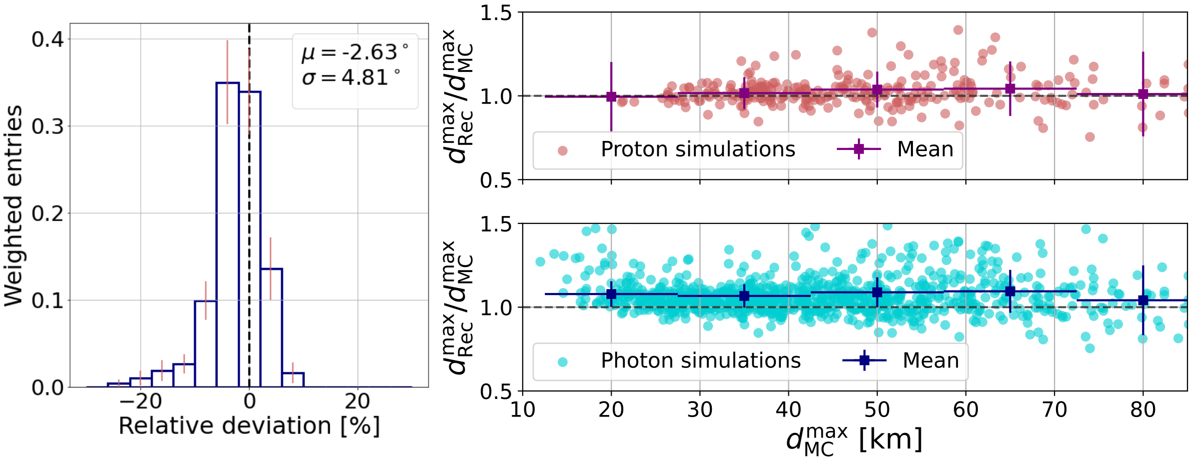

Figure 7.9: (Left) The biased, asymmetric distribution of the relative deviations of reconstructed and MC E^{EM} is shown. The red error bars represent statistical uncertainties. The black line marks the point of no bias. Above described MC quality cuts are used. (Right) Ratio of the reconstructed and MC $d^{\max}$ to shower maximum as a function of the MC distance. Shown are protons (top, red) and photons (bottom, blue). The binned mean and the uncertainty of the estimator as squares shows a consistency with 1 for protons and a bias towards higher ratios for photons. Plots are limited on the x-axis to regions with a reasonable statistic. Above described data quality cuts are used.

third central moment) of -1.27. Moreover, $\approx 5\,\%$ of the events are observed with less than -15 % deviation and also single events with down to -30 % deviation. On the other hand, positive deviations are only observed up to a bit over 10 %.

A bias can also be seen for the geometrical distance of the shower maximum, $d^{\max}$, as shown in Fig. 7.9 (right). The graph shows the ratio of the reconstructed to the MC $d^{\max}$ as a function of the MC $d^{\max}$ for photon and proton simulations. The mean value of the ratio is calculated for bins each 15 km wide. In photon simulations, it is observed that the reconstructed distance is overestimated. The factor of overestimations is almost constant ≈ 1.1 for all distances. Comparatively, proton simulations with the same input parameters do not show this overestimation. Hence, the observed bias arises from physical properties of photon induced air showers. It also demonstrates that the E^{EM} bias already arises from the parametrisation of the shape parameters of the LDF via $d^{\max}$. The parametrisation is often not suited for photon induced showers, as their $d^{\max}$ is beyond the parametrised range. This bias propagates to the E^{EM} calculation.

As discussed, the LDF shape parameters are not fitted directly but parametrised by the fitted distance. One example of the parametrisation is shown in Fig. 7.10 (left). r_{02} (*c.f.* eq. 3.2) is depicted as a function of $d^{\max}$. Single points represent individual events, while blobs represent distinct simulated zenith angles. Red markers depict the mean of each zenith angle, and the green line shows the parametrisation function. A spread

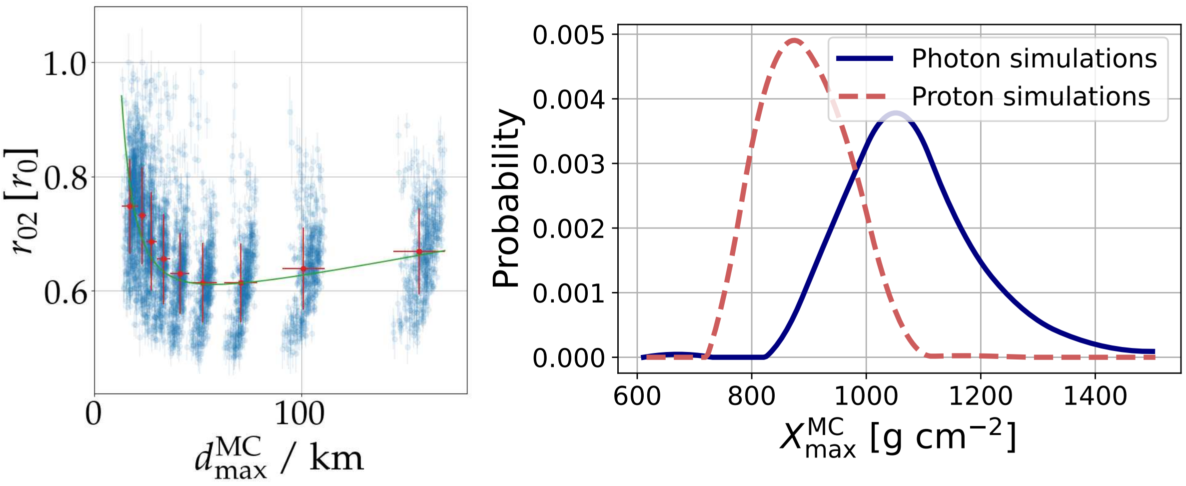

Figure 7.10: (Left) Parametrisation of the shape parameter r_{02} as a function of d^{max} as used in the Auger standard reconstruction. Blue points mark single simulations, the blobs represent distinct zenith angles. The red markers yield the mean of each zenith angle. The green line shows the fitted parametrisation. Plot from [93]. (Right) Distributions of the shower maximum depth for photons (solid blue) and protons (dashed red).

along the axis of r_{02} at the distinct zenith angles arises from a changing X_{max} (higher r_{02} indicate a higher X_{max}). The parametrisation function describes the mean of the zenith angles well, but fails to accurately describe extreme values of X_{max} for hadrons. A bias is observed, which is marginal for the E^{EM} reconstruction for hadrons (*c.f.* Fig. 6.11 in [87]). However, the bias increases for photon air showers which exhibit larger values of X_{max}. Figure 7.10 (right) depicts the normalised distributions of X_{max} for simulated photon and proton air showers. Proton air showers have their shower maximum most probable at $\langle X_{\mathrm{max}}^{p} \rangle \approx 850\,\mathrm{g\,cm^{-2}}$ with the positive tail of the distribution reaching $\approx 1{,}100\,\mathrm{g\,cm^{-2}}$. This is only $\approx 50\,\mathrm{g\,cm^{-2}}$ shallower than the typical maximum for photon air showers at $\langle X_{\mathrm{max}}^{\gamma} \rangle \approx 1{,}050\,\mathrm{g\,cm^{-2}}$. Only a small proportion of photon events exhibit a shower maximum near $\langle X_{\mathrm{max}}^{p} \rangle$ and $\approx 0.5\,\%$ of photon showers have a maximum below $\langle X_{\mathrm{max}}^{p} \rangle$. Thus, the bias observed, changes from an exception for hadron showers to the most probable case for photon showers.

The observed feature leads to the depicted bias in Fig. 7.11. The relative deviation of the reconstructed E^{EM} is shown as a function of X_{max} for photon air showers. An eye-guidance (orange line, not a fit) depicts the general trend of an increasing underestimation of energy for increased X_{max}. For the low values of X_{max}, an agreement with zero in relative deviation is observed. However, for the deeper showers, an underestimation of E^{EM} of $\approx 10\,\%$ is obtained. The aforementioned bias manifests itself in a correlation with the air density at X_{max}, as indicated by the colour scale. Low densities are prone

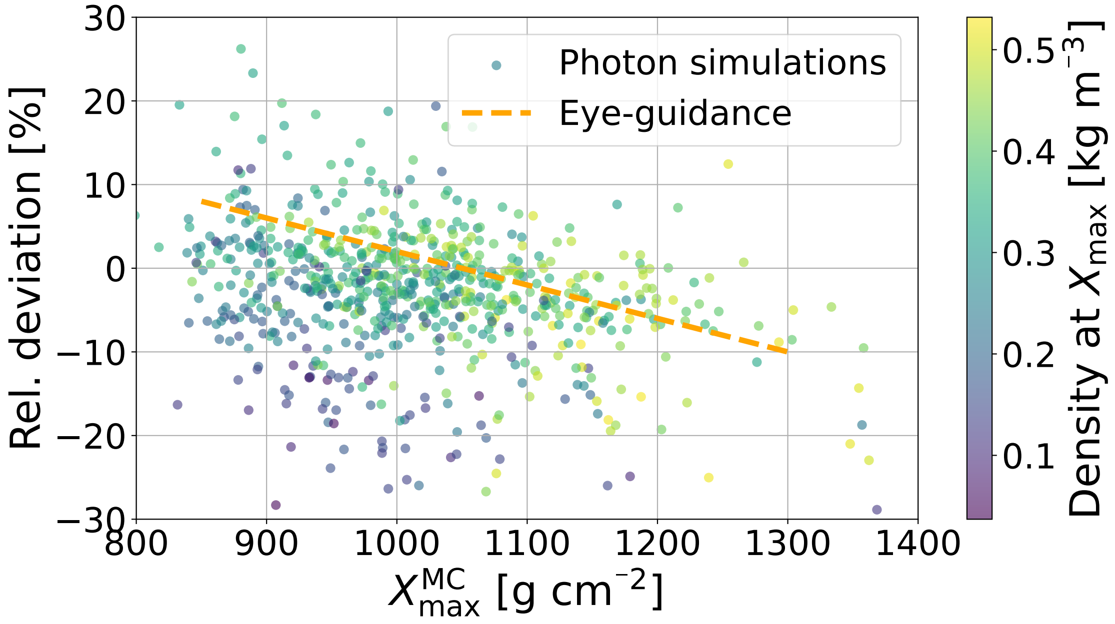

Figure 7.11: Shown is the relative deviation of reconstructed and MC E^{EM} against X_{max}. The colour scale indicates the air density at shower maximum, which also shows a bias (vertical trend). The orange line is not a fit but an eye-guidance for the reader. The above described MC quality cuts are used.

to underestimate E^{EM} in comparison to events with high densities at the same X_{max}. This gradient yields variations in the relative deviation in the order of 5-10 %.

The observed bias results in a shift of the entire photon distribution towards an underestimation of energy, which may pose a challenge in the identification of photons. The reconstructed energy could evolve to a significant parameter in discrimination studies (*c.f.* Sec. 7.4). Particularly, showers with their maximum depth deep in the atmosphere are of great interest, as they will be more distinct from typical hadron showers. Moreover, the energy will hold significant importance in comprehending the source and propagation of photons. Therefore, it is important to discuss ways to correct the bias.

7.3.2 Discussion of a parametrisation correction

There exist multiple approaches to resolve the bias. One possibility was already suggested in [93], Appendix **C**. Introducing a correction factor, d_{750}, for the shape parameter a_{rel} or r_{02}, based on a difference between observer and fixed shower maximum of $750\,\mathrm{g\,cm^{-2}}$ could reduce a dependence on X_{max}. However, it was found that this does not improve the overall performance for hadrons and could introduce new artefacts. The impact on photon showers is unclear. The new parameterisation of the shape parameters is a topic itself and extensive studies have to be performed. Since no viable solution is currently available, two different approaches are presented to ensure an unbiased energy reconstruction. First, a calibration in the calculation from S_{rad} to E^{EM} is discussed. Afterwards, a proof of concept for completely removing the parametrisation is shown.

The proposed ansatz in [93] would require that the implemented method in $\overline{\text{Off}}\underline{\text{line}}$ would need to be changed. The shape parameterisation must be adjusted, which could also influence the outcome for hadrons. However, if a photon (candidate) were to be detected, it would in any case be treated differently and reconstructed carefully with an independent photon analysis. This could be implemented in $\overline{\text{Off}}\underline{\text{line}}$ with a foreseen limited use-case, or one could use the parametrisation and resulting output from $\overline{\text{Off}}\underline{\text{line}}$ and adapt it. The analysis chain remains unchanged until the estimated radiation energy is converted into a corrected E^{EM}. This conversion is normally performed via the power-law fit with the estimated parameters for hadrons. For photons, this parametrisation is repeated, and $E^{\text{EM}}_{\text{MC}}$ is fitted with S_{rad} using the photon simulations with applied MC cuts. Hence, the analyses are only modified in the last step with adapted power-law variables.

The procedure results in changed fitting parameters, which describe events with a high X_{max} better and nearly bias-free. The parameters are shown in Tab. 7.2, the corresponding fit can be found in Appendix C. They are used to calculate E^{EM} of photon simulations using the aforementioned relaxed data cuts. The results are depicted in Fig. 7.12, which shows the distributions of the relative deviation of E^{EM}. It demonstrates that even with relaxed quality cuts, it exhibits superior performance for photon simulations compared to the hadron parametrisation. The mean of the distribution is at $0.5\,\%$ with a standard deviation of $\approx 9.8\,\%$. Using the MC cuts, it shows a standard deviation of $4.2\,\%$, which is comparable to the stated value $\leq 5\,\%$ from [87] with similar cuts. The distribution appears symmetric with no clear bias. The skewness is much more reduced than before, with a value of -0.66. No bias is detected in the distributions binned by zenith angle, azimuth angle, and energy. The average for all distributions is close to zero, only the distribution spread increases for higher zenith angles.

It should be demonstrated that the modified parametrisation reduces the bias against the shower depth. Figure 7.13 (left) illustrates the relative deviation as a function of X_{max}. The slope previously observed (*c.f.* Fig. 7.11) is eliminated, only fluctuations are seen but no significant bias of X_{max}. The colour scale depicts the air density at X_{max}, which indicates a minimal bias against the air density at X_{max}. Nevertheless, it appears to be significantly smaller than it was before.

Table 7.2: Comparison of the parameters used in Eq. 3.3 for protons from [93] and photons

Fitting parameter	S_{19} [GeV]	γ	p_0	p_1 [$\mathrm{kg\,m^{-3}}$]
Hadron parametrisation (regular X_{max})	3.1461	1.9997	0.5045	-2.7083
Photon parametrisation (high X_{max})	3.143±0.039	1.956±0.009	2.29±0.38	-0.54±0.10

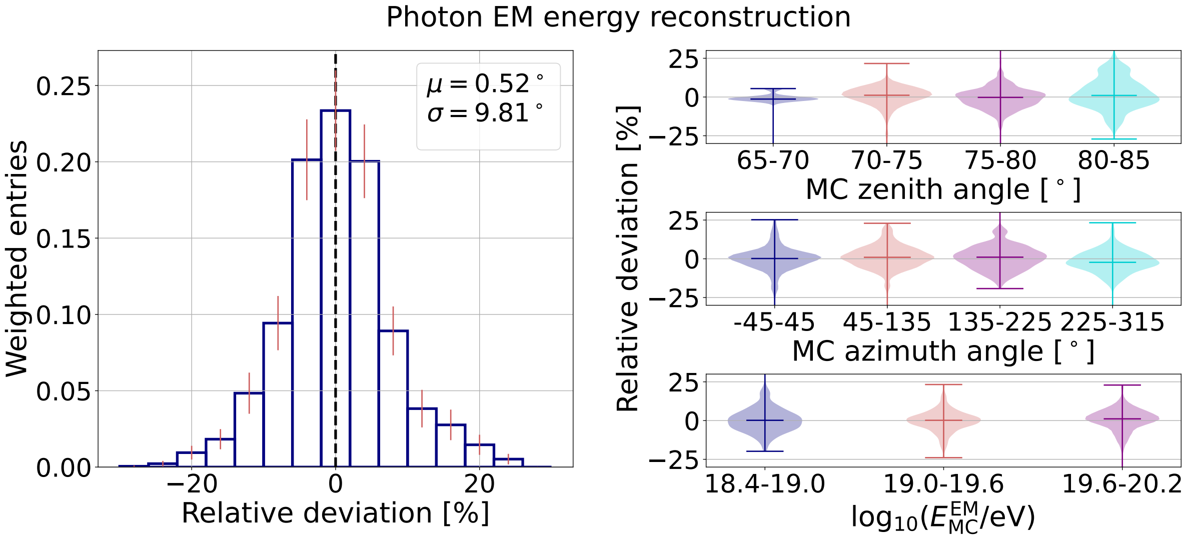

Figure 7.12: (Left) The distribution of the relative deviations of reconstructed and MC E^{EM} is shown with the photon parametrisation of Tab. 7.2. The red error bars represent statistical uncertainties. The black line marks 0. (Right) Distribution as (left) only binned by MC zenith angle (top), MC azimuth angle (middle) and MC E^{EM} (bottom). The colours indicate different bins, the horizontal lines indicate the maximum, median and minimum value. Above described data quality cuts are used.

Events with large (±) relative deviations do not correlate with X_{max} any more. Their deviations rather arise from inaccurate arrival direction reconstructions. Particularly, deviations from the zenith angle reconstruction propagate to the E^{EM} reconstruction. This can be observed in Fig. 7.13 (right). It describes the relative deviation of the E^{EM} reconstruction depending on the zenith angle and deviation of the zenith angle reconstruction. The most significant feature is observed for zenith angles $\geq 75°$. Underestimations in the reconstruction of the zenith angle lead to overestimations of E^{EM}. Inversely, overestimation of the zenith angle leads to underestimation of E^{EM}. Only singular events are observed to exhibit the opposite behaviour. Relative deviations (±) $\geq 15\,\%$ are usually seen for events with zenith angle misreconstructions of more than $0.5°$. If only minor zenith angle deviations are observed, then the E^{EM} reconstruc-

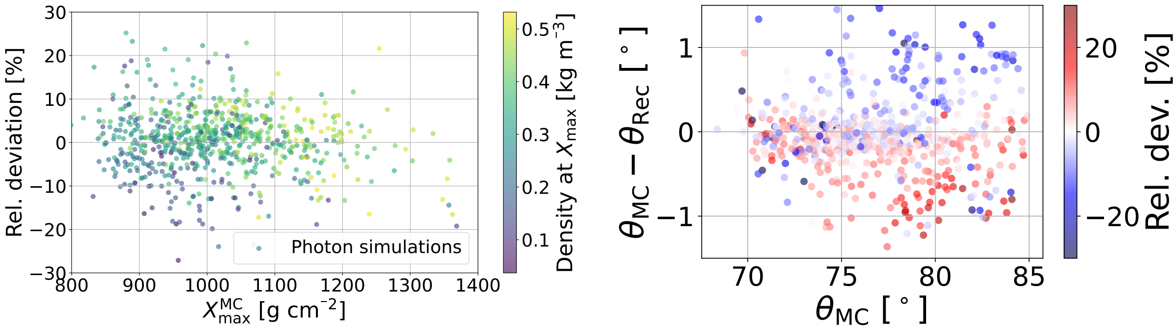

Figure 7.13: (Left) Shown is the relative deviation of reconstructed and MC E^{EM} for different X_{max} with no observable bias. The colour scale indicates the air density at shower maximum, which shows a minimal bias (vertical trend). Above described data quality cuts are used. (Right) Relative deviation of the reconstructed and MC E^{EM} as function of zenith angle and absolute deviation of reconstructed and MC zenith angle. Blue colour represents an underestimation of the reconstructed E^{EM}, red colour indicates an overestimation. Above described data quality cuts are used.

tion is mostly accurate. The influence of zenith angle misreconstructions diminishes for zenith angles $\leq 75°$, the behaviour is more diffuse and no clear dependence is observed. Large relative deviations (±) are also observed in this context for precise zenith angle reconstructions.

The aforementioned characterisation can be observed for the zenith angle, but not for the azimuth. The effect of small misreconstructions of the azimuth angle on the E^{EM} reconstruction is negligible. This is expected given the method of the E^{EM} reconstruction. It arises from the estimated distance to shower maximum, which has an obvious zenith angle dependence but no azimuth angle dependence. Deviations in the azimuth angle reconstructions are solely attributed to the computation of the geomagnetic angle, which constitutes a negligible contribution.

The aforementioned method relies on the knowledge that the air shower is photon-induced. However, the (EM) energy itself could already be an important discrimination variable. Thus, an alternative method should be discussed, which does not depend on the primary type. As the parametrisation is the flawed part for deep showers, it is natural removing the parametrisation. Instead, the shape of the LDF is fitted directly via Formula 3.2. It is evident that such fit can only be performed when there are enough stations. Depending on whether $p(r)$, the core coordinates and distance to X_{max} are fixed in the fit, 6-10 signal stations are needed. Here, all parameters will be fixed.

The following calculation should serve as a proof of concept. Neither is a suitable simulation set available, nor is it the scope of this work, to have a quantitive evaluation of improving the energy reconstruction of air showers. Hence, only one example with extreme values is shown. Moreover, no uncertainty estimation is performed as there are numerous uncertainties in the used atmospheric models, parametrisations, and fits. Again, a full analysis of the uncertainties would be beyond the scope of this example and work.

For a proof of concept, a very deep air shower was selected ($X_{\max} = 1362\,\mathrm{g\,cm^{-2}}$, $E_{\mathrm{MC}}^{\mathrm{EM}} = 49\,\mathrm{EeV}$, $\theta_{\mathrm{MC}} = 74.2°$), which shows an accurate arrival direction estimation but a significant underestimation of E^{EM} of $\approx -23\,\%$ when using the standard parametrisation. The underestimation arises from a bad fit of the LDF to the simulated station signal, which emerges from the parametrisation. The standard LDF is shown in Fig. 7.14, together with a direct shape fit of the LDF. It demonstrates that the modified LDF with multiple free parameters can describe the signals, while the parametrisation fails to do so.

In order to estimate E^{EM}, the modified LDF is integrated[1] in order to get the geomagnetic radiation energy:

$$E_{\mathrm{geo}} = 2\pi \int_0^{5r_0^{\mathrm{fit}}} f_{\mathrm{geo}}(r) \cdot r \;\mathrm{d}r. \tag{7.3}$$

Using E_{geo}, E^{EM} can be calculated directly via the Formulas 3.3 and 3.4. The only parameter unknown is $\langle\rho\rangle$, the density at $X_{\max}$. $\langle\rho\rangle$ can be calculated with a suitable atmospheric model and the geometrical height of $X_{\max}$, which is on the other hand estimated by the zenith angle and $d^{\max}$. The latter is more difficult to calculate, as it was fixed in the fit. But it can actually be calculated by inverting the previously abolished parametrisation. What seems contradictory at first, makes sense as now one parameter ($d^{\max}$) does not describe 6 parameters (the shape parameters), but one can choose out of 6 parameters to accurately describe $d^{\max}$. It was observed in [93] (*c.f.* Fig. 16) that the parametrisation performs differently well for the distinct parameters. r_0^{fit} appears as one of the parameters with the least impact of $X_{\max}$ and also the parameter with the most physical meaning (as estimator for r_{Ch}). Hence, the relation of r_0^{fit} and $d^{\max}$ is inverted and following $\langle\rho\rangle$ is estimated using the atmospheric model also used for the CoREAS simulation. Finally, E^{EM} is calculated to be $E_{\mathrm{MC}}^{\mathrm{EM}} \approx 47.9\,\mathrm{EeV}$. This yields a new relative deviation of -2.3 % and demonstrates that an accurate E^{EM} reconstruction is possible for deep showers as well. Moreover, it shows potential to improve the overall energy reconstruction for non-deep showers as well, as long enough stations are available.

---

[1] The additional factors of 2π and r arise from the integration over the 2-dimensional radio footprint. The integration limit of $5r_0^{\mathrm{fit}}$ is selected for an efficient numerical integration without losing a significant amount of signal.

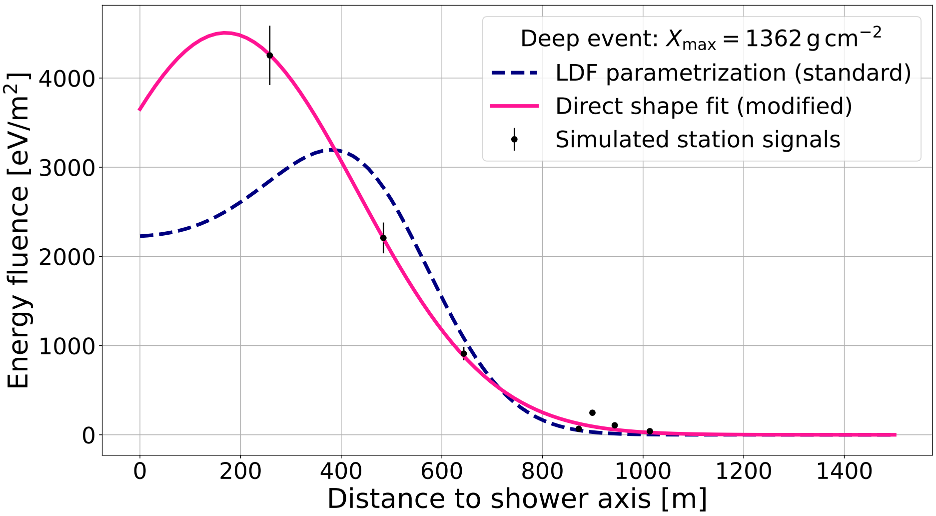

Figure 7.14: Comparison of the fits for the standard LDF parametrisation (blue dashed line) and for the direct shape fit (magenta solid line) to the simulated station signals (black points) of one deep shower.

7.3.3 Estimation of the photon energy

The primary energy can be estimated from E^{EM}, which is almost identical for photon induced air showers. The distribution of the E^{EM} fraction defined as

$$k^{\mathrm{EM}} = \frac{E^{\mathrm{EM}}}{E^{\mathrm{primary}}} \tag{7.4}$$

and its cumulative are depicted in Fig. 7.15 for photons and protons. The distributions differ significantly, with the proton k^{EM} ranging from 0.84 to 0.96. The majority of events are found between a k^{EM} of 0.86 and 0.92, being almost uniformly distributed. Photons exhibit a distinct behaviour, with almost all energy directed towards the EM component. Only $\approx 10\,\%$ of events have a k^{EM} less than 0.98. On the other hand, $90\,\%$ of events have a k^{EM} between 0.98 and 0.99. No event with a higher k^{EM} is found.

Since the distribution of the E^{EM} fraction is quite sharp, the conversion from EM to primary energy is straightforward in comparison to that of hadrons. Under the assumption that photons can be identified, the conversion from EM to primary energy can be approximated by a constant factor, c_E, which is valid for almost all events within $1\,\%$ of uncertainty. The estimation of the conversion factor is derived from the inverse median value of the photon distribution, resulting in a value of

$$c_E = 1.014 \pm 0.001. \tag{7.5}$$

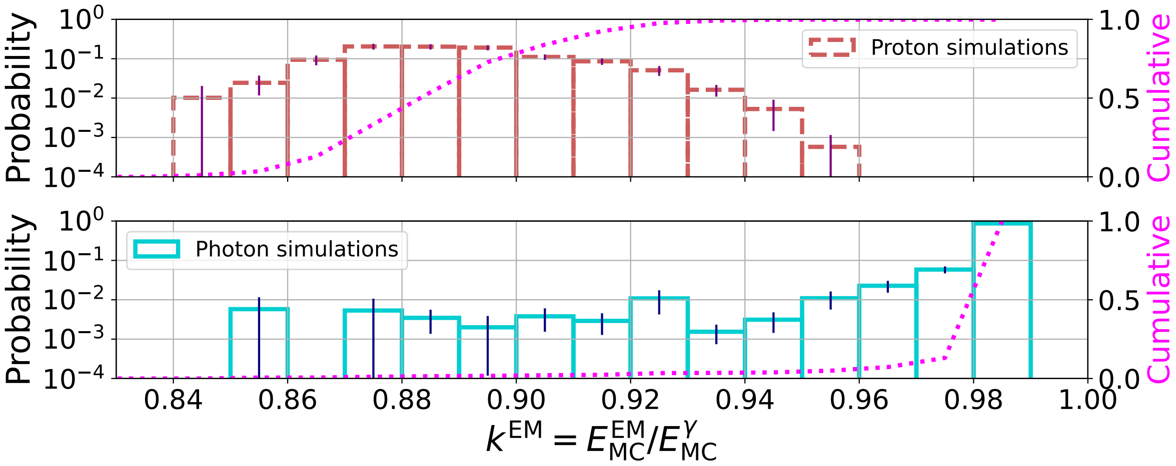

Figure 7.15: Shown is k^{EM} in air showers for protons (top, red) and photons (bottom, blue). The distributions are shown on the left, logarithmic y-axis. The cumulative, normalised distribution (pink line) is shown on the right, linear axis.

This conversion factor will be used in the following for the estimation of the photon energy.

7.3.4 Comparison to the WCD energy estimation

The radio energy reconstruction yields outcomes that exhibit high resolution and high precision. This is also true for WCD reconstructions of hadrons [133]. For inclined photon showers, however, the EM particles are absorbed, and the whole WCD reconstruction is done with few detected muons. It is evident that fewer particles result in larger uncertainties in signal and energy estimation. Although biases can be eliminated, the accuracy of the energy reconstruction is significantly impacted.

A comparison between the WCD and RD reconstruction is depicted in Fig. 7.16 for $\theta \in [65°, 85°]$. It illustrates the reconstructed photon energy of both detectors as a function of their true value. Each simulated event is therefore shown twice (and only if both reconstructions are available), once for the WCD and once for the RD reconstruction. The colour scales indicate the k^{EM}. The two reconstructions have quite distinct features: the RD reconstruction shows a precise and accurate result, with nearly all events close to the 1:1-line and low spread around the line. On the contrary, the WCD reconstruction yields imprecise and inaccurate outcomes. Nearly no events are located near the identity line, and the points themselves exhibit a substantial spread. Only for events with an unusually low k^{EM} (≤ 0.93, attributed to photonuclear interactions), an improvement is observed, resulting in a more favourable correlation with the MC value.

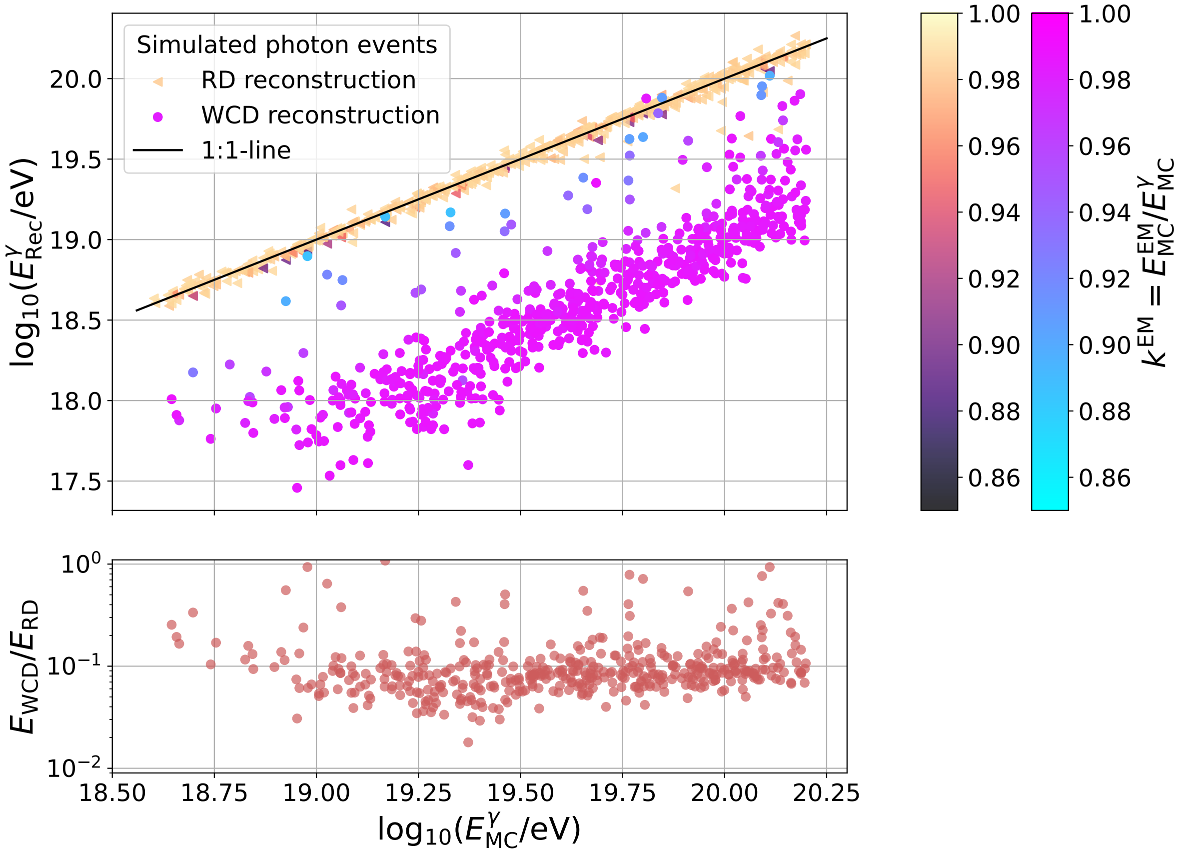

Figure 7.16: The reconstructed energy for photon induced showers at zenith angles $\theta \in [65°, 85°]$ is shown as a function of their MC energy. Each simulated event is depicted twice, once for the RD reconstruction (triangles) and once for the WCD reconstruction (circles). The colour scales illustrate both the fraction of E^{EM} in the air shower, but for a clearer view, the left one is used for the RD reconstructions while the right one describes the WCD reconstructions. The black line shows the 1:1-line. The bottom part shows the ratio of reconstructed energy of the WCD to the RD again for their respective MC energy.

It is possible to illustrate the significant underestimation of the WCD with a simplified example of typical events:

The reconstruction is designed for hadrons, and it correlates certain signal strengths with hadron energies. For photons, less than 2 % of energy goes into the muonic component while it is ≈ 12 % for protons (*c.f.* Fig. 7.15). For inclined showers with mainly muons reaching the detector, the WCD observes ≈ 6 times less signal for photon air showers than for proton air showers, even if they have the same primary energy. Thus, the reconstructed energy should be reduced by this magnitude. This is evident in the ratio of the reconstructed energies, as depicted in the bottom of Fig. 7.16. It yields values of the order of 0.1 with a small but visible primary energy dependence. The values are

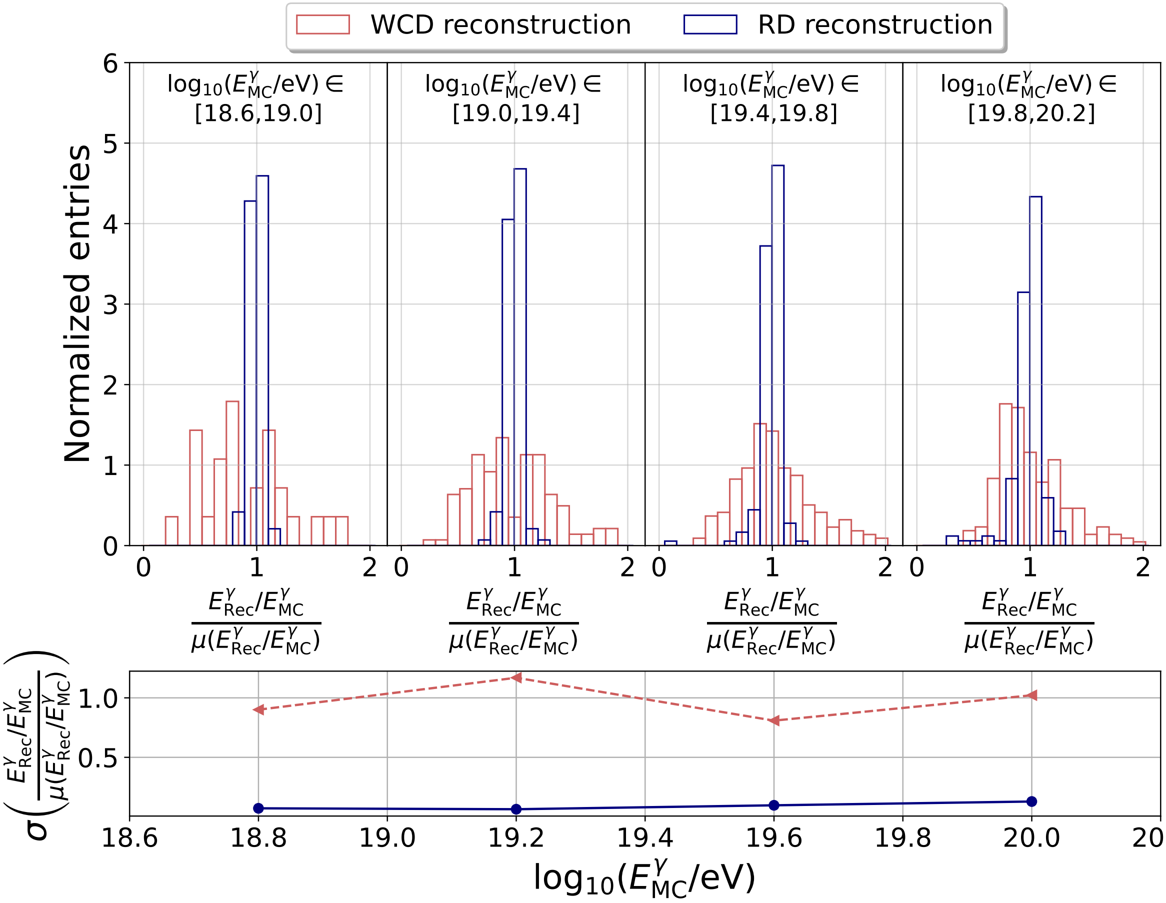

Figure 7.17: (Top) By the mean normalised distributions of the ratio of reconstructed and MC energy for photon induced showers and $\theta \in [65°, 85°]$. The panels show bins of increasing energy from left to right. The colours indicate the WCD reconstruction (red) and RD reconstruction (blue). (Bottom) Standard deviations of the distributions from (top) with the same colour coding and same energy bins.

slightly different from the above-mentioned estimation. This can occur because muon numbers are not just linearly correlating with energy.

The energy underestimation is typically corrected by using look-up tables, which are created utilising photon simulations. In the past, it was done for studies of vertical photon showers performed by Auger, in order to provide an estimate of the true photon energy. The look-up tables are binned, and for different reconstructed energies and zenith angles, a distinct correction factor is applied. The method aims to eliminate biases by shifting the mean of the binned distribution to the true value. However, it does not significantly reduce the spread of the binned distribution. This is depicted as an example in Fig. 7.17. It demonstrates the ratio of reconstructed energy to MC energy for various energy bins. As no look-up table for inclined photon showers is available, it can be imitated by adjusting the distribution by dividing it by the mean value. For comparison of the resolution of the RD and WCD reconstructions, it is done for both detectors. The distributions are therefore centred around the same value of 1. The distributions of the RD reconstruction exhibit a narrow peak at 1 and a low spread within this value. In contrast, the WCD distributions exhibit a broad spread, and only for higher energy bins, a clearly defined peak can be observed. This leads to an elevated standard deviation of the distributions, as depicted at the bottom. The RD distributions exhibit standard deviations of approximately 0.07 for the lower energy bins, and slightly increased standard deviations of 0.09 and 0.13 for the higher energy bins. This remains approximately a factor 10 lower compared to the WCD distributions. Here, one exhibits standard deviations in the order of 1.

It can be inferred that the RD provides a precise reconstruction at large zenith angles that is significantly improved in comparison to the WCD. The RD derives numerous advantages from inclined photon air showers, such as a high k^{EM} or large distance to the detector, which in turn render the WCD less sensitive. Hence, the RD possesses the potential to play a significant role not only in the detection of photons but also in the precise and accurate reconstruction and yields an increased likelihood for the identification of photons.

7.4 Outlook on a discrimination analysis

The previous section showed a significant underestimation of the energy estimation employed with the WCD, while the RD accurately determines the (EM) energy of the air shower. This difference is not expected for proton air showers, since the WCD reconstruction is designed for hadronic primaries. Discrimination studies of photons and protons (or generally hadrons) benefit from this circumstance and can use the weakness of the WCD reconstruction as a separation variable. In the subsequent discussion, the topic of discrimination power will be examined; however, it will not conclude with quantitative findings. This requires a different simulation set (uniform azimuth angles, more simulations), which is not existent at the moment of writing. This discussion should serve as an overview and indication of the level of discrimination power that can be expected. Four basic discrimination variables will be described. It is noteworthy that these parameters are not sophisticated, but rather educated guesses that represent the rationale behind selecting specific variables.

The initial variable pertains to the extent of the particle footprint, as indicated by the number of WCD stations exhibiting particle signal. Hadron primaries typically possess a significant number of stations with signal, sometimes exceeding 100 stations. Photon air showers can also possess many stations with particle signal, however, they typically have smaller particle footprints compared to hadron primaries. The magnitude of the particle footprint may provide a valuable indication that a photon can be excluded as the primary. However, it does not specifically point towards a photon primary, as a low number of stations can also be found for hadrons. The second variable is connected to the shower maximum, which is significantly different for photons and hadrons. The air density at X_{max} is chosen here as variable[2], representing the difference.

The subsequent two variables incorporate on the distinct reconstructions of RD and WCD. The energy reconstruction of both detectors has previously been discussed. The ratio of the estimations is taken as variable on shower level. Similarly, the ratio of the signal on station level can be calculated and summed for the three stations with most RD signal (the radio signal is here interpreted as the fluence magnitude).

The four discrimination variables are depicted in Fig. 7.18 as a scatter matrix for simulations possessing reconstructions of WCD and RD. The diagonal entries depict the distributions for photon and proton simulations, whereas the off-diagonal entries display the scatter plots for each of the two variables. The investigated variables demonstrate quite different discrimination power. The number of WCD stations with signal alone seems to perform the worst. Despite the distinct distribution shapes of photons and protons, they exhibit a nearly complete overlap. The tail of the proton distribution is longer towards a high number of stations. However, it fails to achieve the desired separation. The air density at the shower maximum performs only slightly better, with their maximum of the distribution at different locations. The summed ratio of station signals has distinct distribution shapes, as well as different locations of their maximum. Only a small percentage of proton simulations reach into the region of the photon maximum. The ratio of reconstructed energies exhibits the most superior performance. The distributions of photons and protons have nearly no overlap, with a narrow distribution for the photons. Only single proton events possess values that are comparable to the distribution of photons.

Even though an analysis would be primarily driven by the ratio of energies, other variables can yield valuable information in combination with it. This is indicated in the scatter plots. For instance, the summed ratio of station signals and the number of WCD stations with signal yield a discrimination that surpasses the individually observed discrimination. For low values of the signal ratio, proton air showers often have a high number of WCD signal stations, which can be discriminated from the photon

---

[2] In general, using X_{max} would be the more sophisticated variable. However, the reconstructed X_{max} is at the moment of writing not a parameter calculated in $\overline{\text{Off}}\underline{\text{line}}$. The air density is a parameter strongly connected. It is used here as it should have similar discrimination power.

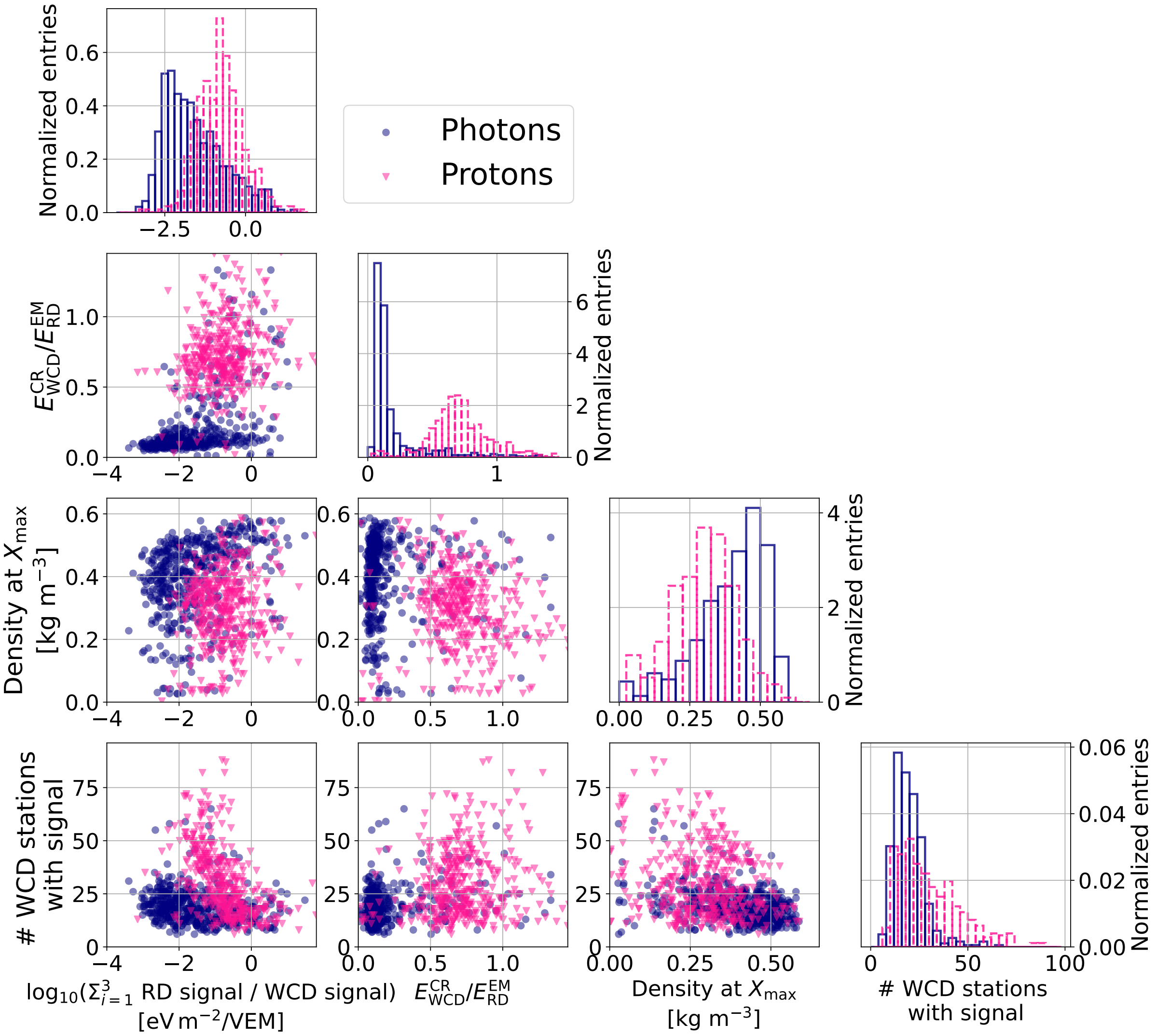

Figure 7.18: Scatter matrix of example discrimination variables (from left to right: summed ratio of the three stations with maximum radio signal, ratio of the WCD CR energy reconstruction and RD EM energy reconstruction, RD estimated density at shower maximum, number of WCD stations with signal). Diagonal entries show the distributions, off-diagonal entries depict the scatter plot of two variables. Photon simulations are shown in blue, proton simulations are depicted in magenta. Shown are only simulations with both RD and WCD energy reconstruction.

distribution. Thus, for a sophisticated discrimination analysis, it is necessary to perform a multivariate analysis. Typically, for photon analyses, the variables are projected onto one axis using e.g. a Fisher discriminant analysis, principal component analysis or a multi-layer perceptron. The best choice depends on the used variables and used training set (simulation or data).

Finally, a few things are worth noting. First, there are many things to enhance the discrimination power. The previous example used minimal quality cuts. Hence, mis-reconstructions of proton showers could end up within the photon distribution, e.g. for the ratio of WCD to RD energy reconstruction. These events could be identified by reasoned quality cuts, which would remove outliers from the proton distribution without cutting too many photon events. Furthermore, binning by the energy and zenith angle could be an easy way to improve the result. Secondly, adapting parameters such as S_b from previous photon searches, but including RD information in this variable, could help to find strong discrimination parameters. With a strong discrimination, which is expected due to the RD, one can also shift the candidate cut. The cut is usually set at the median of the photon distribution, but it is possible to shift it further towards the proton distribution for more photon events. Lastly, it has to be discussed whether multiple discrimination analyses should be performed. The aforementioned case pertains solely to showers that have undergone a successful WCD energy reconstruction. This represents a significant reduction in the distribution of photons. To mitigate this issue, the concept of the RD trigger was investigated in the first place. It needs to be studied, what happens in case a WCD reconstruction is not given and how the discrimination analysis changes with missing WCD information.

CHAPTER 8

APERTURE AND SKY COVERAGE OF THE INCLINED PHOTON SEARCH

The trigger and reconstruction efficiencies can ultimately be used to calculate an aperture. The ideal aperture of Auger can be calculated as

$$\mathcal{A}(\theta_{\text{lower}}, \theta_{\text{upper}}) = 3000\,\text{km}^2\,\text{sr} \cdot \pi \cdot (\cos^2(\theta_{\text{upper}}) - \cos^2(\theta_{\text{lower}})), \tag{8.1}$$

where θ_{upper} and θ_{lower} are the upper and lower bounds of the zenith range. The optimal and feasible aperture is subsequently determined through the calculation of trigger and cut efficiencies for various analyses.

First, the trigger efficiencies of the WCD and of the combination of WCD and RD are combined with the ideal aperture, shown in Fig. 8.1. The aperture in the only WCD case shows a well-ordered behaviour. The trigger efficiency and ideal aperture decreases with increasing zenith angle. Hence, their combination shows the same behaviour with $\approx 10\,\text{km}^2\,\text{sr}$ at the lowest energies for $\theta \leq 80°$ and increasing aperture with energy. For $\theta > 80°$, no aperture is observed for $E_{\text{MC}}^{\gamma} \leq 10\,\text{EeV}$ and $\approx 200\,\text{km}^2\,\text{sr}$ at the highest energies. For the combined case of WCD and RD, two competing effects are visible: decreasing ideal aperture but enhanced trigger efficiency with increasing zenith angle. Thus, for low energies and $\theta \in [65°, 70°]$, it shows the lowest aperture. For higher energies, as the trigger efficiency increases, it reverses and this zenith angle range starts to dominate, establishing an order sorted by the zenith angle.

The comparison of the cases of only WCD and the combination with RD shows a clear development. Generally, for higher energies the difference decreases, being the highest at low energies. Zenith angle wise, the lowest increase in aperture when adding RD can be seen for $\theta \in [65°, 70°]$ ($+181.6\,\text{km}^2\,\text{sr}$). The highest absolute gain in aperture is seen at the lowest energies for the medium zenith angles ranges of $\theta \in [70°, 75°]$ ($200\,\text{km}^2\,\text{sr}$,

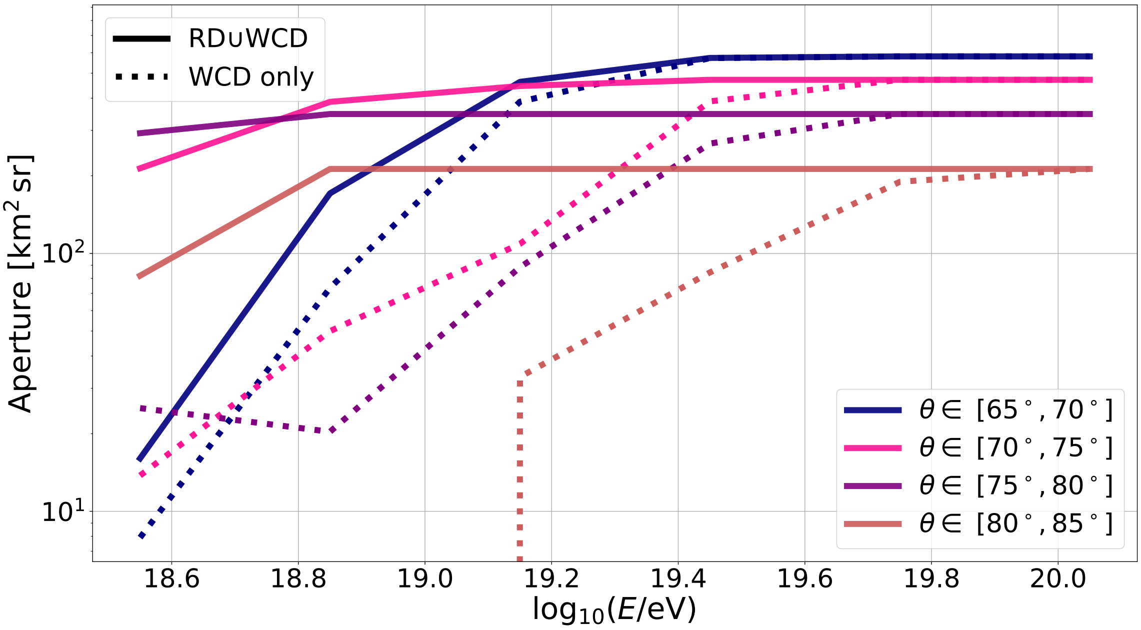

Figure 8.1: Aperture as function of energy. The different colours mark distinct zenith angles with a 5° binning. Solid lines represent the configuration with RD included, while the dotted lines show the current case of just particle triggers. Uncertainties are not shown to keep the plot legible.

$337\,\mathrm{km}^2\,\mathrm{sr}$, $337\,\mathrm{km}^2\,\mathrm{sr}$) and $\theta \in [75°, 80°]$ ($267\,\mathrm{km}^2\,\mathrm{sr}$, $326\,\mathrm{km}^2\,\mathrm{sr}$, $259\,\mathrm{km}^2\,\mathrm{sr}$). The largest relative gain over all energies can be found for $\theta \in [80°, 85°]$ (+120.3 %).

The apertures are now summed for all zenith angles. Figure 8.2 shows a comparison of the different configurations with their respective trigger efficiencies with the WCD photon search (2022) [104], which also includes selection cuts. Hence, for realistic discrimination analyses, the curves except the one from [104] will decrease too. Nonetheless, a comparison is conducted to provide an estimation of the magnitude of the enhancement in aperture. As the trigger efficiency is the only thing folded in the curves from this work, they have the same shape as the trigger efficiency at the different energies. They are just multiplied with the ideal RD aperture of $\mathcal{A}(65°, 85°) \approx 1,611\,\mathrm{km}^2\,\mathrm{sr}$. The WCD search includes the energies 10 EeV, 20 EeV and 40 EeV. The ideal RD aperture and ideal trigger scenario only slightly surpass the WCD photon search aperture at the lowest energy. Moreover, all three curves are significantly higher than the cases of inclined detection solely using WCDs or requesting WCD triggers in T3. For the two bins with higher energies, the aperture of the photon search is higher than for all other curves. However, the relative difference decreases as the trigger efficiency improves when RD is included.

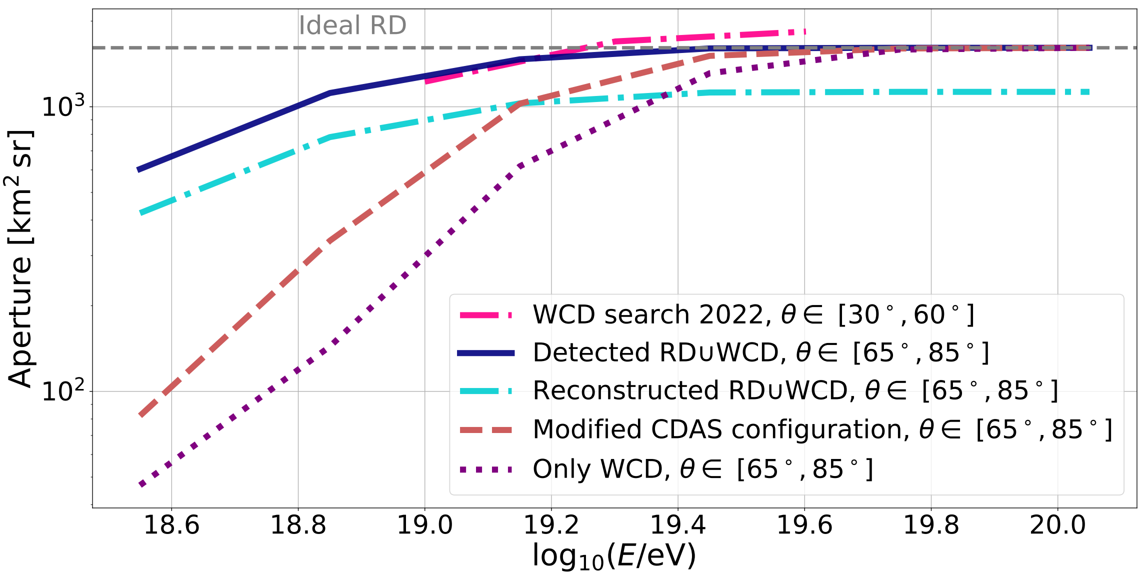

Figure 8.2: The aperture for different configurations is depicted at different energies. Shown are the aperture of the WCD photon search from [104] (cyan dash-dotted), the case of adding RD triggers without restrictions (blue solid), the case of adding RD triggers with the proposed CDAS modification (red dashed) and the current case of just WCD triggers (purple dotted). The grey dashed line shows the ideal RD aperture. Uncertainties are not shown to keep the plot legible.

One observes that the aperture is enhanced by incorporating the RD trigger. The gained aperture should yield new possibilities, not only from a quantitative perspective. The improved efficiency for high zenith angles increases the sky coverage of the Observatory to regions where no photon search is possible yet. This is depicted in Fig. 8.3, where the raw exposure (no efficiencies) is shown in a sky map. It compares two ranges of 20° in zenith angle. In the case for $\theta \in [40°, 60°]$, a major part of the sky map is not covered, including approximately a third of the supergalactic plane. For geometrical reasons, the overall exposure is significantly higher than for the case of $\theta \in [65°, 85°]$. However, most of the exposure is concentrated at one spot at 300° longitude and -30° latitude. This location is also covered by all lower zenith angle ranges. For higher zenith angles, this location is not covered, and the overall exposure is lower, but the sky coverage increases significantly. Now, there is only a comparable small blind spot. The revised sky coverage not only results in increased exposure and novel source locations for photon searches, but also enhances the overlap of sky coverage with Telescope Array. Hence, both observatories are able to perform independent photon searches of the same source location, or conduct cross comparisons among observatories providing a larger sky region for calibration.

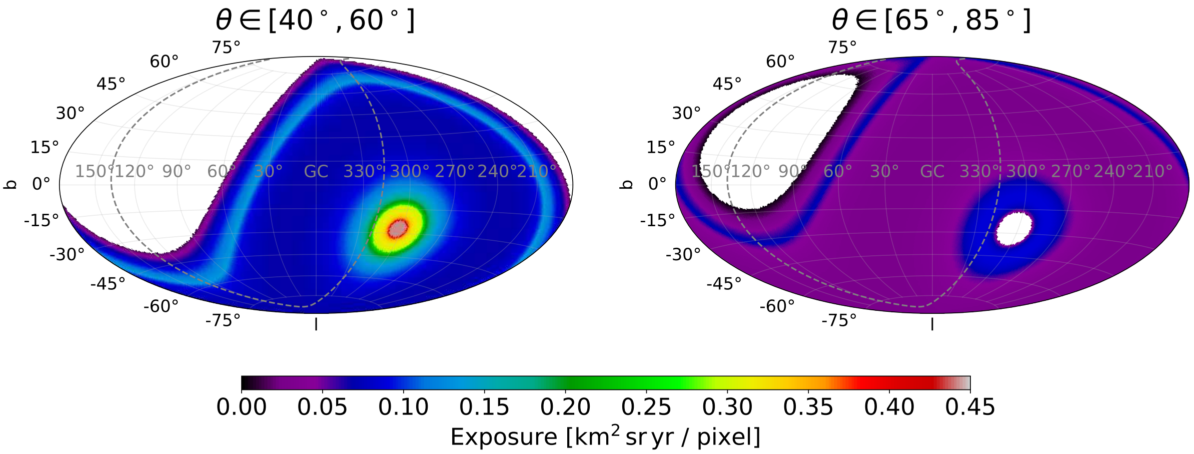

Figure 8.3: Exposure map for the ideal aperture. (Left) Map for the zenith angle range of 40° to 60°. (Right) Map for the zenith angle range of 65° to 85°.

CHAPTER 9

SUMMARY AND OUTLOOK

The detection of an UHE photon would be a milestone in astrophysics and would substantially aid determining the sources of UHE cosmic rays. The Radio Detector, as part of the AugerPrime upgrade, significantly enhances the sensitivity to purely EM air showers and is, thus, well suited for the detection of UHE photons. This thesis investigated the possibility of triggering, reconstruction and identification of inclined photons with the Radio Detector. It was shown that the Radio Detector results in improvements on multiple levels for photon searches, but employing its full potential only with a designated radio trigger.

In Chapter 4, a study of radio noise at the Pierre Auger Observatory was conducted, as radio noise is a substantial challenge for radio triggers and reconstructions. In order to fully understand the origin and occurrences of noise, a characterization was performed utilising periodic recorded noise from multiple times and locations. It has been shown that the noise appears in bursts: while a major time fraction is noise quiet with fluctuations of a few ADC counts, short periods yield strong noise with single dominating frequencies or transient events with air-shower like peaks. Noteworthy is the impact of lightning events, where bursts of radio noise can last over hours. A strong correlation of 0.91 has been determined between lightning occurrences and average radio peak amplitudes. These large spikes were calculated to result in radio trigger rates of more than 600 Hz and would cause crashes of the data acquisition. Due to their pulse shape similarity to air shower signals, it is difficult to suppresse or reject these lightning events. Contrary to the lightning events, mono-frequent and stationary noise sources were located by using the polarisation information of the recorded noise data. It was shown that sources of the 35 MHz-, 55 MHz- and 67 MHz-lines can be determined with single hotspots of origin. The 27 MHz-line, on the other hand, appeared to come from numerous sources at different locations.

A trigger concept was developed, which should be in accordance to both the Pierre Auger Observatory requirements and the handling of the challenging noise situation. Chapter 5 outlined the design of the trigger. It has been discussed that a classic threshold trigger fulfils all the requirements to significantly increase the aperture, while additional features, such as peak counting and inhibit of triggers during noise bursts, suppress the triggering of noise. The concept implemented in the firmware of the Radio Detector was subsequently used to evaluate the design and feasibility of the implementation on larger scales. Two test stations were selected and updated with the firmware and have been run in multiple configurations of the trigger settings. With this test, the findings about bursting noise sources from Chapter 4 were confirmed. Furthermore, it was shown that neither of the tested trigger settings is sufficient to suppress the noise so that the trigger is compatible with the limited bandwidth of the Observatory. Thus, a CDAS modification was presented, which shows a promising suppression of the noise read-out rate by requesting particle triggers in the event building and which could serve as an intermediate step for having a self-standing radio trigger.

Using CoREAS simulations, the inclined photon trigger efficiency was determined in Chapter 6. For the ideal scenario of a classic threshold trigger with an aimed threshold of 25 ADC counts, the trigger efficiency increases from below 20 % for the setup of just particle triggers to over 60 % for photon simulations with $\theta \in [65°, 85°]$ and $\log_{10}(E/\mathrm{eV}) \in [18.4, 20.2]$. It was demonstrated that the largest improvement is seen for the highest zenith angles, where full efficiency is already achieved for $E \geq 10^{18.7}$ eV, while for $\theta \in [65°, 70°]$ it is only observed for $E \geq 10^{19.3}$ eV. Furthermore, it was shown that the radio trigger leads to more read-out stations, improving the reconstruction probability. The ideal scenario was additionally compared to the scenario of implemented CDAS modifications, which was observed to have a lower trigger efficiency, but a 50 % relative increase compared to the current setup. Subsequently, it was discussed that the trigger efficiency with implemented CDAS modification can be improved in numerous ways. The most promising ansatz was demonstrated to be the online reconstruction of the zenith angle, which could help to suppress the dominating noise from the horizon and which would recover most of the trigger efficiency. Lastly, it was shown that the reconstruction of hadron air showers can profit from a radio trigger as well by increased trigger efficiency at low energies and enhanced number of read-out stations.

The reconstruction of photon air showers with the AugerPrime Radio Detector was investigated in Chapter 7. The combination of a radio trigger and an iterative, particle independent reconstruction chain improves the reconstruction efficiency by a factor of four, compared to the current setup. Furthermore, it was demonstrated that the radio reconstruction yields a precise and accurate determination of the arrival direction, with an opening angle $< 0.5°$. In contrast, features in the EM energy reconstruction of photons using the established standard method were obtained. An underestimation of the EM energy was observed for air showers with deep shower maximums, which was quantified and approaches for correcting for this bias were proposed. With applied fixes, an accurate determination of the EM energy was demonstrated with no bias and standard deviation of $< 10\,\%$. Compared to the particle detector reconstruction, the Radio Detector yields a 10 times better resolution. Lastly, it was outlined that the combination of information of both detectors results in a large discrimination power between photon and hadron showers.

Finally, all the findings of the pervious chapters were combined to evaluate the photon aperture of the AugerPrime Radio Detector when employing its full potential with a radio trigger. It was demonstrated that a significant increase in aperture by more than $1{,}000\,\mathrm{km}^2\,\mathrm{sr}$ for $\log_{10}(E/\mathrm{eV}) \in [18.7, 19]$ is achieved with smaller gains for higher energies. A similar aperture as for photon searches for the vertical case is observed. Moreover, an enhancement in sky coverage was achieved, which increases the overlap with other observatories.

This work paves the way for the future implementation of a self-standing radio trigger. It already shows promising results for the detection and reconstruction of inclined photon air showers. Nonetheless, studies should continue to improve the presented results and trigger efficiencies. With more stations installed, more locations to characterise the noise enviroment and additional CDAS test setups, a deeper and more comprehensive study of noise can be conducted. It is in particular of interest whether locations in the South-East are more noise quiet and if the demonstrated trigger is already compatible there. The CDAS test setup would help to implement an intermediate version of the radio trigger, leading to much more information about noise status and resulting trigger rate. With further information and triggered traces, extensive studies of the morphology of triggers could be conducted. This would help to improve the trigger design, which could have additional or advanced features. An important point would be to resolve limitations of the FPGA (which is possible by rewriting the code of the executed FFT for monitoring purposes), only then more advanced trigger concepts are possible. In summary, with additional possibilities and testing facilities, the radio trigger could make the next step for the full deployment, which itself would be a leap towards the detection and identification of photon air showers.

BIBLIOGRAPHY

[1] T. Wulf. Über die in der Atmosphäre vorhandene Strahlung von hoher Durchdringungsfähigkeit. volume 5, pages 152–157. March 1909.

[2] V. F. Hess. Über Beobachtungen der durchdringenden Strahlung bei sieben Freiballonfahrten. *Phys. Z.*, 13:1084–1091, 1912.

[3] K. Scherer, H. Fichtner, and O. Stawicki. The Heliosphere, Cosmic Rays, Climate. In *The Outer Heliosphere: The Next Frontiers*, volume 11 of *COSPAR Colloquia Series*, pages 493–496. Pergamon, 2001.

[4] D. V. Reames. The Two Sources of Solar Energetic Particles. *Space Science Reviews*, 175(1–4):53–92, January 2013.

[5] W. D. Apel et al. Kneelike structure in the spectrum of the heavy component of cosmic rays observed with kascade-grande. *Phys. Rev. Lett.*, 107:171104, Oct 2011.

[6] G. B. Orquera on behalf of the Pierre Auger Collaboration. The second knee in the cosmic ray spectrum observed with the surface detector of the Pierre Auger Observatory . PoS(ICRC2023)398, 2023.

[7] K. V. Ptitsyna and S. V. Troitsky. Physical conditions in potential accelerators of ultra-high-energy cosmic rays: updated Hillas plot and radiation-loss constraints. *Physics-Uspekhi*, 53(7):691–701, October 2010.

[8] E. Fermi. On the Origin of the Cosmic Radiation. *Phys. Rev.*, 75:1169–1174, Apr 1949.

[9] G. M. Webb. First order and second order Fermi acceleration of energetic charged particles by shock waves. *The Astrophysical Journal*, 270:319–338, July 1983.

[10] P. Cristofari, P. Blasi, and D. Caprioli. Cosmic ray protons and electrons from supernova remnants. *Astronomy amp; Astrophysics*, 650:A62, June 2021.

[11] A. Erlykin, T. Wibig, and A. W. Wolfendale. Young supernova remnants and the knee in the cosmic ray spectrum. *Astrophysics and Space Sciences Transactions*, 7(2):179–182, May 2011.

[12] V. Zirakashvili. Cosmic Ray Acceleration beyond the Knee up to the Ankle in the Galactic Wind Halo. *Journal of Physics: Conference Series*, 47(1):185, oct 2006.

[13] T. Vieu, S. Gabici, V. Tatischeff, and S. Ravikularaman. Cosmic ray production in superbubbles. *Monthly Notices of the Royal Astronomical Society*, 512(1):1275–1293, February 2022.

[14] A. Aab et al. Features of the Energy Spectrum of Cosmic Rays above 2.5×10^{18} eV Using the Pierre Auger Observatory. *Phys. Rev. Lett.*, 125:121106, Sep 2020.

[15] A. Abdul Halim et al. Constraining the sources of ultra-high-energy cosmic rays across and above the ankle with the spectrum and composition data measured at the Pierre Auger Observatory. *Journal of Cosmology and Astroparticle Physics*, 2023(05):024, May 2023.

[16] G. Di Sciascio. Measurement of Energy Spectrum and Elemental Composition of PeV Cosmic Rays: Open Problems and Prospects. *Applied Sciences*, 12(2), 2022.

[17] K. Greisen. End to the Cosmic-Ray Spectrum? *Phys. Rev. Lett.*, 16:748–750, Apr 1966.

[18] G. T. Zatsepin and V. A. Kuz'min. Upper Limit of the Spectrum of Cosmic Rays. *Soviet Journal of Experimental and Theoretical Physics Letters*, 4:78, August 1966.

[19] F. W. Stecker. Photodisintegration of Ultrahigh-Energy Cosmic Rays by the Universal Radiation Field. *Phys. Rev.*, 180:1264–1266, Apr 1969.

[20] J. M. Gonzáles on behalf of the Pierre Auger Collaboration. Combined fit to the spectrum and composition data measured by the Pierre Auger Observatory including magnetic horizon effects. PoS(ICRC2023)288, 2023.

[21] E. Guido on behalf of the Pierre Auger Collaboration. Combined fit of the energy spectrum and mass composition across the ankle with the data measured at the Pierre Auger Observatory. PoS(ICRC2023)311, 2021.

[22] The Pierre Auger Collaboration and the Telecscope Array Collaboration. Measurement of UHECR energy spectrum with the Pierre Auger Observatory and the Telescope Array. PoS(ICRC2023)406, 2023.

[23] L. Morejon. *New Interaction Models of Ultra-high-energy Cosmic Rays from a Nuclear Physics Approach*. PhD thesis, Humboldt U., Berlin, 2021.

[24] K.-H. Kampert and M. Unger. Measurements of the cosmic ray composition with air shower experiments. *Astroparticle Physics*, 35(10):660–678, 2012.

[25] A. D. Supanitsky. Determination of the Cosmic-Ray Chemical Composition: Open Issues and Prospects. *Galaxies*, 10(3), 2022.

[26] T. Fitoussi on behalf of the Pierre Auger Collaboration. Depth of Maximum of Air-Shower Profiles above $10^{17.8}$ eV Measured with the Fluorescence Detector of the Pierre Auger Observatory and Mass-Composition Implications. PoS(ICRC2023)319, 2023.

[27] F. Salamida on behalf of the Pierre Auger Collaboration. Highlights from the Pierre Auger Observatory. PoS(ICRC2023)016, 2023.

[28] M. Vecchi et al. The Rigidity Dependence of Galactic Cosmic-Ray Fluxes and Its Connection With the Diffusion Coefficient. *Frontiers in Physics*, 10, March 2022.

[29] P. Abreu et al. Arrival Directions of Cosmic Rays above 32 EeV from Phase One of the Pierre Auger Observatory. *The Astrophysical Journal*, 935(2):170, August 2022.

[30] M. Erdmann, G. Müller, M. Urban, and M. Wirtz. The nuclear window to the extragalactic universe. *Astroparticle Physics*, 85:54–64, 2016.

[31] V. Heesen et al. Detection of magnetic fields in the circumgalactic medium of nearby galaxies using Faraday rotation. *Astronomy amp; Astrophysics*, 670:L23, February 2023.

[32] M. Unger and G. R. Farrar. The Coherent Magnetic Field of the Milky Way, 2024.

[33] R. Jansson and G. R. Farrar. A new model of the Galactic magnetic field. *The Astrophysical Journal*, 757(1):14, August 2012.

[34] X. H. Sun, W. Reich, A. Waelkens, and T. A. Enßlin. Radio observational constraints on Galactic 3D-emission models. *Astronomy amp; Astrophysics*, 477(2):573–592, November 2007.

[35] M. S. Pshirkov, P. G. Tinyakov, P. P. Kronberg, and K. J. Newton-McGee. Deriving the global structure of the galactic magnetic field from Faraday rotation

measures of extragalactic sources. *The Astrophysical Journal*, 738(2):192, August 2011.

[36] A. Batista et al. CRPropa 3.2 — an advanced framework for high-energy particle propagation in extragalactic and galactic spaces. *Journal of Cosmology and Astroparticle Physics*, 2022(09):035, September 2022.

[37] L. Morejon. Probability distributions for UHECRs propagation. PoS(ICRC2023)284, 2023.

[38] G. Golup on behalf of the Pierre Auger Collaboration. An update on the arrival direction studies made with data from the Pierre Auger Observatory. PoS(ICRC2023)252, 2023.

[39] The Pierre Auger Collaboration and the Telecscope Array Collaboration. Update on the searches for anisotropies in UHECR arrival directions with the Pierre Auger Observatory and the Telescope Array. PoS(ICRC2023)521, 2023.

[40] M. F. Skrutskie et al. The Two Micron All Sky Survey (2MASS). *The Astronomical Journal*, 131(2):1163, feb 2006.

[41] C. Lunardini, G. S. Vance, K. L. Emig, and R. A. Windhorst. Are starburst galaxies a common source of high energy neutrinos and cosmic rays? *Journal of Cosmology and Astroparticle Physics*, 2019(10):073–073, October 2019.

[42] M. Tanabashi and et al. Review of Particle Physics. *Phys. Rev. D*, 98:030001, Aug 2018.

[43] A. Bobrikova et al. Predicting the UHE photon flux from GZK-interactions of hadronic cosmic rays using CRPropa 3. PoS(ICRC2021)449, 2021.

[44] C. Bérat et al. Diffuse Flux of Ultra-high-energy Photons from Cosmic-Ray Interactions in the Disk of the Galaxy and Implications for the Search for Decaying Super-heavy Dark Matter. *The Astrophysical Journal*, 929(1):55, April 2022.

[45] O.E. Kalashev and M.Yu. Kuznetsov. Constraining heavy decaying dark matter with the high energy gamma-ray limits. *Physical Review D*, 94(6), September 2016.

[46] M. Kachelrieß, O.E. Kalashev, and M.Yu. Kuznetsov. Heavy decaying dark matter and IceCube high energy neutrinos. *Physical Review D*, 98(8), October 2018.

[47] R. Ruffini, G. V. Vereshchagin, and S.-S. Xue. Cosmic absorption of ultra high energy particles. *Astrophysics and Space Science*, 361(2), January 2016.

[48] G. Breit and J. A. Wheeler. Collision of Two Light Quanta. *Phys. Rev.*, 46:1087–1091, Dec 1934.

[49] S. V. Demidov and O. E. Kalashev. Double pair production by ultra-high-energy cosmic ray photons. *Journal of Experimental and Theoretical Physics*, 108(5):764–769, May 2009.

[50] S. Bonometto and M. J. Rees. On Possible Observable Effects of Electron Pair Production in QSOs. *Monthly Notices of the Royal Astronomical Society*, 152(1):21–35, 04 1971.

[51] P. Abreu et al. Cosmological implications of photon-flux upper limits at ultra-high energies in scenarios of Planckian-interacting massive particles for dark matter, 2022.

[52] R. Engel, D. Heck, and T. Pierog. Extensive Air Showers and Hadronic Interactions at High Energy. *Annual Review of Nuclear and Particle Science*, 61(Volume 61, 2011):467–489, 2011.

[53] W. Heitler. *The quantum theory of radiation*, volume 5 of *International Series of Monographs on Physics*. Oxford University Press, Oxford, 1936.

[54] J. Matthews. A Heitler model of extensive air showers. *Astroparticle Physics*, 22(5):387–397, 2005.

[55] J. Pawlowsky, K. H. Kampert, and J. Rautenberg. Photon-likeness of hadron showers and impact of Lorentz boosting. *arXiv*, page 2407.18318, 2024.

[56] A. Haungs et al. KCDC — The KASCADE Cosmic-ray Data Centre. *Journal of Physics: Conference Series*, 632(1):012011, jul 2015.

[57] A. Aab et al. Reconstruction of inclined air showers detected with the Pierre Auger Observatory. *Journal of Cosmology and Astroparticle Physics*, 2014(08):019, aug 2014.

[58] T. Huege. Radio detection of cosmic ray air showers in the digital era. *Physics Reports*, 620:1–52, 2016.

[59] F. G. Schröder. Radio detection of cosmic-ray air showers and high-energy neutrinos. *Progress in Particle and Nuclear Physics*, 93:1–68, 2017.

[60] D. Ardouin et al. Geomagnetic origin of the radio emission from cosmic ray induced air showers observed by CODALEMA. *Astroparticle Physics*, 31(3):192–200, 2009.

[61] G. A. Askar'yan. Excess negative charge of an electron-photon shower and its coherent radio emission. *Zh. Eksp. Teor. Fiz.*, 41:616–618, 1961.

[62] A. Aab et al. Probing the radio emission from air showers with polarization measurements. *Phys. Rev. D*, 89:052002, Mar 2014.

[63] A. Aab et al. The Pierre Auger Cosmic Ray Observatory. *Nuclear Instruments and Methods in Physics Research Section A: Accelerators, Spectrometers, Detectors and Associated Equipment*, 798:172–213, Oct 2015.

[64] A. Aab et al. The Pierre Auger Observatory Upgrade - Preliminary Design Report, 2016.

[65] J. Abraham et al. The fluorescence detector of the Pierre Auger Observatory. *Nuclear Instruments and Methods in Physics Research Section A: Accelerators, Spectrometers, Detectors and Associated Equipment*, 620(2-3):227–251, aug 2010.

[66] A. Aab et al. Spectral Calibration of the Fluorescence Telescopes of the Pierre Auger Observatory. *Astroparticle Physics*, 95, 09 2017.

[67] D. Schmidt et al. Scintillator Surface Detector simulations for AugerPrime. *EPJ Web of Conferences*, 210:06010, 2019.

[68] Enrique Varela. The low-energy extensions of the Pierre Auger Observatory. *Journal of Physics Conference Series*, 468:2013–, 11 2013.

[69] Abreu et al. Performance of the 433 m surface array of the Pierre Auger Observatory. volume ICRC2021, page 224, 2021.

[70] A. Aab et al. Muons in air showers at the Pierre Auger Observatory: Mean number in highly inclined events. *Phys. Rev. D*, 91:032003, Feb 2015.

[71] G. Marsella on behalf of the Pierre Auger Collaboration. AugerPrime Upgraded Electronics. 2021.

[72] X. Bertou et al. Calibration of the surface array of the Pierre Auger Observatory. *Nuclear Instruments and Methods in Physics Research Section A: Accelerators, Spectrometers, Detectors and Associated Equipment*, 568(2):839–846, 2006.

[73] R. Sato on behalf of the Pierre Auger Collaboration. AugerPrime implementation in the DAQ systems of the Pierre Auger Observatory. PoS(ICRC2023)373, 2023.

[74] A. Abdul Halim et al. AugerPrime surface detector electronics. *Journal of Instrumentation*, 18(10):P10016, oct 2023.

[75] A. Aab et al. Design and implementation of the AMIGA embedded system for data acquisition. *Journal of Instrumentation*, 16(07):T07008, July 2021.

[76] L. Niemitz. *Lightning detection at the Pierre Auger Observatory.* PhD thesis, Bergische Universitaet Wuppertal, 2017.

[77] M. Büsken. A new network of electric field mills at the Pierre Auger Observatory. *Journal of Physics: Conference Series*, 2398:012004, 12 2022.

[78] M. Kasten. Aufbau einer Mess-Station zur kontinuierlichen Bestimmung der Bodeneigenschaften beim Auger Engineering Radio Array, 2015.

[79] P. Abreu et al. Antennas for the detection of radio emission pulses from cosmic-ray induced air showers at the Pierre Auger Observatory. *Journal of Instrumentation*, 7(10):P10011–P10011, October 2012.

[80] A. Nelles. *Radio emission of air showers : the perspective of LOFAR and AERA*. PhD thesis, Nijmegen U., Nijmegen U., 2014.

[81] P. Abreu et al. Results of a self-triggered prototype system for radio-detection of extensive air showers at the Pierre Auger Observatory. *Journal of Instrumentation*, 7(11):P11023, nov 2012.

[82] A. Aab et al. Measurement of the Radiation Energy in the Radio Signal of Extensive Air Showers as a Universal Estimator of Cosmic-Ray Energy. *Phys. Rev. Lett.*, 116:241101, Jun 2016.

[83] M. Büsken on behalf of the Pierre Auger Collaboration. Towards a Cosmic-Ray Energy Scale with the Auger Engineering Radio Array. PoS(ARENA2024)028, 2024.

[84] M. Gottowik on behalf of the Pierre Auger Collaboration. Measurements of Inclined Air Showers with the Auger Engineering Radio Array at the Pierre Auger Observatory . PoS(ICRC2023)274, 2019.

[85] W.D. Apel et al. LOPES-3D: An antenna array for full signal detection of air-shower radio emission. *Nuclear Instruments and Methods in Physics Research Section A: Accelerators, Spectrometers, Detectors and Associated Equipment*, 696:100–109, 2012.

[86] D. Kostunin et al. Present status and prospects of the Tunka Radio Extension. *EPJ Web of Conferences*, 216:01005, 01 2019.

[87] F. Schlüter. *Expected sensitivity of the AugerPrime Radio Detector to the masses of ultra-high-energy cosmic rays using inclined air showers.* PhD thesis, Karlsruher Institut für Technologie, 2022.

[88] S. Argirò et al. The offline software framework of the Pierre Auger Observatory. *Nuclear Instruments and Methods in Physics Research Section A: Accelerators, Spectrometers, Detectors and Associated Equipment*, 580(3):1485–1496, October 2007.

[89] P. Abreu et al. Advanced functionality for radio analysis in the Offline software framework of the Pierre Auger Observatory. *Nuclear Instruments and Methods in Physics Research Section A: Accelerators, Spectrometers, Detectors and Associated Equipment*, 635(1):92–102, April 2011.

[90] G. Burke and A. Pogglo. Numerical Electromagnetics Code (NEC) - Method of Moments, 1981.

[91] A. Reuzki on behalf of the Pierre Auger Collaboration. Drone-Based Calibration of AugerPrime Radio Antennas at the Pierre Auger Observatory. PoS(ARENA2024)029, 2024.

[92] M. Gottowik. *Radio Hybrid Reconstruction and Analysis of Inclined Air Showers with AERA of the Pierre Auger Observatory - Measuring the Hadronic Shower Development and Cosmic Ray Mass Composition.* PhD thesis, Bergische Universitaet Wuppertal, 2021.

[93] F. Schlüter and T. Huege. Signal model and event reconstruction for the radio detection of inclined air showers. *Journal of Cosmology and Astroparticle Physics*, 2023(01):008, January 2023.

[94] J. Abraham et al. Trigger and aperture of the surface detector array of the Pierre Auger Observatory. *Nuclear Instruments and Methods in Physics Research Section A: Accelerators, Spectrometers, Detectors and Associated Equipment*, 613(1):29–39, 2010.

[95] P. Billoir. New proposal to improve the local trigger of the Surface Detector. *Auger internal note, GAP2011-089*, 2011.

[96] P. Billoir. Proposition to improve the local trigger of Surface Detector for low energy showers. *Auger internal note, GAP2009-179*, 2009.

[97] M. Settimo, P. Billoir, and N. Hemery. A study of trigger rates for ToTd and MoPS. *Auger internal note, GAP2015-019*, 2015.

[98] J. Abraham et al. Upper limit on the cosmic-ray photon flux above 10^{19} eV using the surface detector of the Pierre Auger Observatory. *Astroparticle Physics*, 29(4):243–256, May 2008.

[99] N. González on behalf of the Pierre Auger Collaboration. Search for primary photons at tens of PeV with the Pierre Auger Observatory. PoS(ICRC2023)238, 2023.

[100] Y. A. Fomin et al. Estimate of the fraction of primary photons in the cosmic-ray flux at energies 10^{17} eV from the EAS-MSU experiment data. *J. Exp. Theor. Phys.*, 117:1011–1023, 2013.

[101] W. D. Apel et al. KASCADE-Grande Limits on the Isotropic Diffuse Gamma-Ray Flux between 100 TeV and 1 EeV. *The Astrophysical Journal*, 848(1):1, oct 2017.

[102] P. Abreu et al. A Search for Photons with Energies Above 2 $\times 10^{17}$ eV Using Hybrid Data from the Low-Energy Extensions of the Pierre Auger Observatory. *The Astrophysical Journal*, 933(2):125, jul 2022.

[103] A. Aab et al. Search for photons with energies above 10^{18} eV using the hybrid detector of the Pierre Auger Observatory. *Journal of Cosmology and Astroparticle Physics*, 2017(04):009, apr 2017.

[104] P. Abreu et al. Search for photons above 10^{19} eV with the surface detector of the Pierre Auger Observatory, 2022.

[105] E. Oleg et al. Telescope Array search for EeV photons. PoS(ICRC2021)864, 2021.

[106] R. U. Abbasi et al. Search for point sources of ultra-high-energy photons with the Telescope Array surface detector. *Monthly Notices of the Royal Astronomical Society*, 492(3):3984–3993, February 2020.

[107] A. M. Hillas. Angular and energy distributions of charged particles in electron-photon cascades in air. *Journal of Physics G: Nuclear Physics*, 8(10):1461, oct 1982.

[108] D. Heck, J. Knapp, J. N. Capdevielle, G. Schatz, and T. Thouw. *CORSIKA: a Monte Carlo code to simulate extensive air showers.* 1998.

[109] B. Pont. RD Bad Periods. *Auger internal note, GAP2024-042*, 2024.

[110] M. Konzack, H. Bozdog, A. Haungs, and F. Schröder. Specifications of the AERA Beacon and its Software. *Auger internal note, GAP2010-099*, 2010.

[111] Innovation Science Telecommunications, Government of Canada and Office of the Deputy Minister Economic Development Canada. RIC-18 — General Radio Service. *https://ised-isde.canada.ca/site/spectrum-management-telecommunications/en/licences-and-certificates/radiocom-information-circulars-ric/ric-18-general-radio-service-grs*, 2002.

[112] P. Abreu et al. Antennas for the detection of radio emission pulses from cosmic-ray induced air showers at the Pierre Auger Observatory. *Journal of Instrumentation*, 2012.

[113] S. Timmer and D. Nitz. Private communication.

[114] M. Gottowik. Private communication.

[115] J. Neuser. *Cosmic Rays and the Atmospheric Electric Field.* PhD thesis, Bergische Universitaet Wuppertal, 2015.

[116] M. S. Muzio on behalf of RNO-G Collaboration. Multimessenger Potential of the Radio Neutrino Observatory in Greenland. PoS(ICRC2023)444, 2023.

[117] A. Nelles et al. A Survey of Narrowband and Broadband Radio-frequency Interference at AERA. *Auger internal note, GAP2011-062*, 2011.

[118] J.A. Aguilar et al. Triboelectric backgrounds to radio-based polar ultra-high energy neutrino (UHEN) experiments. *Astroparticle Physics*, 145:102790, 2023.

[119] S. W. Barwick et al. Design and Performance of the ARIANNA Hexagonal Radio Array Systems, 2014.

[120] R. Purvinskis et al. Multiple Wavelength Free-Space Laser Communications. volume 4975, pages 12–19, 07 2003.

[121] Data monitoring of the Pierre Auger Observatory. *https://moni.auger.org.ar/*.

[122] T. Huege, M. Ludwig, and C. W. James. Simulating radio emission from air showers with CoREAS. *AIP Conference Proceedings*, 1535(1):128–132, 05 2013.

[123] J. Pawlowsky. available on iRODS:
/pauger/Radio/Simulations/library/RdIdealGrid_high_zenith_photon
/pauger/Radio/Simulations/library/RdIdealGrid_high_zenith_proton.

[124] P. Homola, R. Engel, A. Pysz, and H. Wilczyński. Simulation of ultra-high energy photon propagation with PRESHOWER 2.0. *Computer Physics Communications*, 184(5):1468–1475, 2013.

[125] B. List. Statistical error of efficiency determination from weighted events. `www.desy.de/~blist/notes/effic.ps.gz`, 1999. updated 2003.

[126] R. Uzeiroska. Verbesserung des externen Triggers von AERA für ausgedehnte Luftschauer am Pierre-Auger-Observatorium, 2021.

[127] J. Köhler on behalf of the GRAND Collaboration. Next-Generation Triggering: A Novel Event-Level Approach. PoS(ARENA2024)061, 2024.

[128] F. Schlüter, M. Gottowik, T. Huege, and J. Rautenberg. Refractive displacement of the radio-emission footprint of inclined air showers simulated with CoREAS. *The European Physical Journal C*, 80, 07 2020.

[129] The Pierre Auger collaboration. Reconstruction of inclined air showers detected with the pierre auger observatory. *Journal of Cosmology and Astroparticle Physics*, 2014(08):019–019, August 2014.

[130] J. Sitarek. TeV Instrumentation: current and future, 2022.

[131] C. Bellenghi, P. Padovani, E. Resconi, and P. Giommi. Correlating High-energy IceCube Neutrinos with 5BZCAT Blazars and RFC Sources. *The Astrophysical Journal Letters*, 955(2):L32, September 2023.

[132] R. Abbasi et al. Search for correlations of high-energy neutrinos detected in IceCube with radio-bright AGN and gamma-ray emission from blazars, 2023.

[133] A. Aab et al. Reconstruction of events recorded with the surface detector of the Pierre Auger Observatory. *Journal of Instrumentation*, 15(10):P10021–P10021, October 2020.

Danksagungen

Uff, da ist es wohl geschafft, die Arbeit ist fertig. Was am Anfang wie ein unüberwindbarer Brocken aussah, fiel dann doch leichter als gedacht, was vor allem an den Menschen um mich herum lag, welche mich unterstützt haben.

Der erste Dank gebührt Herrn Prof. Dr. Karl-Heinz Kampert. Seit nun mehr als 7 Jahren gehöre ich Ihrer Arbeitsgruppe an. Diese Zeit hat mich geprägt und es war mir eine Freude, hier zu arbeiten. Ich danke Ihnen für die Ausbildung zum Wissenschaftler, was mich mein ganzes Leben lang begleiten wird.

Ich möchte meiner Zweitprüferin, Frau Prof. Dr. Anna Nelles danken, dass sie das Gutachten für diese Arbeit schreibt. Dies ist nicht selbstverständlich für einen Studenten einer anderen Universität und Kollaboration zu übernehmen, umso mehr freue ich mich, dass sie eingewilligt hat.

Mit absoluter Sicherheit muss ich als nächstes Dr. Julian Rautenberg danken. Es ist und war nicht immer das Einfachste, mit dir zu arbeiten, aber mit Sicherheit das Spannendste und Inspirierendste. Ich kenne kaum jemanden, der seinen Job mit so viel Hingabe und Aufopferung macht, sodass es auch mich selbst angesteckt. Ohne dich wäre ich sicherlich nicht so weit gekommen und ich weiß, wie oft und wie sehr du dich für mich eingesetzt hast. So wie ich heute immer noch von meinen Physiklehrern in der Schule erzähle, welche mich davon abgebracht haben Physik abzuwählen, so wirst du in Zukunft erwähnt, wenn mich jemand fragt, warum ich auf die Schnapsidee gekommen bin, einen Doktor zu machen (deine Macke mit diesem 'Köln' werde ich unerwähnt lassen).

Dem Leser bleibt überlassen zu bewerten, wie gut diese Arbeit letztendlich ist. Sie wäre mit Sicherheit sprachlich und inhaltlich sehr viel schlechter ohne meine Korrekturleser:innen. Danke an Marvin, Sonja, Sven, Leonel, meine kleine Schwester Marisa und Julian! Es hat sehr viel geholfen.

Einen Dank an die Arbeitsgruppe der Astros, es war etwas Einmaliges und es wurde mit euch nie langweilig. Ich bin fest davon überzeugt, dass nur mit guten Kollegen eine erfolgreiche Promotion möglich ist. Über die Jahre sind es zu viele, um alle aufzuzählen, seid euch trotzdem meines Dankes gewiss. Ich werde das jährliche Flunkyball-Spiel mit euch missen.

An alle, die mich über die Jahre begleitet haben, seien es Kommilitonen oder Kollegen und Freunde von Auger. Es hat Spaß gemacht mit euch, was vieles ausmacht. Danke!

Als Letztes möchte und muss ich auf jeden Fall noch meine Familie und Freunde (welche natürlich auch schon weiter oben mit drinstehen) erwähnen, die mich fortwährend unterstützt haben. Bei denen ich auch mal miese Laune rauslassen konnte, wenn es doch nicht so lief, oder die mich bei einem Heißgetränk beraten haben, wenn ich das Ziel aus den Augen verloren hatte. Danke an meine Eltern, Sigrid und Rolf, welche mich seit 27 Jahren nicht besser unterstützen könnten. Danke an meine Schwestern Julia und Marisa, die es verstanden haben, wenn ich über die letzten Jahre auch mal abwesend war. Und natürlich, als Letztes, meine Freundin Sara. Seitdem wir uns kennen, hast du mich motiviert und oft eine höhere Meinung von mir gehabt, als ich es selbst hatte. Du warst der Lichtblick, wenn alles dunkel zu sein schien. Çox saĝ olun!

LIST OF FIGURES

LIST OF TABLES

APPENDIX A: OFFLINE IMPLEMENTATION OF THE RD TRIGGER

Below is the implementation of the `RdSimulationRadioTrigger`-module.

```
#include "RdSimulationRadioTrigger.h"
#include <fwk/CentralConfig.h>

#include <utl/config.h>
#include <utl/AugerUnits.h>
#include <utl/ErrorLogger.h>
#include <utl/Reader.h>
#include <utl/TraceAlgorithm.h>
#include <utl/String.h>
#include <utl/Math.h>

#include <evt/Event.h>

#include <revt/Header.h>
#include <revt/REvent.h>
#include <revt/Station.h>
#include <revt/Channel.h>
#include <revt/StationRecData.h>
#include <revt/StationTriggerData.h>

#include <rdet/RDetector.h>

#include <sevt/SEvent.h>
#include <sevt/Station.h>
#include <sevt/StationSimData.h>
#include <sevt/StationTriggerData.h>

#include <sdet/SDetector.h>
#include <sdet/Station.h>
#include <sdet/StationTriggerUtil.h>


using namespace std;
using namespace revt;
using namespace fwk;
using namespace utl;
using namespace det;
using namespace sdet::Trigger;


namespace RdSimulationRadioTrigger {

  VModule::ResultFlag
  RdSimulationRadioTrigger::Init()
  {
    Branch topBranch =
      CentralConfig::GetInstance()->GetTopBranch("RdSimulationRadioTrigger");
    topBranch.GetChild("InfoLevel").GetData(fInfoLevel);
    topBranch.GetChild("ThresholdMethod").GetData(fThresholdMethod);
    topBranch.GetChild("RadioT2Threshold").GetData(fRadioT2Threshold);
    topBranch.GetChild("RejectRFIThreshold").GetData(fRejectRFIThreshold);
    topBranch.GetChild("RejectRFIMultiplicity").GetData(fRejectRFIMultiplicity);

    ostringstream info;
```

```
  info << "\n\tUsing "<< (fThresholdMethod ? "Geometric sum" : "Maximum channel") << " as RD trigger method \n"
       << "\tThreshold for a radio T2 trigger: "<< fRadioT2Threshold << " ADC counts";
  INFOFinal(info);

  return eSuccess;
}


VModule::ResultFlag
RdSimulationRadioTrigger::Run(evt::Event& event)
{
  // Check if there are events at all
  if(!event.HasREvent()) {
    WARNING("No radio event found!");
    return eContinueLoop;
  }

  ostringstream msg;

  vector<int> RDT2Stations;
  REvent& rEvent = event.GetREvent();
  const auto& eventTime = event.GetHeader().GetTime();

  if(!event.HasSEvent()) {
    event.MakeSEvent();
  }

  sevt::SEvent& sEvent = event.GetSEvent();

  const Detector& Det = Detector::GetInstance();
  const rdet::RDetector& radioDet = Det.GetRDetector();

  // loop through stations and for every station through every channel
  for (auto& rStation : rEvent.StationsRange()) {

    std::pair<ChannelTimeSeries, ChannelTimeSeries> channelAdcTrace;

    for (const auto& channel : rStation.ChannelsRange()) {

      const unsigned int channelID = channel.GetId();

      // Checking if the channel of the processed station contribute to the event.
      // If not, continue with the next channel.
      if (!rStation.HasChannel(channelID) || !channel.IsActive())
        continue;

      if (channelID == 0)
        GetTraceWithoutDCOffset(channelAdcTrace.first, channel);
      else
        GetTraceWithoutDCOffset(channelAdcTrace.second, channel);
    }

    if (channelAdcTrace.first.GetSize() != channelAdcTrace.second.GetSize() ) {
      msg.str("");
      msg << "Station " << rStation.GetId()
          << " is rejected as its channel traces do not have the same length!";
      WARNING(msg);

      rStation.SetExcludedReason(eHardwareMismatch);
      continue;
    }

    // binning should be the same for both channels, just take Ch1
    const int binning = rStation.GetChannel(1).GetChannelADCTimeSeries().GetBinning();

    double peakAmplitude = 0;
    double peakTime = 0;
    int sample = 0;

    std::vector<unsigned int> t2Bins;
    std::vector<unsigned int> rfiBins;
    bool signalT2 = false;

```

```
      // calculate geometric sum of both channels for threshold trigger
      std::vector<double> finalAdcTrace;

      const int maxCh0 = *max_element(channelAdcTrace.first.Begin(),
            channelAdcTrace.first.End(), AbsValue);
      const int maxCh1 = *max_element(channelAdcTrace.second.Begin(),
            channelAdcTrace.second.End(), AbsValue);

      if (fThresholdMethod == 0) {  // maximum of both channels
        if (maxCh0 > maxCh1)
          std::copy(channelAdcTrace.first.Begin(), channelAdcTrace.first.End(),
                    std::back_inserter(finalAdcTrace));
        else
          std::copy(channelAdcTrace.second.Begin(), channelAdcTrace.second.End(),
                    std::back_inserter(finalAdcTrace));
      } else if (fThresholdMethod == 1) {  // geometric sum
        for (unsigned int i = 0; i < channelAdcTrace.first.GetSize() ; ++i) {
          finalAdcTrace.push_back(sqrt(Sqr(channelAdcTrace.first[i]) + Sqr(channelAdcTrace.second[i])));
        }
      } else {
        ERROR("Threshold method not existent.");
        return eFailure;
      }

      for (unsigned int i = 0; i < finalAdcTrace.size(); ++i) {
        if (std::abs(finalAdcTrace[i]) > fRadioT2Threshold)
          t2Bins.push_back(i);
        if (std::abs(finalAdcTrace[i]) > fRejectRFIThreshold)
          rfiBins.push_back(i);
      }

      // if no trigger just move on with next station
      if (t2Bins.empty()) {
        msg.str("");
        msg << "Station " << rStation.GetId()
            << " has no T2 trigger (not above threshold).";
        INFODebug(msg);
        continue;
      }

      /* see if it is really a signal T2 or likely RFI.
         For that check that there are not too many bins over some threshold within 500ns
         after 1mus after the trigger */
      for (auto const& t2bin: t2Bins) {
        const int cnt = std::count_if(std::begin(rfiBins), std::end(rfiBins),
            [&t2bin](unsigned int rfibin){return (rfibin >= t2bin+25 && rfibin <= t2bin+275);});
        if (cnt <= fRejectRFIMultiplicity) {
          peakAmplitude = finalAdcTrace[t2bin];
          peakTime = t2bin * binning / 1000;
          sample = t2bin;
          signalT2 = true;
          break;
        }
      }

      if (!signalT2) {
        msg.str("");
        msg << "Station " << rStation.GetId()
            << " is rejected as it is a RFI trace!";
        WARNING(msg);

        rStation.SetRejectedReason(eNoisy);
        continue;
      }

      // here comes the SEvent part. Pushing it to the SEvent and make WCD traces
      const int sStID = rStation.GetId() - radioDet.GetRdSdStationIdLink();
      RDT2Stations.push_back(sStID);

      if (!sEvent.HasStation(sStID))
        sEvent.MakeStation(sStID);

      sevt::Station& sStation = sEvent.GetStation(sStID);
```

```

      if (!sStation.HasSimData())
        sStation.MakeSimData();

      // okay now pushing some stuff into RD
      // this is ugly, I know, but until now we do not know where the time difference
      // between particles and radio comes from (electronics, physics or both) and how it behaves
      // in simulations vs data. When we investigated that, we should change this. But it works here
      rStation.GetTriggerData().SetSelfTriggerTime(
        (peakTime + rStation.GetRecData().GetParameter(eTraceStartTime)/1000 + 13.2) * 1000 * nanosecond);
      rStation.GetTriggerData().SetTriggerSource(StationTriggerData::eSelf);
      rStation.GetTriggerData().SetSelfTriggerType(StationTriggerData::eT2Threshold);
      rStation.GetTriggerData().SetSelfTriggerBin(sample);
      rStation.GetTriggerData().SetSelfTriggerAmp(peakAmplitude);

      vector<const TimeDistributionI*> traces;

      int startBin = 0;
      int stopBin = 0;
      PrepareTraces(sStation, startBin, stopBin, traces);

      if (traces.size() < 3)
        sStation.SetRejected(sevt::StationConstants::eNoCalibData);

      const auto& dStation = Detector::GetInstance().GetSDetector().GetStation(sStation);
      const int WCDTrigBin = rStation.GetTriggerData().GetSelfTriggerTime() / dStation.GetFADCBinSize();
      const int traceStart = std::max(WCDTrigBin - (int)dStation.GetFADCTraceLength(), startBin);
      Buffer(sStation, eventTime, sevt::StationTriggerData::eRDThreshold, sevt::StationTriggerData::ePLDRD,
             traceStart, WCDTrigBin);
    }

    if (!RDT2Stations.empty()) {
      ostringstream info;
      info << "\nAdding stations:" << '\n' << String::OfSortedIds(RDT2Stations) << " as RD T2s";
      INFO(info);
    }

    return eSuccess;
  }


  VModule::ResultFlag
  RdSimulationRadioTrigger::Finish()
  {
    ostringstream info;
    info << "\n\tThere were " << fNbOfSaturatedChannels << " saturated channels!";
    INFO(info);

    return eSuccess;
  }


  void
  RdSimulationRadioTrigger::GetTraceWithoutDCOffset(ChannelTimeSeries& currTrace, const Channel& channel)
  {
    const auto adcTrace = channel.GetChannelADCTimeSeries();
    const double mean = TraceAlgorithm::Mean(adcTrace, 0, adcTrace.GetSize() - 1);
    for (auto& adcSignal : adcTrace)
      currTrace.PushBack((double)adcSignal - mean);
  }


  bool
  RdSimulationRadioTrigger::AbsValue(double a , double b)
  {
    return abs(a) < abs(b);
  }

}
```

```
<moduleControl>
```

```

  <loop numTimes="unbounded" pushEventToStack="yes">

    <module> EventFileReaderOG                    </module>

    <loop numTimes="1" pushEventToStack="yes">
      <!-- initialize Radio simulation -->
      <module> EventGeneratorOG                   </module>

      <!-- we put changed RdStationAssociator here
           to create SD stations also for no-particle WCDS -->
      <module> RdStationAssociator                </module>
      <module> RdEventInitializer                 </module>

      <module> RdAntennaStationToChannelConverter   </module>
      <module> RdChannelResponseIncorporator        </module>
      <module> RdChannelResampler                   </module>
      <module> RdChannelTimeSeriesClipper           </module>
      <module> RdChannelVoltageToADCConverter       </module>

      <module> SdAccidentalInjectorKG </module>
      <module> G4StationSimulatorOG </module>

      <loop numTimes="unbounded" pushEventToStack="no">
        <module> CachedShowerRegeneratorOG </module>
        <module> G4StationSimulatorOG </module>
      </loop>

      <module> SdSimulationCalibrationFillerOG    </module>
      <module> SdPMTSimulatorOG                   </module>
      <module> SdFilterFADCSimulatorMTU           </module>
      <module> SdBaselineSimulatorOG              </module>
      <!-- initialize Radio simulation -->
      <module> RdChannelNoiseImporter_RD          </module>
      <module> RdChannelADCClipper                </module>

      <module> RdSimulationRadioTrigger           </module>

      <module> TankTriggerSimulatorOG             </module>
      <module> TankGPSSimulatorOG                 </module>

      <module> CentralTriggerSimulatorXb          </module>
      <module> CentralTriggerEventBuilderOG       </module>

      <module> RdStationSimulationRejector        </module>

      <module> EventBuilderOG                     </module>
      <module> EventCheckerOG                     </module>
      <module> RdTimeJitterAdder                  </module>

      <try>
        &SdHASSimReconstruction;
      </try>

      <module> RdChannelADCToVoltageConverter     </module>
      <module> RdChannelUpsampler                 </module>

      <module> RdChannelPedestalRemover           </module>
      <module> RdChannelResponseIncorporator      </module>
      <module> RdChannelTimeSeriesTaperer         </module>

      &RdIterativeDirectionReconstruction;

      <module> RdHASLDFFitter                     </module>


    </loop>

  <module> RecDataWriterNG                    </module>

  </loop>

</moduleControl>
```

Appendix B: Proposed CDAS modification

Below is the implementation of the CDAS implementation. There are no changes after line 277; hence, it is not depicted.

```
 1 /*! \file
 2     \brief Main trigger algorithms
 3 */
 4 #include "XbAlgo.h"
 5 #include "XbArray.h"
 6 #include <cstdlib>
 7 #include <cstring>
 8 #include <iostream>
 9 #include <fstream>
10 #include <string>
11
12 using std::vector;
13 using std::stringstream;
14
15 #define FREE(_x_) { free(_x_); _x_ = nullptr; }
16
17 /// t2 at the end of the second that will be used in both seconds
18 static struct t2 extrat2[MAXOVERLAP], extrat2old[MAXOVERLAP];
19 /// t2 from one of the doublets to be used in the doublet special trigger
20 static struct t2 carmenmiranda[MAXCM];
21 /// the fake trigger, not in cluster with any trigger, to be used when one removes a trigger from a
       cluster
22 static struct t2 fake;
23 static int nextra = 0, delay = 0, delaycm = 0, delaymr = 0, delaydn = 0;
24 /// number of t2 per time bin
25 static unsigned short ncompteurt2[MAXBINNUMBER], ncompteurtot[MAXBINNUMBER];
26 /// histogram of these t2 per time bin, poiting to the precise t2
27 static struct t2 *compteurt2[MAXBINNUMBER][MAXSTATINONEBIN], *compteurtot[MAXBINNUMBER][
      MAXSTATINONEBIN];
28 static int binnumber = MAXBINNUMBER, oldbinnumber = MAXBINNUMBER, binsize;
29 static int cour[5];
30 /// number of t2 cluster
31 static int nbt2cluster;
32 /// t2 clusters
33 static struct t2list t2cluster[1000];
34 /// output of the algorithm: a list of clusters
35 vector < t2list > out;
36
37 int observer = 0;                 // To request a specific station
38
39 /// initialisation of XbAlgoT2 algorithm, building fake station and resetting histograms
40 void XbAlgoT2Init() {
41   fake.ID = FAKE;
42   fake.time = 1100000;
43   for (int j = 0; j < MAXBINNUMBER; j++)
44     ncompteurt2[j] = ncompteurtot[j] = 0;
45 }
46
47 /// Full Array current trigger: 2C1 & 3C2 & 4C4
48 int XbAlgoT3FullArray() {
49   return ((cour[1] > 0) && (cour[1] + cour[2] > 1)) && (cour[1] + cour[2] + cour[3] + cour[4] > 2);
50 }
51
52 /// ToT current trigger: 2C1 & 3C2
53 int XbAlgoT3ToT() {
54   return ((cour[1] > 0) && (cour[1] + cour[2] > 1));
55 }
```

```

/// Function called when more than MAXSTATINONEBIN are in 5 consecutive bins of the time histogram
void HugeShower(struct t2 *input, int nt2, int msec) {
  int nhugestat=0, nrdstat=0;
  // keeping all stations within 100 us to be safe
  for (int j = 0; j < nt2; j++)
    if ((input[j].time > msec - 100) && (input[j].time < msec + 100)) {
      if (input[j].energy == RDVALUE)
        nrdstat++;
      nhugestat++;
    }
  const float rdRatio = (float)nrdstat/(float)nhugestat;
  if (! nhugestat || rdRatio >= rdMaxRatio)
    return;
  // building the event
  t2cluster[nbt2cluster].nelem = nhugestat;
  t2cluster[nbt2cluster].algo = "BIG";
  t2cluster[nbt2cluster].point = (struct t2 *) malloc(nhugestat * sizeof(struct t2));
  int m=0;
  for (int j = 0; j < nt2; j++)
    if ((input[j].time > msec - 100) && (input[j].time < msec + 100)) {
      *(t2cluster[nbt2cluster].point + m) = input[j];
      m++;
    }
  if (nbt2cluster<999) nbt2cluster++;
}

/// Function called to find clusters
void XbAlgoFindCluster(int minstat,struct t2 *input, int nt2, unsigned short *nbt2inbin, struct t2 *
     listt2inbin[MAXBINNUMBER][MAXSTATINONEBIN],int (*T3func)(),const char *algo) {
  int i,j,k,l,m,p;
  int index,nstat;
  int total = nbt2inbin[0] + nbt2inbin[1] + nbt2inbin[2] + nbt2inbin[3] + nbt2inbin[4];
  static struct t2 *liste[100];
  int onlyrd, validTr, totLikes;
  // j: center of the sliding bin-2 -> bin+2 window
  for (j = 2; j < binnumber - 2; j++) {
    // if we get enough stations in the sliding window, and there are stations in the central bin
    if (total >= minstat && nbt2inbin[j] > 0) {
      // if there is more than MAXSTATINONEBIN in the time bins
      // (is here to protect from memory violation if it happened, for big showers)
      if (total >= MAXSTATINONEBIN) {
        if (input && j>5) HugeShower(input, nt2, (j-5) * binsize);
      } else {
        /* for all the stations in the middle of the window */
        for (k = 0; k < nbt2inbin[j]; k++) {
          cour[0] = cour[1] = cour[2] = cour[3] = cour[4] = 0;
          /* counting the neighbour in each crown for all the stations  in the window */
          for (l = -2; l < 3; l++)
            for (m = 0; m < nbt2inbin[j + l]; m++)
              cour[(int) neighbour[listt2inbin[j][k]->ID * ROW + (int) listt2inbin[j + l][m]->ID]]++;
          if (T3func()) { // if the cluster is Ok
            /* we have to remove stations too far away in time */
            /* we do it now to optimise */
            /* now we will use lists of pointers */
            index = 0;
            for (l = -2; l < 3; l++)
              for (m = 0; m < nbt2inbin[j + l]; m++)
                liste[index++] = listt2inbin[j + l][m];
            /* 5us per crown + dtime jitter */
            for (l = 0; l < total; l++) {
              if (abs(listt2inbin[j][k]->time - liste[l]->time)
                  > 5 * neighbour[listt2inbin[j][k]->ID * ROW + liste[l]->ID] + dtime) {
                // station not time compatible => 1 less neighbour, replaced by fake station
                cour[(int) neighbour[listt2inbin[j][k]->ID * ROW + (int) liste[l]->ID]]--;
                liste[l] = &fake;
              }
            }
            nstat = cour[1] + cour[2] + cour[3] + cour[4];
            /* we have to mark stations with 2 t2 in the same cluster:
             * they only count as one, but both are kept                    */
            for (i = 0; i < total; i++) {
              for (l = i + 1; l < total; l++) {
                if (liste[i]->ID == liste[l]->ID) {
```

```
                  cour[(int) neighbour[listt2inbin[j][k]->ID * ROW + (int) liste[l]->ID]]--;
                }
              }
            }
            /* request that > 5% = rdMaxRatio of triggers in valid T3 are not RD
            e.g. 1WCD trigger for up to 19 stations in T3, 2WCD trigger from 20 etc.*/
            onlyrd = 0;
            validTr = 0;

            for (p = 0; p < total; p++) {
              if (liste[p]->energy == RDVALUE)
                onlyrd++;

              if (liste[p]->energy != 0)
                validTr++;
            }
            const float rdRatio = (float)onlyrd/(float)validTr;

            if (T3func() && (rdRatio <= rdMaxRatio)) { // check again the cluster once bad timing stations have been removed
              // found a new cluster: building it
              nstat++;          /* + the central one */
              t2cluster[nbt2cluster].nelem = nstat;
              t2cluster[nbt2cluster].algo = algo;
              t2cluster[nbt2cluster].point = (struct t2 *) malloc(nstat * sizeof(struct t2));
              m = 0;
              for (l = 0; l < total; l++) {
                if (neighbour[listt2inbin[j][k]->ID * ROW + liste[l]->ID] > 0) {
                  *(t2cluster[nbt2cluster].point + m) = *liste[l];
                  m++;
                }
              }
              *(t2cluster[nbt2cluster].point + m) = *listt2inbin[j][k];
              if (nbt2cluster<999) nbt2cluster++;
            }
          }
        }
      }
    }
    // sliding window: add new bin, remove old one.
    total += nbt2inbin[j + 3] - nbt2inbin[j - 2];
    nbt2inbin[j - 2] = 0;
  }
}

/// Main function, processing T2 and returning clusters of T2
vector < t2list > XbAlgoT2Process(struct t2 *input, int nt2) {
  static struct t2 min;
  int nt2cm = 0, ntot = 0;
  int i, j, l;
  unsigned int k, m;
  int mink, supp, tcm, tdn, tmr, nbstat;
  static struct t2list t2mergedclusters[1000];

  out.clear();
  nbt2cluster=0;
  if (nt2 <= 0)
    return out;
  // upgrading configuration if needed
  if (newt2config) {
    delay = trivial_algo / 10;
    delaymr = delaydn = delaycm = carmen_miranda / 10;
    newt2config = 0;
  }
  // fill the histogram with >13 us bins
  // WARNING, there is a 50 usec covering with previous second (actually, 5 bins=5*binsize us)
  // bin size of the histogram is computed dynamically to be fast also when there are few t2s
  // binsize = 500000 / nt2;
  // if (binsize > 1000) binsize = 1000;
  // else if (binsize < 12) binsize = 12; // To get 2 (bins) * 12 (binsize) = 24 us > 20 (4 crowns) + 3 (jitter)
  binsize = 12; // fixed size now
  oldbinnumber = binnumber;
  binnumber = 1110000 / binsize;
```

```
  // filling the histogram with t2 from the previous second
  if (nextra > MAXOVERLAP) {
    stringstream s;
    s << "Too many extra triggers: " << nextra;
    InternalLog(s.str().c_str(),IKWARNING);
    nextra = MAXOVERLAP;
  }
  for (j = 0; j < nextra; j++) {
    extrat2old[j].time = extrat2[j].time - 1000000;     /* -1000000 as it is from previous second */
    extrat2old[j].ID = extrat2[j].ID;
    extrat2old[j].energy = extrat2[j].energy;
    k = 5 + extrat2old[j].time / binsize;        /* +5 for the 50us copy */
    if (5 + extrat2old[j].time / binsize < 0) {
      stringstream s;
      s << "Negative new time: " << 5 + extrat2old[j].time / binsize;
      InternalLog(s.str().c_str(),IKWARNING);
      k=0;                                   /* could happen if bin size change dramatically from one second to the other one */
    }
    if (debug) {
      stringstream s;
      s << "extra t2:" << extrat2old[j].time << " -> " << k;
      InternalLog(s.str().c_str(),IKDEBUG);
    }
    if ((l = ncompteurt2[k]++) < MAXSTATINONEBIN)
      compteurt2[k][l] = &extrat2old[j];
    if ((extrat2old[j].ID == CARMEN) || (extrat2old[j].ID == MIRANDA)
        || (extrat2old[j].ID == MOULIN) || (extrat2old[j].ID == ROUGE)
        || (extrat2old[j].ID == DIA) || (extrat2old[j].ID == NOCHE))
      carmenmiranda[nt2cm++] = extrat2old[j];
    if (extrat2old[j].energy >= TOTVALUE)
      if ((l = ncompteurtot[k]++) < MAXSTATINONEBIN)
        compteurtot[k][l] = &extrat2old[j];
  }
  // filling histogram with all new t2
  nextra = 0;
  for (j = 0; j < nt2; j++) {
    if (input[j].time > 1000000) {
      stringstream s;
      s << "Time too big: " << input[j].time << " from LS " << input[j].ID;
      InternalLog(s.str().c_str(),IKERROR);
    }
    if (input[j].ID<100) continue; // WARNING!!!! Removing infill and doublets here. was is XbPm before!!!!!
    if (input[j].time > 1000000) continue;    /* should never happen */
    k = 5 + input[j].time / binsize;     /* +5 for the 50us copy (it's 5 bins) */
    // keeping t2 from the end of the second for next second
    if (input[j].time > 1000000 - 5*binsize) {
      extrat2[nextra++] = input[j];
      if (nextra >= MAXOVERLAP) {
        stringstream s;
        s << "Too many new extra triggers: " << nextra << ", removing 100";
        InternalLog(s.str().c_str(),IKERROR);
        nextra = MAXOVERLAP-100;
      }
    }
    if ((l = ncompteurt2[k]++) < MAXSTATINONEBIN)
      compteurt2[k][l] = &input[j];
    // filling special doublet trigger list
    if ((input[j].ID == CARMEN) || (input[j].ID == MIRANDA) ||
        (input[j].ID == MOULIN) || (input[j].ID == ROUGE) || (input[j].ID == DIA) || (input[j].ID == NOCHE))
      carmenmiranda[nt2cm++] = input[j];
    // filling tot t2 histogram
    if (input[j].energy >= TOTVALUE) {
      if ((l = ncompteurtot[k]++) < MAXSTATINONEBIN)
        compteurtot[k][l] = &input[j];
      ntot++;
    }
  }
  if (verbose) {
    stringstream s;
    s << "TOT triggers: " << ntot;
    InternalLog(s.str().c_str(),IKDEBUG);
```

```
  }
  /* 2C1&3C2&4C4 configuration disabled in RD CDAS */
//  XbAlgoFindCluster(4,input,nt2,ncompteurt2,compteurt2,&XbAlgoT3FullArray,"2C1&3C2&4C4");
  /* Find clusters with TOT algorithm */
  XbAlgoFindCluster(3,NULL,0,ncompteurtot,compteurtot,&XbAlgoT3ToT,"TOT2C1&3C2");
  // cleaning

  ...
  // from here as before in original CDAS

}

/// frees the malloced part of the list of t2
void XbAlgoFree(t2list in) {
  FREE(in.point);
}

/// builds t3 from a list of t2
t3 XbAlgoT3Build(struct t2list in) {
  // from here as before in original CDAS
}
```

APPENDIX C: PHOTON ENERGY PARAMETRISATION

Formula 3.4 is inverted to fit the estimated S_{Rad} using the MC EM energy. The photon simulations were selected using the MC cuts from Tab. 7.1. The parameters were shown in Tab. 7.2.

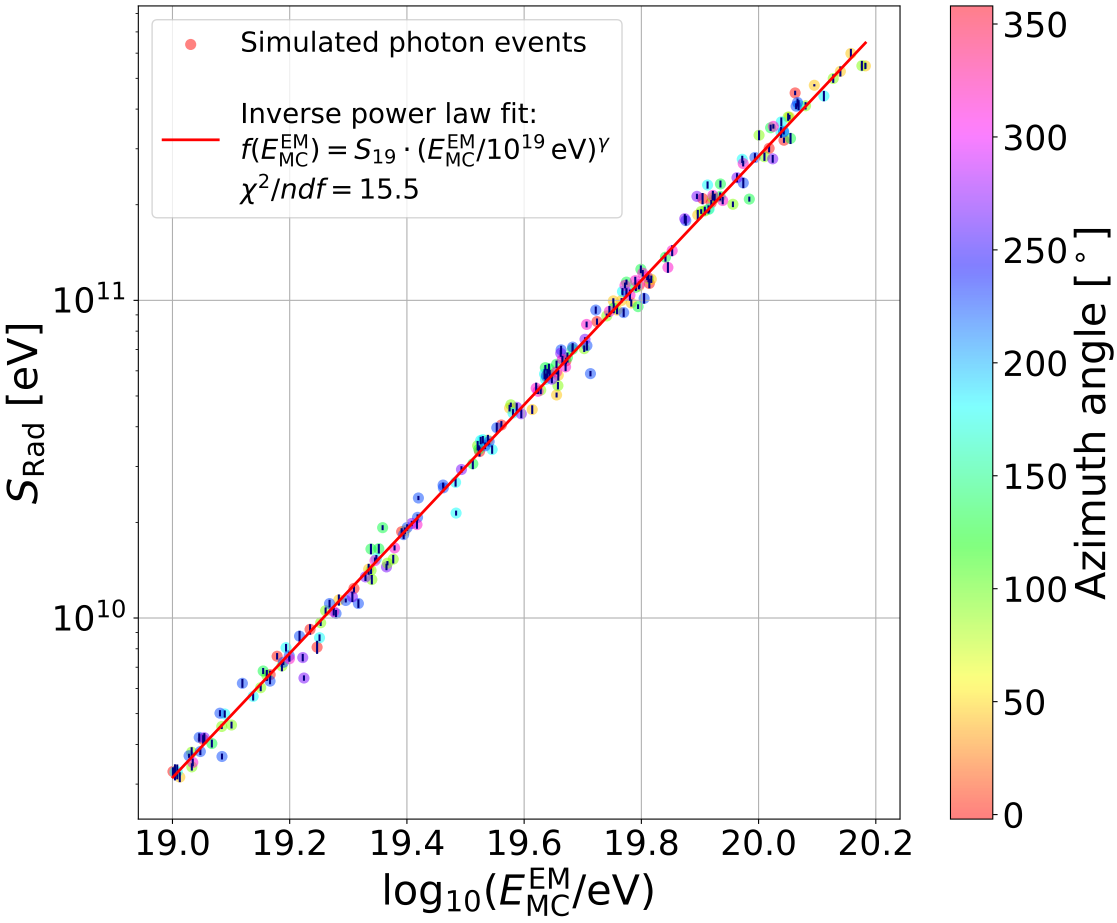

Figure .1: Fit of S_{Rad} using the MC EM energy. The colour scale depicts the azimuth angle of the photon air shower.

Statutory declaration

I hereby declare that the thesis submitted is my own unaided work. All direct or indirect sources used are acknowledged as references. This thesis was not previously presented to another examination board and has not been published.

Eidesstattliche Erklärung

Hiermit versichere ich, die vorliegende Arbeit selbstständig und unter ausschließlicher Verwendung der angegebenen Literatur und Hilfsmittel erstellt zu haben. Die Arbeit wurde bisher in gleicher oder ähnlicher Form keiner anderen Prüfungsbe- hörde vorgelegt und auch nicht veröffentlicht.

Wuppertal, August 7, 2024 **Jannis Pawlowsky**